Development of Ultra High Temperature Matrix Composites using a Reactive Melt Infiltration Process

Zur Erlangung des akademischen Grades eines

DOKTORS DER INGENIEURWISSENSCHAFTEN (Dr.-Ing.)

von der KIT-Fakultät Maschinenbau des
Karlsruher Instituts für Technologie (KIT)
angenommene

DISSERTATION

von

Dipl.-Ing. Marius Kütemeyer

Tag der mündlichen Prüfung: 15.02.2021

Hauptreferent: Prof. Dr.-Ing. Dietmar Koch
Korreferenten: Prof. Jon Binner und Prof. Dr. rer. nat. Michael Hoffmann

Acknowledgment

This thesis at hand was conducted during my employment as a research scientist at the German Aerospace Center (DLR) in Stuttgart. The research within this thesis has received funding from the European Union's Horizon 2020 "Research and innovation program" under grant agreement No. 685594 (C3HARME).
The author would like to thank Professor Dietmar Koch for giving me the great opportunity to define the research topic of this thesis and his support the entire time, I greatly appreciate his trust. I also want to thank Professor Jon Binner for his great advice and reviewing my work, his knowledge always is a great support. Further I would like to thank Professor Michael Hoffmann for his support.
For supporting me and answering many of my questions arising while developing these materials, I would like to thank Dr. Martin Frieß. Furthermore the author would like to especially thank the following people for all the discussions, contribution, support and help: Daniel, Tilo, Stefan, Raouf, Christian, Christian, Oliver, Thomas, Henning, Markus, Markus, Matthias, Bernd, Enrico, Steffen, Omar, Bill, Antonio, Luca, Laura, Henning, Correy, Darren, Joe, Schantall, Laura, Miriam, Moritz, Roswitha, Heinrich.

Contents

List of Symbols vii

Abstract xii

1. Introduction 1
- 1.1. Diborides . . . 4
- 1.2. Demands for Hypersonic Flight . . . 5

2. State of the Art 8
- 2.1. Processing . . . 8
  - 2.1.1. Sintering . . . 8
  - 2.1.2. Polymeric Route . . . 10
  - 2.1.3. Vapor Deposition . . . 10
  - 2.1.4. Colloidal Processing . . . 10
  - 2.1.5. Reactive Melt Infiltration . . . 11
- 2.2. Ceramic Composites . . . 12
  - 2.2.1. Fracture Mechanics . . . 13
  - 2.2.2. Fibers . . . 16
  - 2.2.3. Matrix . . . 17
  - 2.2.4. Fiber Matrix Interface . . . 18
- 2.3. Material Properties . . . 19
  - 2.3.1. Oxidation . . . 21

3. Experimental Methods 26
- 3.1. Density and Porosity Measurement . . . 26
  - 3.1.1. Archimedes Principle . . . 27
  - 3.1.2. Mercury Porosimetry . . . 27
- 3.2. Drop Shape Analysis . . . 28
- 3.3. Electrophoretic Deposition . . . 30
- 3.4. Thermogravimetric Analysis . . . 32
- 3.5. Scanning Electron Microscope . . . 32
- 3.6. Energy-Dispersive X-Ray Spectroscopy . . . 33
- 3.7. X-Ray Diffraction . . . 33
- 3.8. 3D Atom Probe . . . 33

3.9. Mechanical Testing . . . 34
3.9.1. Three Point Bending . . . 34
3.10. Fracture Toughness . . . 35
3.11. Single Filament Fiber Tests . . . 37
3.12. Fiber Volume Content . . . 37

4. Determining Zr Based RMI Process **38**
4.1. Influencing Factors . . . 39
4.1.1. Capillary Structure . . . 39
4.1.2. Phase Formation . . . 40
4.1.3. Contact Angle . . . 42
4.1.4. Exothermic Influence . . . 51
4.2. Material Selection . . . 52
4.2.1. Boron Source and Precursors . . . 52
4.2.2. Fiber Reinforcements . . . 76
4.2.3. Fiber Coatings . . . 78
4.2.4. Melts . . . 86
4.3. Composite Manufacturing . . . 87
4.3.1. Preform Manufacturing . . . 87
4.3.2. Pyrolysis . . . 89
4.3.3. Boron Oxide Infiltration . . . 93
4.3.4. Reactive Melt Infiltration . . . 94
4.4. Discussion of Manufacturing . . . 102

5. UHTCMC Characterization **107**
5.1. Micro Structure . . . 107
5.1.1. Fibers . . . 107
5.1.2. Matrix . . . 110
5.2. Mechanical Characterization . . . 116
5.2.1. Fiber Coated Samples . . . 116
5.2.2. Uncoated Fiber Samples . . . 117
5.3. Oxidation . . . 122
5.4. Discussion of Characterization . . . 125

6. Summary **129**

7. Outlook **133**

List of Figures **134**

List of Tables **138**

Bibliography **139**

A. Appendix **159**

A.1. Calculation of Phase, Mass and Volume Fractions 159

A.2. Image Phase Analysis 160

B. List of Publications **162**

List of Symbols

Latin Symbols:

a	Crack Length
at%	Atomic Fraction
B	Width
C	Contiguity Factor
d	Diameter
D	Thickness
e'	Porosity
E	Elastic Modulus / Young's Modulus
f	Displacement
F	Force
FVC	Fiber Volume Content
g	Universal Gravity Constant
G	Energy Release Factor
h	Height
K	Stress Intensity Factor
l	Length
L	Load Bearing Distance
m	Mass
ot	Oxidation Layer Thickness
p	Gas Pressure
$\dot{q}$	Heat Flux
r	Radius
R	Principal Radius of Curvature
S	Phase
t	Time
u	Velocity
vol%	Volume Fraction
V	Volume
wt%	Weight Fraction
W	Work

Greek Symbols:

γ	Surface Tension
ϵ	Strain
ε	Energy
η	Dynamic Viscosity
θ	Contact Angle
ν	Poisson's Ratio
ρ	Density
σ	Tension
τ	Shear Tension
Γ	Fracture Energy
Ψ	Surface Free Energy

Indices:

$+$	Positive Charged Ions
$-$	Negative Charged Ions
$1, 2, 3, ...$	Counter of States or Substances
X, mol	Molar Volume of Element X
$X, stoic$	by Stoichiometric Distribution of Element X
$1C$	Most Critical State
$3PB$	Three Point Bending
A	Apparent
b	Bulk
B	Bending
C	Critical
$comp$	Compression
$cond$	by Conductivity
$conv$	by Convection
d	Deflecting Cracks
dry	Dry Property of Porous Body
f	Fiber
H_2O	Water Properties
I	Interface
k	Capillary
(l)	Liquid
m	Matrix
max	Maximum of
min	Minimum of
p	Penetrating Cracks
P	Pore
$plast$	by Plastic Deformation
por	of Pores
rad	by Radiation
(s)	Solid
(sl)	Solid-Liquid Interface
scs	Specific Crack Surface
T	Tension
$total$	of the Whole Part
uw	Submerged Property of Porous Body
wet	Water filled Porous Body
WS	of Composite or Part

Chemical Symbols:

Al_2O_3	Aluminum Oxide
B	Boron
B_4C	Boron Carbide
BCl_3	Boron Chloride
BH_4	Borohydride
B_2O_3	Boron Oxide
$B(OH)_3$	Boric Acid
C	Carbon
CO	Carbon Monoxide
CO_2	Carbon Dioxide
Cr	Chrome
CrB_2	Chromium Boride
Cl	Chloride
Cu	Copper
Er_2O_3	Erbium Oxide
H_2	Hydrogen
HCl	Hydrogen Chloride
Hf	Hafnium
HfB_2	Hafnium Boride
HfC	Hafnium Carbide
HfO_2	Hafnium Oxide
H_2O_2	Hydrogen Peroxide
Mg	Magnesium
MgO	Magnesium Oxide
N	Nitrogen
Ni	Nickel
O_2	Oxygen
SiC	Silicon Carbide
Si_3N_4	Silicon Nitrite
SiO_2	Silicon Oxide
TaC	Tantalum Carbide
TiB_2	Titanium Boride
WC	Tungsten Carbide
Y	Yttrium
Y_2O_3	Yttrium Oxide
ZrB_2	Zirconium Boride
ZrC	Zirconium Carbide
Zr_2Cu	Zirconium Copper Alloy
ZN	Zirconium Nitrite
ZrO_2	Zirconium Oxide

Abbreviations:

3PB	Three Point Bending
AsB	Angular-Selctive Back-Scattered Electron Detector
BSZ	Boron-Silica-Zirconia
C/C	Carbon Fiber Reinforced Carbon
DLR	German Aerospace Center
EDX	Energy Dispersive X-Ray Spectroscopy
EsB	Energy-Selective Back-Scattered Detector
FIB	Focused Ion Beam
FMB	Fiber Matrix Bond
FMI	Fiber Matrix Interface
FVC	Fiber Volume Content
HH	He and Hutchinson
LSI	Liquid Silicon Infiltration
PIP	Polymer Infiltration and Pyrolysis
PWT	Plasma Wind Tunnel
SE	Secondary Electron Detector
SEM	Scanning Electron Microscope
SIMS	Secondary Ion Mass Spectroscopy
TG	Thermogravimetric Analysis
TLV	Threshold Limit Value
TPS	Thermal Protection System
UHTC	Ultra High Temperature Ceramics
UHTCMC	Ultra High Temperature Ceramic Matrix Composite
WIC	Weak Interface Composite
WMC	Weak Matrix Composite
XRD	X-Ray Diffraction

Kurzfassung

Ultrahochtemperatur-Keramiken (UHTCs) bezeichnen eine Gruppe von Keramiken, deren Eigenschaften es ermöglichen, sie in einem Ultrahoch-Temperaturbereich von über 2000°C zu verwenden. Entscheidende Eigenschaften von UHTCs sind ein hoher Schmelzpunkt, gute Wärmeleitfähigkeit und Oxidationsbeständigkeit. Mögliche Anwendungen sind Reaktorkomponenten, Raketendüsen, luftatmende Antriebssysteme und Vorderkanten. Frühere Konfigurationen, wie z.B. das Space Shuttle, wurden aufgrund der aerodynamischen/thermischen Belastungen mit stumpfen Geometrien ausgelegt. Der Nachteil dieser Konstruktion ist die geringere Manövrierfähigkeit aufgrund des erhöhten Luftwiderstandes und die damit verbundenen Einschränkungen ihres Wiedereintrittsprofils. Die Verwendung von scharfen Vorderkanten erhöht die aerodynamischen Wärmelasten exponentiell und erfordert daher Materialien wie UHTCs.

Monolithische UHTCs besitzen, wie fast alle monolithischen Keramiken, ein sprödes Materialverhalten mit geringer Schadenstoleranz. Die Erhöhung dieser Toleranz ist neben der Oxidationsbeständigkeit eines der Hauptziele bei der Entwicklung von UHTC-Werkstoffen. Im Rahmen dieser Forschung werden Faserverstärkungen zur Erhöhung der Bruchzähigkeit eingesetzt. Die eingesetzten Fasern sind in der Lage, Risse abzulenken oder zu stoppen, während die einbettende UHTC-Matrix die erforderliche Oxidationsbeständigkeit bietet. Die Entwicklung eines Ultrahochtemperatur-Keramikmatrix-Verbundwerkstoffs (UHTCMC) hat das Potenzial, das Problem der Bruchzähigkeit und Oxidationsbeständigkeit zu lösen. Die Technik ähnelt den Keramikmatrix-Verbundwerkstoffen (CMC), wobei Fasern als zweite Phase in eine UHTC-Matrix eingebettet werden, um die bei der Rissausbreitung entstehende Energie zu dissipieren und somit ein pseudoplastisches mechanisches Verhalten zu erzeugen. Eine Methode, welche bei CMCs zur Herstellung großer Teile eingesetzt wird, ist die reaktive Schmelzinfiltration (RMI), bei der die Reaktion zwischen einer flüssigen Metalllegierung und einer zu infiltrierenden porösen festen Phase ausgenutzt wird. Um ein Verfahren für faserverstärkte Diboride zu ermöglichen, konzentriert sich diese Arbeit auf die Entwicklung eines reaktiven Schmelzinfiltrationsverfahrens (RMI) von Zr-Legierungen zur Herstellung von kohlenstofffaserverstärktem ZrB_2.

Der Zweck dieser Forschung ist es, die Vorgänge des Zr RMI-Prozesses zu verstehen und die mechanische Leistung des Materials zu erhöhen. In einem ersten Schritt werden die Einflussfaktoren, die den Infiltrationsprozess steuern, untersucht und diskutiert. Die Schlüsselfaktoren dieser Untersuchungen sind die Kapillarstrukturen, die sich vor der Infiltration mit der Schmelze bilden, sowie die durch die chemischen Reaktionen verursachten Phasen, der

Kontaktwinkel der verschiedenen Phasen welche die Kapillarkräfte beeinflussen und die durch die exotherme Reaktion freigesetzte Energie. Nach der Definition und dem Verständnis der Mechanismen und Einflüsse während des Herstellungsprozesses werden UHTCMC-Proben hergestellt und untersucht. Die Schlüsselaspekte der analysierten UHTCMC-Proben sind ihre mechanische Leistung im Hinblick auf die Herstellungsparameter und ihre Oxidationsbeständigkeit. Die hergestellten UHTCMCs überschreiten eine Biegefestigkeit von 400 MPa und verdoppeln die Bruchzähigkeit K_{1C} von monolithischen UHTC auf über 10 $MPa\sqrt{m}$. Ihr Oxidationsverhalten wird bei einer Temperatur von über 2000°C in einer sauerstoffreichen Umgebung getestet und die Bildung der von UHTCs bekannten schützenden Oxidationsschichten gezeigt.

Abstract

Ultra high temperature ceramics (UHTCs) refers to a group of ceramic materials whose properties enable them to be used in an ultra-high-temperature regime, exceeding 2000°C. Decisive properties for UHTCs are a high melting point, good thermal conductivity, and oxidation resistance. Potential applications include reactor components, rocket nozzles, air breathing propulsion systems, and leading edges. Previous configurations, such as the Space Shuttle, were designed with blunt geometries due to the aerodynamic/thermal loads. The disadvantage of this design is the lower maneuverability due to the increased air resistance and the associated restrictions of their re-entry profile. The use of sharp leading edges increases aerodynamic heat loads exponentially, and hence, requires materials such as UHTCs.
Monolithic UHTCs, like almost all monolithic ceramics, are subject to a low damage tolerance behavior. Increasing this tolerance, along with oxidation resistance, is one of the key goals of the development for UHTC materials. Within this research, fiber reinforcements are used to increase fracture toughness. Fibers are potentially able to deflect or stop cracks, while the embedding UHTC matrix provides the necessary oxidation resistance. The development of an Ultra High Temperature Ceramic Matrix Composite (UHTCMC) has the potential to solve the problem of fracture toughness and oxidation resistance. The technique is similar to Ceramic Matrix Composites (CMC), utilizing fibers as a second phase embedded in a UHTC matrix to dissipate energy arising from crack propagation, and hence, generating a pseudo-plastic mechanical behavior. One CMC method to produce large parts is reactive melt infiltration (RMI), which exploits the reaction between a liquid metal alloy and a porous solid phase to be infiltrated. In order to establish a process for fiber reinforced diborides, this work focuses on the development of a reactive melt infiltration (RMI) process of Zr alloys to fabricate carbon fiber reinforced ZrB_2.
The purpose of this research is to understand the RMI process and increase the mechanical performance of the material. As a first step, the influencing factors governing the infiltration process are investigated and discussed. The key factors of these investigations are the capillary structure forming before melt infiltration, the phases caused by the chemical reactions, the contact angle of different phases influencing capillary forces, and the energy released by the exothermic reaction. After defining and understanding the mechanisms and influences during the manufacturing process, UHTCMC samples are manufactured and investigated. The key aspects of UHTCMC analyzed are their mechanical performance, with regard to manufacturing parameters, and their oxidation resistance. The manufactured UHTCMCs exceed a bending strength of 400 MPa and double the fracture toughness K_{1C} value from

monolithic UHTC to over 10 $MPa\sqrt{m}$. Their oxidation behavior is tested at a temperature exceeding 2000°C in an oxygen-rich environment, showing the formation of the potential oxidation layers known from UHTCs.

1. Introduction

The worlds growing demand for energy, transport and efficiency require research to find new solutions. While some field of studies found new topics, these topics need advances in interconnected fields as well in order to succeed. New technologies such as fusion reactors or hypersonic vehicles push the envelope of temperature capabilities for materials in extreme environments. The development of Ultra High Temperature Ceramics (UHTC) is a key factor for these types of applications. The reason for their ultra high temperature properties are their strong covalent bonds, especially between metallic diborides and carbides from transition metals group IV and V. These strong bonds attribute the UHTCs with the highest known melting points.

Figure 1.1 gives an overview of specific UHTC properties needed for the design of components in extreme environments. Both fusion and new generation fission reactors have high thermal load requirements for some of the components within the reactors. Fusion reactors must enclose a He plasma within the reactor, which requires a high operating temperature or active cooling systems of first wall components and plasma divertors [1, 2]. Fission reactors must enclose the nuclear fuel and the temperature arising from the released energy. The enclosure of fuel or cladding is a potential component for UHTC applications [3]. During flight operation, the material is also subject to radiation damage, an issue which must be assessed by specialized research facilities, and hence, is not the main focus of application for the investigations of this research.

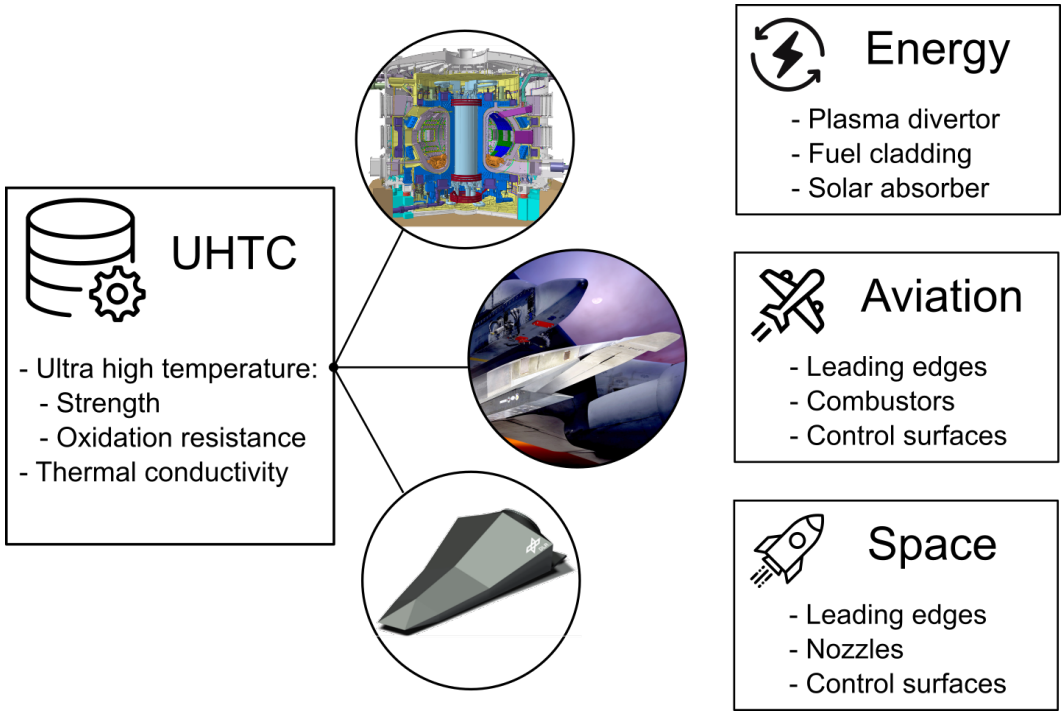

Figure 1.1.: Applications in need of ultra high temperature properties; ITER Fusion reactor (top) [4], X-51 hypersonic waverider (middle) [5] and re-entry experiment SHEFEX III (bottom) [6]

Demands for aviation and space applications are very similar in terms of environmental conditions. In general the only difference is vehicle propulsion. Most blunt re-entry vehicles trade aerodynamic performance with operation temperature in order to survive. Heat loads caused by aerodynamic drag are inversely related to the square root of the leading edge radius, as published by Reimer et al. [7]. The resulting heat loads for small radii or sharp geometries require ultra high temperature properties for the aeroshell material. As described by Jackson et al. [8], new ultra high temperature stable materials have the potential to evolve hypersonic flight vehicles. Refractory metal compounds are of interest for these applications due to their properties such as high melting point, high thermal conductivity, and good oxidation resistance. The investigations founded by the United States Air Force and NASA specify refractory diboride systems as particularly suitable due to their high oxidation resistance [9–13]. Hf and Zr have been the main focus during these studies. Other well-known ceramic compositions such as SiC are subject to active oxidation at extreme temperatures. In addition, diboride ceramics become more oxidation-resistant, see figure 1.4. During passive oxidation of SiC, SiC does provide better oxidation protection [14]. When additional factors such as water vapor from a combustion environment or particles from solid rocket fuel are involved, the application temperature for UHTCs shifts to a lower temperature regime. However, each application scenario must be evaluated according to the operating temperature and oxygen partial pressure in order to choose the right compositions.

Monolithic UHTCs, like almost all monolithic ceramics, possess a low damage tolerance.

This low damage tolerance needs to be taken into account during part design and increases safety margins. In addition to oxidation resistance, increasing fracture toughness is one of the critical points in the development of UHTC materials. Damage tolerance is influenced by the various manufacturing parameters, the raw materials used, and the resulting micro structure. The role of Si in UHTC in particular is discussed widely in literature, described in chapter 2. Generally, Si or SiC is added to achieve a higher density or grain growth during the manufacturing process, and to form a liquid protective layer during oxidation. Monolithic UHTCs exploit different phase compositions in order to achieve a damage-tolerant behavior compared to composites which incorporate a separate phase such as fiber reinforcements. The reinforcement phase is supposed to providing fracture toughness while the UHTC matrix is still capable of sustaining oxidation resistance to the composite. Developing a fiber reinforced UHTC composite will increase fracture toughness by using the same effect known from CMCs. Ultra High Temperature Ceramic Matrix Composites (UHTCMC) will simplify component design, making fabrication of large components plausible. In addition, UHTCMCs provide a perfect substrate for UHTC coatings, through which bonding problems due to thermal expansion mismatch and chemical reactions as seen with CMCs and metals can be avoided. The most common fabrication processes for UHTCs are hot press sintering (HP) and spark plasma sintering (SPS), which, in general, can also be used to fabricate UHTCMCs. However, these manufacturing routes for the fabrication of major parts with an integral design have disadvantages regarding full scale design. Another method known from CMC manufacturing is Reactive Melt Infiltration (RMI). The limiting factors of RMI are the infiltration depth of the melt and furnace size. RMI has a high manufacturing potential and keeps preform design, such as fabric and braiding or winding, flexible. A RMI process which enables the fabrication of UHTCMC parts will increase the flexibility of part design and eventually decrease cost. In order to produce UHTCMC materials at the German Aerospace Center (DLR), each step of the RMI manufacturing process is defined and examined closely. Manufacturing the preform already provides a variety of possibilities to incorporate the reactants necessary for the chemical reactions during melt infiltration. In order to determine an RMI process to fabricate UHTCMC parts, the following investigations are performed.

Initially, the factors influencing the RMI process are investigated and discussed. The results of these investigations will ensure a successful infiltration of the samples necessary for further analysis. Without this fundamental understanding of RMI, the process parameters cannot be adopted to improve material properties. As a next step, the selection of raw materials and the influence of different raw materials used is discussed. Defining a B source is particularly vital for the fabrication of a diboride matrix. The final step for the definition of an RMI process is the investigation of process parameters. Each step is analyzed, and the influence on material properties is discussed. The advantages and disadvantages of each raw material and process must be evaluated in order to achieve a sufficient melt infiltration. However, some evaluations can only be performed if samples pass the entire manufacturing process. In order to obtain reliable results, the complete manufacturing process must be accompanied

by the characterization of the samples' physical and chemical properties. Both the pyrolysis process as well as reactive melt infiltration are subject to these investigations.
After establishing an RMI manufacturing process for UHTCMCs, the composites can be characterized. Hence, the micro structures of these UHTCMCs are investigated and various effects resulting from process variations are described. The mechanical investigations initially focus on the sample strength to compare effects caused by different raw materials and manufacturing parameters. In addition, fracture toughness of UHTCMC samples is measured in order to prove the pseudo-plastic effects of fiber reinforcements in a UHTC matrix. The goal of UHTCMC development is to achieve a higher fracture toughness than monolithic UHTCs, around 5 $MPa\sqrt{m}$ (see section 2.3), and a similar strength to carbon fiber reinforced SiC CMCs, around 200 MPa bending strength, while preserving the oxidation mechanisms from monolithic diborides. These material properties will allow UHTCMCs to be applied in parts like leading edges, combustion cambers and control surfaces. This study focuses on the investigation of carbon fiber reinforced ZrB_2 using an RMI with various Zr alloys.

1.1. Diborides

Starting in the 1800s to early 1900s, borides have been subject to research. This dates back to the work of Moissan [15], who used an electric arc furnace reaching temperatures of 3500°C [16] to produce pure boron [15] and isolate elemental fluorine [17]. Tucker and Moody investigated borides of most transition metals, including ZrB_2 [18]. Apart from the high melting point, Meissner et al. [19] showed interest in the superconducting properties of zirconium boride at very low temperatures. Stoichiometric ZrB_2 was processed by McKenna [20] using the reaction of ZrO_2,B_2O_3 and C to form ZrB_2 and CO. In addition, he used B_2O_3 in a second heating step under vacuum conditions to further reduce the carbon content below ~1wt %. The first to produce pure boron in high quantities was Kiessling [21] in 1948. The laboratory set-up produced only ~1g per cycle but the process was scalable and reached a purity of 99%. Further work on the diboride and refractory compositions was performed in the 1960s by ManLabs Inc. in the USA and G.V. Samsonov in Russia. Both publications already investigated ZrB_2 and HfB_2. ManLabs also performed the investigation of SiC additions to the diboride system. They also performed initial tests on high temperature oxidation, as well as mechanical and thermal properties. The addition of SiC influences properties such as strength [22, 23], fracture toughness [22–24], and oxidation resistance at certain temperatures [25, 26]. For sintering routs, SiC also creates thermal residual stresses during cool down from process temperatures. While the strength of pure ZrB_2 is mainly governed by grain size, properties of SiC doped diboride are effected by the SiC particle/grain size [27].
Besides the high melting points of Hf and Zr diborides, for ZrB_2 around ~3200°C [28], diborides also exhibit high electrical conductivity (~11×10^6 S/m for ZrB_2 at RT) due to the high degree of covalent bonding [29–31].

In recent years, the focus of UHTC development has concentrated on fiber reinforcement to increase UHTC's damage tolerance. Methods used to manufacture these UHTCMCs are sintering [32], Chemical Vapor Infiltration (CVI)[33, 34], and Reactive Melt Infiltration [35, 36].

1.2. Demands for Hypersonic Flight

UHTCs are a key factor in hypersonic flight and other extreme temperature applications. They are one of the few materials able to withstand these temperatures without using active cooling systems and to some degree the occurring oxidation as discussed in several publications [33, 37–40]. During hypersonic flight, the thermal loads are tremendous and, depending on the vehicle shape, even CMC materials exceed their maximum operating temperature. Jackson et al. [8] calculated the total temperature of flight conditions depending on altitude and Mach number, exceeding 2000°C above $Mach7$. Therefore, either investigations regarding transpiration cooling, an active cooling concept to face these high heat loads [41], or UHTCs/UHTCMCs are necessary to withstand these temperatures. Apart from structural weakness, oxidation is a huge problem without active cooling or UHTCs. This is particularly noticeable in a high temperature environment containing atomic and molecular oxygen, as found during re-entry or hypersonic flight in earth's atmosphere, described by Glass et al. [42]. In recent years, the focus of UHTC development has concentrated on fiber reinforcement to increase their damage tolerance. Methods used to manufacture these UHTCMCs are sintering [32], Chemical Vapor Infiltration (CVI)[33, 34], and Reactive Melt Infiltration [35, 36]. Until now, hypersonic research has focused on key technologies without taking an overall conceptual design into account. This is partially linked to the need for materials capable of withstanding the required heat loads. Some flight tests aim to progress beyond the demonstration of fundamental principals. For nearly 50 years, the USA has been developing hypersonic airbreathing technology. In the 1970s, NASA focused on propulsion air frame integration, which was followed by the National Aero Space Plane Program in the 1980s to investigate a scramjet-based combined cycle powered vehicle. Flight tests were performed using the X-43 vehicle with a scramjet design, followed by the X-51 demonstrator investigated by the National Aerospace Initiative and NASA. Russia investigated different propulsion units to be verified at different Mach Numbers. OKB Tupolev designed two configurations for different cruise speeds, Tu-260 for Mach 4 and Tu-360 for $Mach6$. Both are connected to the Tu-2000 program, a flight test design reaching Mach 6. During the 1980s, Germany investigated a hypersonic transport vehicle within the Sänger project. The cruise speed was aimed at Mach 4.4 using a turboramjet propulsion system. Currently, there are multiple hypersonic designs and flight experiments ongoing, namely HYSHOT, HIFiRE and HEXAFLY [43, 44]. All of the designs must handle extreme temperatures at the most exposed parts. Figure 1.2 shows a schematic hypersonic configuration, highlighting the most demanding parts in terms of operating temperature.

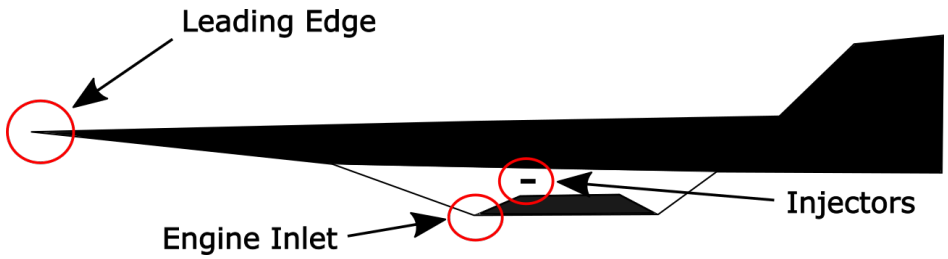

Figure 1.2.: Schematic of high heat loads for scramjet components

All of these parts require a sharp leading edge to reduce aerodynamic drag and to form a defined shock wave. A high thermal conductivity of the material will reduce the thermal stress induced from heat loads. In addition, a high thermal conductivity will allow energy to be dissipated to fewer thermal-loaded parts of the air frame. Current re-entry vehicles utilize insulating TPS materials such as SiC-coated C/C, which require as high of an emissivity as possible. In general, these TPSs are blunt designs which decrease the vehicles performance. Decreasing the radius of the leading edge will increase surface temperature exponentially [7]. Gasch et al. [14] illustrate the heat flux, $\dot{q}$ of a blunt and sharp leading edge in comparison, as illustrated in figure 1.3. According to Gasch et al., utilizing the full potential of heat transfer by increasing thermal conductivity is vital for hypersonic vehicles. As shown in figure 1.3, blunt C/C designs convect heat by radiation alone, $\dot{q}_{rad}$, while a sharp UHTC design can take advantage of conductivity within the material, $\dot{q}_{cond}$, to convect heat. For materials with a low thermal conductivity, the surface temperature is determined by a balance of the incoming heat flux and the energy which is re-radiated.

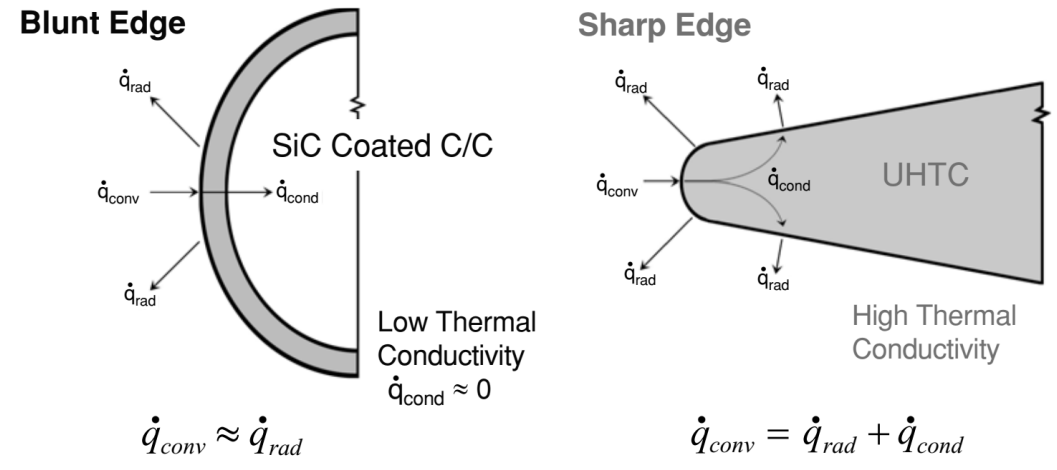

Figure 1.3.: Schematic of heat flux of a blunt and sharp leading edge [14]

From a historical point of view, the first attempts to survive high thermal and mechanical loads of hypersonic flight are missile nose tips. Aerodynamic loads caused by drag during hypersonic flight are responsible for thermal shock during acceleration of the vehicle, and high angles of attack during flight cause bending stresses within these nose tips representing

the main mechanical loads. The early development stages moved from Sitka spruce (wood), Organic Matrix Composites (OMCs), and graphite to C/C composites [37]. In order to sustain an accurate geometry throughout longer hypersonic flight durations, C/C composites must be substituted. Eventually, these requirements lead to intensified investigations of monolithic UHTCs in the 70th. Depending on the nose radius, Mach number, and oxygen partial pressure, either SiC-based or UHTC-based composites are more oxidation-resistant. The wall temperature on the vehicle surface can be calculated from a vehicle's nose radius and Mach Number. This temperature and oxygen partial pressure can be used to decide on the usage of SiC-based or UHTC-based composites on the basis of the active or passive oxidation envelope of SiC. At ultra high temperatures, when SiC is subject to active oxidation, UHTC matrices are more oxidation- resistant. Figure 1.4 shows the transition of passive to active oxidation according to Ogasawara et al. [45] in a high enthalpy flow and a low enthalpy flow of Singhal [46] and Balat [47–49]. Any flight envelope reaching into the lower right section where SiC is subject to active oxidation requires the use of UHTCs.

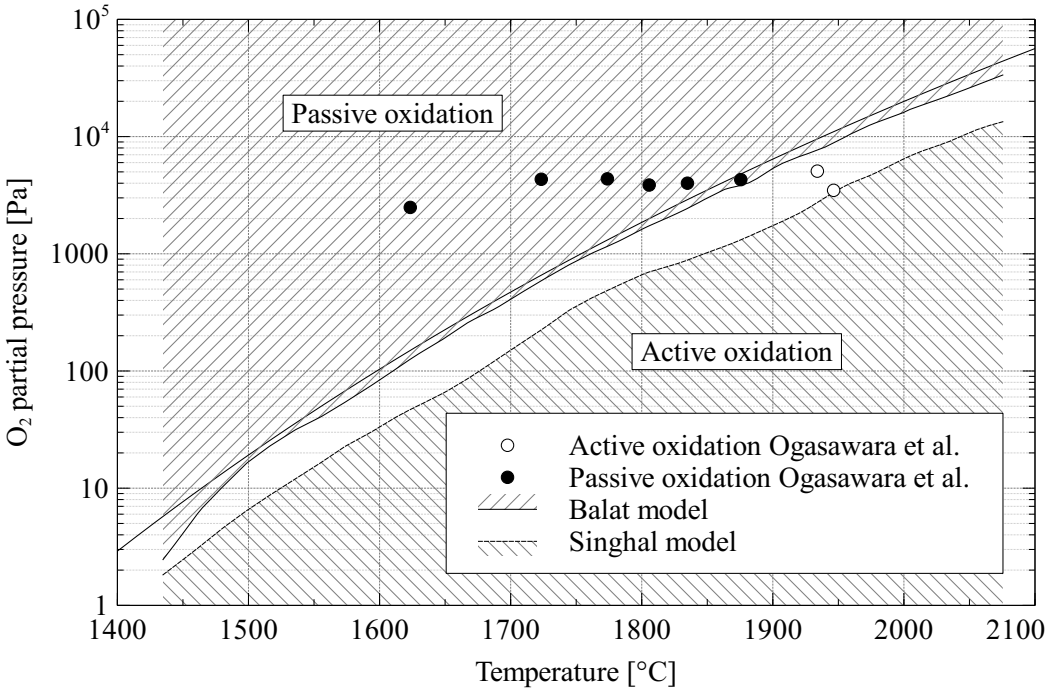

Figure 1.4.: Transition from active to passive oxidation of SiC according to Ogasawara et al. [45] in a high enthalpy flow and a low enthalpy flow of Singhal [46] and Balat [47–49]

2. State of the Art

A large scale of the monolithic UHTCs is manufactured through sintering processes. For this reason, a great deal of research has been conducted to increase the density of UHTCs by sintering additives, such as liquid phases. Additives might not increase the performance of the UHTC itself, but might increase performance due to the influence on the manufacturing process. Due to the large number of experiments on sintered UHTCs, they will also be taken into account as reference.

2.1. Processing

In order to produce stoichiometric ZrB_2, a number of methods have been used [50–52]. Kiessling [52] manufactured many metal borides, including ZrB_2, by high frequency vacuum induction heating using boron and metal powders. Brewer [50] used a similar technique heating the mixed powders in a crucible. Meerson and Samsonov [53] used the following reaction to produce the metal borides:

$$2\ ZrO_2 + B_4C + 3\ C \longrightarrow 2\ ZrB_2 + 4\ CO.$$

They also used an inductively heated furnace and were able to monitor the reactions by observing the CO pressure, reaching a stoichiometric ZrB_2 with very few carbon impurities. A closer investigation of the zirconium boron system was done by Samsonov and Portnoy [54] and showed the formation of ZrB and ZrB_{12}. However, neither of the two compounds were stable at room temperature according to their investigations.
The most thoroughly studied additive to HfB_2 or ZrB_2 is SiC, SiC can further increase the properties of the monolithic diborides. In addition to its positive influence on strength, fracture toughness, hardness, and oxidation, SiC lowers the thermal conductivity like any addition to a monolithic diboride. ZrB_2-SiC composites have shown strengths above 1000 MPa, fracture toughness up to 5.5 MPa $\cdot$ $m^{1/2}$ and hardness over 22 GPa [22, 55–58].

2.1.1. Sintering

All sintering methods start with solid powders forming the intended material composition. Depending on the method, this can also include reactants which form the compound during the sintering process. In addition to pressure and temperature, there are other methods to promote sintering, such as electric fields. The quality and size of the starting powders have

a major influence on parameters necessary for sintering. Therefore, the manufacturing and handling of these powders is important in order to produce dense and high-quality results. Dense bulk ceramics have been manufactured since the 1960s, and require temperatures in excess of 2000°C if hot-pressed from ZrB_2 powders.

Hot Press

There are a number of investigations regarding sintering aids aimed at lowering the temperature in order to gain fully dense ZrB_2. Monteverde [59] investigated the addition of Si_3N_4 (~4vol%) and Chamberlain [22] investigated the addition of WC (~2wt%) to reach temperatures of 1800-1900 °C. Contamination of oxygen also has an effect on the densification as Baik and Becher[60] showed using TiB_2. Oxygen impurities increase surface diffusion and evaporation condensation reactions, and therefore, lower oxygen impurities lead to a higher densification. Clougherty, who was involved in the ManLabs [9] investigations as well, and Kalish [11, 61] used hot pressing to form dense ZrB_2 with SiC additions ranging from 5-50 vol%. They used temperatures from 1800-2100 °C and pressures from 17 MPa up to 1.5 GPa. Monteverde et al. [62] lowered the temperature of densification to 1580 °C and gained >99 % theo. density at 1900°C with 40 MPa pressure by adding sub-micron SiC powder and 4.5 vol% ZrN. In addition to the ZrB_2-SiC phase, the materials also consisted of small phases formed from the reaction of ZrN and oxides on the powders used. Talmy [26] and Wang [63], who used SPS, also investigated the addition of ZrN to ZrB_2 and further decreased the densification temperature. Rezaie [56] examined the influence of HP time and temperature on ZrB_2-SiC composites, with times ranging from 45-180 mins at temperatures from 1850-2050°C. Low temperatures at short times result in small grain sizes and vice versa. The change in the average grain size was not as significant as the change in maximum grain sizes for both SiC and ZrB_2 grains.

Reactive Hot Press As an alternative to sintering powders of the final composition, reactive hot pressing with powders from educts can be performed [64–68]. Due to the reaction during sintering, it is less sensitive to contaminations, resulting in fewer impurities at lower process temperatures. Usually, high purity reacting elements are commercially available, resulting in finer microstructures of ZrB_2. Zhang et al. [64] showed the presence of ZrB_2 and SiC in RHP samples using Zr, Si, and B_4C powders. Wu et al. [65] started with the same powders, but were also able to form ZrC as a third phase by altering the powder composition. Chamberlain et al. [58, 67] used elemental SiC, Zr, B, and small amounts of B_4C to form ZrB_2-SiC composites. The reaction of Zr and B started as low as 600 °C, and fully dense samples were formed at 1700 °C.

Spark Plasma Sintering

In addition to mechanical pressure and temperature, Spark Plasma Sintering (SPS) uses DC current to promote sintering. In order to generate electrical discharge on a microscopic level to promote material diffusion, the DC current is pulsed. The spark discharge locally generates high temperatures between the particles and starts to form necks around the area of contact [69]. Compared to HP processing, higher heating rates are possible due to the current passing through the sample [65].

2.1.2. Polymeric Route

In the 1990s, Su et al. [70] used a polymeric route to produce metal diborides. Their method was similar to the carbothermal reduction of oxides through carbon, but instead of carbon powders, a polymeric precursor was used to decompose into boron carbide. By pyrolysing this solution, they produced metal diboride powders with correct stoichiometry and a particle size down to 200 nm.

2.1.3. Vapor Deposition

In the 1970s and 1980s, various vapor depositions initially focused on coatings [71–75]. Wayda et al. [72] used inorganic borohydrides of $Zr[BH_4]_4$ and $Hf[BH_4]_4$ for the deposition. With this method, it was possible to deposite continuous ZrB_2 and HfB_2 coatings at temperatures down to 100 °C. In addition to the deposition of ZrB_2 or HfB_2, the University of Birmingham has been working on UHTC powder impregnated preforms with additional densification of pyrolytic carbon by CVI [76, 77]. Rubio et al. [77] used a radio frequency CVI facility to reduce to porosity from 77 vol.% to 16 vol.% in 14 h.

2.1.4. Colloidal Processing

Colloidal processing uses particles dispersed in a liquid to form a ceramic greenbody. Inside the colloid, the inter-particle forces must be controlled by barriers formed around particles [78]. Shaping techniques that can be used to form greenbodies are slip casting, gel casting, and freeze casting [79]. Several groups have started using this method for the manufacturing of ZrB_2 [80–85]. Tallon et al. produced ZrB_2 with 93 % theo. density at 2100 °C and pressureless sintering; in combination with HP at 2000 °C and 40 MPa pressure, they reached full densification. Leslie et al. used an improved slurry infiltration to manufacture SiC fiber reinforced SiC-HfB_2[86]. They used an HfB_2 particle containing polycarbosilane (SMP-10; Starfire Systems) for infiltration and Polymer Infiltration and Pyrolysis (PIP) processing. In addition to pressureless impregnation, they used vacuum, vibration, and a combination of both of these impregnation techniques to infiltrate SiC/SiC preforms. After 6-10 cycles of PIP processing, they lowered the porosity to ~10 % using 1300 °C and 1600 °C as pyrolysis temperatures. Paul et al. combined slurry infiltration with UHTC particles with CVI

processing[33]. Li et al. infiltrated 3D carbon preforms with UHTC slurries in addition to PIP processing to form ZrC-SiC and ZrC-ZrB_2-SiC composites without brittle fracture behavior [87, 87]. Wang et al. [88] and Li et al. [89] also combined slurry infiltration with CVI processing, forming C/ZrB_2-SiC and C/SiC-ZrB_2-TaC composites.

2.1.5. Reactive Melt Infiltration

Research regarding melt infiltrated ZrB_2 based UHTCs is scarce. Zhang [90] completed studies of melt infiltration at 1200 °C in a vacuum. Both of Zhang's papers include the creation of B_4C porous bars along with the infiltration of these bars with Zr_2Cu. Dickerson [91] performed a Zr_2Cu infiltration of a porous WC preform to form a ZrC- and W-structure. The advantages and disadvantages of the Zr_2Cu RMI are similar to the Liquid Silicon Infiltration (LSI) in process, low porosity, residual melt, and possible manufacturing of large parts. In the case of a fiber reinforced ZrB_2 matrix composite, RMI results in a lower temperature exposure of the fibers compared to HP or SPS with no additional mechanical pressure. Conversely, the fibers must withstand the melt during the RMI process.
Liquid Silicon Infiltration (LSI) for manufacturing CMCs is documented in the literature by DLR [92–94]. Most commonly, a C_f/SiC_m material is manufactured and SiC_f/SiC_m composites are developed for avionic applications. Compared to the reaction of Zr-RMI, LSI uses carbon and molten silicon to react with silicon carbide; however, the basic infiltration mechanisms are similar for both methods. They both use capillary forces to infiltrate a porous preform with a molten metal and create the ceramic due to a reaction while infiltrating.

Capillarity

The infiltration of small capillary tubes by a liquid, is called capillarity. The effect is a result of the surface tension. In order to describe the capillary system in hydrodynamics, it is necessary to solve the Navier-Stokes Equations. For incompressible Newtonian Fluids with a constant viscosity, the following equation is valid according to Happel [95]:

$$\rho du/dt = \rho(\delta u/\delta t + u\nabla u) = -\nabla p + \eta\nabla^2 u + \rho F. \tag{2.1}$$

ρ is the density of the fluid, u is velocity, and η the dynamic viscosity. The capillary force is F and p is pressure. For a steady flow of an incompressible fluid, the equation can be shortened by the term of inertia to

$$\nabla^2 u = 1/\eta\nabla p. \tag{2.2}$$

In the case of a fluid rising over time in a cylindrical capillary with a diameter of d_k and length l, Hagen and Poiseuille [96] describe the pressure loss of a fluid with an average velocity of $\overline{u}$ as follows:

$$\Delta p_{HP} = 32\eta\Delta l/(d_k^2)\overline{u}. \tag{2.3}$$

Therefore, the differential equation describing the height h of a fluid with the contact angle Θ inside a capillary over time is

$$dh/dt = (d_k^2)/32\eta h((4\sigma\cos\Theta)/d_k - \rho g h). \tag{2.4}$$

For this ordinary differential equation, the solution is [97]

$$t = 32\eta/(d_k^2\rho g)(h_{max}\ln(h_{max}/(h_{max}-h)) - h), \tag{2.5}$$

taking into account the hydrostatic pressure for the maximum height of

$$h_{max} = (4\sigma\cos\Theta)/(d_k\rho g). \tag{2.6}$$

Contact Angle of Molten Metals

The contact angle is defined as the angle between the interfaces of liquid/solid and liquid/gas. A high contact angle has a low degree of wetting and indicates a low solid surface energy. There are two basic methods of determining the contact angles, the Goniometer method and the Wilhelmy method. A key issue for the melt infiltration process is the wetting of the preform and products formed during infiltration. The wetting is influenced by the atmosphere as well as rather small additions to the substrate, for example Ni in ZrB_2, as shown in the work of Muolo et al. [98], where the contact angle of Cu drops by ~120° when using 4wt.% of Ni as a sintering aid. This may not only be a result of the Ni addition, but also the influence of the higher densification of the ZrB_2 substrate and the formation of Ni_2B shown in the work of Voytovych et al. [99]. In addition, Muolo et al. showed the contact angle change of Cu over time, the isothermal heating showed a drop in contact angle after a few minutes [98, 100]. Another aspect that must be taken into account is the wetting of carbon by Cu. Compared to ZrB_2, the contact angle of Cu and carbon is rather high, larger than 100° [101]. Apart from the spreading kinetics, the temperature also has an impact on the contact angle, as shown in the work of Samsonov et al. [28] where the contact angle drops nearly 100 ° from 1100 ° to 1400 °C.

2.2. Ceramic Composites

Ceramic composites consist of two phases, fiber reinforcements and the embedding of these fibers inside a ceramic matrix. Compared to CFRPs, the main objective of the fibers in CMCs isn't increasing their strength, but rather generating a pseudo-ductile behavior of the composite. The ceramic matrix allows for a high temperature application above temperatures

where most metals start decreasing in strength. Figure 2.1 shows the drop in specific strength, $\frac{R_m}{\rho \cdot g \cdot km}$, of different material classes over temperature in an inert atmosphere [102].

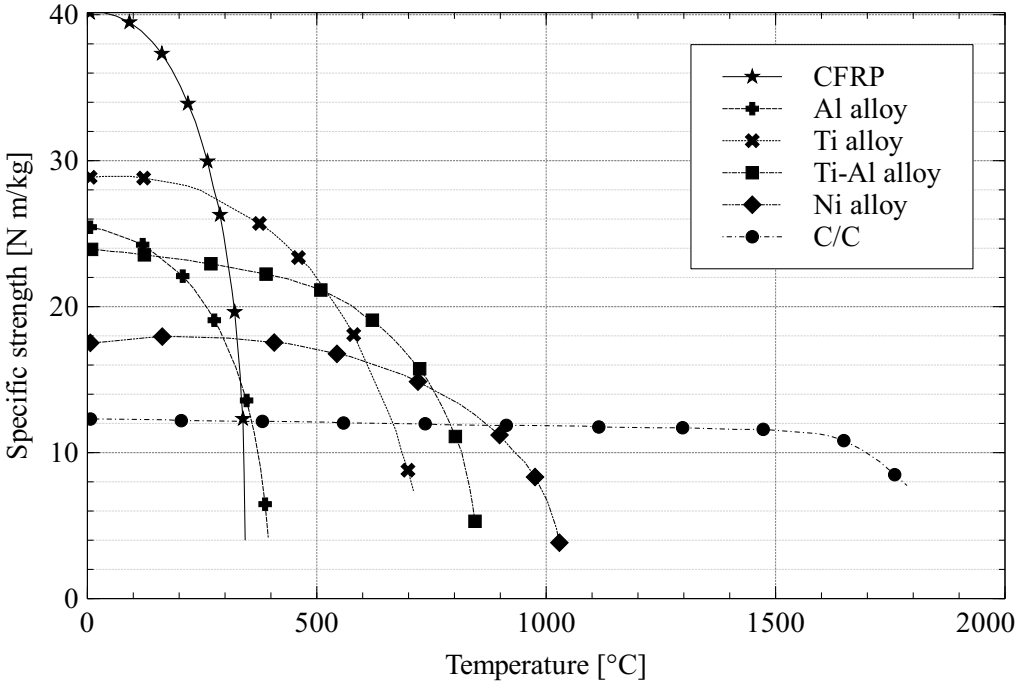

Figure 2.1.: Material-specific strength as a function of application temperature in an inert atmosphere [102]

A common classification of CMCs is the separation into oxide-based and non-oxide-based CMCs. Most commonly, oxide fibers or matrices are not mixed with non-oxide fibers or matrices, however, there are a few exceptions. Due to the topic at hand, this work differentiates between classic CMCs, such as C, SiC, Al_2O_3, SiCN, and UHTCMCs containing a UHTC matrix like ZrB_2, HfB_2, or Zr/Hf/TaC.

2.2.1. Fracture Mechanics

The primary objective of a ceramic composite is the improvement of fracture toughness compared to a monolithic ceramic. Due to the smaller number of defects inside a single fiber, the diameter of the fiber is usually around 7 μm, and strength and strain are higher compared to the matrix even in the same material (2nd paradox of materials [103]). This causes the matrix to fail before the fibers fail (Fig. 2.2).

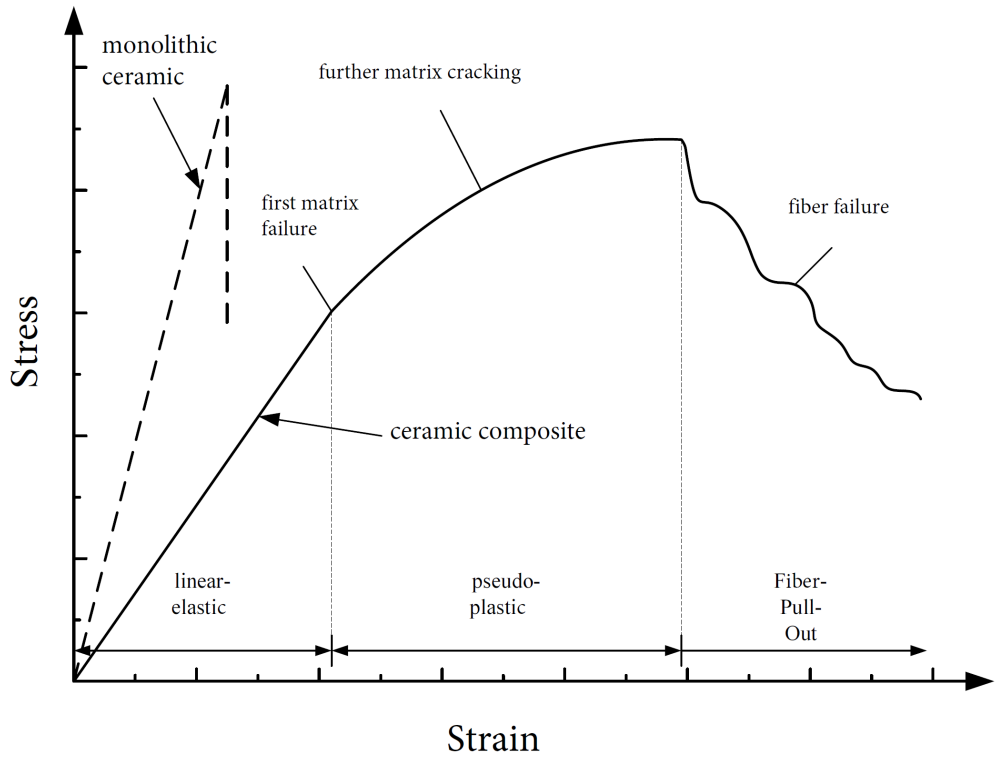

Figure 2.2.: Stress-strain curve of monolithic and composite ceramics [104]

There are two separate ways to achieve this primary objective. Should the fibers exhibit a larger modulus than that of the matrix, the matrix has less tension when the composite is in strain. A propagating crack inside the matrix has relatively low propagating energy, and therefore, the energy for a crack to propagate depends on the modulus. The fibers are able to stop or deflect a matrix crack as long as their modulus is larger. In this case, the fiber matrix interface (FMI) should be strong. In literature, these types of CMCs are known as weak matrix composites (WMC) [105].
If the matrix and fiber modulus are similar, the matrix cracks cannot be stopped by the fibers. In order to stop these cracks from propagating throughout the fibers, a weak FMI is required. In literature, these types of CMCs are called weak interface composites (WIC) [105]. Figure 2.3 shows the relative fracture energy over the elastic mismatch α. He and Hutchinson [106] marked areas for WMCs and WICs in a diagram shown in figure2.3. This type of separation is not clearly defined, and there are numerous transition CMCs depending on their fiber/matrix combination and manufacturing technique. If both the fiber and matrix modulus are similar, the elastic mismatch ($\frac{E_f - E_m}{E_f + E_m}$) becomes zero. A typical WIC is considered to have low relative fracture energy (Γ_I/Γ_f) as well. For WMCs, the elastic mismatch is greater than zero, with typical values of 0.6-0.8. For both types of CMCs, there are different mechanisms to change damage-tolerant. Usually, WMCs have a porous matrix, and further densification of the matrix by infiltration (CVI, PIP) or oxidation may increase the modulus, which could result in brittle failure. WICs tend to have no or very small matrix porosity. In this case, the

FMI can influence the failure mechanisms. If, for example, oxidation causes the weak FMI to harden, the composite can also become brittle.

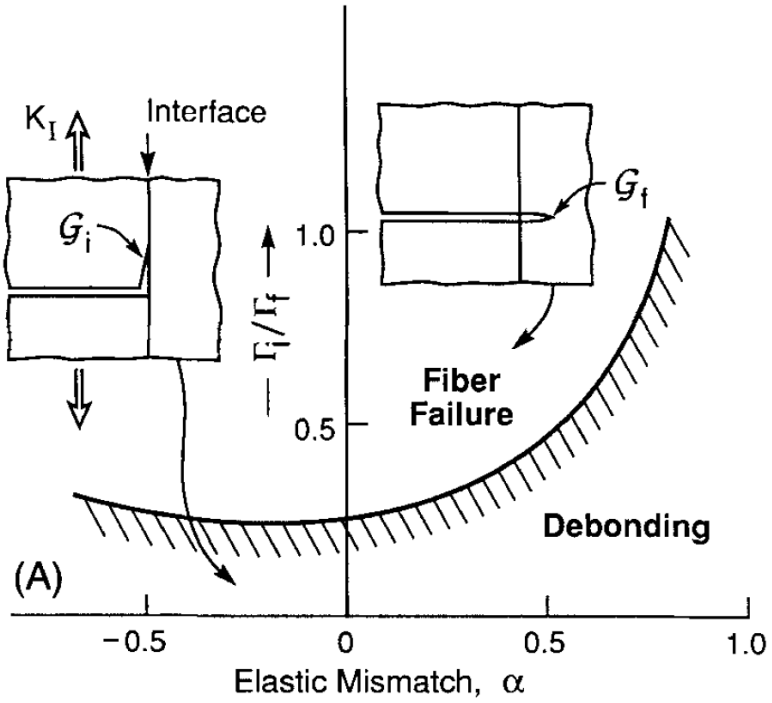

Figure 2.3.: Crack front debond diagram indicating the range of relative interface fracture energy in which debonding occurs in preference to fiber failure [107]

Fundamental fracture mechanisms which can occur in fiber composites are as follows:

- Crack branching,
- Crack deflection,
- Crack bridging, and
- Fiber-pullout.

Some of these are displayed in the schematic of figure 2.4. CMCs typically do not reach their theoretical strength; the reasons for these lower strength values are as follows:

- Fiber damage during CMC processing,
- Fiber ondulation,
- Incorrect FMI, and
- Residual stresses due to different thermal expansion of fiber and matrix.

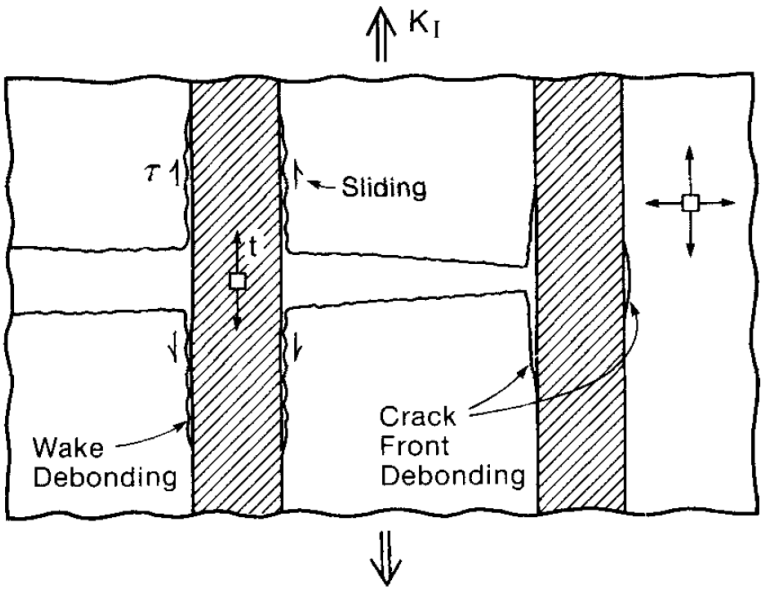

Figure 2.4.: Schematic indicating debonding and sliding behaviors that accompany matrix crack propagation in a WIC [107]

2.2.2. Fibers

In addition to the characteristics necessary for the fibers to act as part of a ceramic composite, it is crucial for them to withstand the manufacturing process. In general, those characteristics consist mainly of the maximum manufacturing temperature but also mechanical pressure and chemical stability. Figure 2.1 shows properties of five general fiber types. Depending on the application requirements for the coating and matrix, the combination of fiber and matrix can be different. Important factors for UHTCMCs are ultra high temperature strength and oxidation resistance.

Except for carbon fibers, most organic fibers cannot be used to manufacture CMCs due to their temperature limitations. For UHTCMCs, even most of the inorganic fibers would exceed their temperature limits during operation. Carbon fibers have the advantage of high temperature strength, but lack oxidation resistance as a result of having neither coatings nor matrix protection. SiC fibers have a much better oxidation resistance, but lack ultra high temperature strength. Tyranno SA3 SiC fibers keep almost all of their initial strength up to 1900 °C as shown in figure2.5. The main factors for high temperature strength of SiC fibers are the manufacturing temperature and oxygen content.

Table 2.1.: Fiber structures and properties [108]

Fiber type	polyester polyamide	aramide fibers	carbon	ceramic (crystalline)	ceramic (amorphous)
Structure	 1D linear 2 phases	 1D linear 1 phase	 2D layered	 3D isotropic	 3D isotropic
Bond type	1D covalent, hydrogen bonds, dipole-dipole, van der Waals	1D covalent, hydrogen bonds, van der Waals	2D covalent, van der Waals	3D covalent, ionic	3D covalent, ionic
crystallinity	medium	paracrystalline	paracrystalline	polycrystalline	amorphous
Orientation	medium	very high	high	none	none

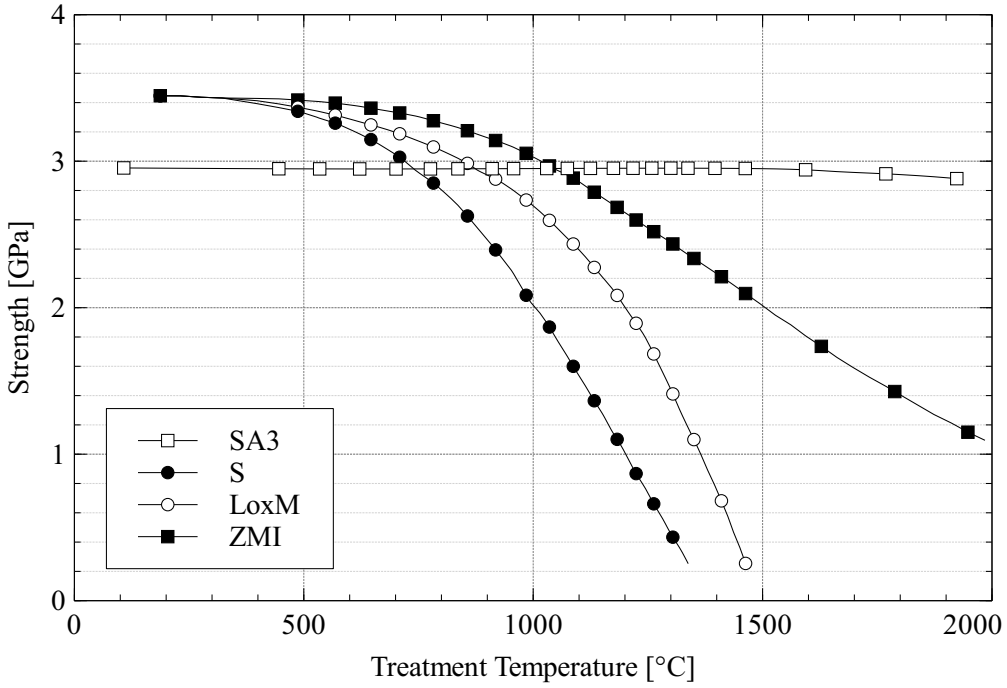

Figure 2.5.: Residual tensile strength of Tyranno Fibers after heat-treatment in Argon for 1h [109]

2.2.3. Matrix

For most applications, it is important to provide high thermal conductivity, oxidation, and corrosion protection for the matrix. There are a variety of manufacturing techniques depending on the matrix composition, namely CVI, PIP, HP/SPS or RMI. All of these methods

can be used to manufacture a UHTC matrix and each of them have their advantages and disadvantages. CVI forms a very uniform UHTC matrix with low manufacturing temperatures, but precursors and process time bring high costs. The infiltration of fiber preforms is simple for PIP precursors; however, this results in high porosity and precursors costs. Most records for monolithic UHTCs are reported using sintering methods such as HP and SPS, but high manufacturing pressures and temperatures are necessary, as well as slurry infiltration of the fiber preforms. RMI produces low porosity without any mechanical pressure or UHTC precursors. However, reactive metal infiltrating requires fiber protection during the RMI process, usually achieved by a fiber coating. The manufacturing of monolithic UHTCs and UHTCMCs is described at the beginning of chapter 2.

2.2.4. Fiber Matrix Interface

WICs need a weak bond between the fiber and matrix in order to improve strength, fracture toughness, and damage tolerance. The weak interface can be achieved by a weak fiber matrix bond (FMB or a weak interface layer. Using a fiber coating, the weak FMB can be implemented between the interface fiber-coating or matrix-coating. A weak interface itself can be achieved via multi-layer coatings, porous coatings, or dislocations inside the coatings, shown in figure 2.6.

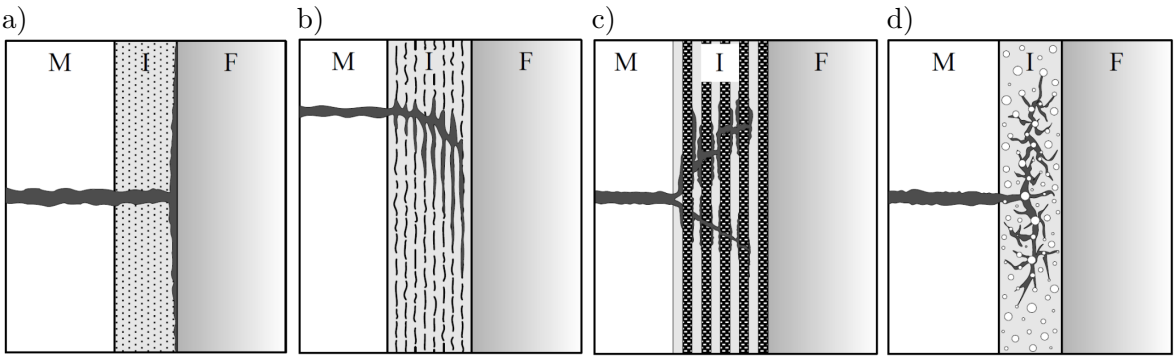

Figure 2.6.: Different types of interfaces in ceramic matrix composites [110]:
a) weak fiber/coating interface,
b) interface with a layered crystal structure,
c) multi-layer interface and
d) porous interface

The following requirements must be met for an interface between the fiber and coating:

- Preservation of mechanical properties of the fiber and
- Bonding between fiber and coating.

Between the coating-matrix interface, the requirements are as follows:

- Protection of coating from the matrix,
- Bonding between coating and matrix,
- Reaction and diffusion barrier,
- Improvement of contact angle, and

- Oxidation protection.

In practice, the various requirements are usually achieved by a two or three-layer coating with either different or graded material compositions. SiC/SiC composites manufactured by LSI, for example, use a carbon outer layer to improve wetting behavior and adhesion of the pyrolysed resin, a SiC intermediate coating to protect the inside coating during melt infiltration, and BN inner coating as a weak interface for increasing fracture toughness [111].

2.3. Material Properties

Diborides, particularly ZrB_2 and HfB_2, have been studied for their high temperature material properties. ManLabs [10, 11, 112–114] carried out a number of investigations regarding the properties of monolithic ZrB_2 and HfB_2. Single crystals of ZrB_2 were investigated by Haggerty and Lee in the 1970s [115]. They researched mainly the deformation of single crystals compression loaded at 1490 °C and 2000 °C. The single crystals showed no macroscopic deformation; only those at 2125 °C had a 4.5% plastic deformation.
ManLabs discovered that the maximum strength of monolithic borides is not at room temperature, which was around 300 MPa, but at elevated temperatures. In the case of ZrB_2, it reaches maximum strength at ~700°C [113]. The temperature dependency was not only noticeable regarding strength, but also for fracture mode. The maximum bending strength correlated with the maximum value of transgranular fracture. They assumed this to be due to relaxation of residual processing stresses caused by the anisotropic CTEs of diborides and grains of different orientation. Other factors, such as yield stress, decrease with increasing temperature, resulting in a reduction of bending strength. Therefore, maximum bending strength is reached before all residual stresses are released.
Compared to other ceramics, borides have an increased thermal stress resistance at elevated temperatures, as shown in figure 2.7.

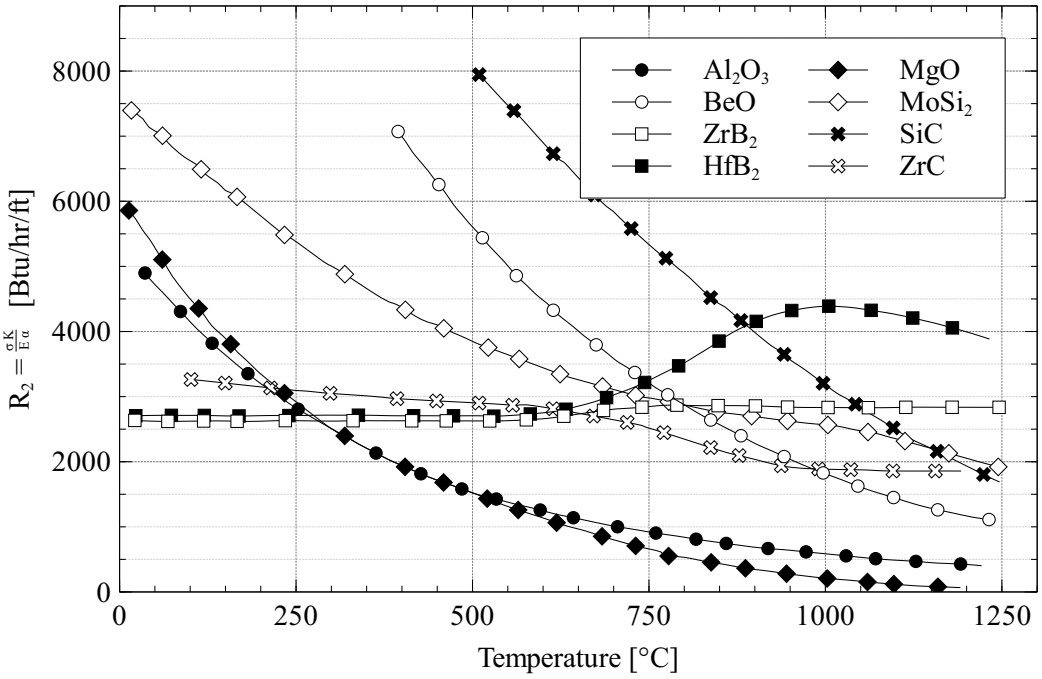

Figure 2.7.: Temperature-dependent thermal stress resistance parameter for steady-state heat flow [113]

In ManLabs's research [11], the addition of SiC helped to obtain a material with grains finer than pure ZrB_2 while strength remained almost constant at 1800°C. Monteverde et al. [23, 25, 59, 62, 116] also investigated various properties of ZrB_2-SiC. In addition to SiC, they added sintering additives such as Si_3N_4, Al_2O_3, and Y_2O_3 and were able to reach an RT flexural strength of more than 700 MPa. This, however, decreased to around 260 MPa at 1200°C. A different investigation compared ZrB_2-15vol%SiC compostions with ZrB_2/10vol%HfB_2-15vol%SiC. The fracture toughness of 4 $MPa\sqrt{m}$ and hardness of ~18 GPa were similar for both compositions. The main effect has grain size and elastic modulus on fracture toughness. As exhibited with other additives, bending strength was reduced to ~250 MPa at 1200°C. Chamberlain et al. [22] investigated the influence of 0-30vol%SiC on mechanical properties. They were able to achieve a strength of over 1 GPa in four-point bending tests. In contrast to previous results, their compositions contained WC additions from grinding the powders and smaller powder particles. Bending strength above 1 GPa has also been reported by other researchers [55, 56, 117]. According to these studies, particle size seems to have a large influence on the strength of monolithic diborides. Rezaie et al. [56] examined the change of SiC particle size in ZrB_2-30vol%SiC composites as well as the grain size by changing the processing time and temperature. Larger grain sizes, which increased with time and temperature, decreased bending strength. Zhu et al. [118] varied the grain size of SiC with four different starting SiC powders ranging from 0.45 μm to 10 μm. As shown in figure 2.8, grain size correlates well with the bending strength of a ZrB_2-SiC composite.

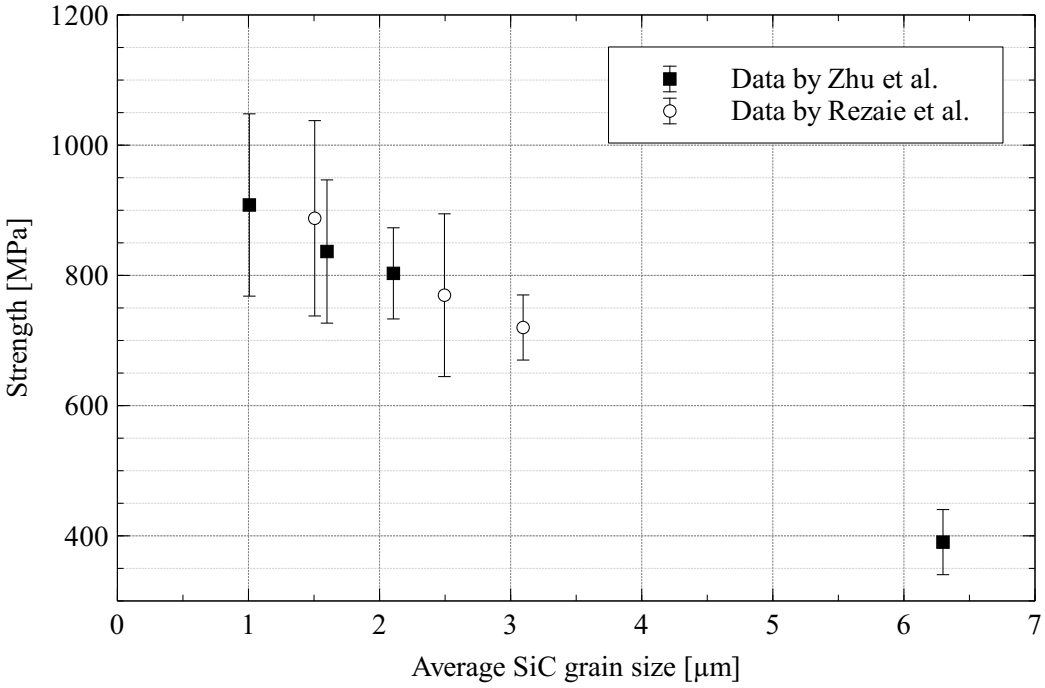

Figure 2.8.: Influence of SiC grain size on strength of ZrB_2-SiC composites [118]

Zhang et al. [90] used RMI to manufacture ZrB_2-ZrC composites. They started with a porous B-SiC preform and infiltrated with Zr_2Cu, resulting in a ZrB_2-ZrC composition with some residual B and ZrCu at processing temperatures of 1200°C. The composites showed a bending strength of 414 MPa, modulus of 184 GPa, and fracture toughness of 5.5 $MPa\sqrt{m}$. Johnson et al. [119] infiltrated porous B_4C preforms with pure Zr at temperatures above 1800°C. They produced ZrB_2-ZrC composites with various amounts of residual Zr phases and discovered that fracture toughness linearly increased from ~11 $MPa\sqrt{m}$ at 0-2vol% metal to 22 $MPa\sqrt{m}$ at 30vol% metal.

2.3.1. Oxidation

Hoffman [120] started his investigation of ZrB_2 in 1953 regarding application in gas turbine blades. Berkowitz-Mattuck and Kaufman followed in the 1960s [114, 121] with their investigation of ZrB_2 and HfB_2. In 1970, Kaufman published the improvement of diboride oxidation resistance by SiC additions [122, 123] and suggested these composites as promising materials for hypersonic application. Further investigations were performed by Tripp et al. [124, 125], also including micro structure analysis of the oxide scale. Until the 1990s, there was a lack of literature in this field. When NASA Ames demonstrated the use of UHTCs for sharp leading edges on a ballistic flight experiment [126, 127], UHTCs research and literature available on UHTCs moved back into focus. More recent studies confirmed the earlier results of the SiC addition increasing oxidation resistance, densification, and thermal shock resistance of ZrB_2 and HfB_2 [12, 23, 25, 39, 62, 116, 128–133]. These composites form a multi-layer oxide scale

at elevated temperatures. They form a refractory oxide skeleton partially filled and covered with amorphous (glass) oxide, which is believed to act as an oxidation safeguard at high temperatures [12, 26, 40, 62, 125, 126, 128, 129, 131–136]. Generally, the combination of ZrB_2 and SiC form the following layers:

- Silica-rich outer surface,
- Zirconia in a columnar skeleton structure with silica between the zirconia grains,
- ZrB_2 region depleted in SiC, and
- ZrB_2-SiC base material.

The main reason for this formation is due to the preferred oxidation of the SiC grains resulting in the depleted SiC layer. As an example, 2.9 shows the oxide layers of ZrB_2-SiC, starting from the top with the silica layer.

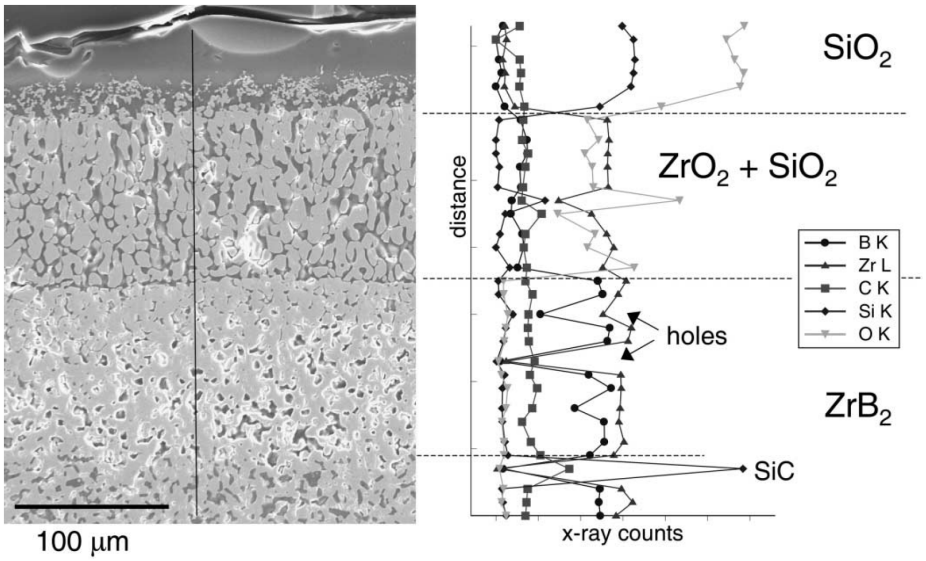

Figure 2.9.: SEM and EDX line of ZrB_2-SiC after oxidation in air at 1627°C for 10 cycles, each 10mins [128]

At approximately 600 °C, monolithic ZrB_2 begins to oxidize and forms a layer consisting of solid zirconia and liquid B_2O_3 [123, 124, 134, 137]. For temperatures below roughly 1100 °C, B_2O_3 forms a continuous liquid passive layer, lowering the oxygen diffusion and resulting in a passive oxidation with reported parabolic (diffusion controlled) oxidation kinetics of ZrB_2 [121, 138]. Oxidation rates in this temperature range depend on the partial pressure of oxygen, which is controlled by the transport of oxygen through B_2O_3(l) [114, 121, 124, 138]. Between 1100 °C to 1400 °C, oxidation rates increase due to evaporation of B_2O_3(l) caused by the high vapor pressure of B_2O_3(l). Oxidation kinetics in this range are controlled by mass gain (ZrO_2(s) B_2O_3(l)) oxide formation and mass loss due to evaporation, resulting in para-linear kinetics [12, 124, 134]. Above ~1400°C, the oxidation rates increase as evaporation

of B_2O_3(l) becomes larger than its formation, resulting in a porous ZrO_2 and rapid linear kinetics [124, 131]. ZrB_2-SiC composites show better oxidation resistance above ~1200 °C, caused by the oxidation of SiC and results in the formation of a silica-rich surface layer [12, 23, 39, 56, 125, 128, 131, 134]. The layer that forms at the surface results from SiO_2 dissolving with B_2O_3. B_2O_3 evaporates much quicker than SiO_2 due to the difference in vapor pressure at high temperatures [39, 131, 137, 139, 140]. This leaves a SiO_2 rich surface layer, which has been reported to provide increased oxidation resistance up to ~1500 °C and is caused by its lower vapor pressure, higher melting temperature, and viscosity, which results in less oxygen diffusion and suppressed B_2O_3 evaporation [56, 114, 125]. A 20 vol% SiO_2 addition to B_2O_3 increases the melting temperature from 450 °C to 700 °C. Literature appears to have a consensus that little B_2O_3 is found in the oxide layer. The amount of B_2O_3 is discussed with more controversy for monolithic ZrB_2 and ZrB_2-SiC at temperatures above 1200 °C, which is likely also due to the difference in oxidation atmosphere and shear forces. For example, Opeka et al. [12] reported 10 wt% of B_2O_3 in monolithic ZrB_2 oxidized between 1200 °C and 1400 °C and Rezaie et al. [141] reported less than 1 wt% B for a ZrB_2-SiC oxidized at 1200 °C for 30 min (calculated). The challenges in detecting low B quantities must be taken into account. Light elements like B are difficult to detect with elemental analysis methods such as . EDX has a low sensitivity to light elements like B, and detection within samples containing Zr is even more difficult due to the overlap at the M x-ray line peaks of Zr and K line peaks of B. Another issue is the preparation of the investigated samples and their oxidized surfaces, which is caused by the hydration sensitivity of B_2O_3. Hence, for the cross-sections of oxidation layers, specimens must be polished using non-aqueous procedures in order to avoid hydration. There has also been a significant amount of research focusing on improving processing techniques for ZrB_2 composites as well as improving oxidation resistance with additional phases [23, 26, 40, 62, 116, 130, 132, 133, 142]. Literature covers several studies using thermodynamic analysis and vapor phase equilibrium such as definition and interpretation of volatility diagrams in order to describe the oxidation behavior of ZrB_2 and its composites [39, 131, 137]. The conclusion of these studies was that materials forming pure oxide scales, such as SiO_2, Al_2O_3, Cr_2O_3, and BeO are not suitable for temperatures above 1800 °C due to a high vapor pressure at the interface of the base material and oxide scale. Recently, work has been performed to further increase the oxidation resistance by improving the oxidation layer composition, influencing melting temperature, viscosity, and oxygen diffusion of the surface layer [39, 132]. For temperatures between 1200 °C and 1400 °C, the oxidation resistance was improved by the addition of TiB_2, NbB_2, TaB_2, VB_2, and CrB_2 as a partial substitution (up to 20 at%) for ZrB_2. Ti, Zr, Nb, V, and Cr oxides were present in the borosilicate surface layer and caused phase separation in the glass. The higher melting temperature and viscosity of the immiscible glasses seemed to be the cause of improvement. At 1500 °C, no significant effect of the additives on the oxidation behavior was reported, likely due to exceeding the miscibility gap in the multi-component glass systems. In recent studies, Opila and Talmy [130, 132] examined the addition of Ta_5Si_3 to the ZrB_2 system. 20

vol% SiC and 20 vol% Ta_5Si_3 improved the oxidation resistance at 1627 °C, but at a higher temperature of 1927 °C, it showed no improvement due to the formation of a non-protective liquid oxide phase. The source for the formation of the SiO_2-rich layer are convection cells, as reported by Telle and Karlsdottir [143, 144]. They report a B_2O_3-rich boron-silica-zirconia (BSZ) liquid flowing to the surface, which then loses B_2O_3 due to evaporation.

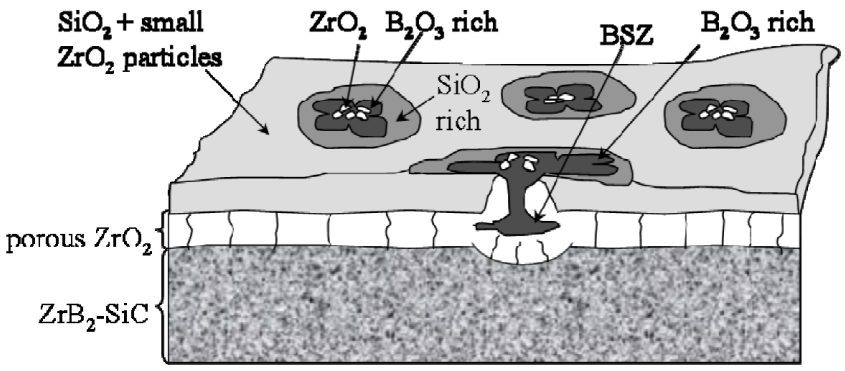

Figure 2.10.: Schematic of convection cells forming on oxidation of ZrB_2-SiC at 1500-1600 °C, showing the surface covered with cells that have ZrO_2 cores (white) located in larger SiO_2 cells (grey) with B_2O_3 rich patterns (black) surrounding the cores [144]

Karlsdottir [144] estimated that inward oxygen diffusion decreases with an increase in SiO_2 content in a B_2O_3-SiO_2 melt. The reason for this is the low diffusion coefficient of oxygen for a pure SiO_2 melt compared to a B_2O_3-rich melt. His calculated diffusion coefficients of oxygen in borosilcate melts are smaller than the diffusion coefficient of oxygen in ZrO_2 reported by Fox et al. [130]. This leads to the assumption that the borosilicate outer layer is an oxygen diffusion barrier during oxidation at higher temperatures, and therefore, controls the oxidation rate [144]. The convection cells cause an inhomogeneous oxidation at a microscopic scale. Uniform oxidation reported in literature could be the result of the fine scale of local events. Karlsdottir assumed uniform oxidation could occur in an early state, causing a pool of BSZ liquid. These BSZ can erupt upon reaching a critical amount of volume and pressure, increasing oxygen diffusion during the eruption. With increasing oxidation time, the number of convection cells decreases as the thickness of SiO_2 increases. The SiO_2-rich layer submerges the convection cells and, once thick enough, suppresses the formation of new cells. Therefore, convection cell mechanisms are claimed to be dominant at the beginning of oxidation and transport SiO_2 to the surface. With continuing oxidation and increasing SiO_2 content, the convection cells disappear [144]. Increasing oxidation temperature increases the number of convection cells forming at the early stage of oxidation, caused by the increased evaporation rate of B_2O_3 and higher vapor pressure. Karlsdottir suggested to focus on the improvement of the oxidation resistance by altering the B_2O_3-SiO_2 glass instead of pure SiO_2 glass.

Plasma Wind Tunnel

Arc Jet or Plasma Wind Tunnels (PWT) have been used for decades to investigate materials for re-entry vehicles, combustors, and more recently, hypersonic vehicles. In general, Thermal Protection Systems (TPS), leading edges, and control flaps have been tested. The heating unit of PWT produces a high-temperature gas stream via combined radiation as well as conductive and convective heat transfer. There are multiple methods to generate plasma. The most common method is the use of an arc jet with an electric arc discharge and a gas flowing through this arc. PWT testing is expensive due to the high power used and the time-consuming setup. The facilities of DLR are described in detail by Esser et al. [145]. PWT provide similar conditions to re-entry, but compared to burner rig tests, shear forces are smaller. Shear forces from the gas flow influence the oxidation behavior by removing the liquid protection layer formed by oxidation of ZrB_2-SiC. Compared to a furnace oxidation test, without shear forces, the outer glass layer of diboride UHTCs is thinner. Usually, PWTs reach a stagnation pressure of less than 500 mbar, resulting in smaller shear forces.

Burner Rig

Burner Rig tests are usually a fast and inexpensive method to examine the oxidation of UHTCs. Different gas combinations can be used for combustion, influencing the flame temperature. If the combination involves oxygen, the oxygen partial pressure can also be varied. A peak temperature of 2800 °C and heating rates of 500 K per second can be reached with oxyacetylene torches [33].

Furnace

Oxidation using a furnace is usually done in stagnating air. Beside the lower heating rates, the tests can either be performed within a closed environment with the oxygen within the furnace volume limited or in an open environment using a continuous flow of air. Open environment tests can be performed with a heating phase in an inert atmosphere before starting oxidation by switching to oxygen-containing gases upon reaching the peak temperature. In general, furnace tests will result in a larger duration of oxidation or annealing due to the slower heating rates compared to plasma wind tunnels or burner rigs.

3. Experimental Methods

Experimental methods and equipment used during the investigation of this thesis will be described in this chapter. Additionally theoretic considerations associated with the analysis of experimental results will be enclosed. For a more detailed explanation to some methods it will refer to literature.

3.1. Density and Porosity Measurement

For both density and porosity the physical units are clearly defined, the definition of which exact reference volume is taken into account can be defined differently. In general there are three different definition for each property. According to DIN EN 993-1 [146] the following definition for density and porosity are defined:

- Density (true density or solid body density; ρ):
  Ratio of mass from a dry, porous body and its true volume. True volume is defined as the volume of a solid body within a porous body.
- Bulk density (geometric density; ρ_b):
  Ratio of mass from a dry, porous body and its total volume.
- Apparent density (ρ_A):
  Ratio of mass from a dry, porous body and the sum of volume from the solid body and its closed pours.
- Open porosity (e'):
  Ratio of volume from open pours of a porous body and its total volume. Open pours are pours which can be infiltrated in vacuum by a fluid media, meaning direct or indirect connected to the surrounding atmosphere.
- Closed porosity (e"):
  Ratio of volume from closed pours of a porous body and its total volume.
- Total porosity (in general porosity):
  Ratio of volume from the sum of open and closed pours of a porous body and its total volume.

To determine the porosity and density values of different samples, the following methods can be used.

3.1.1. Archimedes Principle

According to DIN EN 1389 [147] a dry and porous body can be infiltrated with a liquid fluid, de-ionized water within this study, to determine its porosity and density. The following equations can be used to determine densities and open porosity by measuring the masses as described:

$$\rho_b = \frac{m_{dry}}{m_{wet} - m_{uw}} \cdot \rho_{H_2O} \tag{3.1}$$

$$e' = \frac{m_{wet} - m_{dry}}{m_{wet} - m_{uw}} \cdot 100 vol.\% \tag{3.2}$$

$$\rho_A = \frac{m_{dry}}{m_{dry} - m_{uw}} \cdot \rho_{H_2O} \tag{3.3}$$

with:

ρ_b	bulk density
m_{dry}	dry mass of porous body
m_{wet}	infiltrated mass of porous body
m_{uw}	submerged mass of porous body
ρ_{H_2O}	water density at room temperature
e'	open porosity

Archimedes principle should only be used up to a pore size of 200μ.

3.1.2. Mercury Porosimetry

According to DIN 66133 [148] mercury infiltration can be used to determine the pore size distribution of a porous body. The method uses the pressure dependence of mercury intrusion into open pours. As long as mercury is a non wetting fluid to the porous body, which it is in most cases, it requires pressure to enter the pours. By recording the pressure and mercury volume infiltrated, the pour sizes can be determined. When assuming a cylindrical pore model according to Washburn [149], the radius of pores can be calculated:

$$r_P = \frac{2 \cdot \gamma \cdot \cos(\Theta)}{p} \tag{3.4}$$

with:

r_P	pore radius
γ	surface tension
Θ	contact angle
p	corrected pressure

The measurements are performed with a combination of two mercury porosimetry machines, Pacal 140 and Pascal 240 manufactured by CE Instruments. The resolution of the two machines ranges from $5nm$ to $50\mu m$, calculated with contact angle of $\Theta = 140\,\text{deg}$ and a surface tension of $\gamma = 0.48 N/m$.

3.2. Drop Shape Analysis

Even without a chemical reaction, molecules interact with each other. They are subdivided into four categories, ion forces, dipole, hydrogen bonding and Van-der-Waals forces. Two non mixing fluids have a minimal contact surface to each other, resulting in drop shape form due to cohesive forces. A molecule inside a drop statistically applies the same cohesive force in every direction. A molecule at the drop surface can only experience cohesive forces centripetal to tangential, due to the lack of molecules of the same type. The resulting force is in direction of the drop center, which is the reason for the circular shape. Increasing the surface acquires work, hence every system seeks a state of minimal energy and maximum entropy, fluids tend to form drops. The interaction of different types of molecules on the intersection follows the same principle. These forces are call adhesion forces and the type of interaction is also defined by the molecular structure. A drop of a fluid on a solid substrate experiences both type of forces, the cohesive forces in direction of the drop center and the adhesion forces in direction of the solid substrate. The resulting force of adhesion and cohesion will determine if the drop spreads on the surface (wetting) or tries to keep the surface contact as minimal as possible (non wetting). The drop also experiences interactions at the interface to the gas phase. These forces are much smaller due to the low particle density of gases and low cohesive forces inside the gas. The areas, or two points in a two dimensional analysis, where all three phases are in contact are call three-phase contact points. Energy which is stored in an increased surface of a homogeneous phase, is call surface free energy Ψ. In fluids, surface free energy is defined as surface tension. The processes taking place during a reduction of contact surface of two homogeneous phases are:

- Increasing surface of phase 1
- Increasing surface of phase 2
- Decreasing contact surface between phase 1 and 2

The first two processes require energy, the reduction of contact surface is analog to reducing surface free energy. Instead of the surface tension, inter-facial tension γ_{12} is effective. Dupre defines the energy set free by decreasing the contact surface of two phases as adhesion work W_{12}

$$W_{12} = \Psi 1 + \Psi 2 - \gamma_{12} \tag{3.5}$$

A droplet on a solid surface gives a good example of surface tension minimizing the contact surface. At the same time surface tension between drop and gas is trying to minimize the contact surface of drop and gas. Due to low cohesive forces and small particle density of gases, the inter-facial tension of liquid/gas and solid/gas can be neglected and instead the surface tension of fluid and solid are used. If a drop is in thermodynamic equilibrium, meaning it does not spread or shrink any further on the surface, no force is acting inside the plain between drop and surface. Figure 3.1 illustrates the vector addition of the acting forces. The

relationship between the surface free energy $\Psi(s)$, inter-facial tension $\Psi(sl)$, surface tension $\Psi(l)$ and contact angle from the thermodynamic equilibrium is as follows:

$$\Psi_{(sl)} + \Psi_{(l)} \cdot \cos\Theta - \Psi_{(s)} = 0 \tag{3.6a}$$

$$\Psi_{(s)} = \Psi_{(sl)} + \Psi_{(l)} \cdot \cos\Theta \tag{3.6b}$$

The equation is named after Young, described in his essay [150]. There are a lot of measurement methods to determine the surface tension (ring method, capillary method and more). Inter-facial tension can't be measured directly and different methods exist to use the measurement of the contact angle.

Drop shape analysis is used to determine the contact angle from the image of a sessile drop and the surface tension from the image of a pendant drop.

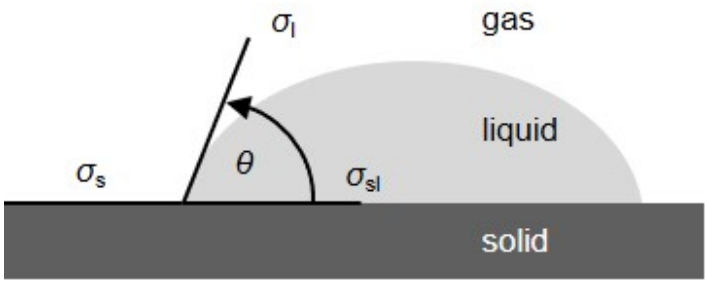

Figure 3.1.: Contact angle schematic of a sessile drop

The measurement is a static contact angle of a drop in thermodynamic equilibrium, in case for the high temperature measurement as a pendant drop. The drop forms upon melting of the liquid phase and the shadow image is recorded using a digital video camera. The digital images are further analyzed using the highest brightness gradients to determine the drop shape and baseline. There are different mathematical methods to describe the contour of the drop, which are then used to determine the contact angle. The two most common used fitting methods are described below:

- Tangent fit typ 1
  The contour of the drop is described using a cone cross section. The parameters of the equation are iterated to best fit the contour, derivation at the three-phase contact points allows to calculate the contact angles.
- Young-Laplace fit
  Young-Laplace equation describes the capillary pressure difference sustained across the interface between two static fluids. It relates the pressure difference to the shape of the surface as follows:
  $$\Delta p = \gamma \left(\frac{1}{R_1} + \frac{1}{R_2} \right) \tag{3.7}$$
  where Δp is the pressure difference and R_1 and R_2 are the principal radii of curvature.

Fig.3.2 shows the contact angle of Cu on a SiSiC substrate at 1150°C, being around 150°C. The green line is the Young-Laplace fit of the drop shape and the purple line is the baseline through the three-phase points.

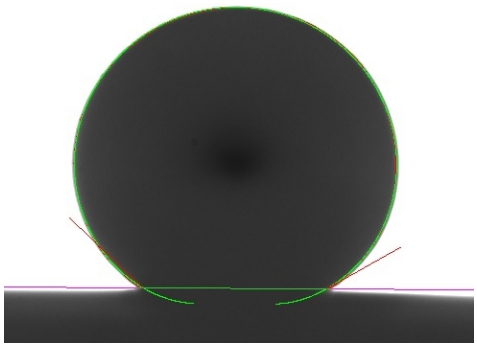

Figure 3.2.: Drop shape image of Cu on SiSiC substrate

To perform contact angle measurements, a furnace is heated via Mo resistance wires coiled around the tube's central section. Due to the need for an inert atmosphere, a vacuum-tight housing is required, and the heating element must be under a constant argon atmosphere. The furnace is linked to a vacuum pump, placed on a separate platform to prevent vibration interference, and two tanks of argon (Linde, Argon 5.0), which allow for both the heating element and the stage chamber to operate effectively between 300-1550°C. The system remains hermetically encased via the use of vacuum seals, and a slight over-pressure is set to maintain the protective gas atmosphere. One end of the tube is fitted with an observation window flange and at the other end sits a seal-able opening used to insert the sample. The stage is illuminated using a LED lamp. The droplet is recorded using a Stingray F-046B camera, with fine-adjustment focus, which allows for 0.5 MP video recording and a contact angle measurement range between 1°-180°, with a resolution of 0.1°. A variety of modeling methods can be used (Tangent, Laplace Young and manual measurement) in the measurement program, depending on the shape and contact angle of the droplet. The furnace controller allows heating rates between 2.5 – 10 °K/min. The temperature inside the furnace is measured using a Type B thermocouple, located directly below the sample stage. Maximum heating rates are 10 K/min up to 1000°C, 7 K/min from 1000°C-1200°C and 5 k/min from 1200°C-1700°C.

3.3. Electrophoretic Deposition

Electrophoretic Deposition (EPD) is a process in which particles from a colloidal dispersion or suspension are deposited onto a substrate by means of electrical charge. The particles must be removed with a certain surface charge, present in the liquid medium, such that they traverse to the opposite charged electrode within the electric field [151]. If the substrate is conductive, an insulating layer between the fabric and the electrode should be applied. The

particles present in the suspension not only move to the charged fabric, but also pass through the fabric, see figure 3.3. As a result, some particles remain stuck in the fabric.

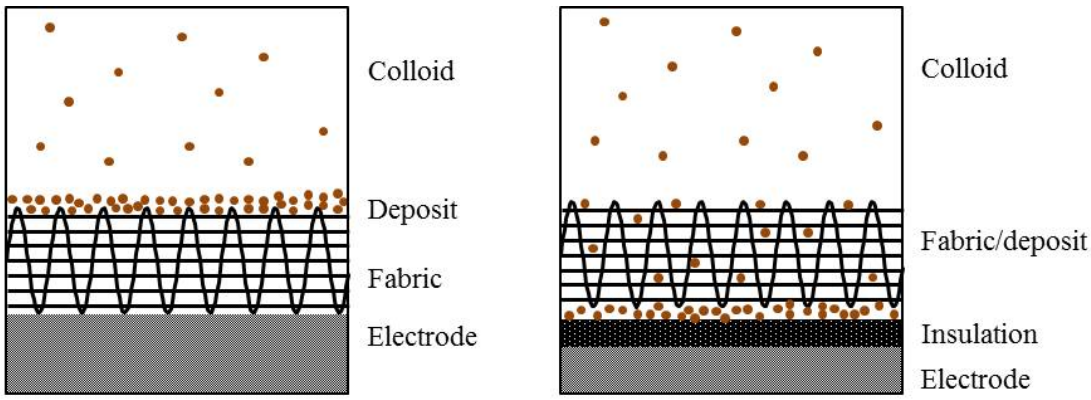

Figure 3.3.: Schematic of the influence of insulation layer during EPD

The following parameters influence the disposition of the process: Suspension:

- Particle size
- Viscosity
- Electric conductivity
- Stability and ζ-Potential

Process:

- Duration
- Voltage
- Conductivity of substrate/fabric

Some of these parameters are linked to each other, so that not all of them can be set independently of each other. The particle size ideally ranges from 1 and 20 μm. Larger particles, make the dispersion more unstable and the deposition of the particles on the substrate becomes inhomogeneous. This has in particular be taken into account for vertical electrode arrangements. In addition, the surface charge must be increased with larger areas in order to move the particles in the electric field. Lower viscosity means less resistance of the liquid that charged particles have to overcome in order to move. Conductivity influences the particle movement within the suspension. If the suspension is too conductive, the particle movement is very slow, but if it is too resistant, the particle charge increases and the stability is lost. Therefore, each system has an optimum working adjustment. The conductivity increases with increasing temperature and an increase in the concentration of polyeletrolytes. A suspension is stable if no aggregation or sedimentation occurs within the relevant time frame. A distinction is made between electrostatic and steric stabilization [152]. Electrostatic stabilization creates a high charge density on the surface of the particles, causing them to repel each other. If a polymer is absorbed on the surface and thus generates entropic repulsion, this is referred to as steric stabilization [153]. There is also a mixture of these two mechanisms, known as electrosteric stabilization using a polyelectrolyte. These are water-soluble polymers with a

long chain length, which have anionic or cationic dissociable groups, e. g. polyacrylic acid or phenols (cationic). Due to the need of free charge carriers available for electrophoretic deposition, only electrostatic and electrosterical stabilization are possible for EPD [153]. If a suspension is too stable, the repulsive forces are very high and the particles cannot overcome them due to the electric field. As with conductivity, there is an optimum range for stability. However, hence it depends on many factors, it has to be determined experimentally [151]. In the case of electrostatic stabilization, which is usually carried out in polar solvents (e. g. water), the stability of the suspension depends on zeta potential. Zeta potential has also an influence on the direction of particle movement. The value can be controlled by adding acids or bases, since zeta potential is dependent of the pH value. The value of zeta potential can also be controlled by adding polyelectrolytes. The greater the distance to the isoelectric point, the more stable the suspension. Zeta potential of 40 mV upwards are considered as stable suspensions [154]. In addition, the wandering particles are favored by a high amount of zeta potential. In non-polar solvents, on the other hand, very small surface charges and zeta potentials are sufficient to produce a stable suspension [154]. With increasing deposition time, the amount of deposit increases linearly. However, the suspension is depleting of charged particles and the deposition layer reaches a threshold. In general, a DC voltage is applied to achieve a defined particle movement. The higher the applied voltage, the faster particles are deposited on the substrate. However, reaching too high voltages can lead to a reduction in quality due to eddies forming and cause uneven distribution. The voltage range should be between 25 and 100 V/cm. The lower the conductivity of the substrate, the more uneven and slower the separation of particles occurs.

3.4. Thermogravimetric Analysis

According to DIN 51006 [155], thermogravimetric analysis (TG) is a method of thermal analysis, determining temperature- and time-dependent mass changes of a substance. The investigations are carried out with a TGA of the type STA409C from Netzsch-Gerätebau GmbH (Selb, Germany). The scale used operates according to the principle of electromagnetic compensation. The temperature range is 20-1550°C using N, Ar or air atmosphere. The flow rate of the respective medium is set to $100 ml/min$. High-purity Ar of quality level 5.0 is used for investigations. The sample mass set between 250-500 mg and heating rate is to $10 K/min$. The relative error of the measured mass loss is $\pm$0.01M. %.

3.5. Scanning Electron Microscope

Scanning electron microscope (SEM) can be used to gain high resolution images with a high characteristic depth of field, reaching resolution up to 1 000 000:1. The SEM uses a electron beam scanning the surface of the investigated target, the measured interaction of electron beam and target is used to create the resulting image [156]. Analysis throughout this work

have been conducted with a field emitting SEM Ultra 55 Plus from Carl Zeiss NTS GmbH. This type of SEM is equipped with a thermal Schottky field emitter, which allows a electron-accelerating voltage between 0.02 and 30 kV. The highest precision of this SEM reaches 1.0 nm using 15 kV. It is equipped with four different detectors: Secondary electron detector ((SE), In-Lens secondary electron detector, energy-selective back-scattered detector (EsB) and angular-selective back-scattered electron detector (AsB). Depending on the focus of the investigations, different detectors have to be taken into account. In addition, the SEM is equipped with a EDX used to determine the different elements inside a sample (see section 3.6 for more details). In order to investigate the samples micro structure each sample is cut, embedded into a conductive resin, ground and polished. Due to the polishing suspensions used, the samples are cleaned in an ultra-sonic bath in between polishing cycles.

3.6. Energy-Dispersive X-Ray Spectroscopy

The energy-dispersive X-ray spectroscopy is used for analyzing material composition within a SEM image. The elemental analysis is based on the stimulation of a characteristic X-ray emission spectra by a high-energy electron beam. Each element emits its specific energy which can be detected in form of a specific X-ray spectra. Using a statistic analysis of the measured X-ray patterns within the SEM, the material composition of the analyzed sample can be determined [156]. Investigation are performed using a X-Max manufactured by Oxford Instruments and integrated on the Ultra 55 Plus SEM (see section 3.5). The X-Max detector size is $20mm^2$ and is calibrated with a high purity silicon crystal. The acceleration voltage is adjusted from 5 kV to 18 kV, depending on the presence of Zr inside the sample, and a minimum of >100.000 counts.

3.7. X-Ray Diffraction

X-ray diffraction (XRD) is a method to analyze crystal structures within a sample. Diffraction will appear in case the wavelength is of the same magnitude as the lattice spacing, represented by the planes in the atomic lattice. The Bragg equation defines the relationship between the wavelength of the x-rays, the atomic lattice and the angle at which the x-rays impinge on the lattice. The diffraction patterns allow a conclusion of the crystal phases present and their crystal structure [157]. XRD spectra are recorded with a D8 Advance from Bruker AXS GmbH and analyzed using the Bruker AXS GmbH software DIFFRAC^{plus} EVA.

3.8. 3D Atom Probe

3D atom probe tomography provides a 3D image of atoms within a solid structure. In order to analyze samples, they usually have to be needle shaped with the tip being at nano scale level. In case of the UHTCMC the region of interests are prepared using a Focused Ion

Beam (FIB). For analysis the sharpened sample is mounted on a cryogenic cooled stage in an ultrahigh vacuum system. In general a atom probe combines the field ion microscope with an mass spectrometer. The 3D image is reconstructed by the trace, speed and mass of each atom measured by the detector. The atoms are evaporated using a pulsed laser before accelerated by the electric field. The analyzed volume is limited to around 10^{-6} nm^3 (around 100 nm needle diameter) with a sensitivity of 100 ppb (parts per billion). The 3D atom probe tomograph used in this study is LEAP 4000X HR manufactured by CAMECA Inc. in France.

3.9. Mechanical Testing

To determine the mechanical behavior three point bending (3PB) and tensile tests are performed at room and elevated temperatures. In general the test are performed according to standard DIN EN 658-3 [158], if the test procedure deviates from this standard, the deviations are mentioned and discussed. All tests at room temperature are performed with universal testing machines from Zwick and elevated tests with the high temperature testing machine Indutherm. For compositions tested with a higher amount of samples, the average and standard deviation considering a normal distribution is calculated.

3.9.1. Three Point Bending

3PB tests are performed on the basis of DIN EN 658-3 [158], using a 10 kN force sensor. If possible the ratio of bearing distance and sample thickness is kept above 20. The upper loading bearing has a radius of $5mm$ and the two lower bearing have a radius of $2mm$. The testing speed of each sample is set to $1mm/min$. The 3PB stress and outer fiber strain on the bottom side of the sample can be calculated according to the following equations:

$$\sigma_{3PB} = \frac{3 \cdot F_{max} \cdot L}{2 \cdot B \cdot D^2} \tag{3.8}$$

with:

σ_{3PB}	tensile bending strength in MPa
F_{max}	maximum bending force in N
L	load bearing distance mm
B	sample width in mm
D	sample thickness in mm

$$\epsilon_{3PB} = \frac{6 \cdot f \cdot D}{L^2} \tag{3.9}$$

with:

ϵ_{3PB}	outer fiber strain
f	displacement of the sample at the upper bearing in mm

In order to account for the stiffness of the testing rig, a compensation measurement is performed and accounted for by the calculation of the strain rates. Bending a sample will not

only induce tension in the lower portion of the sample but also shear through the cross-section of the sample. Assuming the neutral layer is at the center line of the sample, the maximum shear stress is at the center of the sample below the upper bearing and can be calculated according to DIN EN 658-5:

$$\tau_{3PB} = \frac{3 \cdot F_{max}}{4 \cdot B \cdot D} \tag{3.10}$$

with:

τ_{3PB} shear bending strength in MPa

as described in DIN EN 658-5, the inter-laminar shear strength can be determined with a 3PB test using a L/D of 5. However, the material needs to have a certain ratio of shear and tension strength in order to fail at this L/D ratio. If the shear strength is more than 10 times higher than the tensile strength, the sample will even fail for a ratio of 5 in tensile bending.

3.10. Fracture Toughness

Fracture toughness is a measure of the resistance of a material to crack growth. The associated material parameter is the critical stress intensity factor K_C at which unstable crack propagation begins or failure occurs. Materials with a high value for critical stress intensity factor have a high resistance to crack growth. These intensity factors are classified according to the strain occurring at the crack opening:

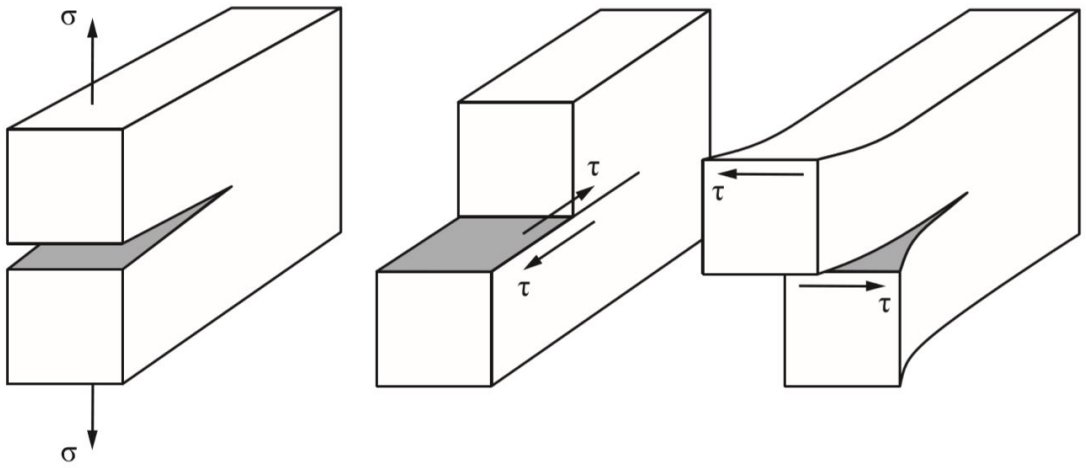

Mode I Mode II Mode III

Figure 3.4.: Crack opening classes; Mode I under tensile stress, mode II under shear stress perpendicular to the crack opening and mode III under shear stress parallel to the crack opening [159]

Mode I corresponds to the load under normal stress and is therefore characteristic of a tensile load. Mode II occurs under shear stress perpendicular to the crack tip and Mode III

under shear stress parallel to the crack tip. The associated critical stress intensity factor is calculated as follows.

$$K_{1C} = \sigma \cdot \sqrt{\pi \cdot a_C} \cdot Y \tag{3.11}$$

Y being a correction factor and a_C the critical crack length. The stronger a specimen is loaded with the corresponding crack, the higher the value for the stress intensity factor K_1 will be. At a certain point the unstable crack propagation starts. K_{1C} corresponds to the most critical case, i.e. the lower limit value. This is calculated from the in plain distortion state, i.e. rupture fracture. In the range of the plane stress state, i.e. shear fracture, and in the mixed state, this value is higher and depends on the thickness of the sample. In these cases, the determined value is referred to as K_Q. Due to these effects, the corresponding standards usually state a minimum component thickness to be tested. In addition, the crack resistance curve can be observe. In this case the stress intensity factor is plotted as a function of the square root of the crack length [160]. The integral of the curve corresponds to the energy which is needed to destroy the specimen. The energy release factor is described as follows.

$$G_{1C} = 2 \cdot \varepsilon_{scs} \tag{3.12}$$

ε_{scs} is the specific crack surface energy. Both equations are coupled in the linear elastic state.

$$K_{1C} = G_{1C} \cdot E^* \tag{3.13}$$

E^* being the reduced elastic modulus and ν the Poisson's ratio, defined according to the state of deformation.

$$E^* = \begin{cases} E, & \text{plane stress state} \\ \frac{E}{1-\nu^2}, & \text{plain distortion state} \end{cases} \tag{3.14}$$

Considering the energy it can be explained, why metals have a higher fracture toughness than ceramics. The stress required to cause plastic deformation, in ceramics, are higher than fracture stress. This is caused by the ionic and covalent bonds of ceramics. As a result, ceramics do not show any plastic deformation close to the crack tip, but instead break brittle. The plastic deformations in metals, on the other hand, lead to an increase in the fracture surface energy [161].

$$K_{1C}^2 = \frac{2 \cdot (\varepsilon_{scs} + \varepsilon_{plast}) \cdot E}{1 - \nu^2} \tag{3.15}$$

ε_{plast} being the plastic deformation energy.
The samples during this research are tested according to ISO 15732 standards and evaluation of the results are performed according to standard and Gross et al. [162].

3.11. Single Filament Fiber Tests

Single-filament tensile tests are performed according to DIN EN 1007-4. Tests are conducted in a servo-motor testing machine designed from the institute at the University of Bremen: This testing machine is equipped with a load cell ULC-1N (Interface Inc., Arizona, USA) for measurement of applied loads and a linear variable differential transducer LVDT AX/1/S (Solartron Metrology, Bognor Regis, United Kingdom) for measurement of specimen displacement. Due to the difficult handling of the single filaments, samples are first glued to a paper frame using UHU Plus Schnellfest (UHU GmbH & Co., Bühl, Germany). The paper frame is designed for the correct positioning and alignment of the fiber with the testing machine, as well as for defining gauge length of the specimens. Gauge lengths are 25 mm, as defined by standards. After positioning the sample, sides of the paper frame are cut so only the fiber is set in tension. Samples are tested until failure with a testing speed of 1 mm/min. In total, 30 samples are tested for each fiber condition. The strength of each filament is calculated using its cross-section. The cross-section area of each filament is determined after the test by analyzing the fracture surface using an optical microscope SENSOFAR PLμ 2300 (Sensofar Group, Terassa, Spain). Weibull distribution is used to describe the strength of the tested filaments. Characteristic strength and Weibull modulus are determined using a probability analysis. With this testing set-up, the deformation of the fibers could not be directly measured due to the combined displacement measured, resulting from the deformation of the fiber and the deformation of the testing rig. Consequently, the displacement of the system is determined prior to testing. These value are then used to determine the deformation and the elastic modulus of the single filaments.

3.12. Fiber Volume Content

Fiber Volume Content (FVC) is the fraction of fibers volume inside a composite compared to the matrix volume, usually every additional phases like fiber coatings or pores will be added to the matrix volume. From the volume of the composite and the total fiber mass used, FVC can be calculated using the following equation:

$$FVC = \frac{V_f}{V_{WS}} = \frac{m_f}{\rho_f V_{WS}} \tag{3.16}$$

with:

FVC	Fiber volume content
V_f	Fiber volume $[cm^3]$
V_{WS}	Composite volume $[cm^3]$
m_f	Fiber mass $[g]$
ρ_f	Fiber density $[g/cm^3]$

4. Determining Zr Based RMI Process

The ability to fabricate UHTCMCs and their material properties is strongly influenced by a variety of process parameters. Fiber reinforcements in particular require detailed investigations in order to increase fracture toughness of the composite. The key aspects are sufficient impregnation with reactive powder and minimal degradation during infiltration with liquid metal alloys. This chapter will provide an overview of the various mechanisms necessary to achieve RMI, the possible raw materials, and the manufacturing process.

The physics governing the infiltration process of Zr or Si-based RMIs are similar. They both use capillary forces to infiltrate a porous preform with molten metal and create ceramics due to the reaction during infiltration. For a Zr_2Cu-based RMI, the reactions occurring during infiltration, depending on the precursors and powders used, are as follows:

$$4B + Zr_2Cu \longrightarrow 2ZrB_2 + Cu, \tag{4.1}$$

$$2B + +Zr_2Cu \longrightarrow ZrB_2 + ZrC + Cu, \tag{4.2}$$

$$2B_4C + 3Zr_2Cu \longrightarrow 4ZrB_2 + 2ZrC + 3Cu, and \tag{4.3}$$

$$2B + Zr_2Cu + SiC \longrightarrow ZrB_2 + ZrC + SiCu. \tag{4.4}$$

Equation 4.4 describes the infiltration of preforms from polycarbosilane and boron powder, equation 4.2 from phenolic and boron powder, equation 4.3 from boron-carbide, and equation 4.1 pure boron powder. In order to manufacture stoichiometric ZrB_2/SiC using RMI, the following aspects must be taken into account:

- the necessary porosity for the boron preform in order to produce a dense stoichiometric matrix
- the necessary pore size distribution to reach all boron
- the necessary ceramic yield for a dense stoichiometric matrix

From the chemical equation, the theoretic volume distributions for each phase and the necessary porosity can be derived:

$$V_{total} = V_{ZrB_2} = V_{por} + V_B. \tag{4.5}$$

Equation 4.6 can be derived from equation 4.1 by replacing the volumes with molar volumes. Division by the molar volume ZrB_2 yields

$$e_{B,stoich} = \frac{V_{por}}{V_{ZrB_2,mol}} = 1 - \frac{V_{B,mol}}{V_{ZrB_2,mol}}. \tag{4.6}$$

4.1. Influencing Factors

This section describes which mechanisms influence an RMI process, and thus, must be taken into account before manufacturing UHTCMC samples. The following sections will indicate the effects caused by different capillary structures, phases forming during the reaction of Zr alloys, and contact angles between preform components and different melts. Each of these must be taken into account in order to be able to infiltrate with molten Zr and manufacture a ZrB_2 matrix. To make the infiltration of the porous preform possible, capillary forces must be high enough to allow for melt infiltration into the preform. This depends on pore size, wetting angle between melt and preform, atmosphere during infiltration, dynamic viscosity, and surface tension [93].

4.1.1. Capillary Structure

The capillary structure is the transport system used to distribute the liquid Zr and allows for a homogeneous reaction with boron. The two characteristic parameters to describe the system are overall porosity and pore size distribution. Due to the volume expansion during the reaction of Zr with B or C, these factors are more essential for a Zr-RMI than a conventional LSI using Si and C.

Porosity

It is important to keep the capillary system open during infiltration. Due to high volume expansion by forming ZrB_2 from boron, factor of ~1.5, a rather high porosity of the preform is necessary. Figure 4.1 shows the influence of the boron powder density on the preform porosity necessary to achieve stoichiometric ZrB_2 from boron and Zr_2Cu, assuming no porosity is left in the ZrB_2. The values are calculated based on equation 4.6. However, if the porosity of the preform is higher than necessary for stoichiometric ZrB_2, there will be an excess of residual melt as well as an excess of boron if below this value. The same calculations can be performed for the formation of ZrC via a reaction of C with Zr_2Cu melt. The points in figure 4.1 mark the actual porosity of different precursors, and the colored lines show the stoichiometric porosity needed for 50 vol.% ZrB_2 and 50 vol.% ZrC, formed either by C + B or SiC + B. As shown in figure 4.1, the porosity of the preform must be higher for stoichiometric ZrC, assuming same carbon and boron density. For samples containing carbon and boron, the porosity of the preform must be between these boundary conditions. The stoichiometric porosity for

equation (3), occurring when using polycarbosilane, is shown as the purple graph. Compared to the formation of ZrC from C, the formation from SiC requires a much lower porosity.

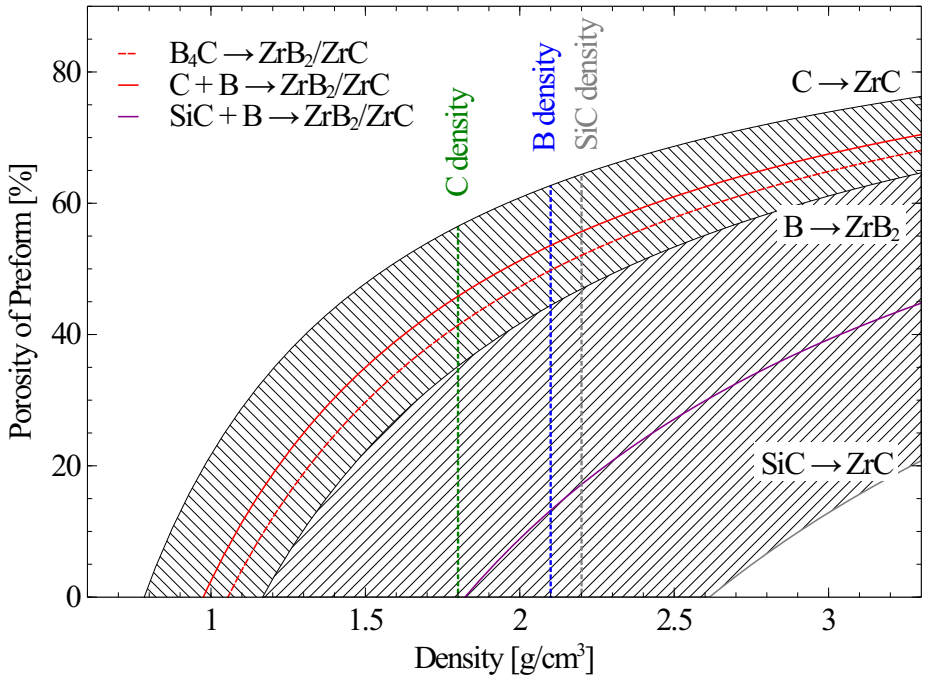

Figure 4.1.: Matrix porosity as a function of density before reaction

Figure 4.1 assumes a variable density for each of the reactants. However, variations in density of each raw material are only possible within a small range. Generally, the required porosity can be lower for lower densities within one reaction scenario. In terms of manufacturing and handling preforms, a preform with lower porosity is less sensitive to delamination or other damages. This makes the formation of ZrC much easier when using SiC as raw material compared to the high porosity necessary when using pure C.

4.1.2. Phase Formation

During RMI, different reactions occur depending on the melts and preform composition and form different phases. In addition to the raw materials, temperatures at the beginning of the infiltration process also influence phase formation. Figure 4.2 shows the volume expansion at various infiltration temperatures. Infiltrations at 1100, 1200 and 1300 °C indicate a large increase in thickness during RMI. Additional heating does not reverse the process, and all experiments have been performed with the same polycarbosilane preform type. The bottom right pictures show the same sample infiltrated at 1300 °C (left) and 1500 °C (right). The large expansion ratio variations are due to the limited infiltration depth at lower temperature caused by a blockage of infiltration channels from volume expansion.

Figure 4.3 shows an XRD analysis of a PCS sample infiltrated at 1300 °C compared to infiltration at 1500 °C. Infiltration at 1300 °C shows a large volume increase, while infiltration

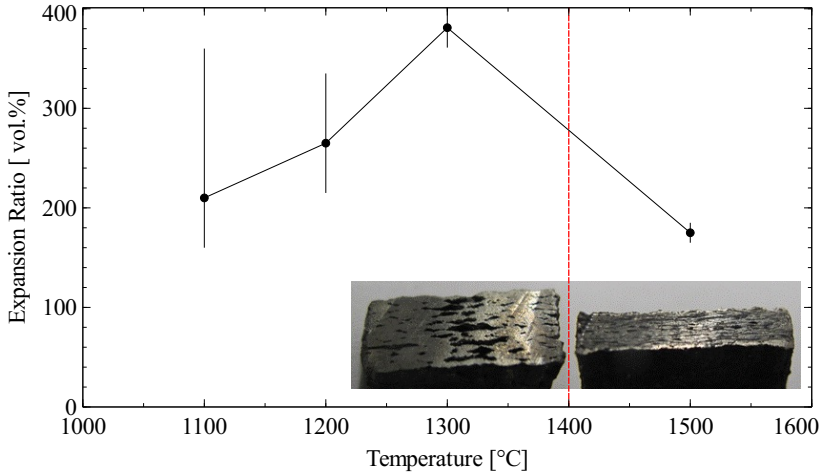

Figure 4.2.: Temperature influence on volume expansion during infiltration

at 1500 °C has a much smaller volume increase. XRD shows that peaks of Zr and Si compounds disappear when changing the infiltration temperature. As described by Kütemeyer et al. [163], the volume expansion is caused by the formation of Zr2Si at lower temperatures.

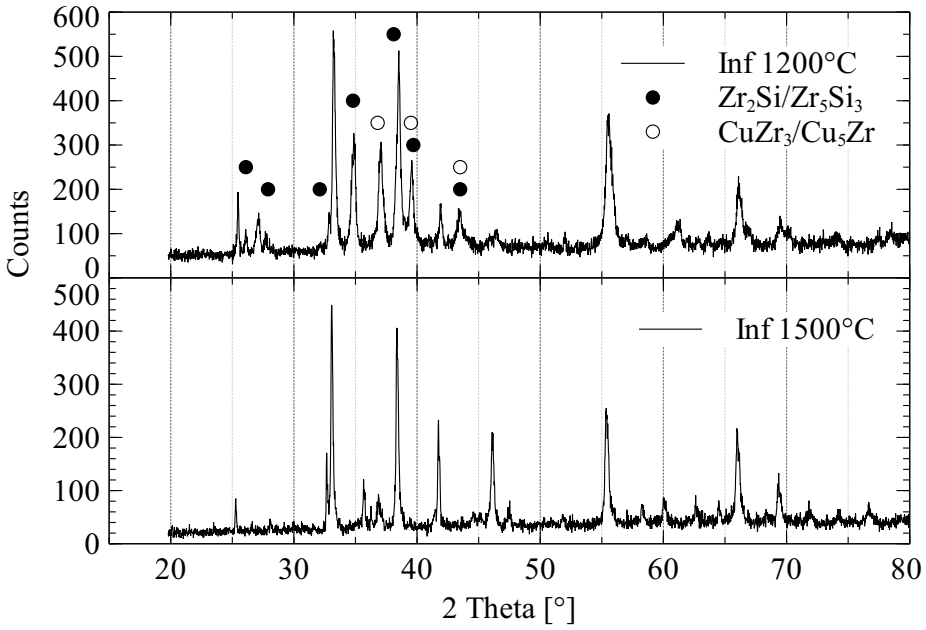

Figure 4.3.: XRD of a polycarbosilane sample at 1300 °C and 1500 °C

Infiltrating a two-phase alloy like Zr_2Cu or Zr_2Ag, results in a segregation of different phases due to the shift in concentration when part of the alloy reacts to form ZrB_2. While Cu or Ag phases help to reduce the melt temperature, the segregation occurring within the infiltration zone can also cause problems. The driving mechanism for infiltration are capillary forces, which depend on many factors discussed in section 4.1.3, including the contact angle between the melt and pore channel wall. The infiltration alloy will react with the infiltrated pore channels, resulting in a depletion of Zr in the propagating infiltrating melt. These Cu

or Ag rich phases have a higher contact angle than the initial alloys, hence, reducing the capillary forces driving the infiltration. Contrary to this effect, the concentration gradient builds between the melt reservoir and infiltration zone. The channels filled with molten alloy try to counterbalance the concentration. This effect occurs much slower than the reaction depleting Zr. Figure 4.4 shows the Cu rich phases forming at the solidified infiltration zone.

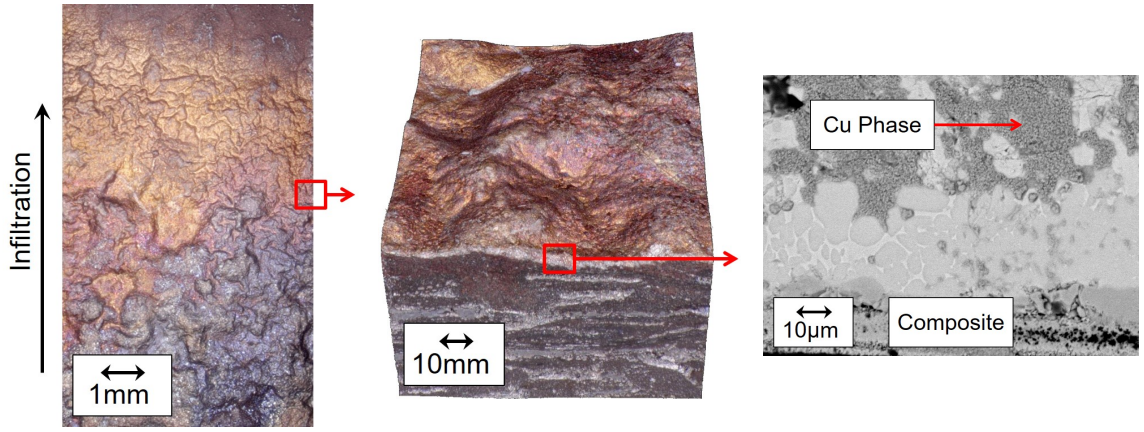

Figure 4.4.: Cu-rich phases forming at the propagating infiltration zone

4.1.3. Contact Angle

A summary of available techniques used to measure these contact angles is provided by Yuan and Lee [164] and ranges from direct measurement via telescope-goniometers, the capillary tube method, and the nanoscale dispensing (NADIS) technique, among others. Kütemeyer et al. [36] details the use of the drop shape analysis (DSA) method, which fits the silhouette of a molten metal drop according to the Young-Laplace algorithm, allowing for accurate measurements of the drop volume and contact angle. Similar methodology is also employed by a variety of other researchers in the field [98, 165–168] and is utilized in this study. Despite established methodology, literature discussing the wetting behavior between UHTC compounds and metal alloys is scarce. Over the past two decades, a range of studies has been aimed at the wetting of liquid silicon on carbon [9, 168–170] due to the common use of LSI as a method of creating CMCs [170], but little research has been conducted in regards to other promising UHTCMC materials such as borides, nitrides, and carbides. The chemical mechanisms of wetting between C and Si have been explored, as seen in the research of Li and Hausner [165]. Such studies cannot be found for refractory metals. Many of the existing studies focus on the wetting behaviors of non-alloyed, noble metals (Cu, Ag, and Au) on pure, monolithic ceramics, which are used primarily for the purpose of ceramic-metal joining. There is almost no available wetting data for refractory alloys (which are used in the RMI process) on UHTC compounds due to the extremely specialized use of this combination. Muolo et. al.'s [98, 171] studies detail the wetting behavior of Cu and Ag alloys on ZrB_2. Despite Ag's and Cu's poor wettability (140° and 120° respectively) with UHTCs, contact angles drop (<80°) when

alloying group IV metals (Ti, Zr, and Hf). Passerone et. al. [100] investigated the influence of various pure melts (Cu, Ag, Au) on ZrB_2, supporting Muolo's findings highlighting the good wetting behavior of pure Au (51°). Aizenshtein et al. [172] investigated the wetting influence of liquid metals (Au and Cu) on TiB_2 substrates, showing similar results, which he attributes to the metallic-like characteristics of borides. He shows the good wetting behavior of Cu and Au on TiB_2 (50° and 15° respectively) compared to ZrB_2, suggesting the promising use of B as a wetting enhancer, owing to the >30° drop in contact angle when exceeding 6 at.%. Further research by Rhee [173] indicates a pure Ag wetting behavior on TaC with a contact angle of 129°.

Determining the influence that reaction products, additives, fiber coatings, and various impurities within the preform have on wetting is important when characterizing the system. Mortimer's [101] research into the wetting of C by Cu alloys showed a significantly larger angle than those seen on ZrB_2 (up to 100° more), which indicate improved infiltration possibilities through a fiber coating. Muolo et al. [98] investigated the influence of Ni impurities within a ZrB_2 matrix, discovering a drop in the contact angle of Cu by ~120° when 4wt. % Ni is used as a sintering aid. Voytovych [99] attributed a similar drop in contact angle to the greater densification of the ZrB_2 composite, in combination with Ni_2B formation, exhibiting a more favorable wetting behavior. Nitrides, such as AlN, Si_3N_4, and ZrN were also found during various studies by Monteverde [174, 175] to increase densification when used as sintering aids, which is caused by their enhanced wetting behavior. Further studies into nitrides by Klein [176] found high contact angles of pure Cu and Ag on N substrates. However, Klein also observed the addition of 3 wt.% Ti to Cu and Ag alloys increased performance immensely, once again reaffirming the improvement on the contact angle by alloying refractory metals. The impact of the wetting behavior of Zr alloys containing Ag, Cu, C, B or other materials on various UHTC compounds is important when selecting preform components such as fiber coatings. The research of Hernesniemi [177] compares the performance of Zr-Ag and Zr-Cu alloys on nitride ceramics, with $AgZr_3$ clearly outperforming ZrCu and Zr_5Cu by over 100°. Prior research conducted by Kütemeyer et al. [36] considered the wetting behaviour of Zr_2Cu on TiB_2 with complete wetting seen at temperatures as low as 1200°C. The addition of B was found to be detrimental to contact angles at temperatures below 1300°C, but beneficial above these temperatures. The use of Zr_2Cu with the addition of 1 at.% B also increased infiltration depth substantially. Temperature also has a well-recorded impact on contact angles. This can be seen in studies conducted by Samsonov et al. [28], showing contact angles dropping nearly 100° between 1100°C - 1400°C when using Cu alloys. These findings are supported by Yasinskaya [178], who presents consistent contact angle drops above 1200°C for various heated borides, carbides, and nitrides. The impact of heating rate on wettability is not as well discussed. The spreading kinetics of each material has a significant effect on wettability. Muolo's research determined a contact angle drop between Ag, Cu, and Zr melts and a (ZrB_2) Ni substrate as large as 120° over a 20 minute time frame [98, 171] following a pattern of steady drops. These findings are supported by Voitovich [179], attributing Cr

and Cu alloy spreading to the time-dependent diffusion of atoms. Studies on the influence of droplet size and surface roughness over wettability are reviewed by Drelich [180], concluding a large contact angle hysteresis will increase the influence of droplet volume.
In order to incorporate temperature changes, contact angles of various Zr-melts are plotted over their temperature range, starting at melting and ending at either wetting angles below ~10° or 1550°C. Values are recorded when a homogeneous drop is formed and correct measurements can be conducted. These initial starting points of each data set depend on the melt composition and initial reactions with the substrate. The properties of the molten alloy itself can have an influence on the formation of the drop shape. In addition to the solid or liquid fraction, the morphology and connectivity of the solid phases are the structural parameters that determine the formation. A quantitative description of the microstructure morphology can be obtained with the help of the microstructure parameter, the shape factor SF, and the phase size (grain size) GS [181]. The shape factor is defined as

$$SF = \frac{U^2}{4\pi A} \tag{4.7}$$

with U being grain circumference and A grain surface. F > 1 refers to grains with a complex shaped surface and F = 1 to spherical shapes. Shape factor largely influences the viscosity of the solid-liquid suspension. Parallel to the growth of the solid phase, the solid phase connectivity, i. e. the strength of the three-dimensional skeleton, also increases. The degree of skeleton phase formation of the solid phase can be described using continuity C [182]. This is a measure of the contact between adjacent particles of a phase. The contiguity is determined by the proportion of the entire boundary of a phase that represents the interface to the same phase. The following equation applies for the solid phase: [181]

$$C^{(s)} = \frac{2S^{(ss)}}{2S^{(ss)} + S^{(sl)}} \tag{4.8}$$

The grain boundary area S^{SS} is between the solid phase, i. e., the area between the contiguous grains and not separated by melt. $S^{(sl)}$ is the phase interface between solid phase and melt. In the case of $C^{(s)} = 0$, the grains are isolated and completely surrounded by melt, while with increasing $C^{(s)}$ the grains grow together, and thus, skeletal formation increases. Conversely, in the $C^{(s)} \rightarrow 1$ case, the solid phase is fully agglomerated and cannot be converted into a suspension by applying shear stresses.
Different compositions of the melt-alloys are combined with different substrates, representing the compounds of the RMI preform. Zr, Cu, Ag, B, and C are used within the alloys and C, SiC, ZrB_2 and TiB_2 as substrates. Contact angles are measured as a function of temperature. In general, Zr_2Cu alloys show smaller contact angles than pure Cu and Ag on tested substrates. Up to 1400°C, Cu shows a high contact angle for most substrates; For TiB_2, the contact angle decreases above 1400°C. Zr_2Cu wets all substrates very well. For SiC substrates, the drop in contact angle starts at 1320°C, as shown in figure 4.13.

TiB_2 Wetting Behavior

Zr_2Cu begins to melt at around 1020°C with wetting at an angle of 56°. Small drops in the contact angle (25°) can be seen at 1026°C and again (15°) at 1057°C. By 1065°C, the melt fully wets the substrate. A uniform reaction layer, approximately $50\mu m$ thick, forms across the TiB_2 surface. EDX analysis in figure 4.5 suggests the layer consists of a ZrB_2 phase with trace amounts of a $ZrTi_2$ and ZrCu. On the substrate side of the interface, a thin Ti_2B layer less than $10\mu m$ wide can be found. Zr_2Ag forms a full droplet at 1202 °C with wetting at

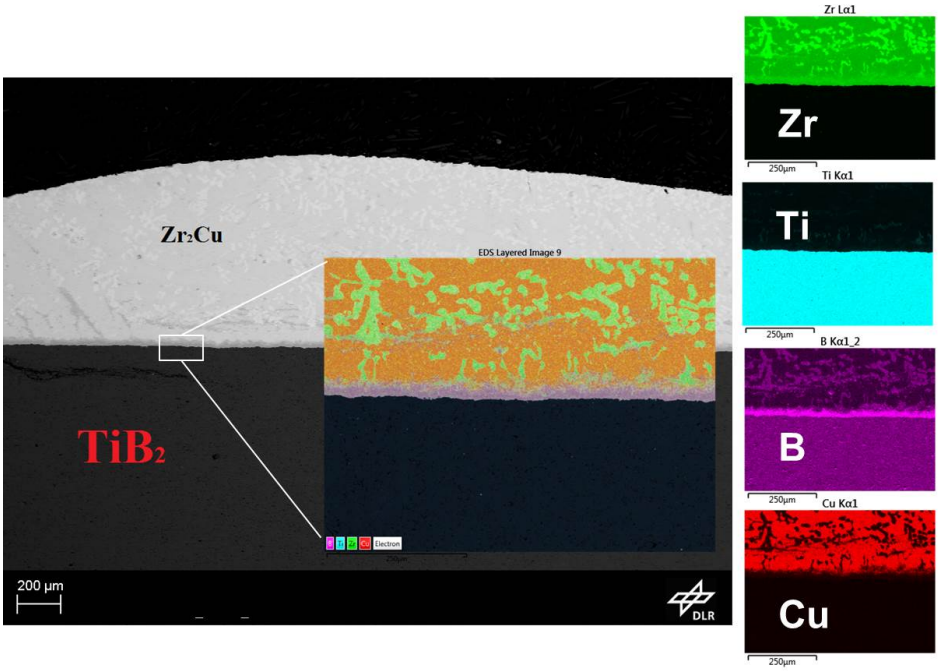

Figure 4.5.: EDX analysis of TiB_2 substrate after wetting with Zr_2Cu

an angle of 13°. The sample displays extremely fast spreading and the contact angle falls below 10° at 1209 °C. At 1230 °C, a reaction occurs, and the melt begins to spill over the sides of the substrate. The EDX analysis of the TiB_2-Zr_2Ag system shows a relatively thin reaction band across a majority of the substrate ($13\mu m$), but varies in some areas to as wide as $43\mu m$. Three distinct phases form in the layer. Using EDX, solid slabs of TiB, along with a few at.% Zr appear to be the most prominent, shown as the green blocks between layers in figure 4.6. A $Zr_2B_5Ti_3$ (or ZrB_2 mixed with TiB_2) phase (light blue) forms between the slabs, while a layer of $Zr_4B_{14}Ti_2$ sits on top. The substrate appears to have decomposed after having been in contact with the melt. B of decomposed TiB_2 seems to form Zr-B phases within the reaction layer. Inside the melt, Ag is found floating above the reaction layer, but not within the reaction layer. Zr_2Cu+1% B forms a droplet at 1022 °C, holding an initial contact angle of 67°. The melt spreads quickly, completely wetting the substrate at 1055 °C. At 1102 °C, it completely wets the TiB_2 substrate. EDX analysis indicates a $36\mu m$ thick reaction band, containing a mixture of ZrB_2 and Zr_2B_7Ti, see figure 4.7. A thin layer of TiB can also be seen close to the substrate at the beginning of the reaction layer. Further

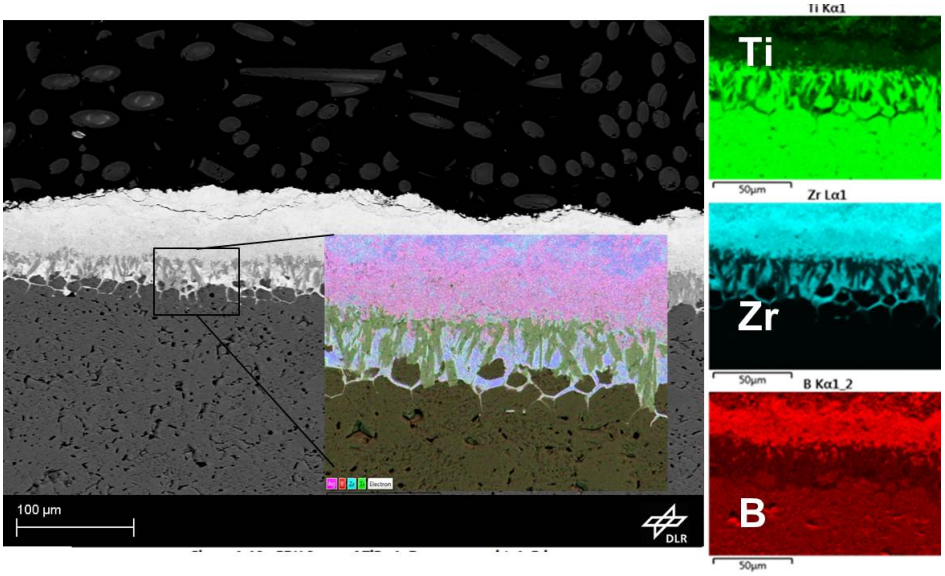

Figure 4.6.: EDX analysis of TiB_2 substrate after wetting with Zr_2Ag

towards the surface of the melt, ZrCu is found along with small areas of $ZrTi_2$. Overall, the degradation of the substrate is minimal in comparison to TiB_2-Zr_2Ag. Zr_2Cu+1% C shows an initial contact angle of 70° at 1025 °C. The melt angle decreases slowly until 1066 °C, after which the angle drops 10° at 1067 °C and completely wets the substrate. Two distinct layers are seen at the interface, showing a combined width of approximately $30\mu m$. According to the EDX results, a thin band ($10\mu m$ thick) of $Zr_3B_{14}Ti_3$ is found at the lower part of the reaction layer, below a $20\mu m$ layer of ZrB_3 and ZrB_2, see figure 4.8. The substrate becomes substantially decomposed by the melt, leaving behind a mixture of TiB and TiB_3 phases among the TiB_2. C phases are difficult to find in the melt, and ZrC appears to be absent. Further into the melt, Zr_2Cu_2Ti appears in small sections. Figure 4.9 shows a summary of melts measured on a TiB_2 substrates. Both Cu and Ag-based alloys drop rapidly in contact angle upon melting, however, Ag melts do have a higher melting temperature. In both cases, an addition of 1 at% of B further decreases the contact angle.

TaC Wetting Behavior

Zr_2Cu forms a full droplet at 1017 °C with an initial contact angle of 63°. This value drops rapidly as the temperature rises through 1020-1050 °C. The sample is subject to the same reactions in the center of the melt as seen in the other Zr_2Cu systems. Beyond 1125 °C, full wetting of the substrate occurs. At 1450 °C, the full substrate is covered by the melt. A thick reaction band is formed with a layer of residual melt above, at a combined thickness of $300\mu m$, see figure 4.10. Phase behavior at the interface is similar to the TaC-Zr_2Ag system, which also forms uniform layers with an increased phase density closer to the surface of the substrate. EDX indicates that the reaction layer ($110\mu m$) is comprised primarily of Zr_3C_6Ta (dark grey) and Ta_3C_6Zr (light grey) phases and contains minimal Zr_2Cu or Cu.

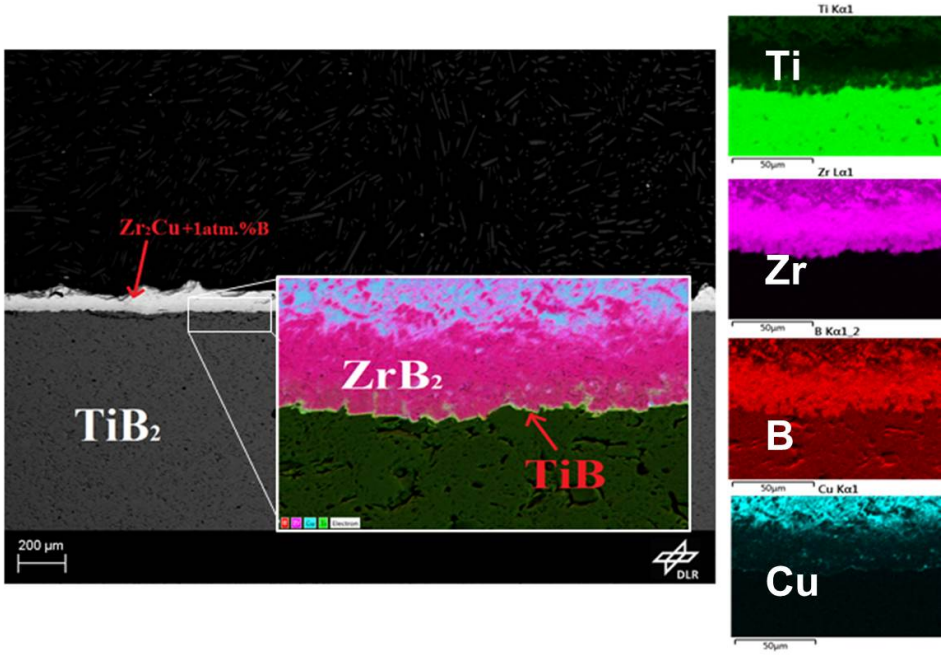

Figure 4.7.: EDX analysis of TiB_2 substrate after wetting with Zr_2Cu-1 at% B

Along the surface of the substrate, thin tendrils of Ta_3C_6Zr can be seen extending into the melt. The residual melt layer has sparser reactions, containing pockets of the same phases dispersed among ZrCu. This phase sparsity increases towards the surface of the melt, which is primarily Zr_2Cu (dark grey), with spots of $Zr_{10}Cu_5Ta$ (light grey). The Zr_2Ag alloy begins to melt at 1198 °C, with an initial contact angle of 19°. At 1205 °C, the melt has wet the surface completely. A thin, tantalum-rich reaction layer of Ta_5C_4 is formed uniformly along the substrate surface with a relatively constant thickness of 2.6μm, see figure 4.11. The EDX analysis indicates that Ta diffuses into the residual melt, leaving a region of tantalum-deficient TaC_2 at the substrate's surface. Tendrils of Ta_3C_6Zr form above the reaction layer, extending like thin needles into the melt. Above this phase, small, non-continuous dot-shaped phases of $Ta_7C_{12}Zr$ (and others with varying stoichiometry) are formed with a decreasing amount of these phases as the distance from the substrate increases. The dark areas close to the boundary are ZrC_2 phases. The EDX analysis of the bottom of the substrate indicate the presence of a small amount of residual Ag. The TaC-Cu system displays the highest wetting angles of all tested samples. Melting occurs at a temperature of 1106 °C with a contact angle of 145° (matching prior results obtained by Samsonov et. al [28], 140°); the sample continues to wet poorly until 1240 °C. Above this temperature, the angle drops rapidly to 110° within 2°C. Another large drop in contact angle, approximately 35°, is observed at 1425 °C. Above 1500 °C, the melt begins to contract and becomes solid. Despite the low contact angle, the AsB analysis of the TaC-Cu system shows no significant chemical reactions at the liquid-solid interface. There is a smooth and distinct boundary between the two original materials. XRD analysis of the system indicates a small amount of Ta_4C_3.

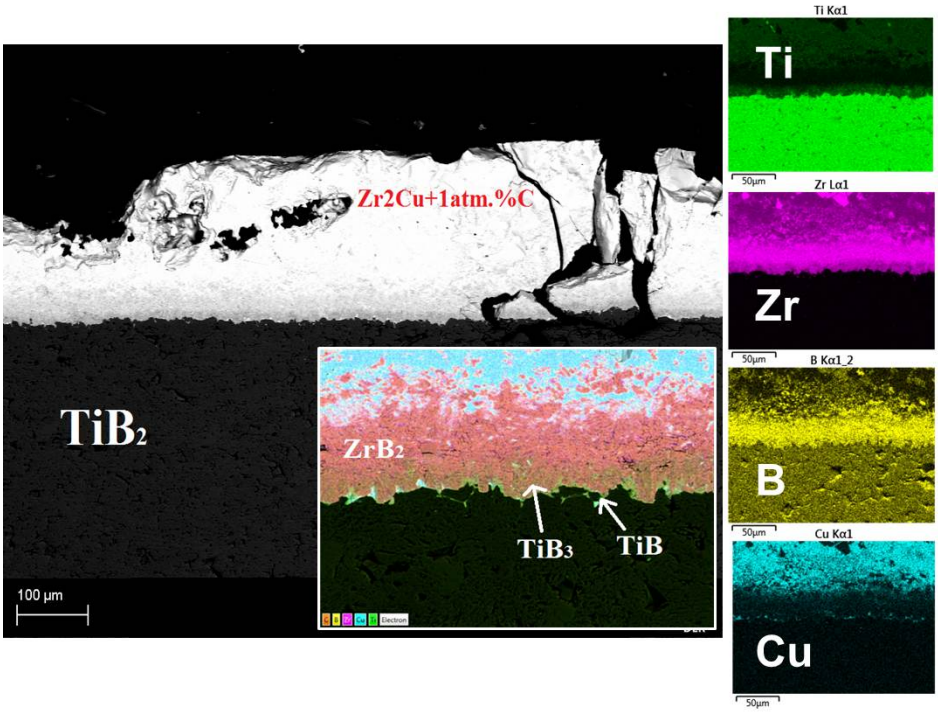

Figure 4.8.: EDX analysis of TiB_2 substrate after wetting with Zr_2Cu-1 at% C

ZrB_2 Wetting Behavior

As part of the capillary system feeding melt into the reaction zone, ZrB_2 is an important phase in terms of keeping the infiltration sustained. Achieving dense and pure ZrB_2 substrates is rather difficult. Usually, sintering aids are used to reduce sintering temperatures or prevent grain growth [40, 56, 58, 183]. Both high porosity and reacting phases resulting from sintering aids prevent a precise measurement of the Zr-alloy contact angle measurements. Either the Zr reacts with the additional phases or the alloy infiltrates the residual porosity. Pure Cu and Ag with a very high initial contact angle and low reactivity are measured on the ZrB_2 substrates. Figure 4.12 shows the results compared to TiB_2 substrates. Both Cu and Ag decrease in contact angle at lower temperatures on ZrB_2 when compared to TiB_2 with Cu, below 1200 °C. In contrast to TiB_2, Cu does drop in contact angle at lower temperatures than Ag on ZrB_2. Various performed infiltration trials confirm the sustained infiltration by ZrB_2 as well as TiB_2. Zr-alloys are measured on ZrB_2 substrates, which is displayed in figure 4.17 and compared with other substrates.

Wetting Behavior of Preform Phases

As described, contact angles of ceramic phases are important due to their ability to sustain infiltration. Phases present during the start of the infiltration or in front of the reaction zone also determine the initialization of the RMI process. Carbon, boron, B_4C, and SiC show different behaviors when in contact with selected melts. Due to their highly reactive

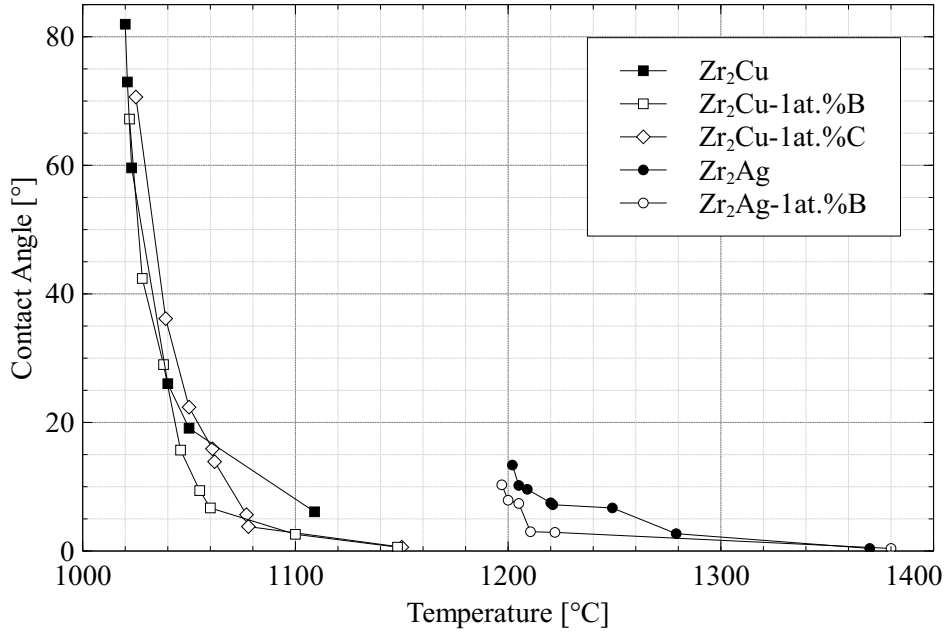

Figure 4.9.: Contact angle of various Zr-melts on TiB_2 substrate

behavior, some of the substrates cannot be measured. On boron substrates, for example, the reaction is so rapid and the diffusion rate of boron inside the Zr melts so high that drops form solid ZrB_2 shortly after melting. Judging by the large spread of the solidified drop, these contact angles do not pose a problem during infiltration. Pure Cu and Ag melts also allow for a comparison of the behavior of various substrates and Zr-alloys. As discussed in this section, carbon content of the substrates has an essential influence on the contact angles. For Cu and Ag, this effect is more severe than for pure Zr-alloys, as seen in figure 4.14, while pure Zr cannot be measured due to the temperature limitation of the available facilities. Contact angles of Zr on carbon are too high to allow infiltration of carbon preforms by capillary forces, as tested with C/C preforms. Using polycarbosilane as a precursor, SiC is formed during pyrolysis and becomes an important factor in terms of wetting behavior. Graph 4.13 compares the contact angle of various melt combinations on a sintered SiC substrate. While Cu based alloys immediately drop in contact angle on TiB_2 after melting, they remain constant for over a 300 K range on SiC before dropping to low contact angles (<5 °). Above 1350 °C, the capillary forces are high enough to infiltrate samples. Using phenolic resin as a precursor, the major phase formed during pyrolysis is carbon. As previously mentioned, carbon has a significant influence on the wetting behavior. While Cu and Ag keep a contact angle above 125 °, Zr_2Cu and Zr_2Cu-1at%B gradually decrease in contact angle upon melting, as seen in figure 4.14. Carbon substrates used are glassy carbon with a very low open porosity. Decreasing contact angles are likely caused by the reaction of Zr and C, forming a thin ZrC layer. The ZrC reaction zone slowly increases, resulting in a continuous decrease in contact angle. Additions of 1 at% B alter the reaction behavior of Zr and C, decreasing the contact angle more rapidly after an initial melting phase. During the initial melting, the higher

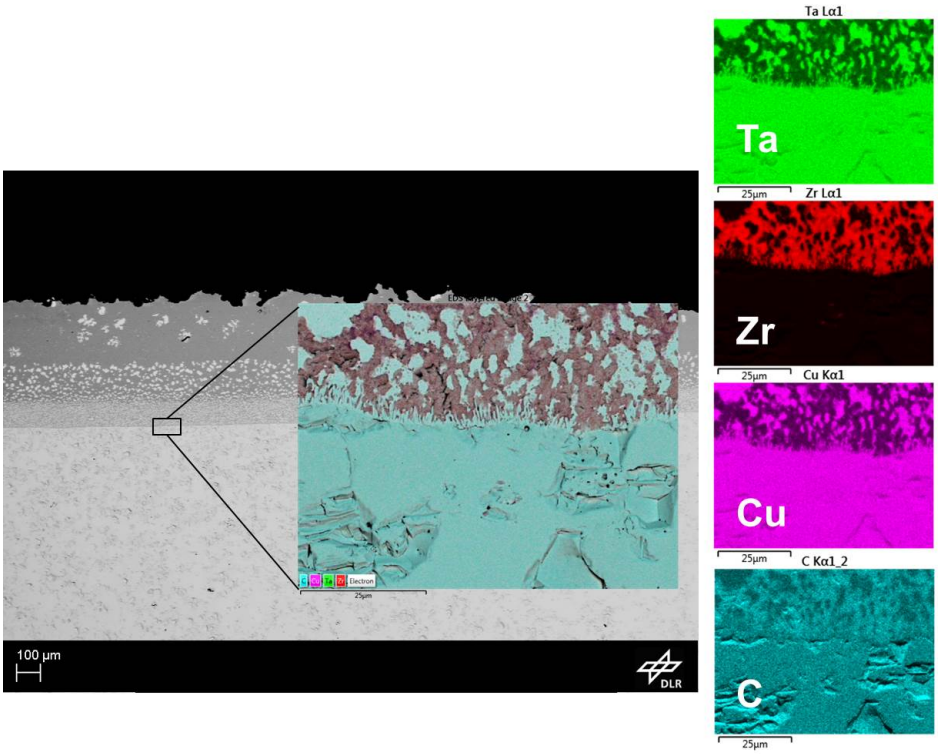

Figure 4.10.: EDX analysis of TaC substrate after wetting with Zr_2Cu

viscosity of Zr_2Cu-1at%B compared to Zr_2Cu, see section 4.2.4, results in a higher contact angle upon melting.

When treated with B_2O_3, carbon from the phenolic resin forms B_4C. As described in section 4.2.1, this treatment has various advantages regarding pore size distribution and powder treatment. Another advantage can be seen in figure 4.15, in which Zr-Cu alloys drop in contact angle even below 1100 °C. As with C and SiC substrates, pure Cu maintains a high contact angle of around 125 ° throughout the measured temperature range.

The B particles used in each of the slurries also influence infiltration. Figure 4.16 shows the contact angle of pure Cu and Ag on a B substrate compared with Cu measurements on a B_4C substrate. Contact angle behavior of pure Cu and Ag are similar to the behavior of ZrB_2 and TiB_2, showing a rapid drop in contact angle upon reaching a certain temperature. Cu has a large drop in contact angle above 1250 °C and Ag at above 1350 °C. Zr-alloys could not be measured on B substrates due to high diffusion rates of B. The ZrB_2 reaction happens so rapidly that a solid irregular shape forms shortly upon melting.

Figure 4.17 shows the comparison of Zr_2Cu on various substrates. With the exception of SiC and C, every substrate investigated drops in contact angle before 1200 °C. SiC exhibits a delayed drop at around 1350 °C, and C only gradually decreases up to 1500 °C, showing the highest contact angles.

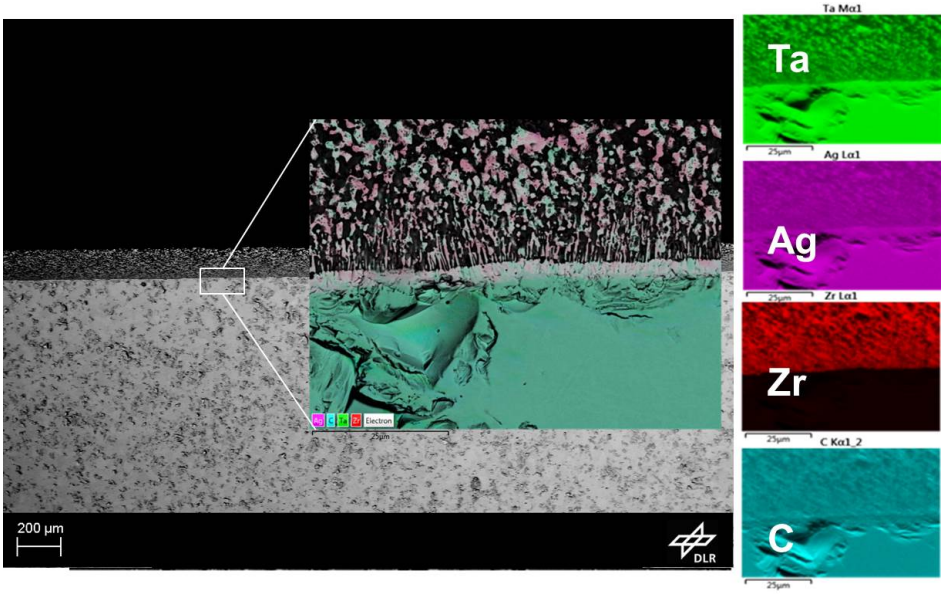

Figure 4.11.: EDX analysis of TaC substrate after wetting with Zr_2Ag

4.1.4. Exothermic Influence

Reactions occurring during RMI are of exothermic nature, both for Si-based and Zr-based systems. This exothermic energy influences several aspects of the RMI process. The self-induced temperature increase can be calculated from the released energy. This temperature peak influences the following parameters of the RMI:

- Contact angle,
- Viscosity,
- Reaction behavior of the melt, and
- Phase formation

Reacting phases present during RMI, such as C and B, induce a heat flux, which is partially compensated due to the specific heat capacity of non-reacting phases, such as ZrB_2 fillers, TiB_2 fiber coating, and residual melt phases. Figure 4.18 shows a schematic of heat fluxes appearing during RMI. The discharge of energy due to the heat capacity of these passive phases is crucial in order to reduce fiber degradation.

In order to determine the influence of ZrB_2 passive powders on the reaction of Zr alloys and B, HT-TG/DTA measurements are performed using Zr_2Cu as the melt alloy. Figure 4.19 shows the measurements of different powder compositions in combination with Zr_2Cu granules. The highest exothermic reaction is measured for mass ratios of Zr_2Cu:B:ZrB_2 5.689:1:1 due to the additional reaction of the Zr alloy with the ZrB_2 powder surface. Keeping the overall powder-to-alloy-ratio constant reduces and postpones the exothermic reaction, as seen from ratios Zr_2Cu:B 5.689:1 and Zr_2Cu:B:ZrB_2 5.689:0.5:0.5. In addition, the mass loss of the measurements, containing the same amount of B powder, is similar due to evaporation

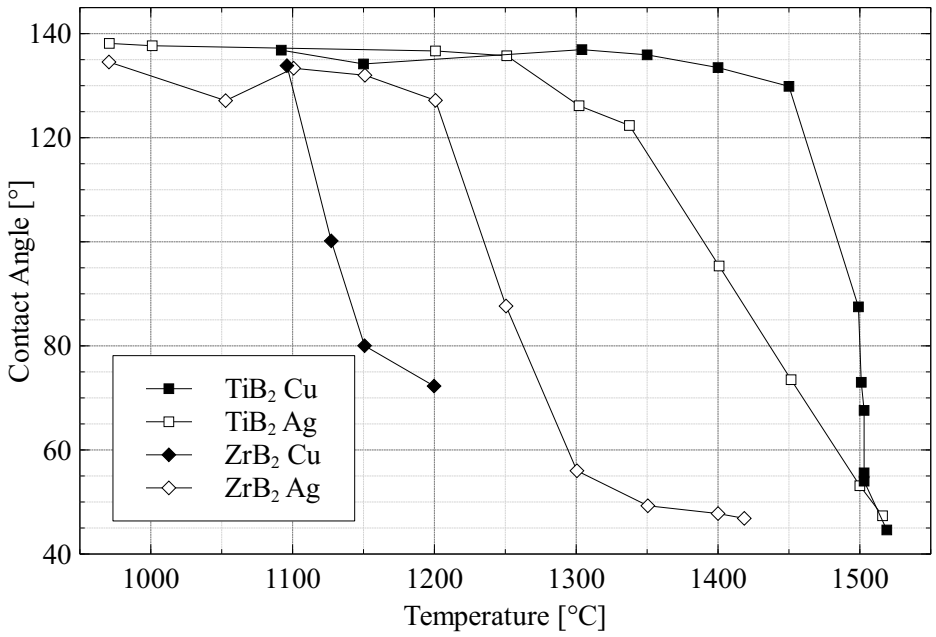

Figure 4.12.: Contact angle of ZrB_2 substrate and different melts

of boric acid forming on the powder surface. The samples containing less B powder show a slightly decreased mass loss.

4.2. Material Selection

This chapter specifies which raw materials are chosen for the development of UHTCMCs, fiber types, fiber coatings, precursors, and fillers. In order to develop a UHTCMC via RMI, there are various manufacturing boundary conditions which have to be taken into account for each component.

4.2.1. Boron Source and Precursors

In general, there are three different methods to create a boron preform: deposition with gas media, liquid precursors, and solid powders. In order to integrate the fibers into the UHTC matrix, it is necessary to infiltrate the fiber rovings. For boron, this limits the possibility of the solid and liquid routes. Melting pure B in order to infiltrate the fibers would require high temperatures and result in a chemical reaction. Polymers able to form boron links are not yet commercially available, and most doped polymers have a low boron content. Most liquid B compounds are either sensitive to oxygen or have the potential to generate high exothermic reactions, which is why they have been used as rocket fuels [184]. The reaction of B_2H_6 to B_2O_3 is one of the most exothermic reactions known. Therefore, it was investigated as a propellant for military applications. However, the substances involved were found to be too difficult to handle due to their instability, toxicity, and adhesive nature. Most B compounds are very difficult to handle, especially when fabricating large quantities. One possible solution

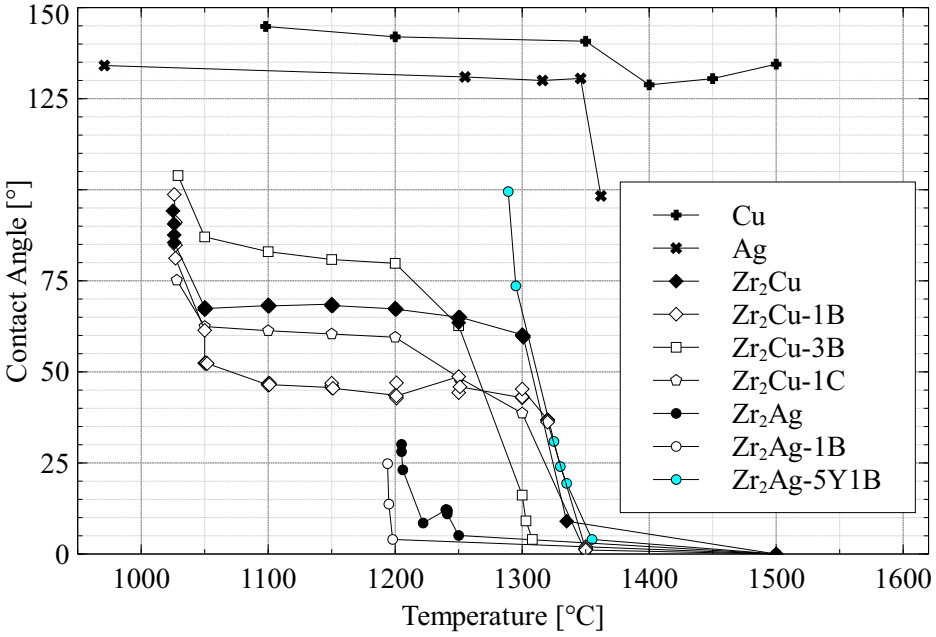

Figure 4.13.: Contact angle of various Zr-melts on SiC substrate

is to use a B slurry. This requires dispensing B powder within a liquid infiltration media. The amount of B able to be dispersed depends on the viscosity of the liquid media. To ensure infiltration of the fibers, the viscosity of the slurry and the stability of the dispersed powders must be investigated. It is preferable to remove the liquid media during curing, leaving a minimum of additional substances, but enough to secure the boron powder.

Synthesis of Boron

Crystalline boron can be synthesized by thermal decomposition of BCl_3, BBr_3, or BI_3 on Ta or W surfaces. The structure can be controlled by the surface temperature. Boron is known to form four allotrope crystal modifications:

- Red α rhombohedral boron $\rho = 2.46 g/cm^3$,
- Dark grey β rhombohedral boron $\rho = 2.35 g/cm^3$,
- Black α tetragonal boron $\rho = 2.31 g/cm^3$, and
- Red β tetragonal boron $\rho = 2.36 g/cm^3$.

Amorphous boron is synthesized by the reduction of B_2O_3 with Mg, having lower purity and a density of $1.73 g/cm^3$.

$$B_2O_3 + Mg \longrightarrow 2B + MgO + 533kJ.$$

Amorphous boron transforms into the stable form of β rhombohedral boron by releasing 3.7 kJ at ambient pressure.

$$Amorphousboron \longrightarrow \beta - rhombohedricboron + 3,7kJ.$$

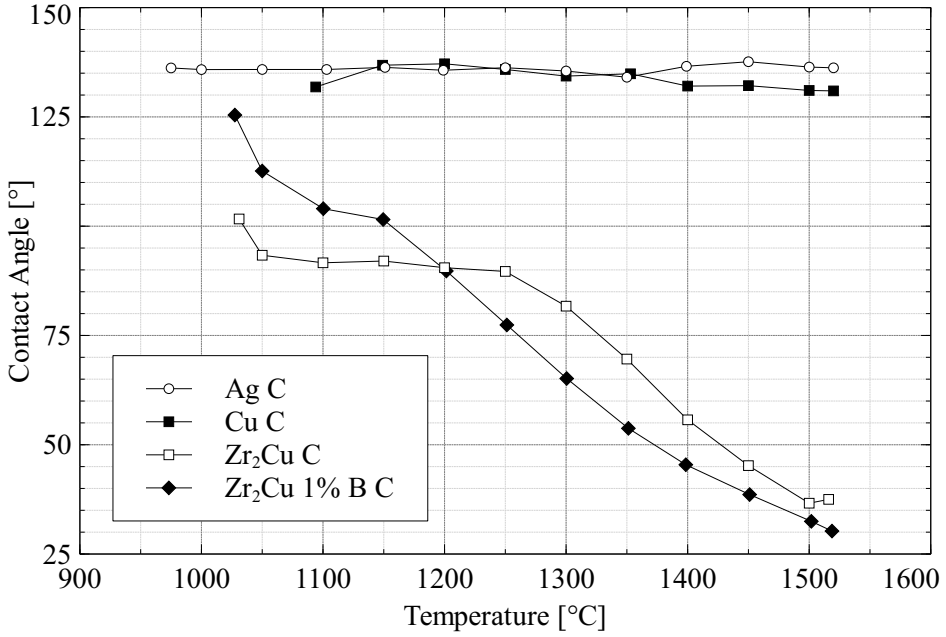

Figure 4.14.: Contact angle of carbon substrate and various melts

Boron places between metals (Be) and non-metals (C) within the periodic table affecting its physical properties. The melting temperature of boron is 2250 °C; its electric conductivity is low at room temperature, but increases by a factor of 100 at 600 °C. Its hardness is almost as high as boron carbide [185].

Boron Precursors

The following B compounds could be used as a B source for UHTCMC manufacturing without using a B slurry. Most of the compounds in liquid or gaseous state at room temperature are toxic and very reactive. In order to evaluate their possibilities and restraints, the most interesting compounds will be discussed.

The most favorable precursors cross-link B chains and, similar to C in the LSI process, build a C_f/B preform after pyrolysis. Such precursors are subject to research (Institute of Inorganic Chemistry, Würzburg, Germany, Prof. Dr. Braunschweig), but not nearly in quantities large enough to manufacture a composite. The two classes of precursors investigated are C-based precursors, such as phenolic resin or thermo-softening plastic, and Si-based precursors, such as polycarbosilanes or polysiloxanes. The three classes of Si-polymers containing boron, polyborosiloxanes, polyborosilanes, and polyborosilazanes as shown in fig.4.20 are very sensitive to air, making impregnation of fiber preforms difficult. Nitrogen bonds of B and Si possess a versatile chemistry due to their reactive nature. In addition, their B content is not high enough to dispense the B powder. The only liquids containing sufficient B are boranes, which are very difficult to handle due to their high hydrogen content and sensitivity to air.

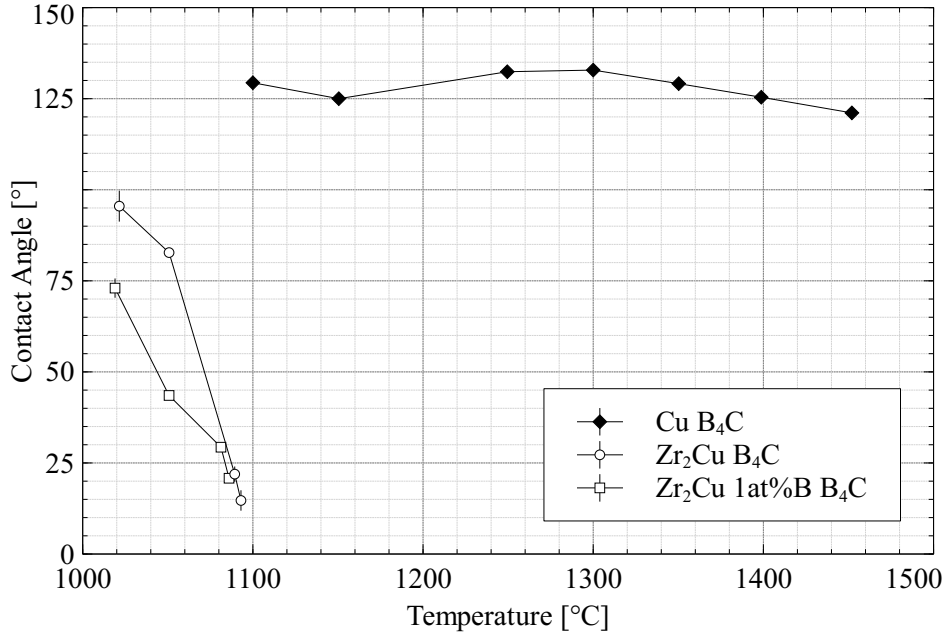

Figure 4.15.: Contact angle of B_4C substrate and various melts

Hydrides The chemistry of boron hydrides had not been investigated until the 20th century. Alfred Stock started these investigations according to volatile hydrides groups. In order to prepare, purify, and characterize these hydrides, the research team used vacuum line synthesis techniques to handle the toxic and air-sensitive hydrides [186]. The measured molecule mass of BH_3 matched the dimeric molecule $(BH_3)_2$. Higher boron hydrides follow this manner by combining identical or different boron hydrides, which would not be stable on their own. Diborone is a colorless, toxic gas (threshold limit value (TLV) 0.1 ppm) which is sensitive to hydrolysis and ignites in air. Every polyborane is toxic; tetra borane is a colorless gas, penta to nona boranes are colorless fluids, and from deca borane onward are colorless to yellow solids. Tetra and penta boranes, with the exception of B_4H_{10}, self-ignite in air. Higher molecular boranes do not react with oxygen in ambient environments. The sensitivity to hydrolysis behaves similarly to their oxygen sensitivity. Penta borane B_5H_9 (TLV 0.005 ppm) and deca borane $B_{10}H_{14}$ are the most stable boranes [185]. However, their TLV levels make it impossible to use them for UHTCMC manufacturing using DLR facilities.

Boron Halogens All boron halogens are toxic and form boron trihalides, dibortetra halides, and bormono halides. BF_3, B_2F_4, and BCl_3 are colorless gases at room temperature. BCl_3, B_2Cl_4, and B_2Br_4 are colorless liquids at room temperature, and B_2Br_4 decomposes at room temperature. BI_3, B_2I_4, $(BCl)_4$, $(BBr)_4$, and $(BI)_4$ are colorless or yellow-red crystals at room temperature. In addition to their toxicity, they form boron acid and correlating hydric acid with atmospheric humidity at room temperature [185, 187]. Due to safety regulations, these types of species are not allowed within high temperature furnaces, and therefore, cannot be used for manufacturing.

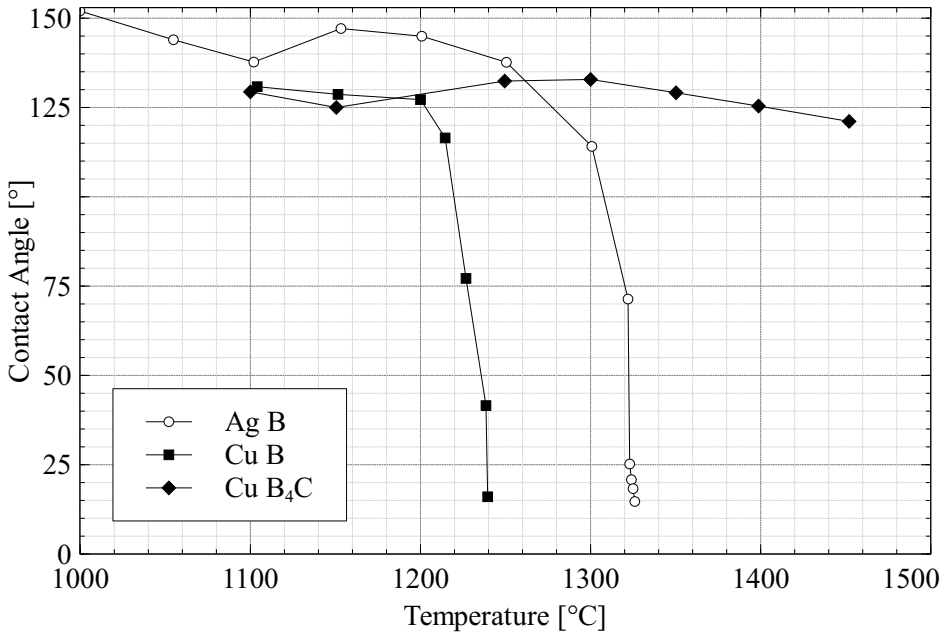

Figure 4.16.: Contact angle of B and B_4C substrate and various melts

Borazine Carbon atoms share the same number of electrons as a boron and nitrogen atom. Therefore, C-C and B-N groups are isoelectric to one another. The molecules ethane, ethene, ethine, or benzol, and accordingly, the B-N molecules correspond to ammine borane, amino borane, imino borane, and borazine, with their covalent bond distance being similar (approximately 0.04 Ålarger). Borazine is a colorless liquid of low viscosity. At room temperature, borazine will attach 3 mole of H-X, such as H_2O, Methanol, and HCl. Relating to their structure and physical properties, the inorganic B-N groups are very similar to their isoelectric C-C counterparts. However, they are much more chemically reactive [185]. Due to their nitrogen content and the formation of BN, borazines are not suited for melt infiltration. The contact angle of BN and Zr alloys is too high to allow for an infiltration of the capillary systems.

Boron CVI

In addition to slurry infiltration, a boron-based CVI process has been investigated as a boron matrix source. Das et al. [188] investigated boron chemical vapor deposition (CVD) on beryllium surfaces. They found the decomposition of B_2H_6 to be superior to the reduction of BCl_3 by H_2. Berjonneau et al. [189] performed a study on $HBCl_2$ as a precursor of the B element used in combination with C precursors to be used for B_4C coatings. According to their generated kinetic laws and validation in a large range of experimental conditions, they assumed a CVI of B_4C to be possible. Vandenbulcke et al. [190, 191] varied CVD process conditions, inlet gas phase composition, mass flow rate of reactants, and temperature

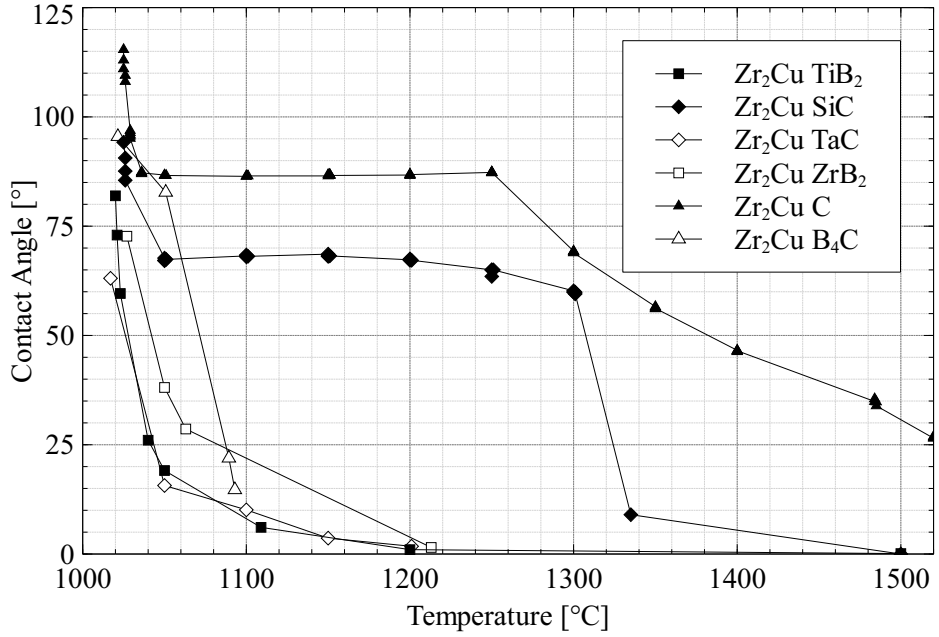

Figure 4.17.: Contact angles of various substrates

to manufacture the full range of B structures. The trials for boron CVI were performed by Archer Technicoat LtD (ATL), using BCl_3 and H_2 according to the following equation:

$$BCl_3 + H_2 \longrightarrow HBCl_2 + HCl.$$

In order to reduce volume, which must be filled by CVI, the fabrics are impregnated with a ZrB_2 slurry before stacking and processing. Sample plates, one with TiB_2 fiber coating and one with plain carbon fabric, are prepared. It is essential that the CVI process bond the fabrics and powders, building an active matrix for RMI. B depositions as coatings have previously been performed by ATL, but these trials aimed for an infiltration. Conditions

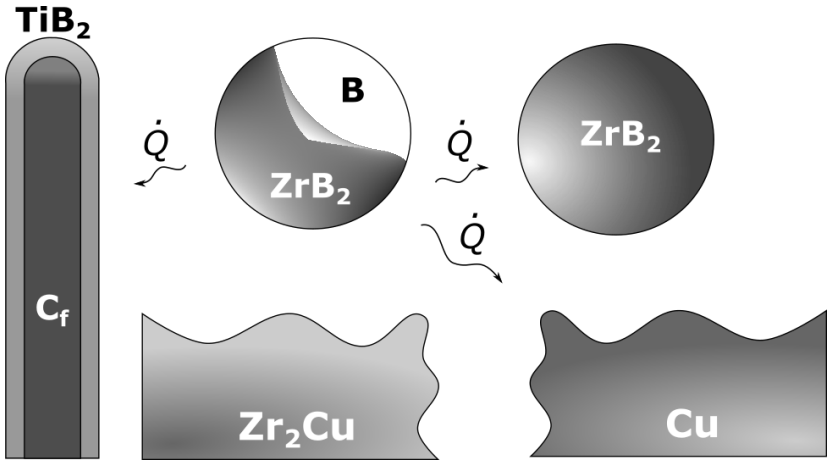

Figure 4.18.: Schematic of heat flux during RMI

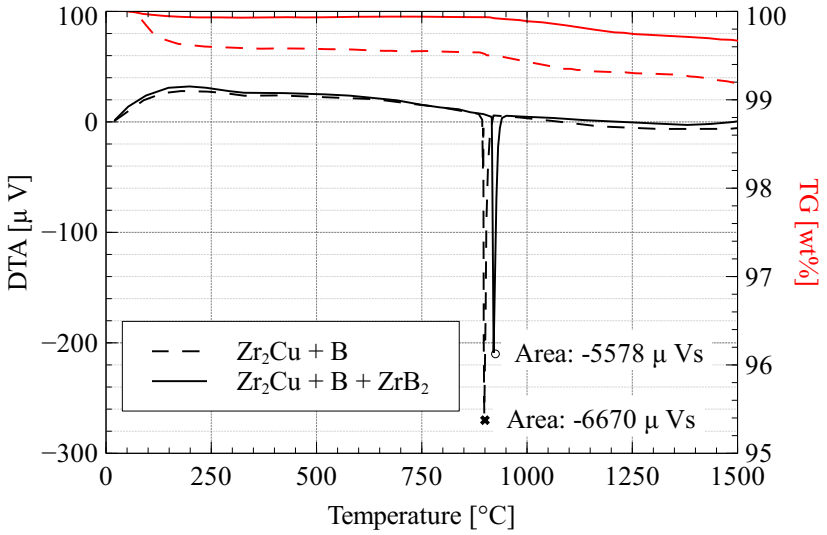

Figure 4.19.: HT-DTA measurement of Zr_2Cu and B powder with and without ZrB_2 addition

previously used for boron were changed in an attempt to favor infiltration by slowing the deposition rate and reducing the reaction pressure level. The fabrics were clamped between graphite jigs during CVI. These jigs were placed on a support structure in the deposition chamber. Masses of the jigs and the fabric were recorded before and after the process, showing only a mass change of the graphite jigs. From these mass change data, the deposition of boron onto the jigs was much more favored than the infiltration into the fabrics. Although there was a boron deposition, it appears that most of this was on the jigs and little to no infiltration has happened in the fabric. Process concentrations and temperatures have already been reduced significantly for this process, leaving no margin in the test chamber for further reduction. The process seems too surface-sensitive to be suitable for CVI. As recommended by ATL, detailed research and extensive investigations are necessary to achieve a sufficient infiltration of the fiber preforms.

Boron Slurry

A B slurry contains dispersed B powder within a liquid media. Generally, the particles are stabilized within the media. There are four important properties for the liquid media of the B slurry:

- Low viscosity to enhance fabric impregnation,
- Allowing the powder to be stabilized,
- Adapted ceramic yield to generate the right amount of porosity, and
- Low contact angle with Zr melts after pyrolysis.

Precursors forming a high carbon content after pyrolysis limit RMI due to the contact angle of Zr and C. In terms of the contact angle, polysiloxanes and polycarbosilanes allow for a better infiltration depth. When using Si-based precursors they should have a low viscosity and low ceramic yield. Low viscosity is required to improve slurry infiltration of the fabrics

and low ceramic yield is required to keep additional phases as small as possible and to provide the necessary porosity. The UHTCMC investigations are performed with a polycarbosilane precursor from Starfire Systems, SMP-877, hereafter referred to as SMP or polycarbosilane, and a phenolic resin from HEXION, BAKELITE PF 8978, hereafter referred to as phenolic. SMP has a viscosity of 40-120 cPs at 25°C and a ceramic yield of 58-62 wt% (1000°C pyrolysis). The phenolic resin has a viscosity of 270-330 mPas at 20°C, and the ceramic yield can be varied with pyrolysis temperature. In addition to single-step processes, two-step processes are investigated. Two steps allow for the separation of the fabric from impregnation and bonding of the B powder. For these processes, water and ethanol-based B slurries are used to impregnate the fiber preforms prior to resin infiltration.

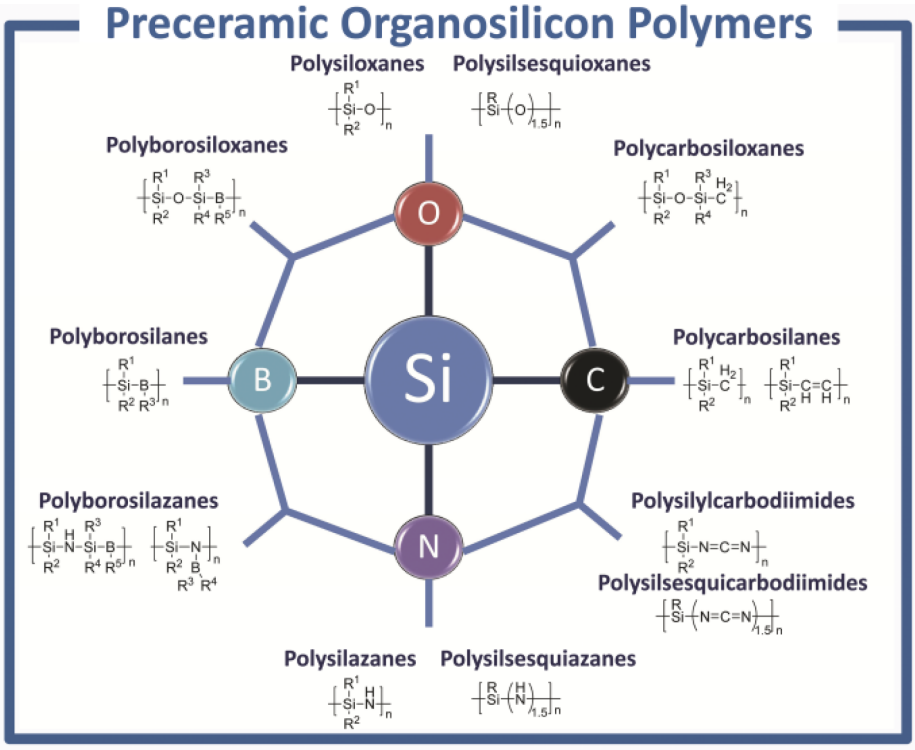

Figure 4.20.: Main classes of Si-polymer as precursors for ceramics [192]

Boron Powder and Powder Treatment In general, there are two different commercial boron powders available: amorphous powder with a density of ~1.8g/cm^3 and crystalline powder with a density of ~2.3-2.5g/cm^3. The crystalline powder has the disadvantage of high cost and, as explained in section 4.1 by figure 4.1, using it would require an even higher porosity of the preform.

Influence of volume expansion While the volume expansion described in chapter 4.1.2 is caused by formation of undesired residual melt phases, this section deals with the volume expansion caused by the reaction forming the UHTC matrix. Due to the difficulties con-

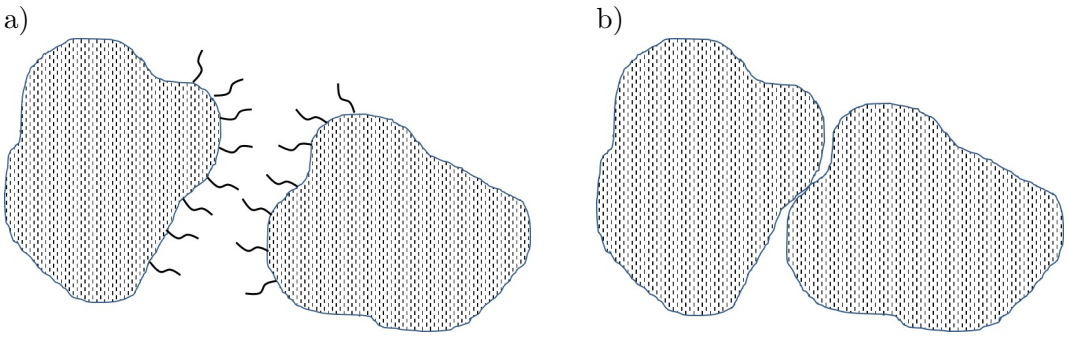

Figure 4.21.: Schematic of boron powder formation

cerning boron sources as described in the state of the art, the manufacturing of UHTCMCs via RMI focuses on boron particles dispersed within a liquid. While the slurry infiltration is discussed in a separate chapter, this chapter will concentrate on the influence of using boron powders as a boron source for RMI. The reaction during RMI has a volume expansion of 148% due to the formation of ZrB_2, see equation 4.2. When using a combination of B powder and SiC from polycarbosilane, the volume expansion drops to 110% due to the formation of ZrB_2 and SiC, see equation 4.4. By forming ZrC from SiC, the volume reduction helps decrease the overall expansion. The ratio of ZrC and ZrB_2 could be adapted to suppress the combined volume change to zero. This would increase the less oxidation-resistant ZrC phase, but would only work if the boron powder were stabilized within the polycarbosilane. Figure 4.21 shows the difference in the particle formation if the powder is a) stabilized or b) not stabilized. Stabilizing B requires sensitive additions ([193, 194]) and is difficult to sustain during greenbody manufacturing. The stabilization mechanisms must overcome the mechanical pressure that occurs during curing of the polymer. Figure 4.22 shows the various effects during the formation of ZrB_2. Part a) shows the two B particles separated either by stabilization or coating before RMI, while part c) shows the two particles without separation. Both are marked with a reference thickness to describe the volume expansion. If the configuration a) is infiltrated with Zr, the space caused by stabilization or the fugitive coating can be filled with ZrB_2 volume. If configuration c) is infiltrated, the contact areas of the particles force a volume expansion of the whole composite due to ZrB_2 formation. Fugitive coatings or additives, chemical reactions, and resin shrinkage are a few methods used to implement inter-particle space before RMI. If a coating is used to ensure inter-particle space, it must be released during pyrolysis or melt infiltration. The simplest method is oxidizing the B powder to form a B_2O_3 layer. This B_2O_3 layer becomes volatile at pyrolysis temperatures and must form B_4C with the phenolic resin when pyrolysed. In ambient air, B oxidizes and forms B_2O_3 at elevated temperatures. Rizzo et al. [195] describe the oxidation at temperatures between 600 °C and 1000 °C, 22-26 % of the amorphous B has oxidized after 24 hours, however, at temperatures above 1000 °C, a suboxide known as B_7O is produced, and vaporization of B_2O_3 occurs, including the formation of BN at temperatures between 1110 °C and 1300 °C. The oxidation of B_4C was investigated by Ashish et al. [196]. They found B_2O_3 as an initial

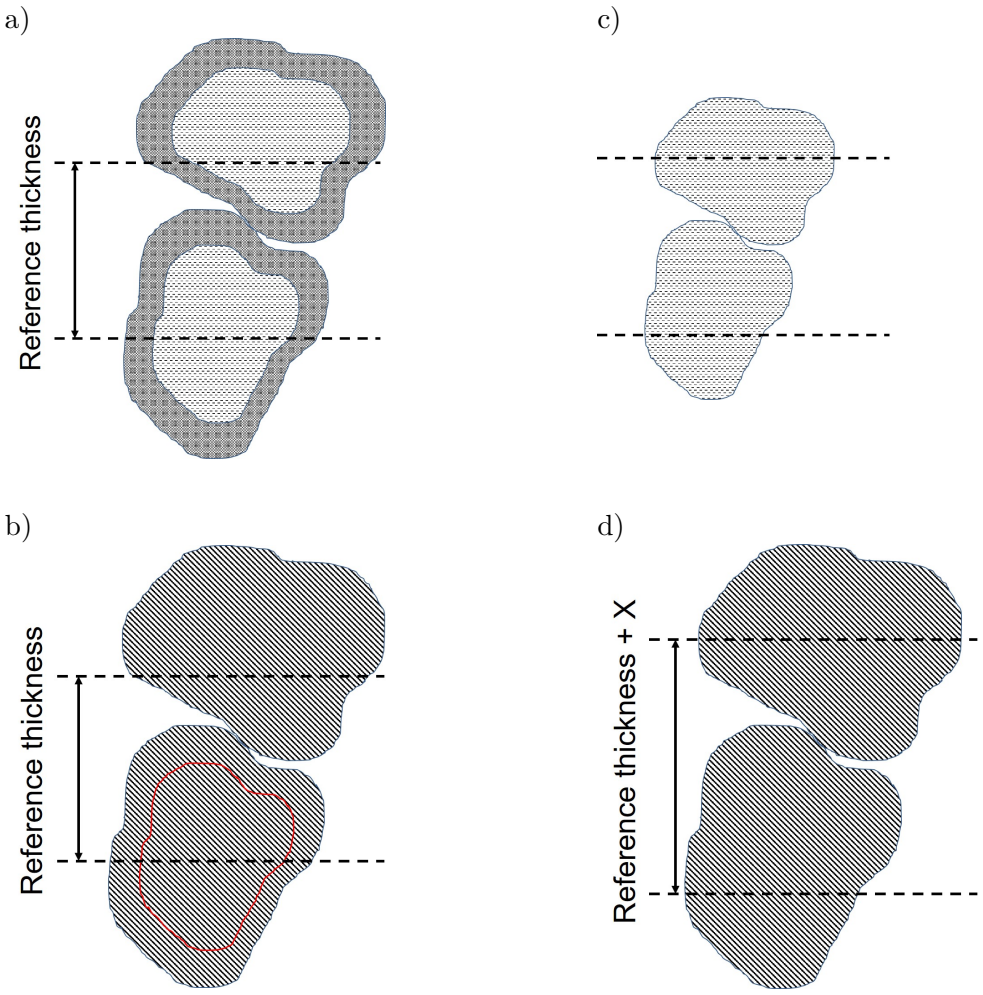

Figure 4.22.: Schematic of B powder expansion, with and without controlled distance

product of the oxidation with a glassy layer of B_2O_3 forming on the outside as oxidation progresses. This glassy layer has a slow-growing oxidation rate, which is governed by diffusion of oxygen through B_2O_3. It remains stable up to 1273 K and blocks CO_2, being an oxidation product. An additional study conducted by Li et al. [197] further investigated this glassy layer and defined the following three different oxidation mechanisms:

- 1. Diffusion of oxygen through the solid matrix reaching the interface surface of non-reacted B_4C particles,
- 2. Chemical reaction between B_4C grains and oxygen at the interface of B_4C/B_2O_3, and
- 3. Diffusion of CO_2 or CO through the B_2O_3 layer to the external surface of the oxidation layer.

The equation describing the oxidation reaction of B_4C is

$$B_4C + 4O_2 \longrightarrow 2B_2O_3 + CO_2. \tag{4.9}$$

The experiments are performed using B_4C powders with various particle sizes. These are spread homogeneously with a 2 mm thickness into a platinum crucible, measuring 20 mm x 20 mm in size. The degree and depth of oxidation are significantly affected by the particle size of the B_4C powder, showing an increasing oxidation depth with decreasing size displayed, see figure 4.23. Therefore, the oxidation reaction is a surface reaction, and the rate of oxidation depends on the surface area of B_4C [197]. Li et al. also compared isothermal and non-isothermal oxidation of boron carbide powder. The highest oxidation rates occur between 800 K and 1100 K at non-isothermal state. Low mass gains are recorded up to 800 K. Slow heating rates result in faster oxidation rates. Higher temperatures favor oxidation for isothermal oxidations with higher oxidation rates at the beginning. Due to the fast growing oxidation layer at high temperatures, the oxidation rates stagnate compared to lower temperatures. Comparing isothermal and non-isothermal oxidation, the degree of oxidation of a non-isothermal process is approximately 15% larger than that of isothermal processes. In

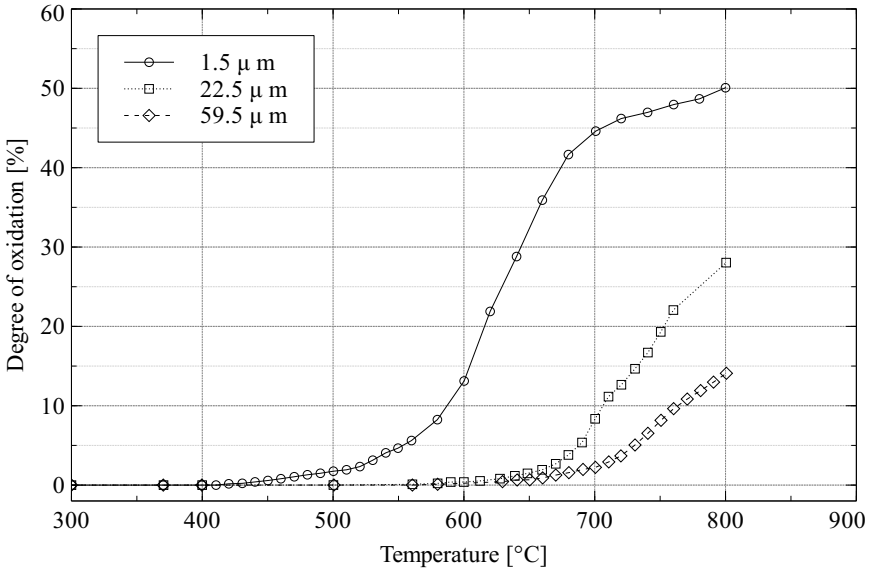

Figure 4.23.: Degree of oxidation for various B_4C particle sizes [197]

order to oxidize the outer layer of each B particle, the powder can be treated with hydrogen peroxide (H_2O_2). The following equation describes the formation of B_2O_3 using H_2O_2:

$$2B + 3H_2O_2 \longrightarrow B(OH)_3 + 3H_2O \tag{4.10}$$

$$B(OH)_3 \longrightarrow HBO_2 + H_2O \tag{4.11}$$

$$4HBO_2 \longrightarrow H_2B_4O_7 + H_2O \tag{4.12}$$

$$H_2B_4O_7 \longrightarrow 2B_2O_3 + H_2O \tag{4.13}$$

The formation is an exothermic reaction, initialized by the high surface energy of the micron-sized boron particles. Once the powder has been treated and each particle has been

coated with B_2O_3, the reaction cannot be initialized again. XRD investigations in figure 4.24 show the formation of B_2O_3 and $B(OH)_3$ peaks after treatment. The top graph shows an XRD of B powder as received and the bottom graph after H_2O_2 treatment. Exposure of B powder in water does not change XRD results, compared to original samples. After H_2O_2 treatment, a considerable amount of $B(OH)_3$ forms, which is also described in literature [198, 199]. The dehydration of boron acid can be separated into two steps: the metaboric acid (HBO_2) at temperatures above 170°C and the tetraboric acid at temperatures above 300°C. As described by Balci et al. [199], the maximum conversion and conversion rate depend on heating temperature and time. Solubility of pure B_2O_3 in furfuryl alcohol, the solvent in this phenolic resin, is lower than the solubility of boric acid. In order to preserve as much B_2O_3 on the surface of the particles as possible, the powders should be heat treated up to 300°C in order to dehydrate the boron acid. Details regarding oxidation of boron powder can be found in section 4.3. This B_2O_3 layer influences the micro structure of the pyrolysed matrix and pore size distribution of the capillary system.

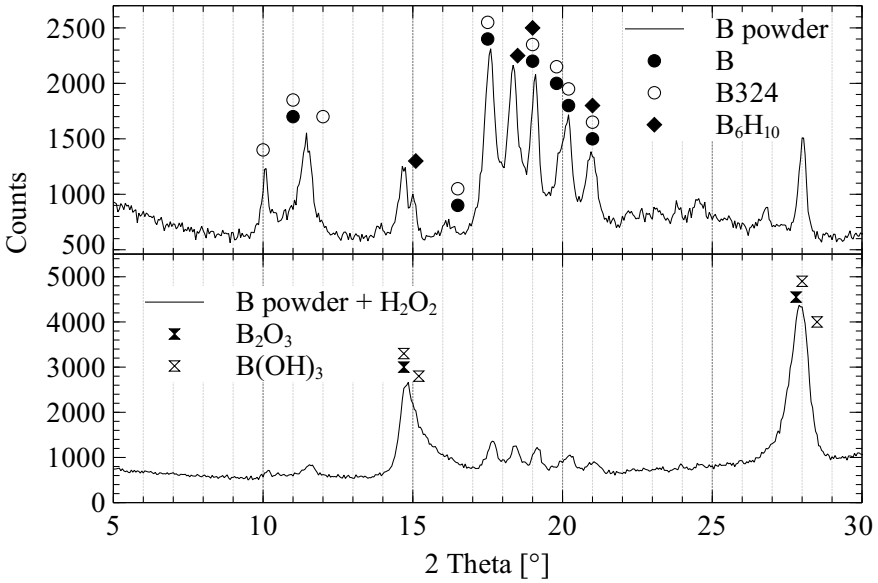

Figure 4.24.: XRD of boron powder and H_2O_2 treated boron powder

In order to determine the influence of peroxide amount on the oxidation layer thickness on B particles, various H_2O_2-B mixtures were investigated. Mass gains of each mixture were determined at 80°C, 170°C, and 300°C to see the amount of acid and oxide forming. After an initial mass loss upon heating at 80°C due to water evaporation, the samples were subject to mass gain, see figure 4.25. Mass change is caused by the formation of boron acid, which is dehydrated according to the following two heating steps. As there is now increased mass gain at 300°C between 70 ml and 140 ml of H_2O_2, 70 ml of H_2O_2 is sufficient to form a dense acid layer. Lower mass gains of the 35 ml H_2O_2 sample at 300°C, are a result of an insufficient amount of H_2O_2 to form a dense layer of boric acid, leaving non-reacted B on the surface. The oxidation layer thickness after H_2O_2 treatment can be calculated from the

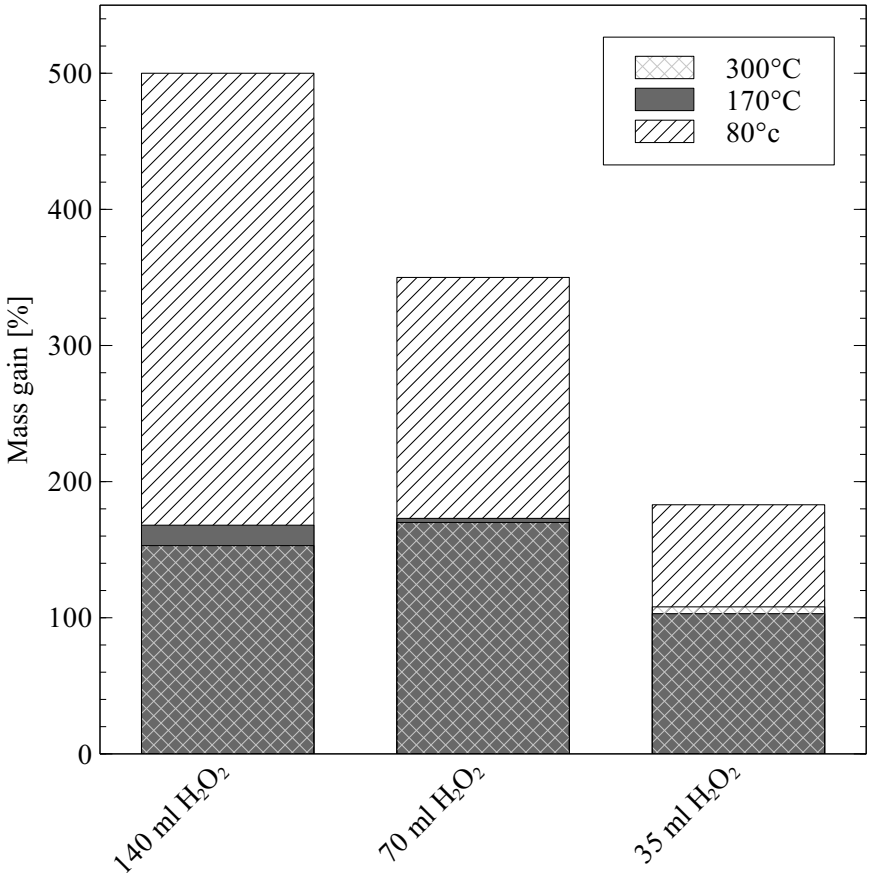

Figure 4.25.: Mass gain of H_2O_2 treated B powder

relative weight change and average particle size. B is considered to be spherically in shape and the weight change is assumed either by boron acid or boron oxide formation, with the respective density used. The following equation gives an approximation of the oxidation layer thickness:

$$ot = (\frac{3\delta m_B}{4\pi\rho_{B2O3}} - (\frac{d}{2})^{\frac{1}{3}})^{\frac{1}{3}} - \frac{d}{2}. \tag{4.14}$$

Where ot is the oxidation thickness, δm is the oxidation mass gain, m_{Bp} is the mass of a single boron particle calculated from the volume of a particle, and $\rho_B 2O3$ is the density of boron oxide. This method for the calculation of the oxidation layer thickness is only an approximation and does not take effects such volume change of the particle into account.

Investigations of Resins and Additives ZrB_2 content is a main focus in the manufacturing of UHTCMCs. As a result, B content within the composite is essential. As discussed in previous sections, using a B slurry is the most effective method in terms of handling, cost, safety regulations, and volume expansion. In order to manufacture UHTCMCs, the slurry precursor must fulfill the following requirements:

- Low ceramic yield,
- Sufficient wetting behavior of the melt after pyrolysis,

- Shape stability during pyrolysis, and
- Low viscosity.

Epoxy (Epikote LR 385, Lange & Ritter) and polyester (Enydyne and Norsodyne, Lange & Ritter) resins have a low carbon yield [200], making them interesting in terms of low contact angles with the molten alloys. However, they do form a liquid phase when decomposing during pyrolysis, which can be seen in the negative melting peak of the DSC measurement 4.26. Therefore, they are not investigated in detail for preform manufacturing.

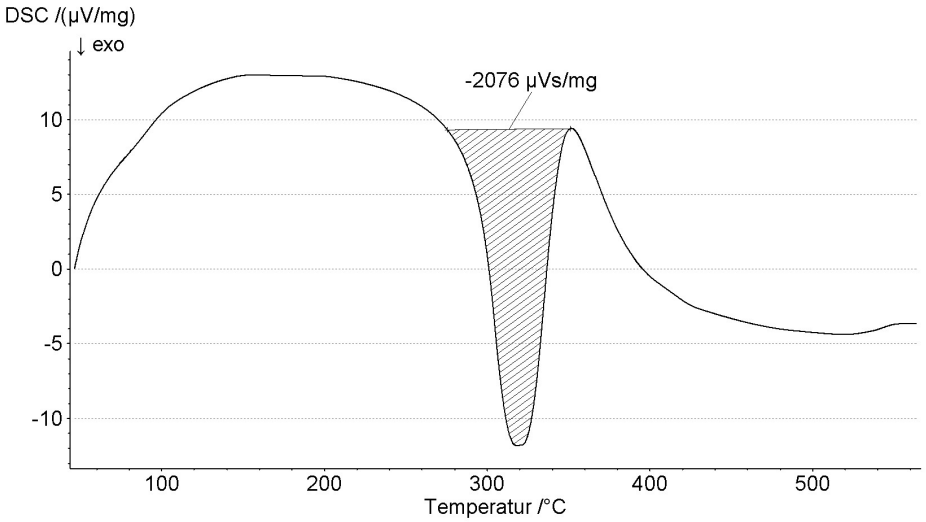

Figure 4.26.: DSC measurement of epoxy resin

Thermosoftening plastics (EK83, EMBE GmbH) are difficult to infiltrate into the fabric when using a high boron content due to their high viscosity upon melting. The use of warm pressing at temperatures above melting temperature also does not allow for fiber bundle penetration. Due to their low viscosity and stability during pyrolysis, the following liquid phases are used for slurry fabrication:

- Polycarbosilane, SMP-877 Starfire Systems,
- Phenolic Resin, HEXION BAKELITE PF 8978,
- H_2O, and
- Ethanol.

Polycarbosilane shrinks during curing without bonding to particles or fibers, leaving voids between the cured matrix and the particles/fibers, as described by Ziegler et al. [201]. In addition to the resin itself, this behavior is influenced by the surface structure and composition of the particle or fiber. Mainzer et al. [111] described these effects during the investigation of SiC_f/SiC CMC manufacturing using the same phenolic resin. They describe the influence of different fiber coatings on the shrinkage behavior. SiC fibers with SiC coating cause the resin to detach during curing and form solid inter fibers blocks. SiC fiber with sizing, containing a high amount of carbon, causes the resin to stay attached to the fibers and form a porous inter-fiber sponge, as seen in figure 4.27 a). In C/SiC-based composites, the pore structure

can change due to these shrinkage effects between fibers and gusset areas formed by the rovings crossing. The pore structure is more homogeneous due to the powder loading in the B slurry system. The initial pore structure forming upon pyrolysis is different when using phenolic resin or polycarbosilane, as shown in figure 4.27. The polycarbosilane-based slurries, shown in figure 4.27 b), have larger pores, a majority of which are over $1\mu m$, spread over a large bandwidth of diameters. The combination of low contact angles of SiC makes polycarbosilane a suitable candidate for RMI. Phenolic resin has a smaller, very defined peak pore distribution, as shown in figure 4.27 a). The pore size distribution is measured by mercury porosimetry and shown for both precursors in figure 4.28.

While polycarbosilane does not need any additional treatment to allow for RMI, phenolic resin does. Due to the high carbon yield and the small pores forming during pyrolisis, infiltration with Zr_2Cu stops short of ~1 mm into the preform. Depleting the phenolic resin can be used to adapt the pore size distribution of the resin; however, carbon formation will still block infiltration due to the contact angles of carbon and Zr-alloys, as described in section 4.1. The key to enabling a phenolic-based slurry to be infiltrated with Zr-alloys using a B_2O_3 treatment is described in the following section.

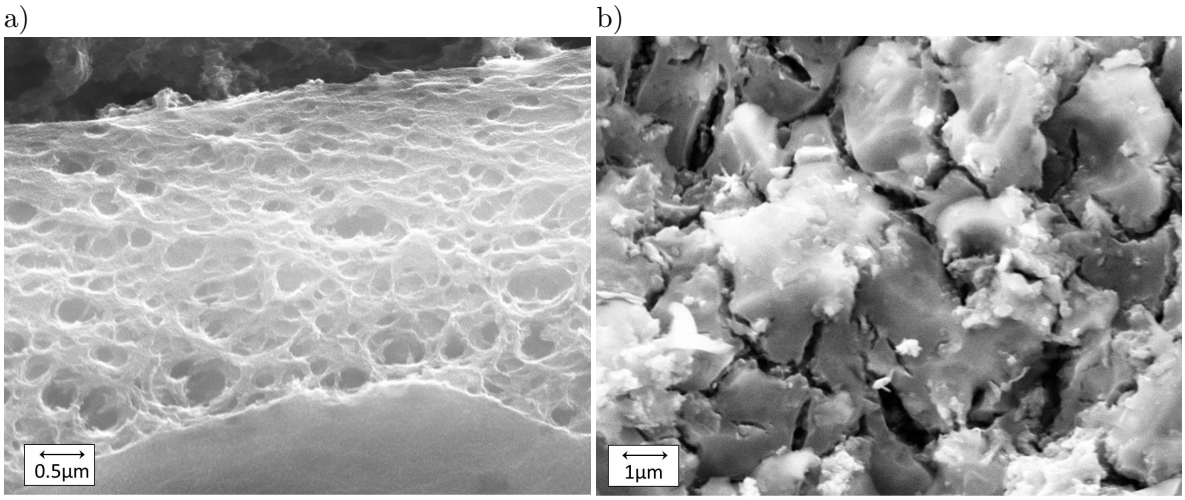

Figure 4.27.: Micro-structure of phenolic a) and polycarbosilane b) resin between fibers after pyrolysis

Boron Oxide Conditioning

A method allowing for Zr-RMI for a phenolic-based B slurry, must increase pore diameters and improve the contact angle within the pore structure. The phenolic resin could be depleted for adaption of the pore size distribution with an additional internal coating of the pore structure after pyrolysis to adopt the contact angle. However, the coating would again influence the

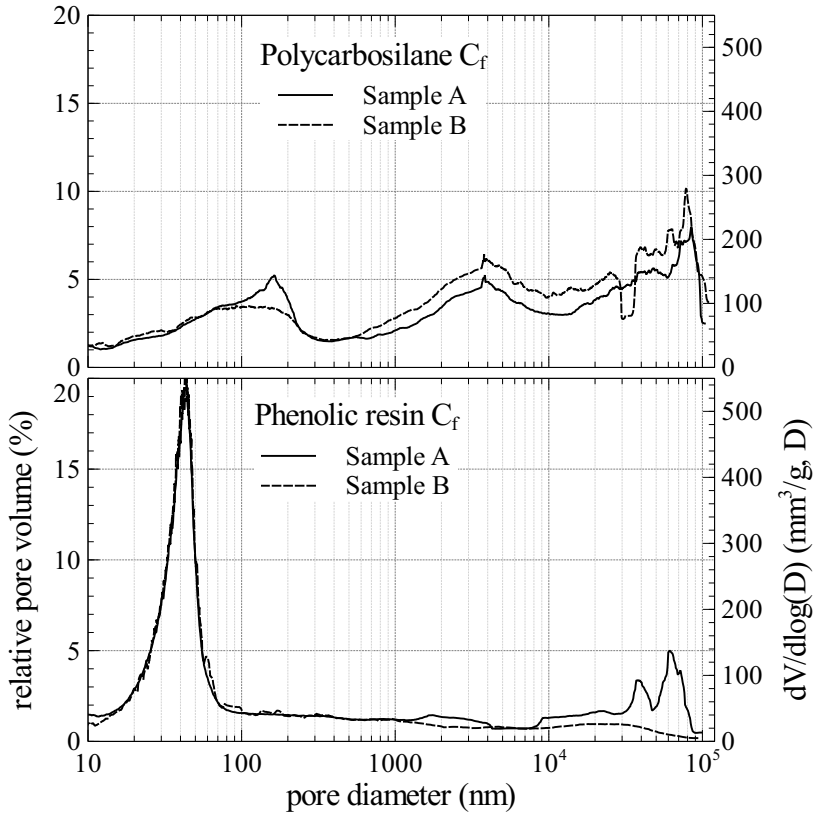

Figure 4.28.: Comparison of the pore size distribution of polycarbosilane and phenolic resin

pore size distribution due to the deposition of suitable coating material. Instead, the following reaction can be used to influence both factors at once:

$$7C + 2B_2O_3 \longrightarrow B_4C + 6CO. \tag{4.15}$$

A decrease in volume, due to loss of CO, enlarges pores, and contact angles are enhanced due to B_4C formation. B_2O_3 has a melting point of ~450°C and begins to infiltrate into the capillary system of the preform upon melting. The B_4C formation starts at higher temperatures according to literature [202–204]. Jung et. al [203] describes the influence of pyrolysis temperature, dwelling time, and carbon content on the formation of B_4C. Figure 4.29 shows an SEM image of a phenolic-based pyrolysed composite on the left and the same composition after B_2O_3 infiltration and pyrolysis at 1800°C on the right. Most of the amorphous C is transformed into B_4C, leaving a larger pore structure.

Figure 4.30 shows the pore size distribution of polycarbosilane, phenolic resin, and phenolic resin after B_2O_3 infiltration. As previously described in this section, polycarbosilane has a very large bandwidth of larger pores compared to phenolic resin. The pore size distribution of a B_2O_3 infiltrated sample is similar in bandwidth and size to polycarbosilane samples, and therefore, promotes infiltration with Zr-alloys. Once the carbon is consumed, additional infiltration cycles do not change the pore size distribution any further, as shown in the

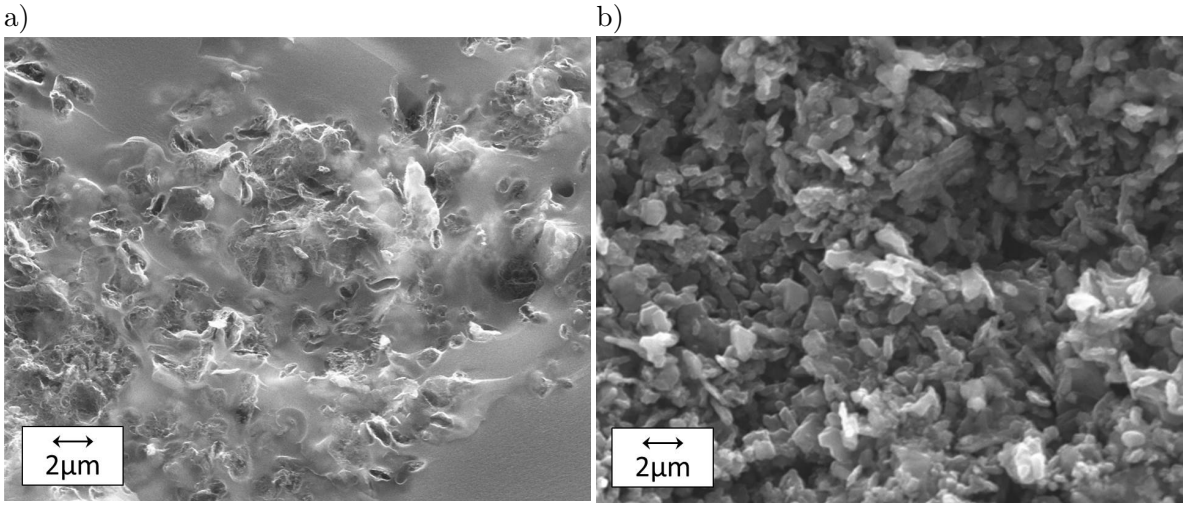

Figure 4.29.: Matrix micro-structure before a) and after B_2O_3 infiltration b)

bottom graph of figure 4.30. The amount of B_2O_3 can be calculated by the ceramic yield of the phenolic resin and FVC.

B_2O_3 melts around 450 °C and starts to evaporate in an Ar atmosphere at around 1400 °C, as shown by TG analysis in figure 4.31. In order to determine the starting temperature of the carbothermal conversion, B_2O_3 mixed with a pyrolysed phenolic matrix is also measured. Due to the formation of volatile CO, a weight change indicates the start of the conversion. When comparing both graphs, weight change due to the CO formation cannot be recorded due to the start of evaporation of B_2O_3, as indicated by the weight change of the pure B_2O_3 sample. After TG analysis, the phenolic sample formed B_4C. This is either due to a reaction of liquid B_2O_3 or due to a reaction with the evaporated B_2O_3. The contact angle measurements of B_2O_3 on a glassy C substrate are also displayed in figure 4.31. Recorded contact angles are high and never drop below 65°. According to literature, molten B_2O_3 has a viscosity of 5,000-100,000 mPa s [205, 206]. Due to the high contact angles and high viscosity, the conversion of C into B_4C might be initiated by the reaction with evaporated B_2O_3. Contact angles on B_4C substrates fall below 50° at temperatures above 750°C. This indicates that once the conversion to B_4C has started, infiltration is promoted by lower contact angles. The calculated volume of B_2O_3 decreases on B_4C substrates from $4.15\mu l \pm 0.019$ to $0.67\mu l \pm 0.07$ during heating from 1450 °C to 1575 °C. The high evaporation rate inhibits a drop shape analysis at temperatures above 1500 °C.

Figure 4.32 shows an XRD analysis of a pyrolysed phenolic-based sample, in additions with C fibers, in comparison to an identical sample infiltrated with B_2O_3. In an Ar atmosphere, each sample is pyrolysed at 1300 °C, and infiltration is taken to 1800 °C in order to start B_4C formation. The XRD shows that both B and B_4C signals become more prominent. This is due to the formation of B_4C as well as consumption of the amorphous C from the phenolic precursor, as seen in the SEM images in figure 4.29.

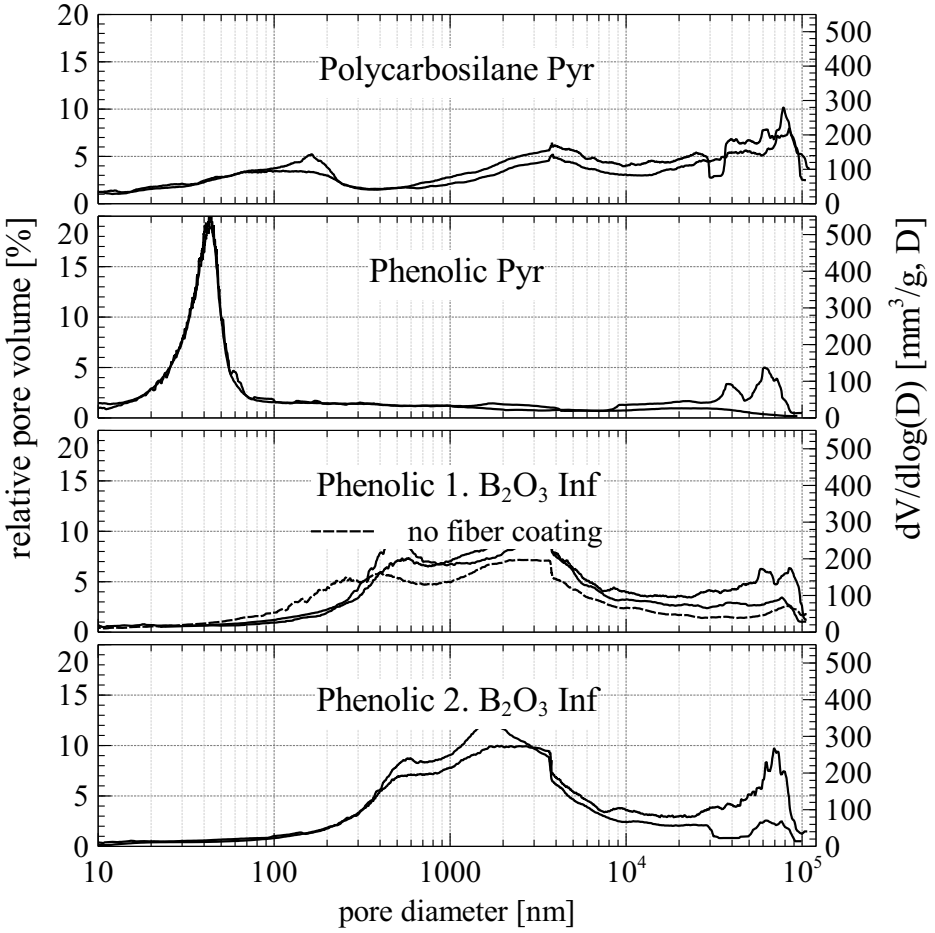

Figure 4.30.: Pore size distribution of pyrolysed polycarbosilane, phenolic resin, and phenolic resin after B_2O_3 infiltration

Figure 4.33 displays the pore size distribution of phenolic resin using a H_2O_2 B powder treatment and a triisopropyl borate infiltration. H_2O_2 treatment is performed after impregnation of the fabric with boron powder.

Impregnation Methods In order to achieve damage-tolerant UHTCMC behavior, the fibers must be distributed homogeneously within the matrix. Therefore, each fiber bundle must be impregnated with B powder to form ZrB_2 between the fibers. Three different methods are analyzed according to their boron impregnation:

- Electrostatic Deposition,
- Spraying, and
- Calender.

Electrostatic Boron Deposition The dispersion of B particles in water forms boron acid. B_2O_3 forms on the surface of B powder in air, reacting in water to boric acid ($B(OH)_3$).

$$B_2O_3 + 3H_2O \longrightarrow 2B(OH)_3. \tag{4.16}$$

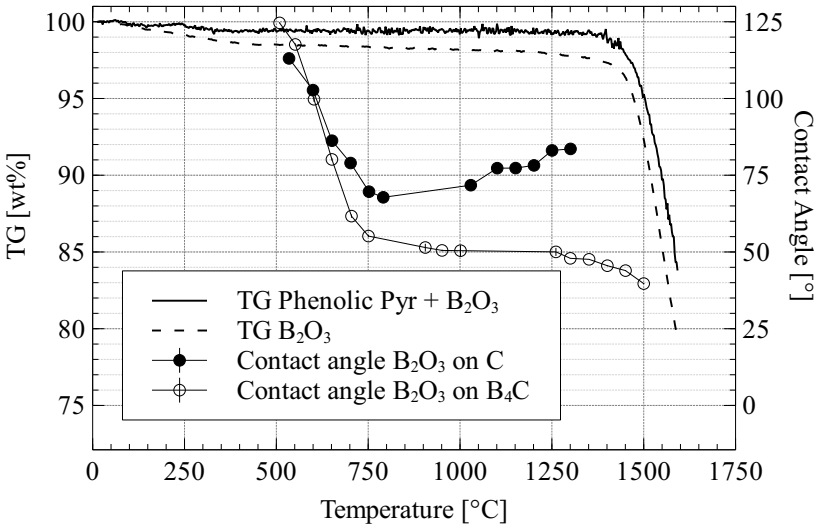

Figure 4.31.: TG and contact angle analysis of B_2O_3 in an Ar atmosphere

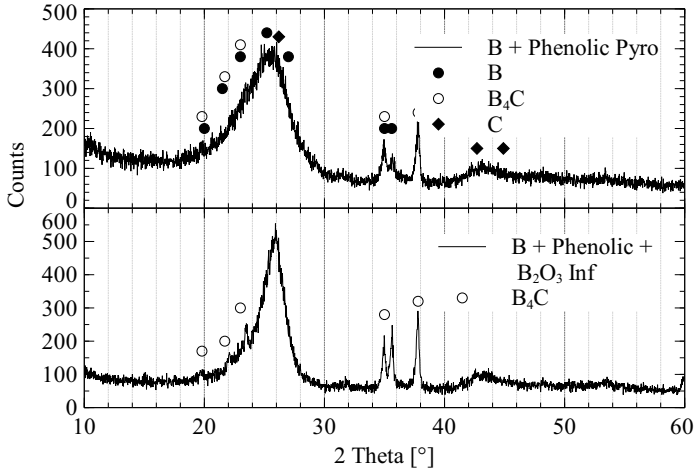

Figure 4.32.: XRD of pyrolysed phenolic samples with and without B_2O_3 infiltration

If B_4C or $B(OH)_3$ is added to water or to an organic solvent miscible with water, OH^- groups form on the surface of the particles [207, 208].

$$B(OH)_3 + H_2O \longrightarrow [B(OH)_4]^- + H^+. \tag{4.17}$$

Applying an electric field moves the $B(OH)_4$ ions to the anode. Hyam et al. [194] measured the zeta potential of a dispersion of B in acetone with respect to particle size. A pH-value of approx. 7 was generated when applying a voltage of 23 mV and 34 mV. Therefore, the isoelectric point of B in acetone should be in the weak alkaline range. In order to assess the sedimentation behavior of the different dispersions, static tests are conducted. B powder is dispersed in each liquid to be tested and observed within a laboratory glass with identical amounts of slurries. Each glass is sealed to prevent falsification of the results by evaporation.

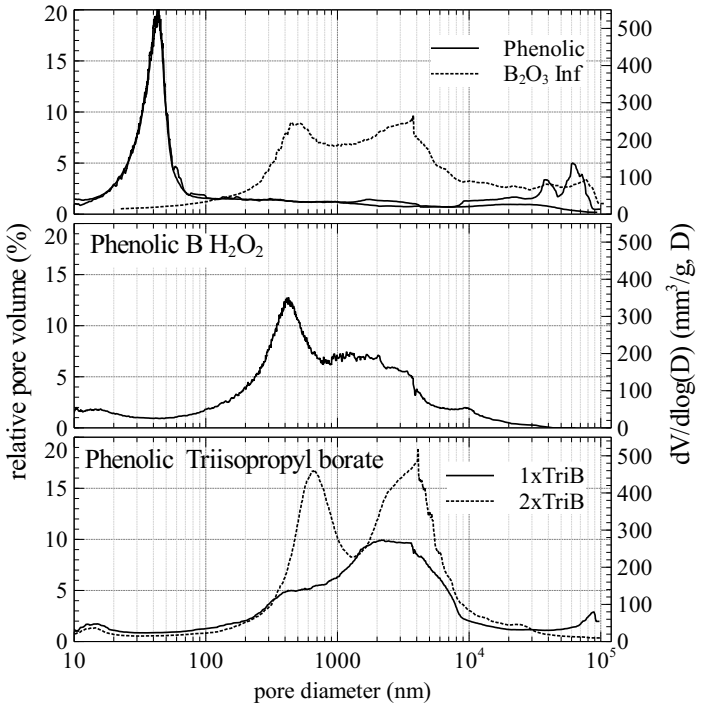

Figure 4.33.: Pore size distribution of pyrolysed phenolic resin and phenolic resin after B_2O_3 treatments

After a period of 3 hours, the sedimentation is assessed, i.e. to what extent the descent front has drifted. Table 4.1 shows a summary of the results from the sedimentation tests.

The sedimentation is graded as "+" meaning an improvement, "-" for a deterioration, and "0" for no change in the sedimentation behavior compared to a pure water solvent. The use of acid and strong bases as stabilizers leads to a significant deterioration of the sedimentation behavior. These approaches are not an option for EPD impregnation and are not be investigated further. Acetone does not stabilize the suspension, and the use of urea and cyanoguanidine does not indicate any change in relation to water as a solvent. The use of phenolic resin as a stabilizer leads to a slight improvement in sedimentation behavior. Stabilization with polyethylene glycol, especially the short-chain variant (200; PEG200), stabilize the most. Even after several days, the mixture of PEG200 and water does not show any significant sedimentation. While good stability is important for the following considerations, it should not be so high as to restrict any movement. A moderate stability of a suspension could be compensated by a vertical arrangement of electrodes with corresponding separation and sedimentation direction. Multiple experiments were performed with varying electric fields and deposition substrates. The weight change of both cathode and anode substrates is used to determine the B deposition. Both phenolic resin and polyethylene glycol show no weight difference between the cathode and anode. The combination of viscosity and stability of these two suspensions limits the movement of B particles. Increasing conductivity of the water-based suspension from $0.27\frac{\mu S}{cm}$ to $60\frac{\mu S}{cm}$ by adding NaCl does not increase the amount of B powder deposited either. The energy input into the water suspension is the limiting

Table 4.1.: Stability of boron suspensions

Stabilizer		Addition	pH	Stabilization	Stability
H_2O (10ml)		/	7	/	/
Ethanol	10ml	/	7	/	0
Acetone, C_3H_6O	10ml	/	7	/	-
Phenolic	10ml	/	7	electrosterical	+
Polyethylene glycol C_2H_4O 200	10ml	/	7	steric	+
Citric acid monohydrate $C_6H_8O_7$,H_2O	1g	H_2O (10ml)	1	electrosterical	–
Ammonia NH_3	3g	H_2O (10ml)	13	electrosterical	–
Sodium hydroxide NaOH	0.4g	H_2O (10ml)	14	electrosterical	–
Urea NH_2CONH_2	2.5g	H_2O (10ml)	7	/	0
Polyethylene glycol 200	7.5ml	H_2O (2.5ml)	7	steric	++
Polyethylene glycol 8000	0.5g	H_2O (10ml)	7	steric	+
Cyanoguanidine $C_2H_4N_4$	0.1g	H_2O (10ml)	7	/	0

factor due to a high conductivity, increasing temperature and essentially reaching boiling point. The intensity of the electric field influences the B content deposited on the substrate. Increasing the electric field from $17\frac{V}{cm}$ to $28\frac{V}{cm}$ increased the deposited B content from $6.5w.\%$ to $11.3w.\%$, using an electrode distance of $7.2cm$. Exceeding $28\frac{V}{cm}$ increases the temperature of the water suspension to its boiling point. After approximately 4 minutes, a slight circular movement of the suspension begins. The current directs from the cathode to the anode and becomes stronger, reaching a maximum after approximately 7 to 9 minutes and ceases after 13 to 14 minutes. The mass increase of the B deposition is linked to the movement of the particles visible as current streams. Therefore, it can be assumed that a separation of the particles only takes place during the observed movement. If an EPD is selected according to the previously defined parameters, the duration of the deposition should not exceed 15 minutes. For fabrication with EPD, a B content of $\frac{1}{30}\frac{g}{ml}$ is used, resulting in a viscosity of $0.196Pas$ and a conductivity of $0.27\frac{\mu S}{cm}$.

Calender Boron Deposition The Calender used for B impregnation of fabrics is a foulard manufactured by Mathis AG, which is equipped with rotating steel cylinders and a rubber coating. Rotation speed and pressure between both cylinders can be adjusted. Figure 4.34 shows the schematic of the foulard mechanism including rotation speed v and pressure P.

In order to determine the influence of these parameters, tests are conducted with a 10:4 weight ratio ethanol B slurry. Table 4.2 shows the weight increase on carbon fiber fabrics with varying speed and pressure. Low B weight gain only appears using a combination of low

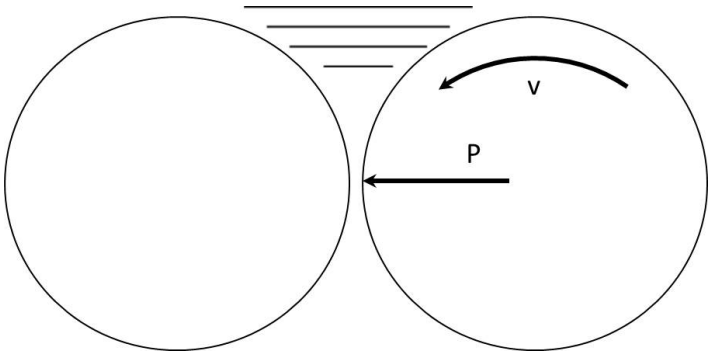

Figure 4.34.: Schematic of foulard mechanism

pressure and low rotation speeds. In order to achieve a high boron deposition, pressure and rotation speed should be as high as possible. Viscosity of each suspension will, however, limit the impregnation of the fabrics. If viscosity and foulard pressure are too high, the fabrics will not feed into the foulard cylinders. Therefore, each suspension is used with the highest foulard pressure possible for impregnation.

Table 4.2.: Influence of foulard parameters on boron content

	$1m/min$	$5m/min$
1 bar	6.39 wt. % ±0.88	9.36 wt. % ±1.22
3 bar	10.74 wt. % ±1.33	10.32 wt. % ±0.80

In order to determine the influence of different suspensions, ethanol, water, and polycarbosilane are used as B suspensions and the B weight gain of each is measured. The fabric samples are fed through the rollers, which is covering the fibers with B. After evaporation of the liquid phase, in the case of ethanol and water, the weight gain can be used to calculate B mass ratios. The results are summarized in figure 4.35. In the case of polycarbosilane, the samples are cured, and the percentage increase in mass of B is calculated from the original ratio of B and the resin. Compared to the use of ethanol, there is a clear increase in boron deposition using polycarbosilane, with an even greater increase when using water as a medium. Increasing the powder ratio is not feasible for ethanol and polycarbosilane, therefore, the tested mixtures are already the most viscous variant that can be processed. This shows that an increase in B content of the mixture initially leads to an increase in B content on the fabrics. However, if the B ratio is further increased, the increase in the boron content on the fabric stagnates. A ratio of 10:7 leads to difficulties feeding the fabrics into the foulard due to an increase in viscosity. 10:7 mixtures have a dynamic viscosity of $6.32 Pas$ compared to $2.32 Pas$ with a ratio of 10:5, at a shear rate of $0.685 \frac{1}{s}$. Higher viscosity also causes fiber distortion within the fabric. Investigating repeating impregnation cycles, the fabrics are initially coated with the water-boron mixture, using a 10:5 mixture. This is followed by drying the fibers and repeating the impregnation process. The percentage increase in B mass is calculated in relation to the initial mass of the non-coated fabrics. These repeating cycles do not

significantly increase B deposition, which is caused by the rigid coated fabrics and brittleness of the coating layer. During the second impregnation, the coating on the surface cracks and detaches. The mass of the coating increases locally, but total weight gain is reduced. After three cycles, there is no significant increase in mass gain. Repeating the process step several times does not lead to any further increase in B content. This observation can also be made when using ethanol as a liquid phase. Using polycarbosilane, the B content can be increased by repeating the process. This is possible due to curing the resin after the first cycle at 100 °C. This bonds the B particles to the fabric layers, keeping the sheets flexible. No cracking in the first coating layer is seen when applying the second layer. The mass ratios correspond to the previously determined ratio of 10:4.

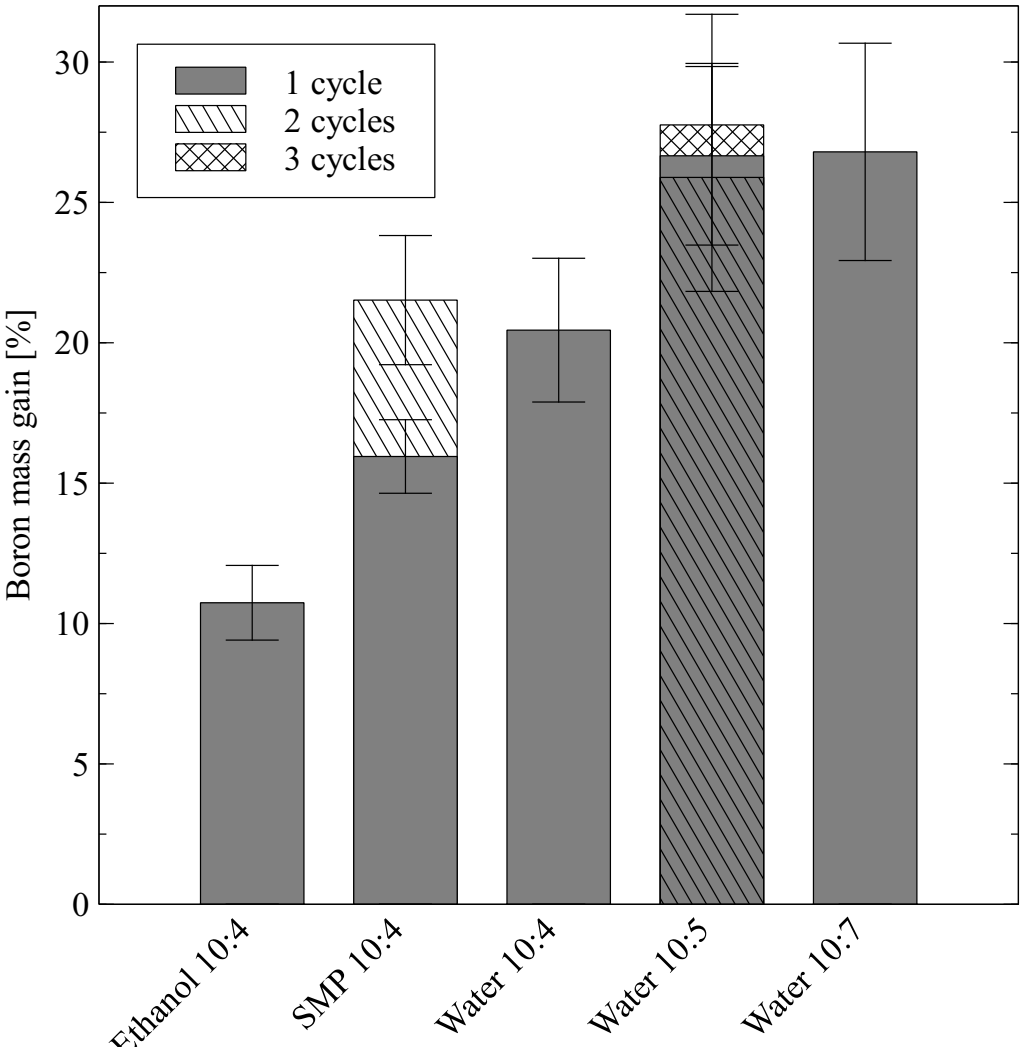

Figure 4.35.: Influence of boron suspension on foulard deposition

Combination of Foulard and EPD In order to determine the influence of the B deposition via a combination of foulard and EPD, both processes are applied in sequence. Fabric samples

are first impregnated with EPD and followed by the foulard process. After drying the fabrics after EPD, large areas of the thick coating detach. This leads to weight loss for most samples as well as increased fiber distortion. With no drying between the two processes, flaking and cracking of the coating is prevented. Nevertheless, a percentage increase in weight compared to the sole use of a process is not achieved, as the particles are washed away. In this case, the percentage increase in mass is only $11.40 ma.\%$, summarized in figure 4.3.

Table 4.3.: Process combination of foulard and EPD on boron content

	EPD	Foulard	EPD + Foulard
Boron mass gain [%]	24.71 ± 6.51	26.66 ± 3.18	11.40 ± 2.09

Boron and Zirconium Diboride Mixtures As described in section 4.1, passive fillers help reduce the high temperatures from exothermic reactions, and therefore, the fibers' preforms can be impregnated with a mixture of active and passive powders. In these investigations, the preforms were impregnated with a mixture of B and ZrB_2 powders. ZrB_2, H.C. Starck Grade B 1.5-3.0μm, is of similar particle size as the B powder. Due to the higher density of ZrB_2 powder compared to B powder, the particles sediment much more rapidly in water, polycarbosilane, and phenolic resin. In order to stabilize the powders for impregnation, a number of additives were investigated using 50 vol% B and 50 vol% ZrB_2. The powder mixtures were dispersed in water and phenolic resin using a 40 wt% ratio. Sedimentation was recorded after 24 h, three days, and one week. The results and additives used, BYK-Chemie GmbH, are listed in the table 4.4 below.

BYK-7420ES shows the best results in stabilizing the B-ZrB_2 powder mixture, with no sedimentation after one week.

Figure 4.36 shows the pore size distribution after pyrolysis at 1800°C of 100 vol.% B powder and a powder mixture of 50 vol.% B and 50 vol.% ZrB_2. Due to the high density of the ZrB_2 powder, the powder loading of the slurry changes in percentage. Two powder loading compositions inside the phenolic resin, 30 and 80 wt.%, were examined. Water was used as a dispersion for the third slurry combination in figure 4.36. The single fabrics were impregnated with a 80 wt.% 50 vol.% B and 50 vol.% ZrB_2 powder mixture and BYK-7420ES as a stabilizer before drying at 90°C in order to keep a tetraboric acid layer surrounding the B particles. Due to the higher amount of phenolic inside the 30 wt.% preform, more C is converted to B_4C, which results in the formation of larger pores when compared to the 80 wt.% preform or the pure B slurry. The 80 wt.% preform has a similar pore distribution as the pure B preform, and therefore, does not affect the reactive melt infiltration in terms of pore diameter. Using a water-based impregnation of the fabrics influences the pore distribution due to the solubility of B_2O_3. The B particle oxidation layer was partially removed during the impregnation with a water based slurry. Consequently, there was not enough B_2O_3 enclosed inside the preform to convert the phenolic C into B_4C during pyrolysis. This effect is visible

Table 4.4.: Stability of B/ZrB_2 suspensions

Additive	Powder Amount	Solution	Stabilization	Stability
DisperBYK-108 1 wt. %	40 wt. %	Phenolic	steric	-
DisperBYK-108 4 wt. %	40 wt. %	Phenolic	steric	0
DisperBYK-108 4 wt. %	80 wt. %	Phenolic	steric	++
DisperBYK-103 3 wt. %	40 wt. %	Phenolic	steric	0
DisperBYK-103 7 wt. %	40 wt. %	Phenolic	steric	0
DisperBYK-103 7 wt. %	80 wt. %	Phenolic	steric	++
BYK-154 1.5 wt. %	40 wt. %	Phenolic	steric	0
BYK-154 7 wt. %	40 wt. %	Phenolic	steric	0
BYK-9076 2 wt. %	40 wt. %	Phenolic	steric	+
BYK-9076 7 wt. %	40 wt. %	Phenolic	steric	+
BYK-9076 15 wt. %	40 wt. %	Phenolic	steric	+
DisperBYK-2155 2 wt. %	40 wt. %	Phenolic	steric	+
DisperBYK-2155 7 wt. %	40 wt. %	Phenolic	steric	+
DisperBYK-2155 7 wt. %	80 wt. %	Phenolic	steric	++
DisperBYK-2010 11 wt. %	40 wt. %	Phenolic	steric	0
DisperBYK-2010 25 wt. %	40 wt. %	Phenolic	steric	-
BYK-7420ES 1 wt. %	40 wt. %	H_2O	steric	-
BYK-7420ES 2 wt. %	40 wt. %	H_2O	steric	++
BYK-7420ES 2 wt. %	80 wt. %	H_2O	steric	++
DisperBYK-103 3 wt. %	40 wt. %	H_2O	steric	-
DisperBYK-103 7 wt. %	40 wt. %	H_2O	steric	-

in figure 4.36 at the bottom graph, where the pore size peak below 100 nm results from unconverted C from phenolic resin, see figure 4.30.

4.2.2. Fiber Reinforcements

In general, both SiC and C fibers can be used to manufacture a UHTCMC. Additionally, HfC and TaC fibers have been developed by MATECH (Westlake Village, CA, USA), but are not commercially available. Due to their high modulus and negative Gibbs Free Energy for the reaction with liquid Zr, they would be an interesting option for UHTCMCs without fiber coatings. Because these fibers are not available, SiC and C (pitch-based) fibers were used throughout the investigations. Due to the application temperature, Tyranno SA3 fibers were chosen for their high-temperature residual strength, as shown in chapter 2 figure 2.5. The pitch-based Nippon Graphite Fiber Corporation YSH-50A, XN-60, and XN-80 C fibers were chosen due to their high thermal conductivity, high modulus, and preform handling. Both types of fibers are sensitive to fiber degradation due to liquid melt infiltration with Zr. Due to their layered structure, see fig. 4.37, pitch-based carbon fibers will more likely allow for a damage-tolerant mechanical behavior. As described by Reimer et al. [209], some pitch-based

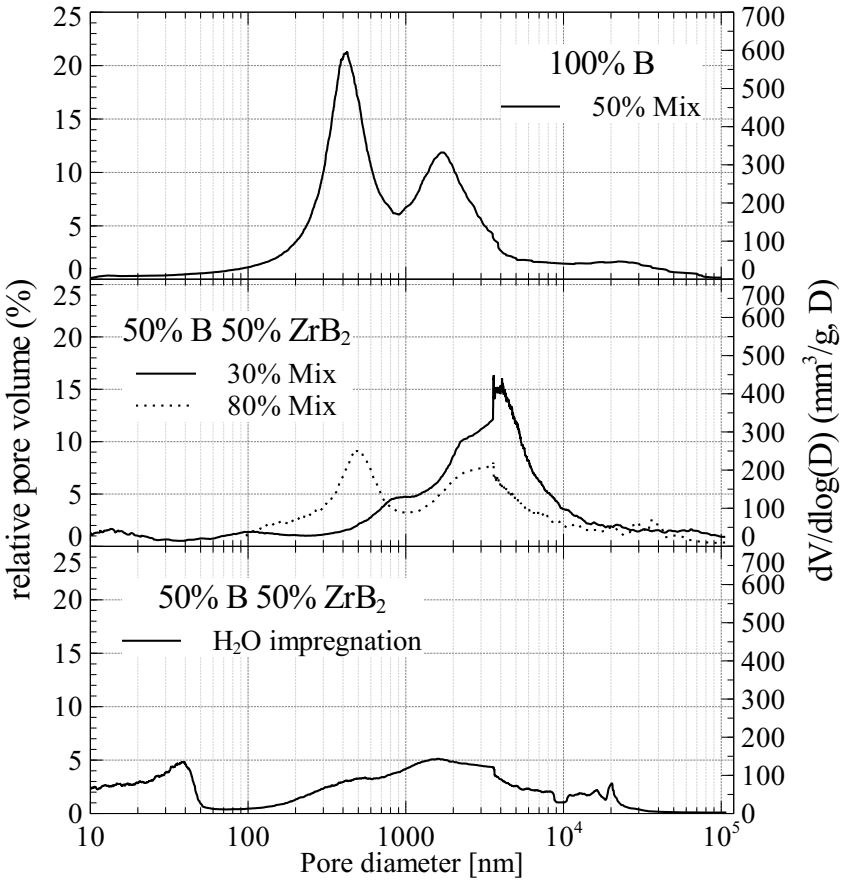

Figure 4.36.: Pore size distribution of pure B slurry and B/ZrB_2 mixture

carbon fibers cause a fiber pull-out and crack deflection on their internal layers, leaving the task of melt and oxidation protection for the fiber coating.

Sauder et al. investigated the strength and modulus of Rayon, PAN, and pitch-based C fibers up to 2400 °C [210]. Anisotropic pitch-based carbon fibers show the least degradation of their RT strength and stiffness values above 2000 °C. According to Sauder et al., the start of nonlinear elastic or inelastic deformation depends on the fiber texture. The crystal orientation within the fiber structure causes shear stresses, which increase with temperature. Once these shear stresses reach a critical value, the behavior of the fiber becomes inelastic due to local cracking and sliding, as seen in figure 4.38. The cracks formed are responsible for the degradation of the fibers. The orientation of the fibers' crystal structure with respect to the fiber axis influences the elastic to inelastic transition temperature, which tends to be lower for isotropic fiber structures. Figure 4.39 shows the relative softening of rayon and PAN, as well as isotropic and anisotropic pitch-based carbon fibers over temperature, whose decrease in modulus is determined relative to their RT modulus. The fibers derived from anisotropic pitch show the smallest decrease in relative strength and modulus, making these type of fibers the most interesting candidates for UHT application and composites.

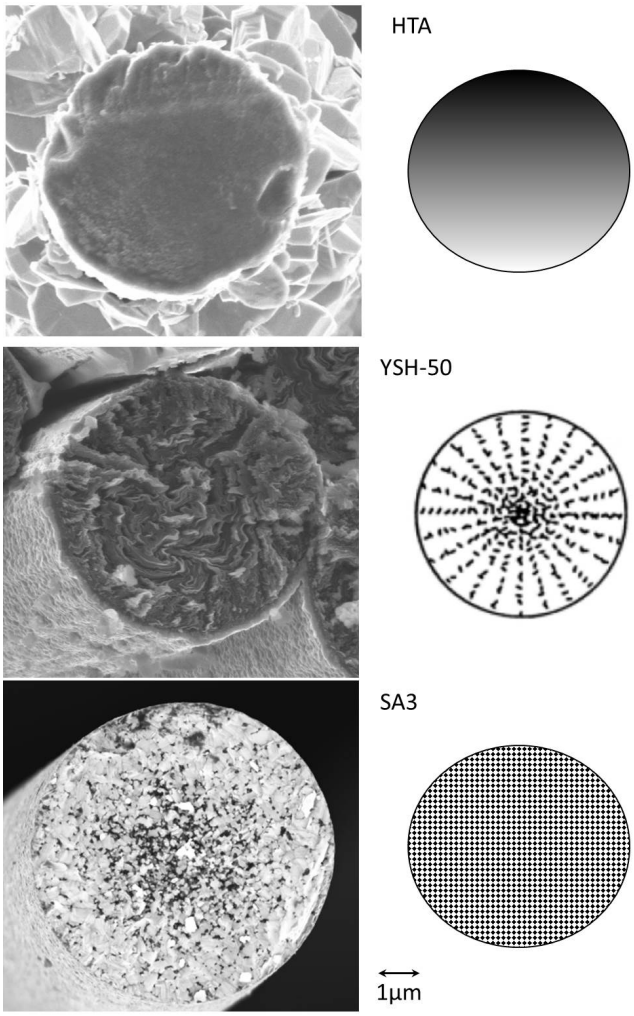

Figure 4.37.: Layered structure of a pan-based carbon fiber (HTA), pitch-based (YSH-50), and SiC fiber (SA3)

4.2.3. Fiber Coatings

The main focus of a UHTCMC fiber coating in regard to RMI manufacturing is to protect the fibers from being converted to ZrC by the liquid Zr. In order to achieve this protection, the coating must also withstand the manufacturing procedure up to melt infiltration, which includes pyrolysis in environments rich in C and B. Figure 4.40 shows the degradation of a SiC fiber due to the melt infiltration. The degraded fiber does not retain its original strength and also does not allow for a sufficient fiber matrix inter-phase.

In order to determine a coating material capable of withstanding liquid Zr or a Zr alloy, various fiber coatings were investigated. Identical to the manufacturing of UHTCMC, the fiber coatings were investigated while heating the melt and coating sample separately. Table 4.5 shows the different coatings and fiber materials tested in contact with Zr_2Cu at 1500 °C. Due to contact angle measurements, ZrB_2 and TaC fiber coatings are also viable candidates. However, processes to coat these species are very scarce and not feasible for fabrics.

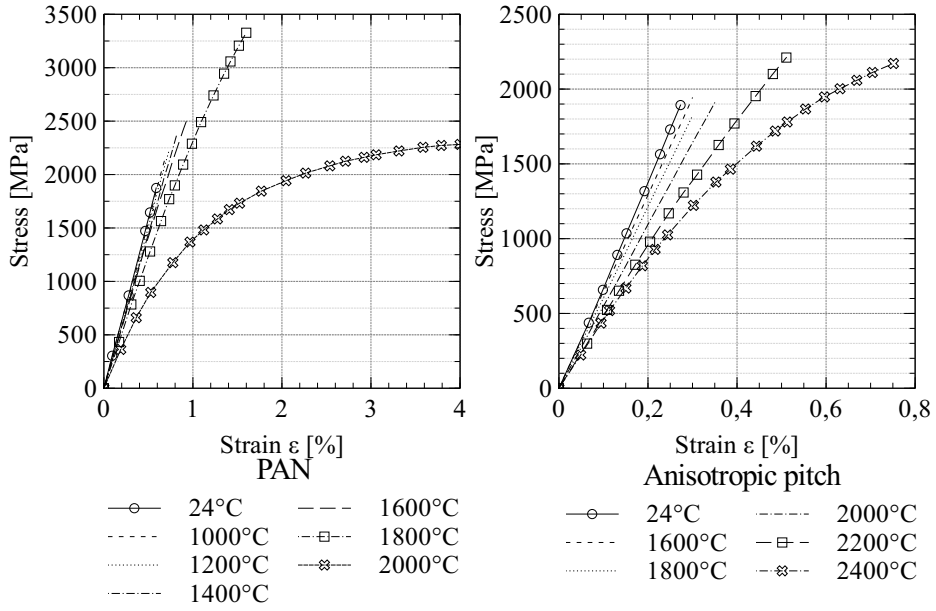

Figure 4.38.: Mechanical behavior of PAN and pitch-based carbon fibers at elevated temperatures and tensile loading

Table 4.5.: Process combination of foulard and EPD on boron content

Fiber type	Coating	Degradation by RMI	ΔH of Zr and coating at 1500 °C [kJ]
C	TiB_2 by CVD	moderate	-43
C	Y_2O_3 by PVD	full	240
C	B by CVD	full	
SiC	SiN by dip coating	full	-660
SiC	PyC by CVD	full	-188
SiC	BN-SiC by CVD	partial	-134
ZrO_2	-	full	-424
W	Er_2O_3 by CVD	full	229

TiB_2 Fiber Coating

TiB_2 is a suitable protection for C fibers during the RMI process. Oxidation resistance of TiB_2 at ultra high temperatures is, however, inferior compared to ZrB_2 [9, 39, 211]. Hence, the TiB_2 coating thickness should be as thin as possible. In addition, a thick fiber coating will begin to seal the fiber bundles, not allowing any B slurry or melt to infiltrate into the bundle. Figure 4.41 shows the TiB_2 coating thickness after a) 2 h and b) 4 h of CVD process time. Due to the linear behavior of this process, as long as bundles aren't sealed and surface areas start to change rapidly, the 4 h process produces twice the coating thickness of around $4\mu m$.

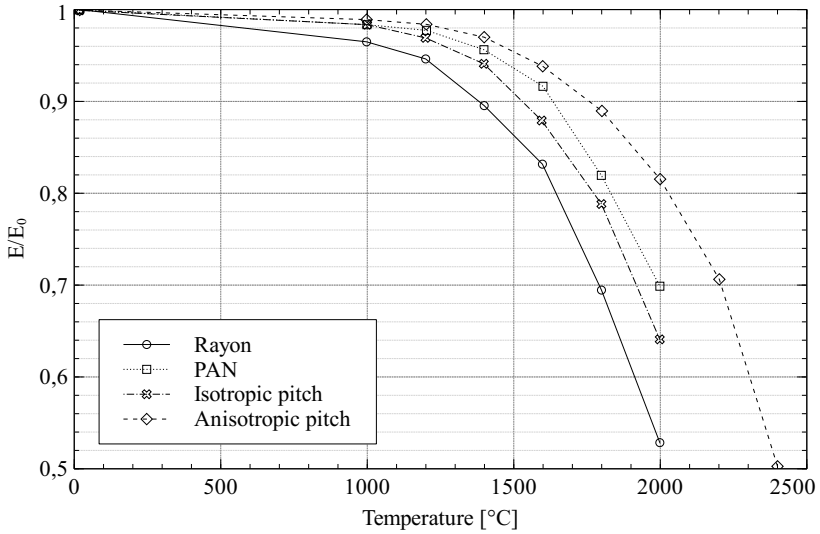

Figure 4.39.: Decrease in relative RT young's modulus E(T)/E_0 over temperature; E_0 = E (24 °C)

Influence of TiB_2 Fiber Coating on Boron Impregnation Due to the different surface compositions and structures of the TiB_2-coated fibers, B impregnation processes are influenced by the different wetting behaviors of each suspension, surface roughness, and hardness of the coating. In order to compare the amount of B deposited in each step, mass gain is measured in specific weight gain $\frac{mg}{cm^2}$. A comparison using $ma.\%$ as in section 4.2.1 cannot be applied due to the different area weight of the pure C and coated fabrics. Table 4.6 shows the decreased amount of B deposited onto the coated fibers. For TiB_2-coated fibers, ethanol enhances the amount of B applied. Using polycarbosilane and an additional drying step as described in section 4.2.1, the coating behavior for the second cycle can be improved. By not applying the second layer onto the TiB_2-repellent coating, but onto the dried polycarbosilane, the wetting and deposition becomes similar to the process using C fabrics. B depositions of each cycle and fabric are shown in table 4.7.

Table 4.6.: Influence of fabrics on deposited boron content

	C_f $\frac{mg}{cm^2}$	C_f + TiB_2 coating $\frac{mg}{cm^2}$
Foulard H_2O	38.23 ±1.88	14.00 ±0.83
Foulard Ethanol	15.44 ±1.13	15.68 ±0.80
EPD	35.51 ±2.53	14.00 ±1.20

Table 4.7.: Influence of fabrics on deposited boron content by multiple cycles

	C_f $\frac{mg}{cm^2}$		C_f + TiB_2 coating $\frac{mg}{cm^2}$	
	1x	2x	1x	2x
Foulard Polycarbosilane	18.9 ±1.3	31.0 ±1.9	7.9 ±0.8	24.2 ±1.4

Figure 4.40.: Degradation of a SiC fiber after RMI

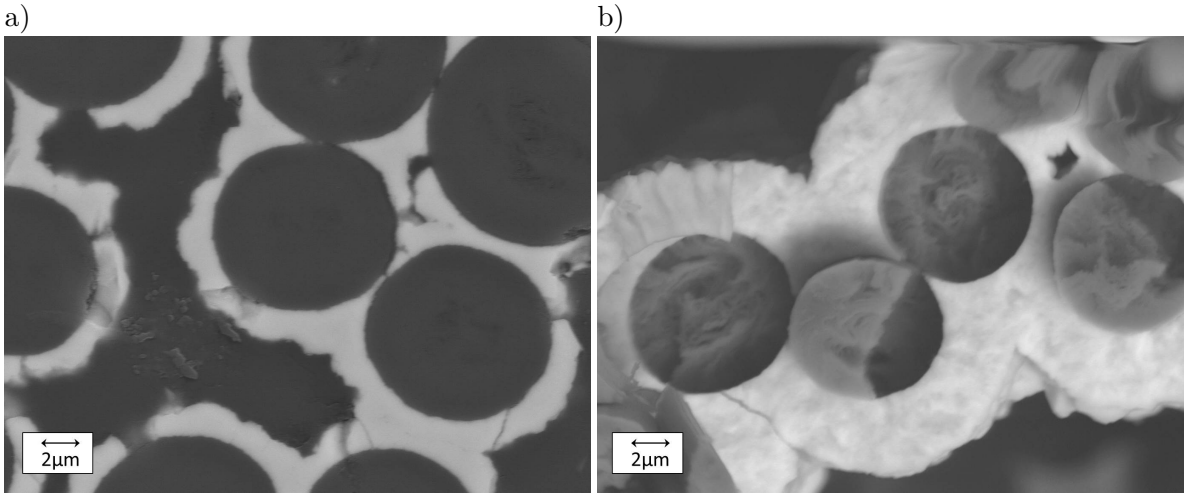

Figure 4.41.: TiB_2 fiber coating after a) 2h and b) 4h CVD coating time

Influence of Fiber Coating

In order to determine the influence of the TiB_2-CVI coating process on fiber strength, single fiber tests were performed at the University of Bremen. The tests were performed with XN-80 (Nippon Graphite Fiber Corporation) fibers, including fiber sizing. In order to separately determine the effects of process temperature and the CVI reactions, three stages were analyzed, as received, thermal de-sizing at 1000 °C in argon atmosphere and TiB_2 coated. The strength calculation of the two non-coated series was based on the fiber diameter, whereas the the strength calculation of the coated fiber was based on the fiber diameter including the coating thickness. A TiB_2-coated carbon fiber is a small composite itself and has no homogeneous stress distribution.

As described, the CVI process influences the fiber strength, which must be taken into account for fiber selection and further composite design. Without the protection of TiB_2 coating, fiber degradation and decrease in strength may be even higher during RMI. TiB_2 influences the fiber matrix interphase and crack propagation due to the difference in modulus from the ZrB_2 matrix, TiB_2 coating, and C_f. A decrease in the Young's modulus with an increasing temperature, as described by Sauder et al. [210], also has an effect on crack propagation, and therefore, on the composite strength. Sauder et al. also investigated anisotropic pitch-based C_f, similar to the XN-80, showing a decrease of less than 2% up to 1000 °C in Young's modulus. The investigated strength increased up to 2200 °C, in contrast to the strength measured in this investigation. In addition to the influence of temperature, the drop in strength at temperatures up to 1000 °C in this investigation may also have been caused by de-sizing. Fibers used in the works of Sauder et al. were heat-treated prior to the strength measurement in order to remain stable during tensile tests. Sizing or surface treatment of the C fibers was used to reduce the influence of surface defects caused by the carbonization process [212]. Vautard et al. found a high density of surface-functional groups by plasma-based surface treatment without reducing mechanical properties. These groups cause better interfacial adhesion. XN-80 fibers in this investigation have an epoxy-based sizing, which decomposes during heat treatment and CVI coating. De-sizing temperature for strength tests is set to match the maximum process temperature of CVI coating. Table 5.3 shows the average strength and Young's modulus of single filament tests. Untreated fibers retain the highest strength and stiffness values, followed by de-sized and TiB_2-coated fibers. Sauder et al. did not record a drop of more than 2% in Young's modulus up to 1000 °C. The drop in stiffness in this investigation is either caused by the influence of decomposition of the sizing or by a different behavior of the XN-80 fibers. The strength of XN-80 fibers drops by almost 30% when coated. This decrease in strength is a combination of decreased fiber strength and an influence of the TiB_2 coating strength. However, losing strength during RMI without fiber coating would be much more severe. Figure 4.42 shows the Weibull probability plot of each set of fibers. In addition, the drop in strength of the treated fibers and the spread of fiber strength within each set changes as well. While de-sized fibers have the highest spread, TiB_2-coated fibers exhibit the lowest spread. As mentioned by Vautard et al., the increase could be caused by surface defects present on the de-sized fibers, which in contrast are sealed by TiB_2 on the coated filaments.

Table 4.8.: Mechanical properties, ultimate stress σ_0, and Modulus E of single filament tests

	Untreated	De-sized	TiB_2 coated
σ_0 [MPa]	4269	3922	3046
E [GPa]	802 ± 91	737 ± 197	646 ± 154

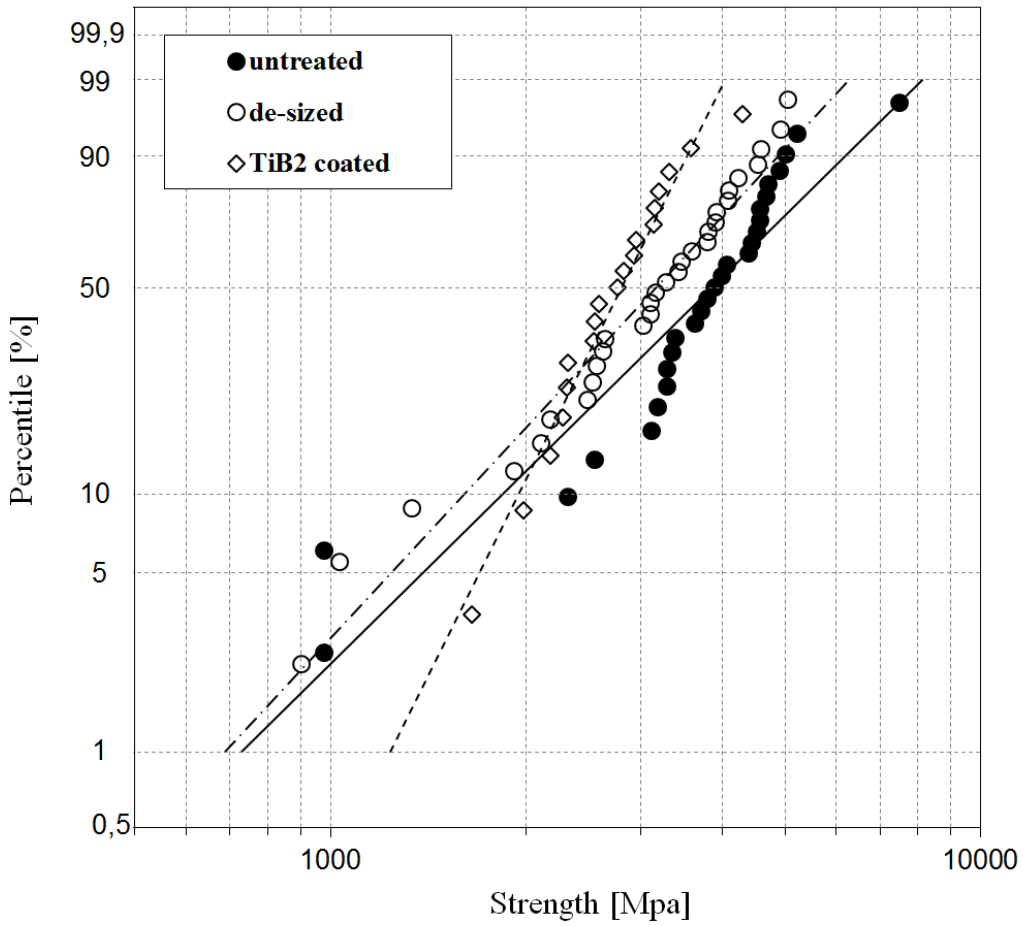

Figure 4.42.: Weibull distribution of single filament strength

Influence on the Composite

He and Hutchinson (HH) described the ability of a composite to deflect cracks along the interface or penetrate the fibers [106, 213]. HH investigated various angles of the crack impinging on the fiber. They concentrated on the first Dundurs parameter, α, and neglected the second parameter, assuming the lateral contraction being similar between matrix and fiber.

$$\alpha = \frac{E_f(1-\nu_m^2) - E_m(1-\nu_f^2)}{E_f(1-\nu_m^2) + E_m(1-\nu_f^2)}. \tag{4.18}$$

Ahn et al. further investigated the model of HH by varying the second Dundurs parameter, fiber volume content, and various lengths of deflected and penetrating cracks [214]. HH proposed that crack deflection occurs when the ratio of energy release rate of deflection over penetration is larger than the ratio of surface fracture energy ratio of deflection over penetration. G_p is the critical energy release rate and is equal to the surface energy of the fiber Γ_f, the surface energy G_d is equal to the surface energy of the interface Γ_i. In general,

the surface energy of the matrix Γ_m is larger than Γ_i. Therefore, the resulting deflection criterion at the fiber matrix interface can be described as

$$\frac{G_d}{G_p} < \frac{\Gamma_i}{\Gamma_f}. \tag{4.19}$$

The energy release rates are calculated from the potential energies of either deflecting or penetrating cracks ε_d and ε_p.

$$G_p = \frac{\varepsilon_p - \varepsilon_r}{\pi r_f^2 - \pi(r_f - ap)^2}. \tag{4.20}$$

$$G_d = \frac{\varepsilon_d - \varepsilon_r}{2\pi r_f a_d}. \tag{4.21}$$

ε_r is the initial reference energy necessary to extend a crack in the matrix toward the fiber matrix interface, applying a fixed remote load and with a fiber diameter r_f. The crack length of the advancing initial crack along the fiber matrix interface is described as ad, whereas penetrating the fiber is described by a_p [214]. Contrary to increasing strength with smaller fiber diameters, equations 4.19, 4.20, and 4.21 show an increasing ratio of energy release rates. Therefore, if the Dundurs parameters are constant, meaning the same matrix and fibers, the ability to deflect cracks will increase with increasing fiber diameter. Figure 4.43 shows the energy release rates calculated for a composite with fiber volume fractions of 1% and 40%. The calculated graphs, just as with HH, describe the ability to deflect a crack if the composite's cracking stress is below the critical value. The limit for brittle failure changes with FVC, as seen in 4.43. According to the model, an increasing FVC decreases the ability to deflect cracks along the fiber matrix interface.

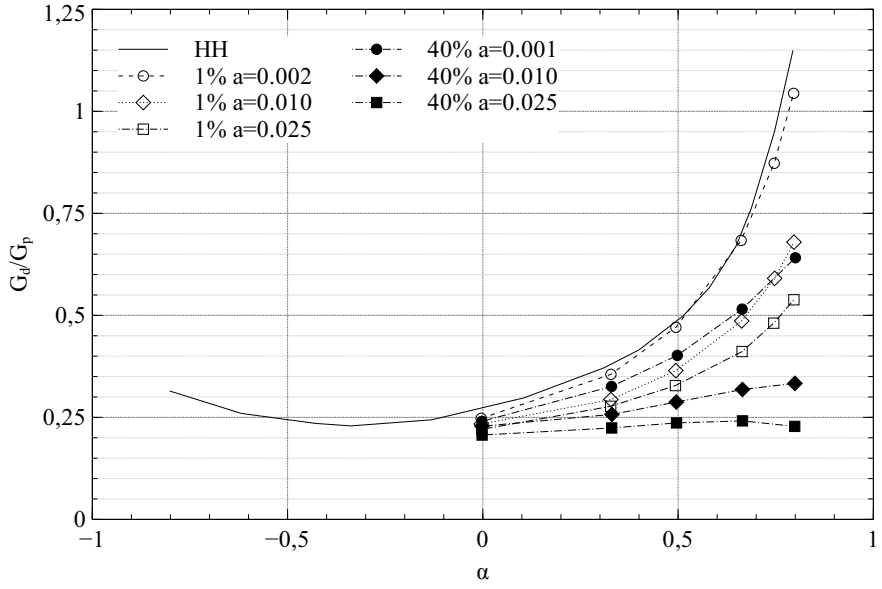

Figure 4.43.: Influence of fiber volume content on energy release rate fraction over the first Dundurs parameter [214]

However, a composite's fracture toughness is not solely based on the deflection mechanisms. W. Curtin [215] describes a theory to predict the pull-out work and ultimate tensile strength of CMCs as function of material properties, including fiber radius and volume fraction. For example, an increasing fiber radius has a positive effect on the work of pull-out, but decreases the ultimate tensile strength. While Ahn et al. [214] showed that the ability to deflect a crack on the fiber matrix interface decreases with fiber volume content, Curtin showed that increasing fiber volume content increases the work of pull-out, which is in agreement with the investigations of Chulya et al. [216]. Chulya et al. distinguished two cases, (1) the single matrix fracture for a strong interface and (2) the multiple matrix fracture for a weak interface, which are essentially divided into brittle and non-brittle failure. Figure 4.44 shows the influences on the critical matrix cracking stress for case (2), decreasing with fiber radius and increasing with fiber volume content.

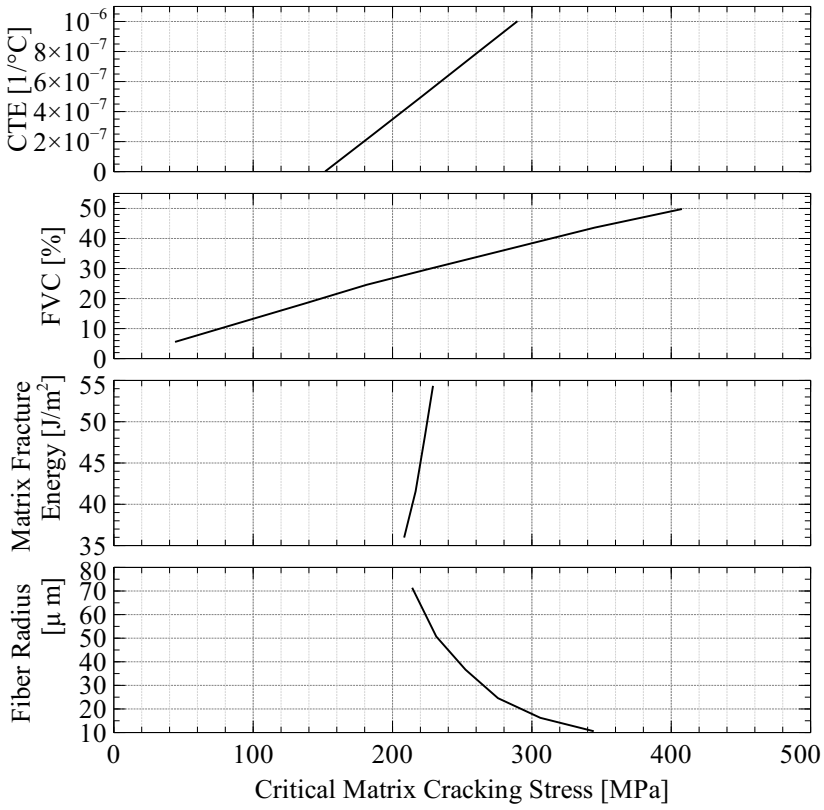

Figure 4.44.: Parametric studies of critical matrix cracking stress for multiple matrix cracking cases [216]

Zoli et al. investigated a carbon fiber reinforced ZrB_2 matrix, comparing various FVCs and slurry preparations [32]. Zoli et al. reported an increase in fracture toughness with increasing fiber volume content and a drop in flexural strength. Due to manufacturing, the composites differ in density and porosity, thereby influencing the stress distribution within the composite and affecting crack deflection mechanisms. The distribution of SiC additions was also reported to have an effect on fracture toughness, which could arise from various moduli

of SiC and ZrB_2. Hu et al. also reported decreasing fracture toughness with decreasing fiber volume content. However, all samples are of different ZrB_2-SiC compositions, porosity, and density [217].

The concept of strong interfaces, proposed by Pompidou et al., has been used to estimate the interface strength of the fiber/matrix bond [218]. Strong fiber/matrix bonds ensure the propagation of cracks along the fiber, and thus, provide a quasi-ductile behavior of the composite. Interface strength was considered when choosing various fiber and matrix combinations for the composite. According to Pompidou et al. [218], stress components perpendicular to the interface result in debonding ahead of the crack tip, followed by crack deflection. A model derived from finite element calculations of stress states at the crack tip in a cell of materials with various Young's moduli was used to assess the interface strength and suggest the best combination from the available candidates. Interface strength (σ_i) can be used to predict the behavior of crack propagation in a composite. Without the interface strength, the curve is used to predict the probability of debonding or deflecting the crack along the fiber. Young's modulus ratio (E_f/E_m) of the components is used to estimate a strength ratio (σ_i/σ_f) of the composite. Using the fiber or coating strength (σ_f), the interface strength (σ_i) can be estimated. It should also be noted that using anisotropic pitch-based fibers will influence the stress distribution within the fiber. This means that these fibers will influence crack deflection, depending on their structure. As seen by Reimer [209], this leads to a debonding within the fiber itself, most likely due to the lower radial modulus of these types of fibers. The influence of TiB_2 coating on crack deflection can be estimated according to these models. When assuming the following values, $E_f = 802GPa$, $E_m = 220GPa$ as measured by Zhang et al. [219], $\nu_f = 0.26$ as measured by Loidl et al. [220], and $\nu_m = 0.22$ measured in chapter 5, the first Dundurs parameter is calculated to be 0.576 according to equation 4.18. This estimates the G_d/G_p fraction to be around 0.55 according to the HH model in figure 4.43. Taking into account the reduction of the fiber modulus due to TiB_2 coating measured in table 5.3, the first Dundurs parameter drops to a value of 0.5. This means the G_d/G_p fraction is also reduced to around 0.5, and hence, the ability of the composite to deflect cracks is reduced.

4.2.4. Melts

The Zr-alloys used for RMI investigations are Zr_2Cu, Zr_2Ag, and pure Zr. Each of these is also investigated using B as a third or second phase to the alloy. Due to the similarity of Zr and Hf, most of the developed methods can also be performed using Hf-alloys and elevated infiltration temperatures. Eutectic compositions, for example, have the same molar compositions for Zr-Cu/Hf-Cu, Zr-Ag/Hf-Ag, and Zr-B/Hf-B. According to literature, Au would also be an interesting candidate with a contact angle of 50° on ZrB_2 [100]. Passerone et al. showed the penetration of Au along the grain boundaries of a ZrB_2 structure, as shown with Cu in section 5.1.2. Due to the high melting temperature of pure Zr and the temperature limit of 1700 °C for most high temperature testing equipment, contact angles and viscosity

were only investigated for Zr-Cu and Zr-Ag alloys. All preform phases, B, B_4C, and SiC, have a sufficient contact angle with each of the Zr-alloys. The details of the contact angle analysis for each combination can be found in section 4.1.

Viscosity of Melts

In addition to contact angles, the viscosity of melts influences infiltration. Figure 4.45 shows the viscosity of Zr_2Cu, Zr_2Cu-1at%B, and Zr_2Ag-1at%B over temperature at shear rates of 10, 25, and 50 1/s. Zr_2Cu, being the only one with no B addition, shows an expected decrease in viscosity when the temperature is increased. Both alloys containing B increase rapidly in viscosity within 100 °K upon melting. All decrease in viscosity with increasing shear rates. Above their melting temperature, Zr_2Cu and Zr_2Cu-1at%B are similar in viscosity. In the range of 1000-1100 °C, Zr_2Cu-1at%B begins to increase in viscosity, while Zr_2Cu begins to decrease in viscosity. Zr_2Ag-1at%B decreases in viscosity until 1350 °C, showing an increase in viscosity at 1400 °C. Experiments were performed with graphite crucibles, which can cause reactions with the liquid Zr or changing the alloy composition to include C. SEM and EDX analyses show a small ZrC layer on the crucible and rod after testing. Microstructures of Zr_2Cu-1at%B and Zr_2Ag-1at%B show scarce ZrB_2 particles as well as Zr-rich phases inside the Zr_2Cu/Zr_2Ag melt after testing. Both melts infiltrate a few *mm* into the carbon crucible and rod. Measurements from Zr_2Cu are more stable with increasing shear rates when compared to Zr_2Cu-1at%B, most likely due to the formation of ZrB_2 particles within the melt. Slightly above melting temperature, at 1027 °C, both alloys have a similar viscosity across the shear rate spectrum. Until 1350 °C, Zr_2Ag-1at%B has the lowest viscosity of the tested melts.

4.3. Composite Manufacturing

The DLR has a long history of RMI using the Liquid Silicon Infiltration (LSI) process. In order to produce a ZrB2 matrix, two aspects must be taken into account. One is to form a porous B-containing preform with a capillary system to be entered by molten alloy. Therefore, a powder-based fabricated slurry was used to infiltrate the fiber bundles. Another aspect is infiltration of Zr-based melts. The three-step process for UHTCMCs manufactured by RMI is shown in fig.4.46.

Each of these manufacturing steps is described in detail in the following sections. Each section further distinguishes between polycarbosilane- and phenolic-based composites.

4.3.1. Preform Manufacturing

The manufacturing process of the preforms is separated into B impregnation and resin curing. Each precursor was mixed with amorphous B powder 95/97 from Tradium and used for impregnation of single C fiber sheets, XN-80 from Nippon Graphite Fiber Corporation. The

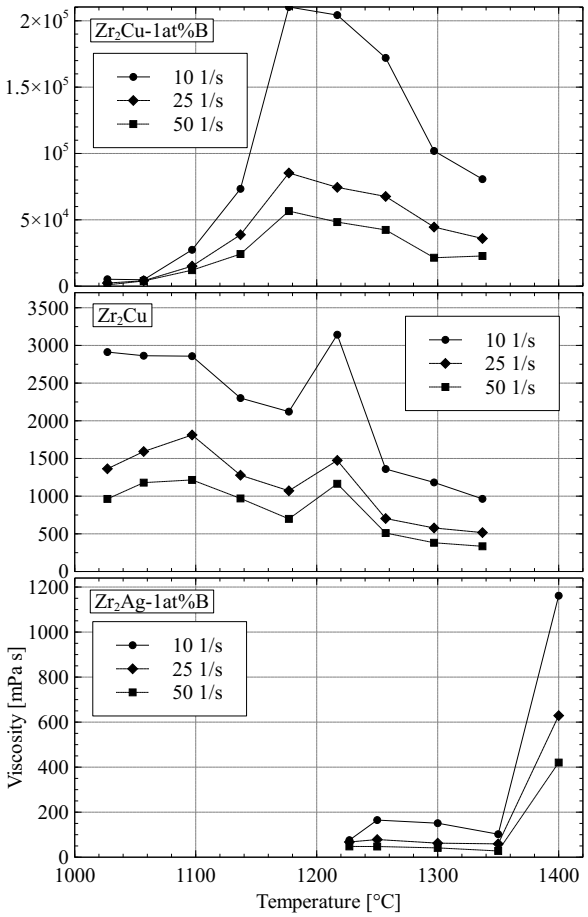

Figure 4.45.: Viscosity as a function of temperature at three different shear rates for various melts

phenolic resin route was fabricated using a mixture of amorphous B powder and ZrB_2 at a volume ratio of 1:1.

Slurry Infiltration

All sheets were impregnated using a foulard from Mathis AG. The powders were mixed with the precursors prior to handling in the foulard. The foulard has two cylinders rotating under a pressure contact. Pressure was initially set to a higher pressure level, 3 bar, to impregnate each fiber sheet. Two successive impregnations were then performed at a lower pressure level, 1 bar, to remove excess resin and ensure homogeneous impregnation. The fiber sheets were stacked into a mold and transferred to warm press or Autoklav for curing. Due to the improved contact angle of SMP-877 compared to phenolic precursors, polycarbosilane was used directly as the liquid phase during impregnation. The B content of the mixtures was set to 70 wt%. H_2O was used as a liquid phase during impregnation for phenolic precursors, with a powder content of the mixtures of 80 wt%. Detailed results for precursor selection can be found in section 4.2.1. The H_2O-impregnated sheets were stacked and dried at 80 °C.

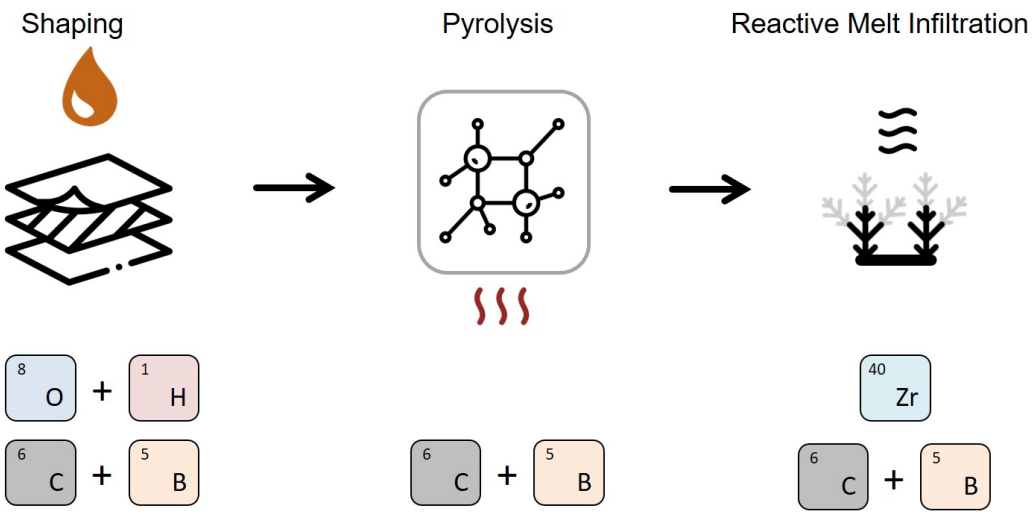

Figure 4.46.: Schematic of RMI process

Resin Infiltration

Polycarbosilane-impregnated stacks were cured within the warm press in a N atmosphere at 300 °C. FVC was set to 30 % by controlling displacement within the warm press. During cross-linking, SMP-877 showed a mass loss, indicating dehydrocoupling in addition to the hydrosilylation. Dried H_2O-impregnated sheets were infiltrated with phenolic resin at room temperature using the vacuum assisted resin infiltration method. After infiltration, the stacks were cured within the Autoklav at 180 °C at a pressure of 10 bar. The pressure of 10 bar ensures an FVC of around 30 %.

4.3.2. Pyrolysis

As mentioned in chapter 2, enabling RMI via capillary forces requires a channel structure or porosity within the samples. The thermal chemical decomposition in an inert atmosphere breaks apart larger molecules, producing volatile species. For most polymers, this is related to mass loss, and therefore, a loss in volume as well. This loss in volume is used to generate the necessary capillary structure.

Pyrolysis of Polycarbosilane

The polymer to ceramic conversion of SMP-877 was studied via TG analysis. Figure 4.47 shows the TG measurement of the polycarbosilane SMP-877 with and without B powder addition. Major mass loss was recorded at temperatures up to 650 °C due to dehydrocoupling. Above 850 °C, no significant mass change was recorded. The B-containing sample was filled with 46 wt% powder. Both measurements showed the same behavior up to around 1250 °C. The sample with the B addition showed a further decrease in mass yield. Calculating from mass fraction and polycarbosilane mass yield without any reaction during pyrolysis, the mass

yield of the 46 wt% sample should be 83 wt%. This mass loss is due to evaporation of the B_2O_3 on the surface of the B powder. Polycarbosilane includes a small amount of C that can react with B_2O_3. The rest of B_2O_3 began to evaporate, which is indicated by the second drop in the TG measurement in the 46 wt% mixture. A detailed research of the pyrolysis process

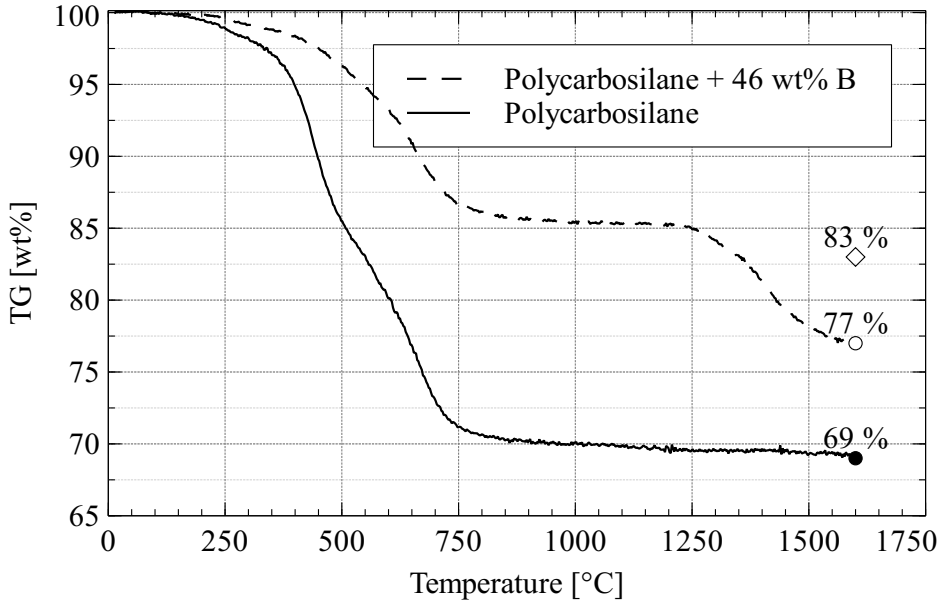

Figure 4.47.: TG analysis of polycarbosilane in Ar atmosphere

and species forming was investigated by Kaur [221] for a similar polycarbosilane, SMP-10. Kaur studied the composition of monolithic SiC derived from SMP-10. As SMP-877, SMP-10 forms near stoichiometric silicon carbide with an excess amount of C. Kaur investigated processing in ambient air to incorporate oxygen within the polycarbosilane to reduce carbon content. At higher temperatures, above 1700 °C, SiC is nearly stoichiometric due to the carbothermal conversion of SiO_2 to SiC. The heat treatment in air slightly increased the oxygen content when compared to a heat treatment in an Ar atmosphere. Release of CO gas during the formation of monolithic SiC increases the porosity. In addition, Kaur describes an increase in pore sizes with increasing pyrolysis temperature. A similar effect is seen for SMP-877, which is discussed later in this chapter.

Pyrolysis of Phenolic Resin

The phenolic resin used in this study is of a novolac type. Their high carbon yield upon thermal decomposition makes them suitable candidates for RMI or any other application in need of high carbon content. Novolac type resins in particular are used in the production of casting molds with a high particle loading [222]. The general decomposition of the phenol-formaldehyde resin is due to bond breaking of aromatic rings and methylene bridges [223]. During pyrolysis, fixed gases are the major products formed, followed by phenol [224]. The temperature gradient between 650-900 °C influenced the quantity of low-volatile ingredients

formed as pyrolysis products [225]. The polymer to C conversion of phenolic resin was studied by TG analysis. Figure 4.48 shows the TG measurement of phenolic with and without a B powder addition. Major mass loss was recorded at temperatures up to 750 °C. Above this temperature, no significant mass change was recorded. The B-containing sample was filled with 46 wt% powder. Both measurements show the same behavior up to around 1350 °C. The sample including the B addition only showed a slight decrease in mass. Calculating from mass fraction and phenolic mass yield without any reaction during pyrolysis, the mass yield of the 46 wt% sample is around 67 wt%. Compared to the polycarbosilane measurement, the phenolic resin yields enough C for B_2O_3 to convert to B_4C. Unlike the measurement of pure B_2O_3 powder and C from pyrolysed phenolic resin in section 4.2.1, the B_2O_3 is trapped inside the phenolic resin on top of the B powder. Therefore, more B_2O_3 reacts with surrounding C and forms B_4C than evaporates.

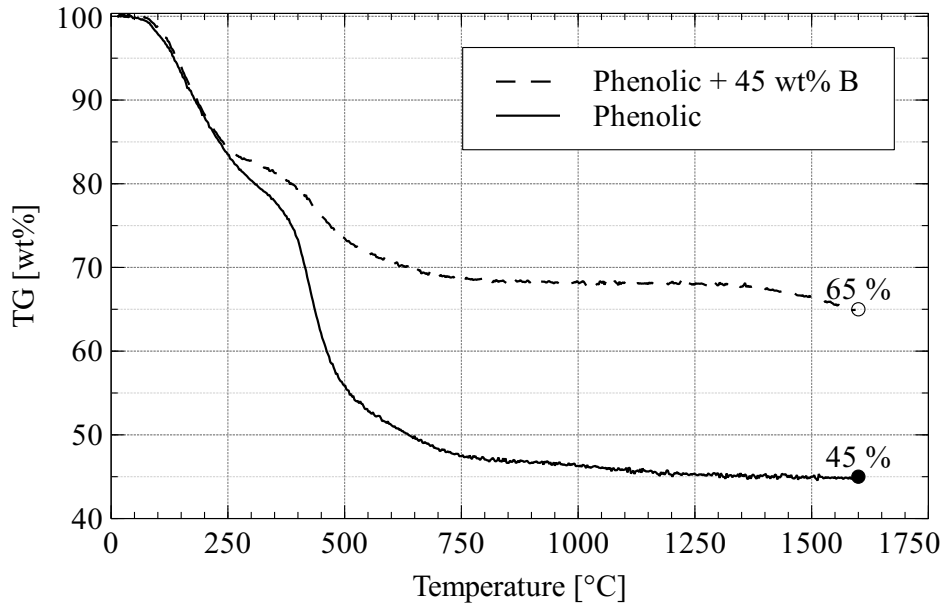

Figure 4.48.: TG analysis of phenolic resin in Ar atmosphere

Pyrolysis of Composites

During pyrolysis, composites behave similarly to the resins used in terms of mass change and phase formation. The major differences are the pore size distributions and mass fractions. The following investigations of composites during pyrolysis were performed with TiB_2-coated XN-80 C fibers and polycarbosilane B slurries or uncoated coated XN-80 C fibers and phenolic B slurries. As described for pyrolysis of pure resins used, the pyrolysis temperature has an influence on the overall porosity as well as pore size distribution of the matrix. Two-dimensional fiber weaves prevent shrinkage of the matrix in the fiber weave plane, and therefore, increase the effect of porosity and pore size distribution change. In general, small cracks form along the fiber pattern contributing to the overall capillary channel structure. Figure 4.49 shows

the influence of pyrolysis temperature on mass loss and porosity of composites manufactured with polycarbosilane and phenolic resins. As described in the sections above, the mass loss of both resins increases with pyrolysis temperature, creating a higher porosity of around 10 vol% for each.

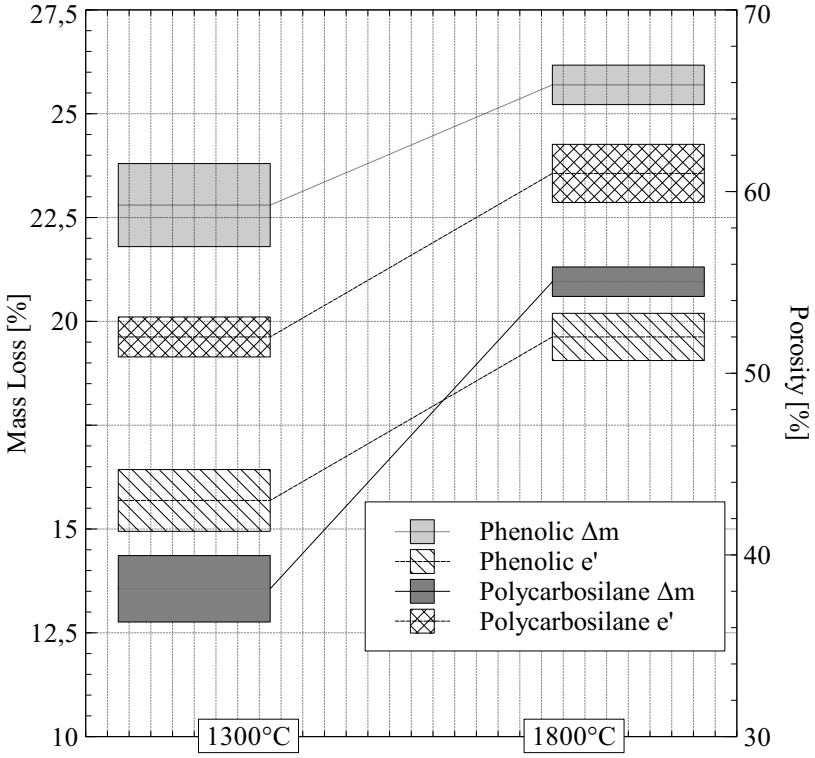

Figure 4.49.: Influence of pyrolysis temperature on mass loss and porosity

Due to the air exposure when drying the impregnated fabric stacks after B slurry impregnation, the B powder forms a B_2O_3 layer on the particle surface. As described in section 4.2.1, carbothermal conversion with B_2O_3 also influences pore size distributions. Figure 4.50 shows the pore size distribution of phenolic and polycarbosilane pyrolysed at 1300 °C and 1800 °C. Both resins exhibit a shift to higher pore diameters, with a larger shift in the phenolic resin. The major effect causing an increase in pore diameter of the polycarbosilane is the carbothermal conversion of SiO_2 to SiC and increased crystallization of SiC, whereas the major effect of the phenolic resin is carbothermal conversion of B_2O_3 to B_4C and increased graphitization. As described in section 4.2.1, phenolic-based samples form a much wider pore size distribution band at larger pore diameters when forming B_4C. Pyrolysis at 1300 °C is not sufficient to initiate the reaction of B_2O_3 to B_4C, resulting in a small pore size distribution at pore diameters below 100 nm. Polycarbosilane samples show a much larger pore size distribution band at 1300 °C even with pyrolysis, slightly increasing in diameters when pyrolysed at 1800 °C.

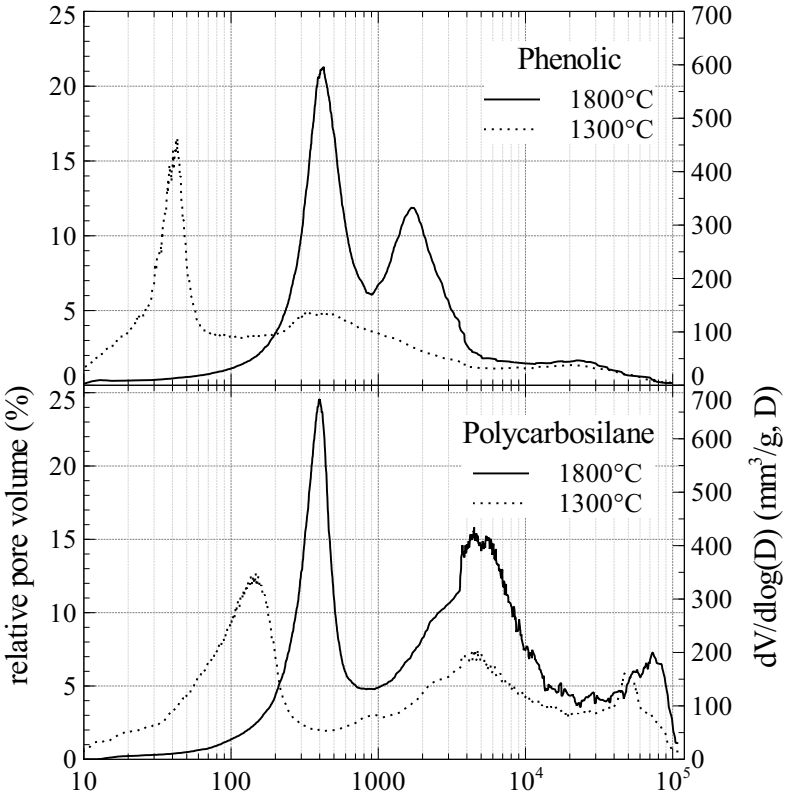

Figure 4.50.: Influence of pyrolysis temperature on pore size distribution

4.3.3. Boron Oxide Infiltration

In order to increase the B content and enhance wetting behavior, phenolic-based samples are treated with B_2O_3. As described in section 4.2.1, higher temperatures promote B_4C formation. Therefore, the composites containing C fibers, phenolic resin, and B powder were covered with B_2O_3 powder and heated in an Ar atmosphere to 1800 °C. The amount of B_2O_3 used for this infiltration was calculated assuming a stoichiometric formation of B_4C via the carbothermal conversion. The amount of C was calculated from the content of phenolic resin within the samples and its C yield upon pyrolysis.

The channel structure forming upon pyrolysis distributes B_2O_3 inside the composite structure. Without the protective coating of the C fibers, they are converted into B_4C. This means a severe decrease of fiber strength in areas where channels are close to the fibers. This effect can be minimized by B_2O_3 additions prior to phenolic infiltration, as described in section 4.1. Enclosing the B_2O_3 within the C formed from the phenolic resin, for example using oxidized B powder, the B_4C is formed using the pyrolysed C before reaching C fibers. Figure 4.52 shows the mass loss during pyrolysis at 1800 °C and the resulting overall porosity of a powder mixture of 50 vol.% B and 50 vol.% ZrB_2. Due to the high density of ZrB_2 powder, wt.% changes in comparison to pure B powder pyrolysis. Two powder loading compositions inside the phenolic resin were used, 30 and 80 wt.%. Due to the higher amount of powder inside the

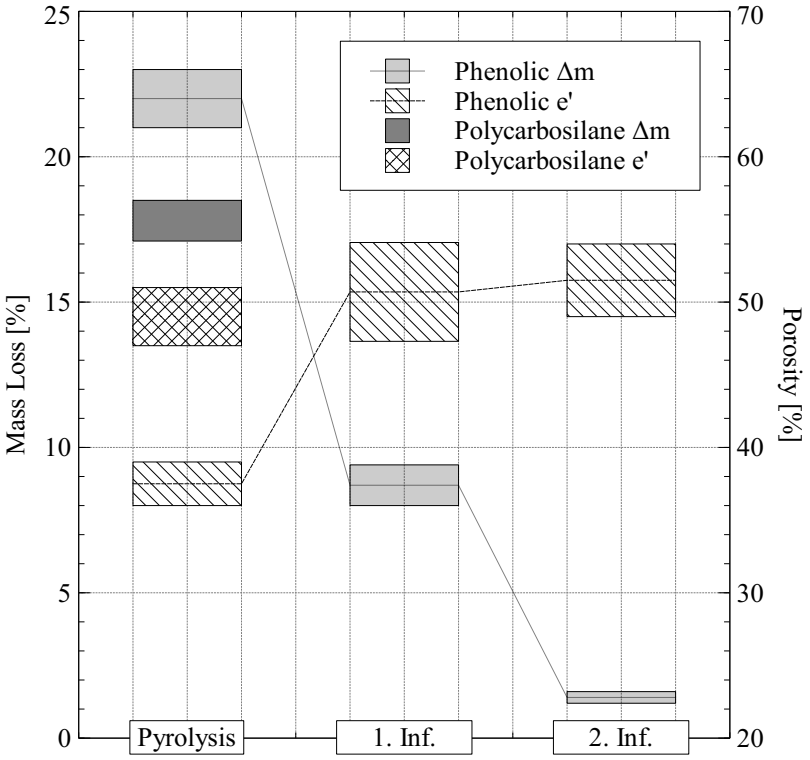

Figure 4.51.: Influence of B_2O_3 infiltration on mass loss and porosity

preform, mass loss decreasd with increasing powder loading. Water was used as a dispersion for the third slurry combination in figure 4.52. The single fabrics were impregnated with an 80 wt.% 50 vol.% B and 50 vol.% ZrB_2 powder mixture and BYK-7420ES as the stabilizer before drying at 90 °C in order to keep a tetraboric acid layer surrounding the B particles. Due to the high stability of water-based slurries, powder impregnation is much more effective. The greater amount of powder inside the preform decreases overall porosity after pyrolysis. Due to the formation of boron acid, a result of the reaction of water treatment and B powder and its dehydration upon reaching 300 °C during pyroylsis, the mass loss is much higher for water-based impregnation.

4.3.4. Reactive Melt Infiltration

RMI utilizes capillary force to initiate and sustain a flow of liquid metal into a fiber-reinforced preform. As described in section 2, this mechanism is controlled by viscosity, density, contact angle, surface tension, and pore diameter. Due to the reaction occurring between the preform elements and melt, the geometry of the pore structure changes. In the case of Zr and B, the pore volume decreases when a smaller B amount forms ZrB_2, which is higher in molar volume. In addition, the exothermic reaction induces a large increase in temperature, which changes the viscosity, density, contact angle, and surface tension of the molten metal. Most of these

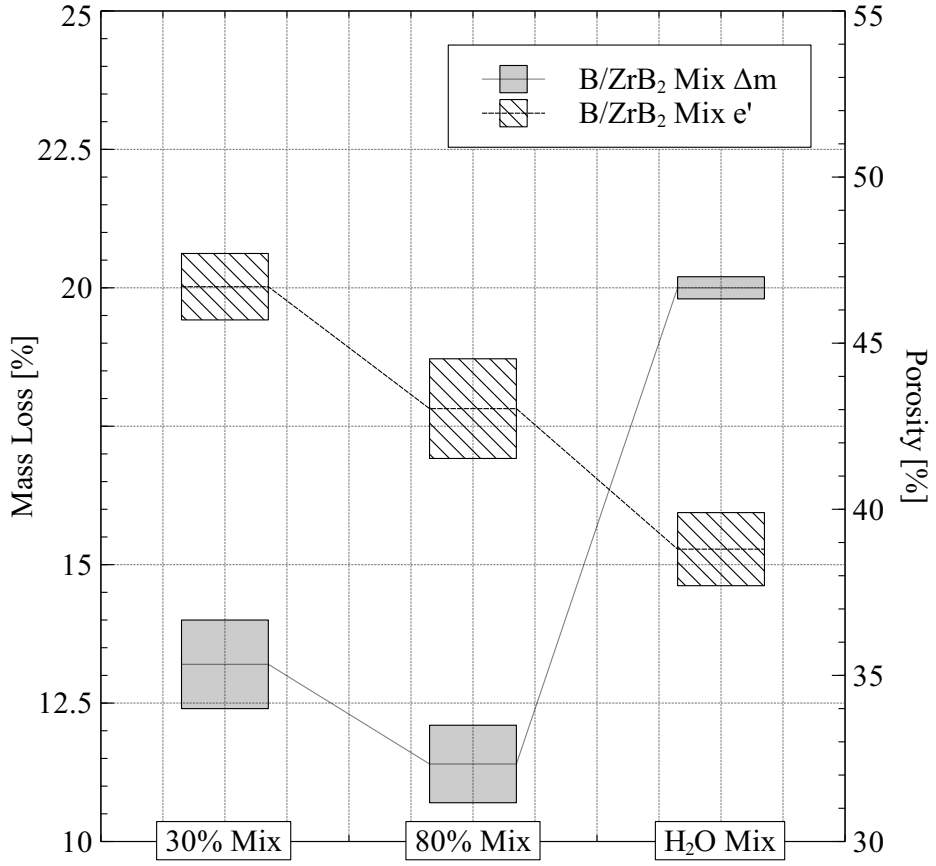

Figure 4.52.: Mass change during pyrolysis and porosity of pure B slurry and B/ZrB_2 mixture

values become more favorable for the infiltration process with the exception of the increase in volume, which could result in choking the capillary flow. Phases involved during infiltration also change, especially within the infiltration zone. Pore walls change from B with phases to ZrB_2, again, influencing RMI parameters. Compared to single-phase infiltration like LSI, In this study, Zr infiltration utilized a Zr alloy in contrast to a single-phase infiltration like LSI. These alloys also change in composition during the different stages of RMI. In the case of Zr_2Cu alloy, the infiltration zone depletes in Zr, forming a Cu-rich front. The investigation of these phases has already been described in chapter 4.1, while the influence on RMI and manufacturing parameters is discussed in this section.

Equipment

In order to influence the temperature of the initial reaction during infiltration, the melt and sample must be heated separately. Conventional high temperature furnaces, as used for LSI, heat the melt and sample in the same crucible. Once the alloy begins to melt, the infiltration process is initialized. The temperature can still be increased over the initial start of the infiltration. However, due to the rapid infiltration time compared to furnace heating

rates, the increase in temperature is comparable to an annealing process. A separated setup provides two advantages over a conventional furnace. First, no non-adherent layer is required due to the separate cool-down period of the melt and sample. Second, the actual infiltration temperature is controlled. A schematic of the lifting setup is displayed in figure 4.53.

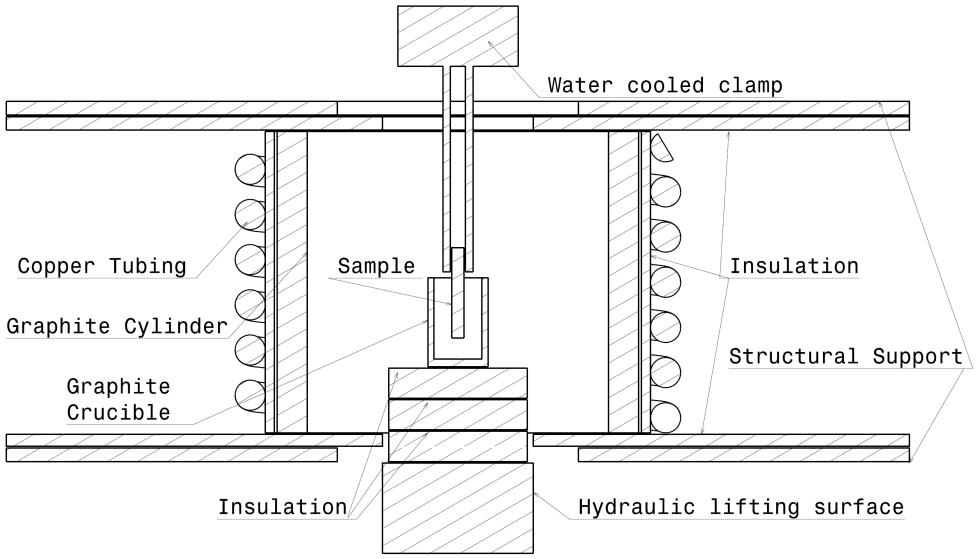

Figure 4.53.: Schematics of lifting mechanism used for RMI

The modified version of the experimental furnace uses a principle similar to the displayed system. The major differences are larger crucibles, better atmosphere and pressure control, and movement of the sample rather than the crucible. Without the lifting mechanism, an adherent layer is crucial to keep the samples from bonding to the crucibles. Monolithic diborides react the least with a Zr-based alloy, however, contact angles are rather low, as shown in section 4.1. Due to the thermal stability and the high contact angles, dense carbon crucibles or graphite layers achieve a sufficient separation without using large amounts of excess melt. Diboride crucibles with a glassy carbon separation layer would be the most favorable setup.

Simulation of RMI

As described in section 2.1.5, the infiltration height of a liquid within a capillary system can be calculated. The differential equation 2.4 describes this process. This equation does not incorporate factors such as chemical reactions, transverse capillaries, or limitation of capillary velocity. As Gern describes in his work [93], the differential equation of the simplified system

can be adopted. As stated by Gern, the differential equation describing the realistic system, including transverse capillaries and limitation of capillary velocity, is as follows:

$$\rho v_w^2 \cdot \ddot{h}h + 1.16\rho v_w^2 \cdot \dot{h}^2 + \frac{8\eta v_w^2}{d_k^2} \cdot \dot{h}h + \rho g \cdot h - \frac{2\sigma cos\Theta}{d_k} + 106\frac{e'_B\eta}{e'_D\overline{D_m}^2}v_w\Delta l_D \cdot \dot{h} = 0. \quad (4.22)$$

As partially described in section 2.1.5, ρ is the density of the liquid melt, v_w the distortion factor, h the infiltration height, η the dynamic viscosity of the melt, d_k the capillary diameter, σ the surface tension of the melt, Θ the contact angle of melt and capillary, e'_B the porosity of the sample, e'_D the porosity of the choke, $\overline{D_m}$ the mean choke pore diameter, and Δl_D the length of the choke. A mathematical description of these dynamic processes results in extensive systems of time-dependent differential equations. Depending on the type and complexity of these problems, they contain linear or nonlinear terms. In order to solve these systems as described in equation 4.22, a Python [226] script was implemented using a SciPy function [227] and Matplotlib visualization [228]. Gern discussed this in detail for a Si infiltration process in which the physical values of the melt and preform change for Zr infiltration. Apart from these values, the increase in volume due to the chemical reaction of Zr, B, and C changes the infiltration behavior as discussed in section 4.1. Gern proposed a choke to account for a porous media feeding the Si during infiltration. The terms used to limit the infiltration velocity can also be adopted to serve as a choke arising from the reduction of pore channels due to the volume expansion from the chemical reaction. Depending on the pore channel shape, this volume expansion reduces the pore diameter by more than half. In order to determine the influence of different physical values, their influence on infiltration height was analyzed separately from each other, using the following values as a baseline: The values for surface tension and density were calculated from Zr and Cu values found in

Table 4.9.: Baseline physical values for calculation of infiltration height

$\rho = 6\frac{g}{cm^3}$	$\Theta = 10°$
$v_w = 1.35$	$e'_B = 45\%$
$\eta = 0.2Pa \cdot s$	$e'_D = 17\%$
$\sigma = 1.2\frac{N}{m}$	$\overline{D_m} = 15\mu m$
$\Delta l_D = 7mm$	

literature [229–231]. The values for Zr_2Cu alloy were determined by a simple rule of mixture, and the influence of these values will be discussed in more detail in this section.

This baseline calculation uses Gern's choke factors from his calculations for Si infiltration. From figure 4.54, it can be seen that the infiltration heights are much smaller than those of Si infiltration, and the highest values are reached for a pore size of less than 10 μm comparatively. Large pore channels, according to simulation, do not reach above 2 cm in height. Due to the volume expansion during RMI, smaller pores are more likely to be blocked. According to calculations, a high overall porosity consisting only of extremely small pores, smaller than 10 μm, would achieve the highest level of infiltration. Large pores are necessary

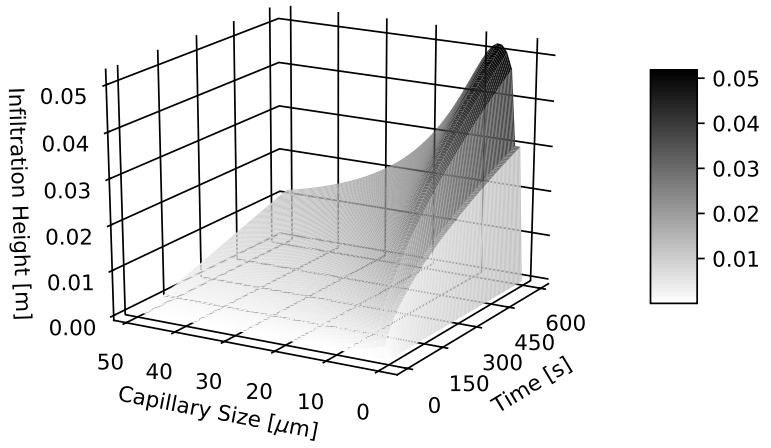

Figure 4.54.: Calculated infiltration height for baseline values

for the manufactured samples in order to continue feeding the already reacted composite into the infiltration zone trough. The simulated infiltration height continues to increase until it eventually reaches h_{max}. From experiments, increasing infiltration time over $10min$ results in a severe degradation of the fiber coating or C fibers. In addition, the difference in infiltration height for different pore diameters decreases as the infiltration speed slows over time. Figure 4.55 shows the evolution of the infiltration height when reaching 10,000 and 100,000 seconds. In order to further increase the degree of infiltration, the melt and preform

a) b)

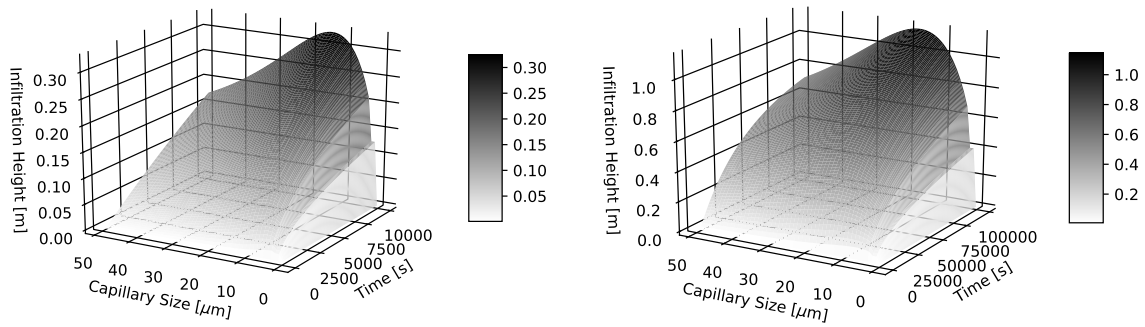

Figure 4.55.: Simulated infiltration height after a) 10,000 sec. and b) 100,000 sec.

phases can be adopted to control melt density, viscosity, and contact angle between the melt and preform, and surface tension. Due to the trigonometric $cos()$ behavior of the contact angle, the infiltration height is significantly influenced when approaching 90°, and is affected much less with smaller angles <30°, as shown in figure 4.56 for 1° and 70° angles. It is

a) b)

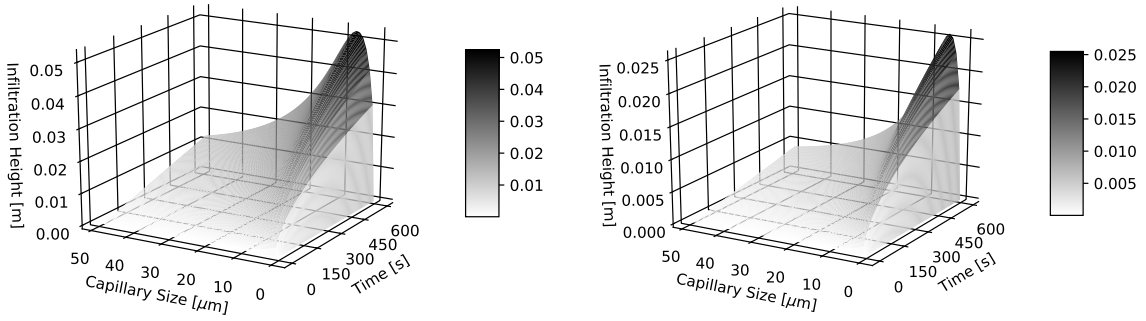

Figure 4.56.: Simulated infiltration height with contact angle of a) 1° and b) 70°

essential to reduce contact angles below approximately 30°, especially below 90°, to initiate infiltration. However, to further improve infiltration height, surface tension and viscosity are of higher sensitivity. Changing surface tension by a factor of 10 is shown in figure 4.57. Changing the viscosity of the melt by the same factor has a similar influence on infiltration

a) b)

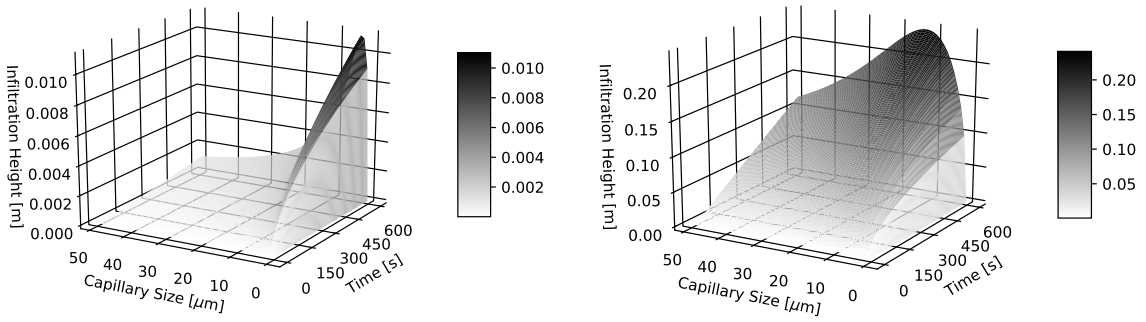

Figure 4.57.: Simulated infiltration height with a surface tension of a) 0.12 and b) 12 $\frac{N}{m}$

height, see figure 4.58. In order to further improve infiltration height, surface tension must be increased while decreasing viscosity.

Using the choke diameter to account for a decrease in pore diameter due to the chemical reaction influences infiltration height and infiltration height distribution for each open capillary diameter. If diameters decrease too much after the chemical reaction, infiltration height decreases dramatically. Increasing the choke diameter will shift maximum infiltration height beyond the displayed capillary diameters. In general, diameters of the same size as the choke diameter have the largest infiltration height, which is caused by the decrease in infiltration speed of larger pores and blockage of smaller pores. Figure 4.59 shows the influence of a choke diameter from 1.5 and 150 μm.

a) b)

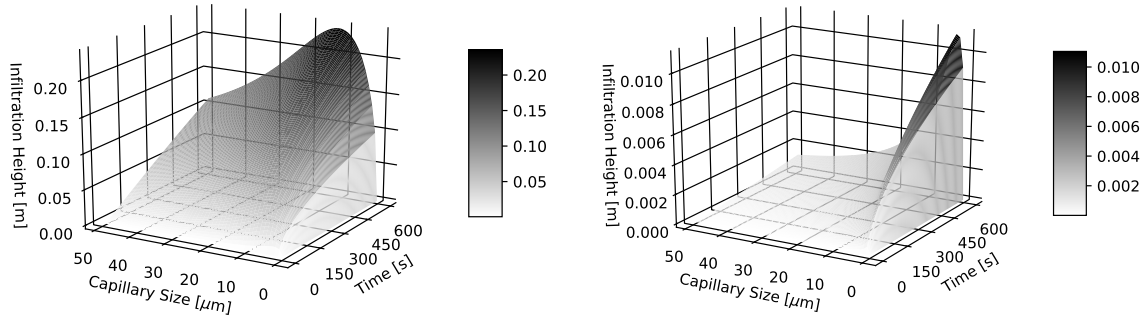

Figure 4.58.: Simulated infiltration height with melt viscosity of a) 0.02 and b) 2 $Pa \cdot s$

a) b)

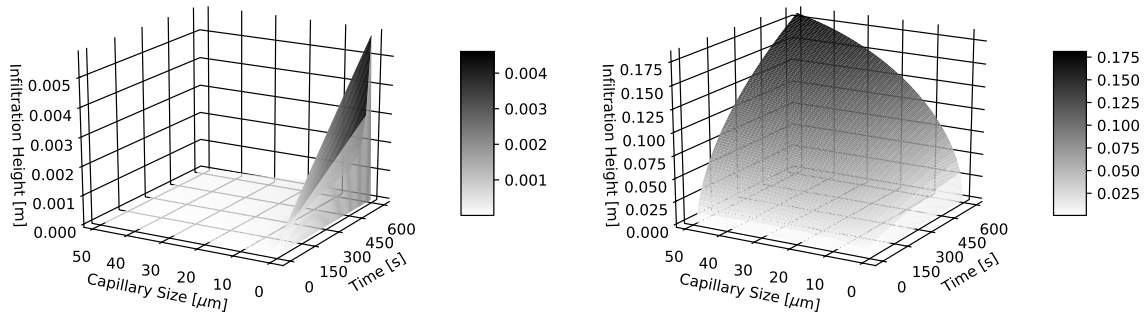

Figure 4.59.: Simulated infiltration height with a choke diameter of a) 1.5 and b) 150 μm

The overall porosity of samples has a minor effect on the infiltration height and the pore diameter distribution. However, this arises via a theoretically continuous distribution of pore diameters in combination with the choke diameter used to account for the chemical reaction. In reality, the overall porosity is influenced by the distribution and the amount of pores present in the samples. If the pore diameter or overall porosity becomes too small, the infiltration process is choked due to the sealing of pores by volume expansion.

Degree of Infiltration

This section describes how deep a composition can be infiltrated with molten metals. As most samples are lowered from above into a crucible of molten metal, this is also referred to as infiltration height. Due to the two dimensional fiber reinforcements, the capillary system formed during pyrolysis is different in and out of the fiber plain. It is significantly controlled by shrinkage and prevention of shrinkage due to fibers, resulting in a higher crack-like pore structure within the fiber plain. Therefore, there is a distinction in infiltration height along the fiber plain and infiltration depth, perpendicular to the fiber plain, within this study.

Both melt and preform composition influence the degree of infiltration. Within this study, preforms manufactured from polycarbosilane and phenolic-based resins are investigated. The Zr alloys investigated are as follows:

- Zr_2Cu,
- Zr_2Cu 1 at% B,
- Zr_2Ag,
- Zr_2Ag 1 at% B, and
- Zr_9B.

The viscosity of the molten alloys influences infiltration time and degree, measured for some of the melts in section 4.2.4. Viscosity also influences the retention of the liquid melts in larger pore structures forming within the samples. If viscosity is very low, as is the case in Zr_2Ag alloys, no melt is drained during cool-down in larger pore structures. As described in section 4.3, the pyrolysis temperature also influences pore size distribution, and hence, the degree of infiltration. Due to the volume expansion involved during ceramic formation, the pore structures must be large enough without being blocked by the ceramic forming within the channel structure. As described in section 4.1, ZrC, formed from C and Zr, has the highest volume expansion, followed by ZrB_2, formed from B and Zr, and ZrC, formed from SiC and Zr. Due to different phases within the preforms of polycarbosilane or phenolic-based samples, the degree of infiltration changes depending on the preform-melt combination. The addition of Si in particular changes the phases forming at a low infiltration temperature when using poycarbosilane. In the case of SiC, the formation of ZrC is very favorable due to low volume expansion. However, Zirconium-Silicates are formed at low temperature infiltration, causing an extreme expansion of the preform, see 4.1. The major process parameters influencing the degree of infiltration are atmosphere, pressure, infiltration temperature, and infiltration time.

Infiltration Time As described by equation 2.5, the time necessary for the molten alloys to infiltrate a certain height can be calculated. This equation does not incorporate factors caused by the chemical reaction of melt and channel structure. The volume expansion of ZrC formations in particular influence the pore structure. If the preform matrix structure is strong enough to retain the sample thickness, the volume expansion will choke infiltration, whereas a weak preform matrix, not able to retain sample thickness, will allow the entire sample to expand, and hence, increase the pore channel structure between them. When submerging the samples, 5 mins are sufficient to fully infiltrate 80 x 50 x 5 mm samples with Zr_2Cu 1 at%B.

Reducing Cu Phases and Porosity

Zr-Cu alloys form residual Cu phases within the non-reacted melt inside the pore channels as well as along the grain boundaries between UHTC phases. While it is very difficult to influence the grain boundaries through post-treatment, the residual melt or Cu phases can be depleted. Infiltrated UHTCMC samples can be post-treated in W-granules in order to reduce Cu phases due to the low contact angles of W and Cu and the high contact angle

at low temperature (still above melting point) of Cu and ZrB_2. Both Samsonov et al. [28] and the contact angle measurements in this study show the high contact angle of Cu at low temperatures before decreasing at around 1150 °C. As described by Caccia et al. [232], depletion of the Zr_2Cu via WC in order to form a ZrC/W metal composite, SiC, or B_4C is used in this study to form the ceramic matrix forcing out the liquid Cu phases due to the volume expansion. Figure 4.60 shows the expelled Cu phases on top of a UHTCMC sample annealed at 1000 °C for 2 minutes. According to EDX measurements, the drops forming in the annealed section are Cu-rich Cu-Zr phases. In the center of the annealed sample, larger drops form at the surface of the sample, while off-center small Cu phase drops start to appear at large magnifications with lower temperatures between 500-900 °C. At higher temperatures and higher Cu phase volumes, the small drops aggregate and form large drops. After the initial metal infiltration, the residual porosity can be used to infiltrate additional

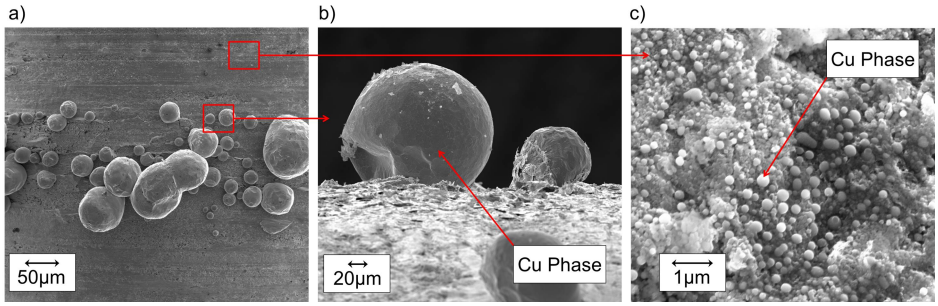

Figure 4.60.: Cu segregation on annealing UHTCMC sample; a) heated middle section of the sample, b) Cu droplet, and c) small Cu drops forming at lower temperatures off-center on sample

active reactants, such as B or C, in order to further decrease porosity and Cu content upon heating. The infiltrated B or C additions will react with the residual melt inside the composite to form ZrC or ZrB_2 respectively.

4.4. Discussion of Manufacturing

In order to put all the different factors influencing RMI into context, their influence on each other and the influence on manufacturing samples will be discussed. The necessary overall porosity depends on the elements present in the preform, which are B, C, and SiC. The porosity is influenced by the ceramic yield of the precursors and their pyrolysis temperature. In order to minimize non-reacted phases, either from melt or preform, the composition should be as close to stoichiometric as possible. As simulations suggest, see section 4.3.4, the capillaries forming during pyrolysis should be smaller than 10 μm. However, reaching a matrix porosity of over 50% with such small channels is very difficult, and the possibility of blocking the infiltration due to the expansion of the bulk material between two pore channels is very high. Furthermore, the channel structure is influenced by the volume expansion of various phases as well as the ability of the precursor to maintain its adhesion to the fiber structure.

If the expansion is large enough, it will delaminate the sample and induce large crack-like pore channels. These effects must be counteracted by the correct porosity distribution within the preform, otherwise these effects will cause cracks, which will be filled with residual melt, and due to the reaction with fibers generate high ceramic contents. In practice, using a wide spread spectra of pore channels shows the best results regarding the homogeneity of infiltration. Using a polycarbosilane and boron powder slurry as a preform matrix, the pore structure formed during pyrolysis has this wide spread spectra of pore channels without any further treatment. This is true as long as the volume expansion does not exceed a factor of 1.5, which is the case for any Si-based precursors due to the volume expansion of Zr-Si phases. To avoid this expansion, the infiltration temperature must be raised above 1500 °C. The increased infiltration temperature causes fiber degradation and must be dealt with using a fiber coating. The coating protects the carbon fibers from the aggressive melt. A different approach is to avoid Si and use a slurry containing only C with B powder. Due to the high contact angle of C and Zr melts, this approach requires an additional transformation of the preform matrix. In this case, B_2O_3 can be used as an additional reactive infiltration to generate a porous B_4C preform matrix. Similar to the polycarbosilane route, this leads to a wide spectra of pore channels and a ZrB_2-ZrC matrix. The contact angle of B_4C also favors infiltration at temperatures as low as 1200 °C. The B_4C preform requires a much higher overall porosity due to the volume expansion of ZrC from C. This is easily accounted for due to the mass and volume loss of C-O species during B_2O_3 infiltration of the C preform. Without the volume expansion from Si, this process allows for the reduction of the Zr alloy infiltration temperature. The B_2O_3 treatment also requires fiber protection in order to prevent the fibers from reacting to B_4C. The distribution of B_2O_3 is important to avoid fiber degradation and to dispense the necessity of a fiber coating. This requires B_2O_3 to be dispersed prior to pyrolysis within the C-matrix. Achieving such a distribution is most easily done using an oxide layer on the boron particles, which must be dispersed inside the resin prior to fiber impregnation anyways. To further reduce the infiltration temperature, the infiltrating alloy must be adopted to reduce the contact angle while retaining an adequate viscosity. These effects are described in more detail in section 4.3.4. The final effect to allow for a process without any fiber protection is energy dissipation into passive phases during RMI. These can be phases within the preform as well as phases within the melt alloy. For ZrB_2-based UHTCMCs using a Zr_2Cu alloy, these two phases are ZrB_2 powder within the slurry and residual Cu expelled during RMI. The combination of all these effects reduces the reaction of melt and carbon fibers to a degree of minimal fiber degradation low enough to manufacture a composite without fiber coating.

Figure 4.61 shows a schematic of the phases forming during the infiltration of a capillary inside a B preform. As the Zr_2Cu enters the capillary and passes the already reacted ZrB_2, the Cu content increases by the amount reacting with the B diffusing from the bulk B to the liquid Zr_2Cu, forming an additional ZrB_2 layer on top of the ZrB_2 from the liquid-solid reaction. Most of the Zr is depleted at the reaction zone of Zr_2Cu and B, resulting in a

Cu rich Cu-Zr alloy upward of the reaction zone. This Cu-Zr alloy essentially also reacts with the B wall, however the Zr content could be too low to react or the length from the main reaction zone can be imagined considerably small. As the temperature decreases from the reaction zone upward and the high contact angle increases with Cu content, the Cu-Zr alloy forms a concave meniscus with the B preform. The temperature decreases up- and downward of the reaction zone, while the Cu content is increasing along the capillary. The

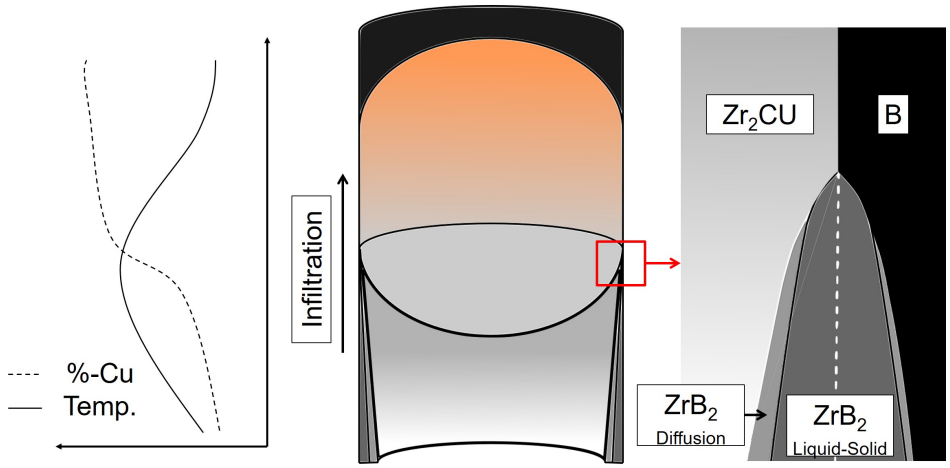

Figure 4.61.: Schematic infiltration process of Zr_2Cu entering a capillary within a B preform

major phase to control when manufacturing a diboride-based matrix system by RMI is B. In order to generate an interconnected diboride matrix, an active B phase is necessary. While the necessary ceramic yield of any B precursor would be sufficient due to volume expansion during melt infiltration, either B content is too low or the available quantities are too small. Amorphous B powder is available in large quantities at much lower prices and without any special handling due to H_2O or O_2 sensitivity. Two precursor variations were used for the slurry preparation. One route, using polycarbosilane, includes a Si phase in the UHTCMC. The other, using phenolic resin, requires an additional B_2O_3 treatment. Both of these preforms require a two-stage impregnation cycle using the foulard. Relying on the fiber crack deflection mechanisms to increase fracture toughness of the UHTCMC, fibers inside the composite must retain their strength up to the application temperatures of UHTCMCs. The chosen commercially available fibers which retain their ultra high temperature strength are C fibers. The SiC fibers decrease in strength at temperatures above 2000 °C, and fibers such as TaC, HfC, and HfB_2 are not yet available. Due to their large diameter and high temperature strength, XN-80 fibers manufactured by Nippon Graphite Fiber Corporation were used for the UHTCMC fabrication. As with most pitch-based C fibers, they exhibit a layered C structure necessary for achieving a damage-tolerant behavior. The unidirectional fabrics are impregnated with a slurry, using amorphous B powder from Tradium with an average particle size of 2 μm. In addition to passive elements inside the B slurry, the melt itself can be used to include additional phases inside the matrix. These can either influence the formation of oxide layers or influence the mechanical characteristics of the matrix. In addition to Zr,

the phases included inside the melt alloy can influence the degree of infiltration. Since they influence factors such as viscosity, surface tension, and contact angle, they are described in theory in section 4.3.4. Due to their influence on melt temperature, the alloy phases also influence the degree of fiber degradation. The most interesting melts due to their viscosity and contact angle are Zr_2Cu with a B addition and Zr_9B. Zr_2Cu has the advantage of a lower viscosity, while Zr_9B does not include any Cu phases into the grain boundary of the UHTC matrix. In addition, these alloys can be extended by Y additions to influence the oxide layer forming at UHT. Passive phases used during manufacturing are the TiB_2 fiber coating for the polycarbosilane route and ZrB_2 Grade A powder from H.C. Stark for the phenolic route. As most additions to a bulk ZrB_2 negatively influence properties like ultra high temperature strength and conductivity, any addition, except other UHTC's like HfB_2, should be kept to a minimal. Especially when they concentrate at the grain boundaries, like Cu and Si.
As described in this work, two different variations of C_f/ZrB_2 UHTCMCs were investigated. The first utilized a TiB_2 coating to protect the C_f during RMI, using a polycarbosilane precursor which results in a $C_{f\text{-}TiB2}/ZrB_2$-ZrC composite. The second relinquishes the fiber coating and transforms a C-containing preform with B_2O_3 into B_4C, resulting in a C_f/ZrB_2-ZrC composite with a smaller amount of ZrC than the fiber-coated method. Impregnation of the fibers is best achieved by using a chalender. The difference in impregnation for coated and non-coated fibers is the addition of ZrB_2 powder and slurry stabilization for the non-coated version. In addition, the non-coated version needs the B_2O_3 treatment, which requires an addition of B_2O_3 powder or oxidation of the B powder inside the slurry as described in section 4.3. While the polycarbosilane only needs a pyrolysis temperature of 1300 °C to form SiC, the non-coated version needs a pyrolysis temperature of 1800 °C in order to form B_4C from C and B_2O_3. The opposite is true for infiltration temperature of the melts between coated and non-coated preforms. The SiC present in the TiB_2-coated samples prevents a reduction in the infiltration temperature due to the formation of Zr-Si phases and their large volume expansion. Without the SiC, as is possible with non-coated samples, the infiltration temperature can be reduced close to the melting point of each alloy. Figure 4.62 demonstrates the two methods of reducing fiber degradation. Image a) shows the almost complete reaction to ZrC of an uncoated fiber without adapting the process parameters. Image b) shows the same carbon fiber with almost no degradation due to a process adaption using phenolic resin and image c) shows a TiB_2 carbon fiber manufacture according to the process of carbon fiber from image a).

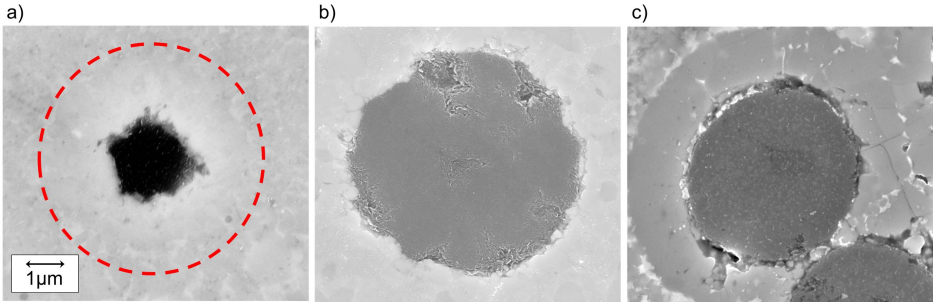

Figure 4.62.: Degradation of carbon fiber a) with plain carbon fibers, b) with adapted RMI process, and c) with TiB_2 fiber coating

5. UHTCMC Characterization

This chapter analyzes the structure and properties of RMI fabricated UHTCMCs. The different phases and compositions of the micro structure were investigated. These results were used to determine their effects on mechanical properties and oxidation. A large variety of mechanical tests were conducted for UHTCMC without fiber coating and phenolic fabrication rout. Both key characteristics, damage tolerance and oxidation resistance, were examined with these type of UHTCMCs. In addition, fiber coated samples using the polycarbosilane route were compared using bending strength and oxidation resistance. Fiber coated samples were also used to determine the influence of various Zr alloy compositions on mechanical strength. Fabrication parameters, such as slurry impregnation, pyrolysis and infiltration time, were kept identical for each investigation. The only variation of infiltration temperature within one set of samples was Zr_9B alloy. Due to its high melting point, infiltration temperature must be increased.
The following sections give an overview of advantages and disadvantages for the variations of manufacturing parameters. Depending on the application requirements, different fabrication routes can be chosen to improve material performance. The investigated routs were given a set of variations to adapt the material's composition.

5.1. Micro Structure

The micro structure discussed in these sections will help the reader understand the influence of different process variations as well as determine a correlation between microstructural effects and mechanical properties. While the influences of various parameters during manufacturing has already been discussed in chapter 4, this section will investigate the RMI micro structure of various UHTCs and UHTCMCs.

5.1.1. Fibers

As mentioned in section 4.2.2, high temperature stable C fibers are preferred for UHT applications. During the process development of RMI, various fibers and fiber coatings were investigated. Some of these results are further discussed in this section to determine their influence for various applications. The investigated fibers discussed in the following section are as follows:

- SiC_f,

- C_f uncoated, and
- C_f with TiB_2 coating.

The following investigations show the influence on each fiber type, all of which are based on a Zr_2Cu melt infiltration. The main influence on the composite properties is degradation of the fibers caused by the reaction with Zr_2Cu. The degradation can be influenced by protecting the fiber with a coating capable of withstanding the RMI or by adapting the process parameters to decrease the reaction of the melt and fiber to a minimum. SiC and C fibers were both converted to ZrC if they were not protected. Figures 5.1 a) and b) show the degradation from the original fiber diameter, marked in red. As described in section 4.3.4, infiltration time, temperature, and melt composition have a large influence on fiber degradation. Figure 5.1 shows the same fiber type fabricated with identical preform methods, in b) infiltrated at 1500 °C for 5 mins and in d) infiltrated at 1200 °C for 5 min. The fiber shown in figure c) was infiltrated at 1500 °C for 5 mins using a protective TiB_2 fiber coating. The process parameters, and therefore the degree of fiber degradation, must be balanced with the degree of infiltration necessary to achieve a sufficient infiltration and formation of UHTC phases.

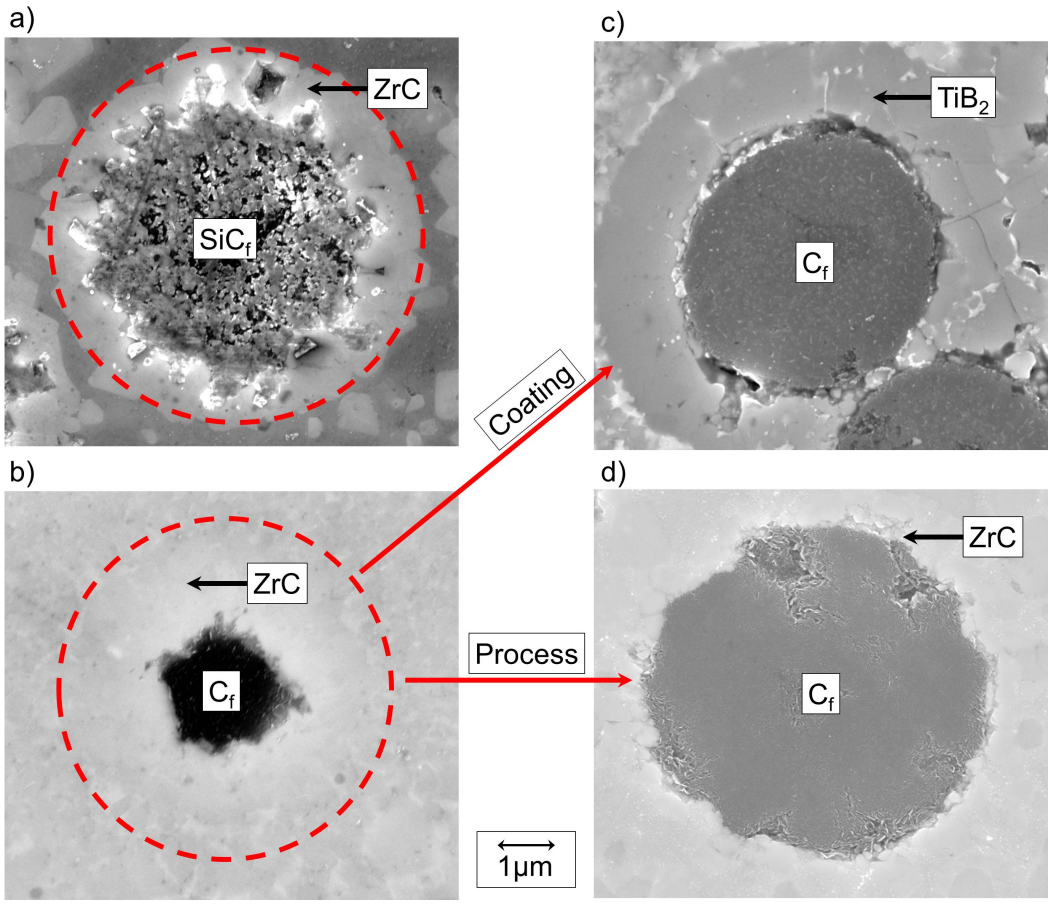

Figure 5.1.: Degradation of carbon fiber a) with plain SiC fibers, b) with plain carbon fibers, c) with TiB_2 fiber coating, and d) with adapted RMI process

In addition to investigating the fiber diameter within the micro structure, it is difficult to determine the loss in fiber strength resulting from RMI. The mechanical characterization of the full composite in section 5.2 was used to determine the influence. Pitch-based C fibers, however, have a large advantage compared to SiC and pan-based C fibers. As described by Reimer et al. [209] and in section 4.2.2, the layered structure of pitch-based C fibers shows an intrinsic fiber interface. Even if the fiber matrix interface is too strong to allow for a fiber pull-out or crack deflection, the interface will be shifted to the inside and between the fiber layers. Figure 5.2 shows this decomposition of the pitch-based C fibers when embedded into a UHTC matrix. Image a) shows the tip of a fiber being pulled out of the matrix with various lengths of the C layers. Image b) shows the other side of a pulled-out fiber, leaving a hole inside the UHTC matrix with the other half of the carbon fiber on the bottom. The fiber channel consists of ZrC due to the reaction of C and Zr during RMI. However, the fiber can use its intrinsic interface to slide along the C layers. Image c) and d) show long filaments being pulled out of the matrix within a tensile test sample. Most of the pull-out fibers show this decomposition effect along the fiber axis. This intrinsic pitch interface effect and the high modulus of the pitch C fibers create a high damage tolerance for UHTCMCs, as shown in section 5.2 and by other researchers [233, 234]

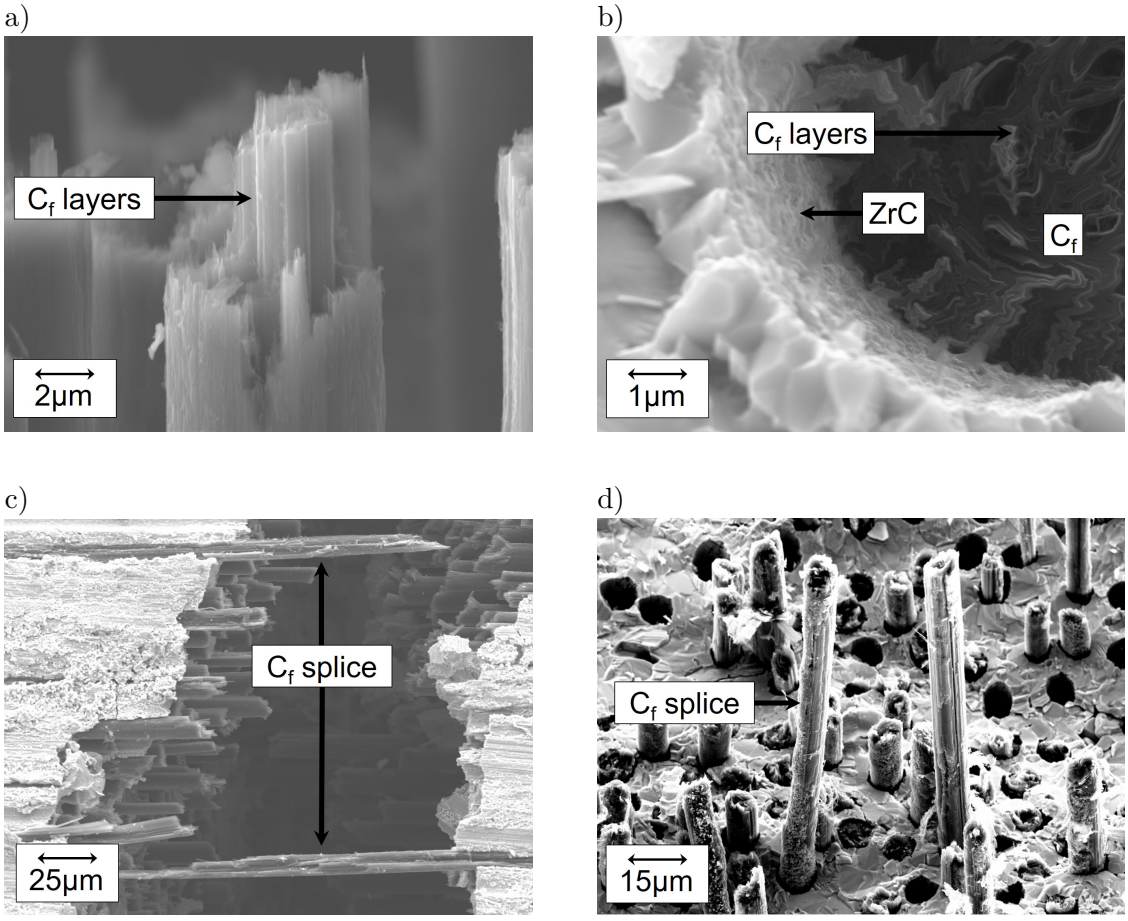

Figure 5.2.: Intrinsic fiber interface of pitch-based C_f within a UHTC matrix

5.1.2. Matrix

This section discusses the influence of various processing methods on the micro structure of the UHTC matrix formed during RMI between the fiber reinforcements. The goal of the matrix micro structure composition is to increase UHTC content as much as possible without limiting manufacturing of larger samples. In these investigations, ZrC, ZrB_2, and TiB_2 were the considered UHTC phases. As described in chapter 4, various precursors influence the residual melts remaining between the UHTC phases. All of the precursors used, phenolic and polycarbosilane, formed a ZrB_2 and ZrC matrix. The viscosity of the precursors influenced the maximum amount of powder loading when manufacturing the slurries. In addition, the volume expansion of the different phases during RMI varied and changes the composition of ZrB_2, ZrC, and residual melt. Figure 5.3 shows the matrix of a UHTCMC fabricated using a polycarbosilane precursor and B powder. The matrix is composed of ZrB_2 and ZrC grains, with Zr_2Cu residual melt and Zr_2Si phases between these grains. Zr_2Si formed during the reaction of Zr_2Cu with SiC, essentially generating the ZrC phase when using polycarbosilane. Image a) shows the matrix using a 40 wt.% powder loading and image b) a 60 wt.% powder loading. Due to the volume expansion of ZrB_2 when forming from B, ZrB_2 content increased within the matrix by around 30 vol% as shown in table 5.1. Volume ratios of table 5.1 were calculated from image gray scale analyses of various SEM images within each sample. Non-representative areas such as gussets, voids, and high fiber content areas were not used for the determination of these volume ratios.

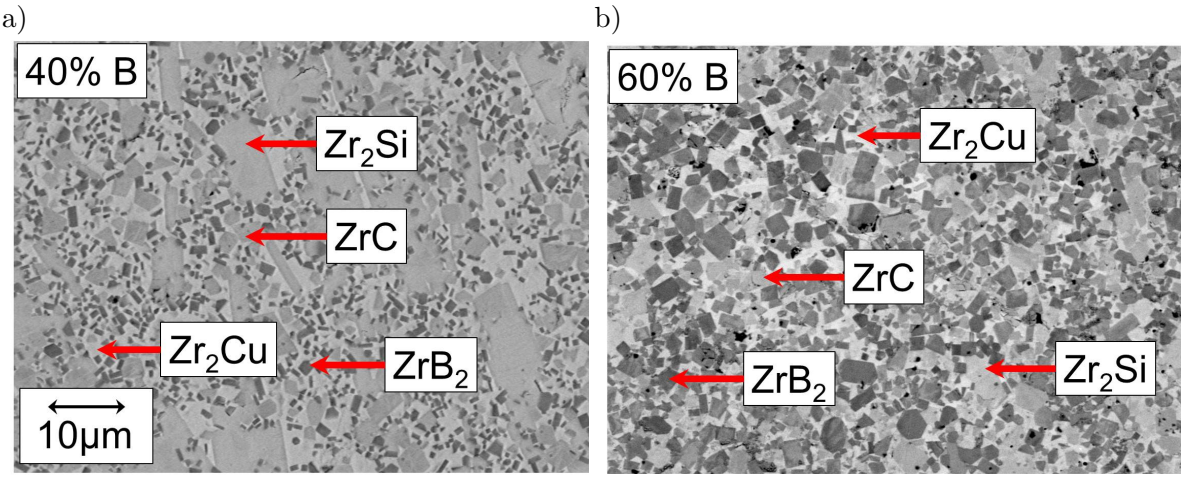

Figure 5.3.: UHTCMC matrix of polycarbosilane slurry with 40 wt.% and 60 wt.% B after Zr_2Cu infiltration

Figure 5.4 shows the micro structure formed when using a phenolic precursor with a) 30 wt.% and b) 40 wt.% B powder. Due to the higher viscosity of the phenolic resin, powder loading is not as high as with polycarbosilane. This limits the volume fraction of ZrB_2 within the UHTC matrix. However, there were no residual Zr_2Si phases. The large volume expansion when forming ZrC from C in combination with lower powder loading resulted

in a high volume fraction of ZrC inside the UHTCMC matrix. Table 5.1 displays image analysis values of UHTC phases compared to polycarbosilane samples. When comparing 40 wt.% B powder mixtures, ZrB_2, and ZrC, the volume ratios are higher for a phenolic precursor. This is due to the formation of Zr_2Si phases when using polycarbosilane and the large volume fraction exploited by these phases. However, higher UHTC volume ratios can still be achieved by a polycarbosilane sample due to the higher powder loading possible during fabric impregnation.

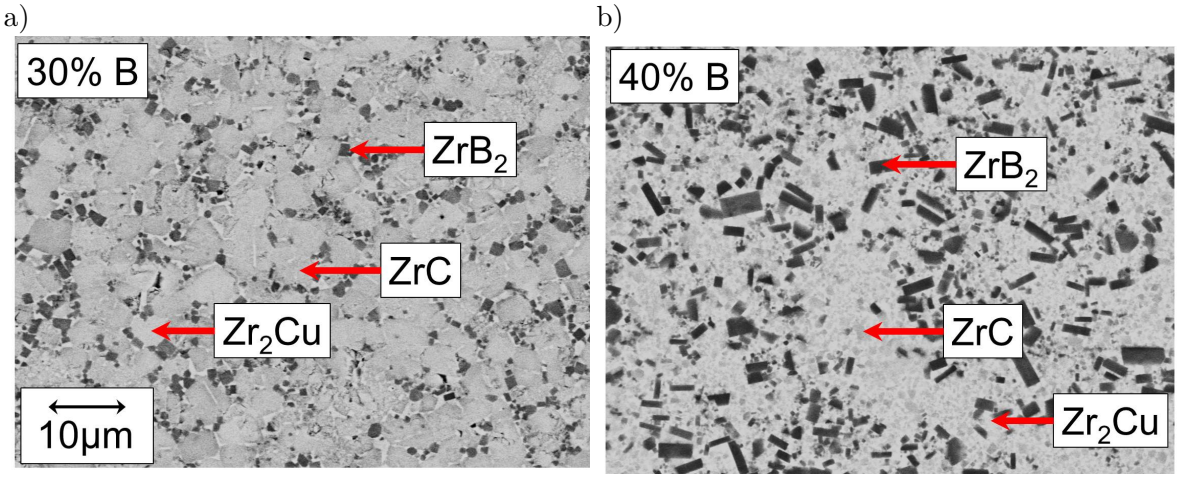

Figure 5.4.: UHTCMC matrix of phenolic slurry with 30 wt.% and 40 wt.% B after Zr_2Cu infiltration

The matrix of a phenolic sample including a B_2O_3 treatment after pyrolysis is shown in figure 5.5 b). As pure phenolic samples, the matrix is composed of ZrB_2 and ZrC grain with residual melt between the grains. As the images and volume ratios in table 5.1 reveal, the amount of ZrB_2 increaseed by 15 vol% due to the conversion of C into B_4C.

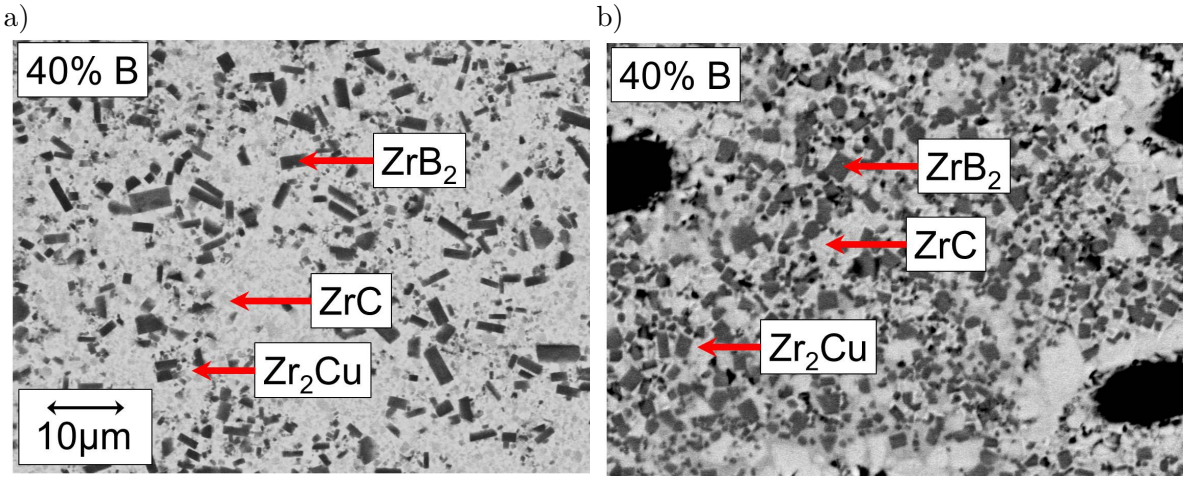

Figure 5.5.: UHTCMC matrix of phenolic slurry with 40 wt.% B and 40 wt.% B including B_2O_3 treatment after Zr_2Cu infiltration

Table 5.1.: Volume ratio of ZrB_2 and ZrC within the UHTC matrix

Resin	B powder content wt%	ZrB_2 content vol%	ZrC content vol%
Polycarbosilane	40	20 ± 2	35 ± 2
Polycarbosilane	60	50 ± 2	30 ± 2
Phenol	30	15 ± 3	70 ± 3
Phenol	40	25 ± 2	45 ± 2
Phenol and B_2O_3	40	40 ± 3	40 ± 3

In addition to Zr_2Cu, Zr_2Ag was used as an infiltration alloy due to the results from contact angle measurements. Each alloy was modified by a 1 at% B addition and, as shown in chapter 4, the contact angles of Zr-Cu and Zr-Ag melts decreased when adding 1 at% B. In addition, the amount of B necessary to form ZrB_2 increased. Zr_9B was chosen as a third candidate for these investigations, even though its contact angle could not be determined due to its high melting point. The advantage of Zr_9B is the absence of any low melting phases and large ZrB_2 grain, which form during RMI. All trials were performed with the same heating rates, dwelling time at peak temperature, and infiltration times. The infiltration time was set to 20 min in order to ensure a full infiltration of each sample. Each preform manufacturing rout was tested with each of the alloys and evaluated according to its mechanical properties and phases formed within its micro structure, shown in figure 5.6. In each of the six variations, ZrB_2 and ZrC were the main phases. The various alloys influenced the residual melt between the UHTC grains. Both preform manufacturing methods showed similar fracture surfaces in three-point bending tests. The main difference in fracture surfaces is due to the different melts used for infiltration. While Zr_2Cu-1%atB and Zr_2Ag-1%atB are similar, the Zr_9B infiltrated samples have a different fracture behavior, as shown as an example for the phenolic preform in figure 5.11. The different behavior is due to the incomplete infiltration of the fiber bundles when using the Zr_9B alloy. Either the viscosity of the alloy was not low enough to fully infiltrate the bundles or the formation of ZrC and ZrB_2 and their volume expansion prevented a full infiltration.

The infiltration of B_2O_3 decreased the ceramic yield of preforms via mass loss due to CO formation. In terms of RMI for ZrB_2, a high porosity and low C content is favorable. Most critical for the B_2O_3 treatment is an eventual fiber degradation. As the Zr melts, the B_2O_3 infiltrates using the capillary system of the preform, also reaching into the fiber bundles. Due to the TiB_2 fiber coating already protecting the fibers from Zr-melt, this aspect does not cause any problems upon manufacturing with polycarbosilane. Evaporation of the B_2O_3, as shown by TG measurements 4.3, must be compensated by additional B_2O_3 and fast heating rates above 1400 °C. Additional investigations can determine whether B_2O_3 infiltrates as a liquid into the pore system or as a gas phase upon evaporation. The C fibers in this comparison were coated with $2\mu m$ TiB_2. Therefore, more fibers were degraded during RMI, forming a matrix-dominant behavior. The highest bending strength was achieved using the Zr_2Cu-1at%B, melt with very little difference between the polycarbosilane and phenolic preforms, see table 5.3.

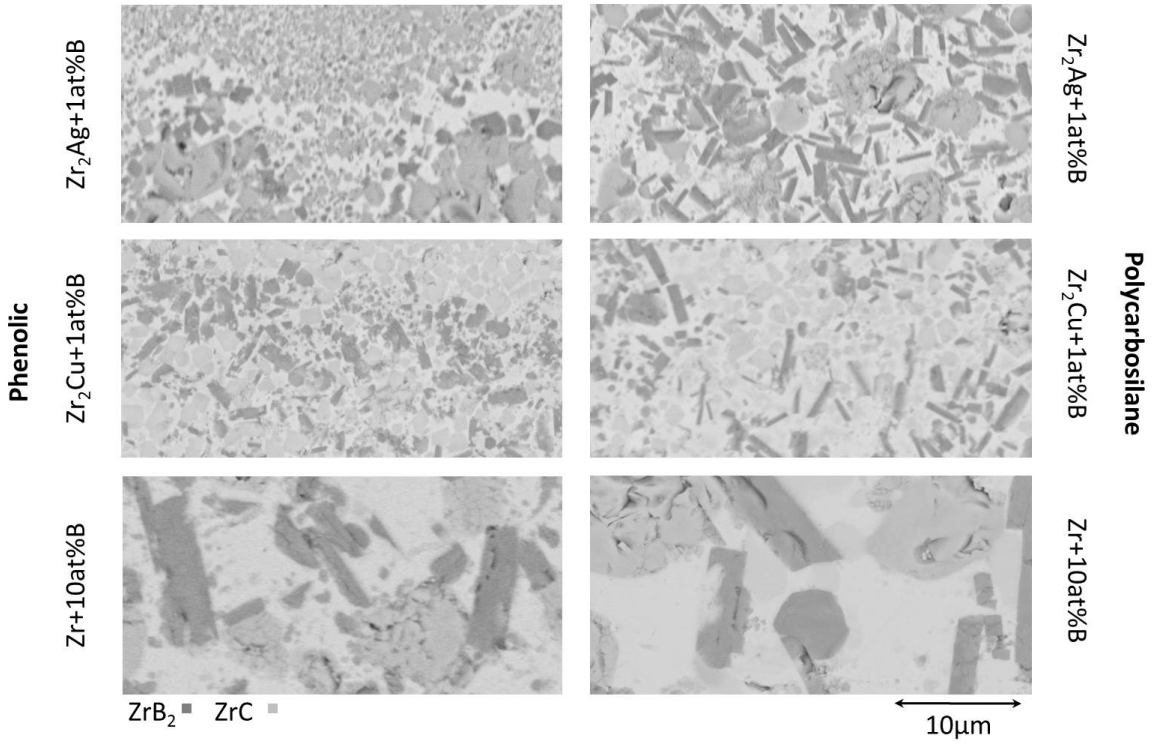

Figure 5.6.: Matrix variations within the micro structure when using varioius melts and preforms

In addition to the absence of Cu phases within the Zr_9B-infiltrated samples, the ZrB_2 grains formed within these samples were almost 10 times larger. Both larger grains and higher infiltration temperature could influence bending strength. Zr_2Ag-1at%B-infiltrated samples generated the lowest bending strength. By examining the tested samples, larger crack-like pores were found within the matrix of the samples, which appear more frequently between each fabric layer. These pores could be formed due to the lower viscosity of the Ag-based melts, draining the center of large pore channels, or they could be formed by evaporating Ag with a boiling point of 2210 °C, which could be achieved due to the exothermic reaction, further increasing sample temperatures from 1500 °C at initializing infiltration. Cu would increase this temperature limit to a boiling point of around 2595 °C.

Atom Probe

The RMI ZrB_2/ZrC matrix was analyzed using a 3D atom probe. The B source for the investigated samples was the amorphous B powder dispersed inside a phenolic resin. After impregnation of the TiB_2-coated fiber preforms, the samples were pyrolysed and formed a porous B/C matrix. In order to reduce the amount of C present in the matrix prior to infiltration with Zr alloys, the samples were treated with B_2O_3 to form a B/B_4C matrix. The formation of B_4C enhances the wetting behavior of Zr alloys in addition to an increased porosity as described in [235].

Zr_2Cu alloy was used as a Zr source for the ZrB_2/ZrC formation. Cu additions reduced the infiltration temperature, 1500 °C in this case, and reduced the reactivity of the Zr in order to minimize degradation of the C fibers. The major part of the Cu phases was ejected from the composite due to the high contact angles of ZrB_2 and ZrC, as described by Samsonov and Kütemeyer et al. [28, 163, 235]. The 3D atom probe tomography of IWKS revealed residual Cu phases within the grain boundaries of the ceramic matrix. Compared to Al alloys, where Cu dissolves into the aluminum crystal lattice, ZrB_2 forms a solid solution and the slow cooling causes precipitation along the aluminum grain boundaries. For Al, rapid cooling can suppress this effect and enhances maximum strength and hardness [236]. Infiltration at 1500 °C in an Ar atmosphere with an additional exothermal heating due to the formation of ZrB_2, having a melting temperature of around 3000 °C, does not reach temperatures high enough to allow for the formation of a solid solution. According to the 3D atom probe tomography, Cu was present at every grain boundary, including transitions from TiB_2, ZrC, and ZrB_2 to each other. Figure 5.7 shows the 3D atom probe sample during preparation. The needle being prepared has an approximate length of 300 nm and has been extracted close to one of the C fibers.

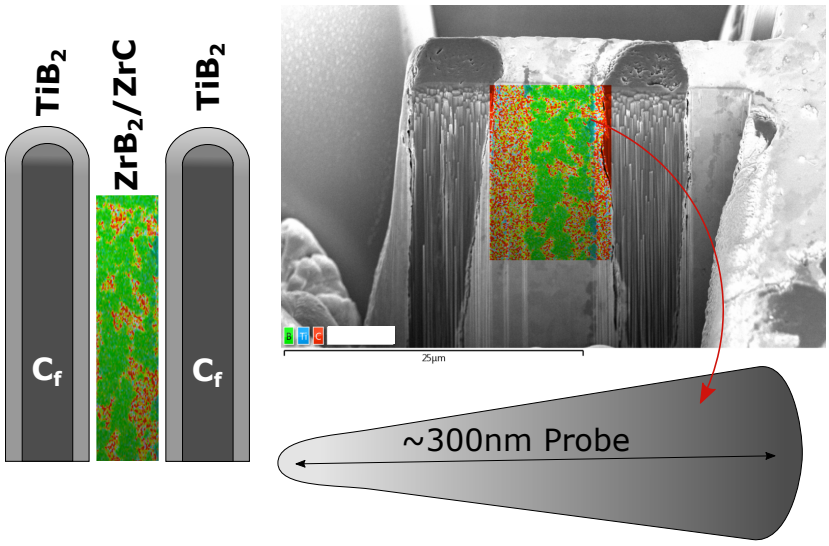

Figure 5.7.: SEM image during preparation of 3D atom probe sample

As shown by the left side of the needle displayed in figure 5.8, a TiB_2 grain is detected. The grain boundary to ZrC, being the next phase from the left side, contains a layer of Cu atoms. On the top right section of the needle, a small area of ZrB_2 can be noticed, also separated by a Cu containing boundary layer. In addition to the Cu within the boundary layer, residual Cl atoms from the CVI TiB_2 fiber coating can be detected within the TiB_2 grains, shown in the bottom right part of figure 5.8. A clear separation of Cu atoms between all grains of a few nm is visible, present in both of the two needles being extracted from RMI samples.

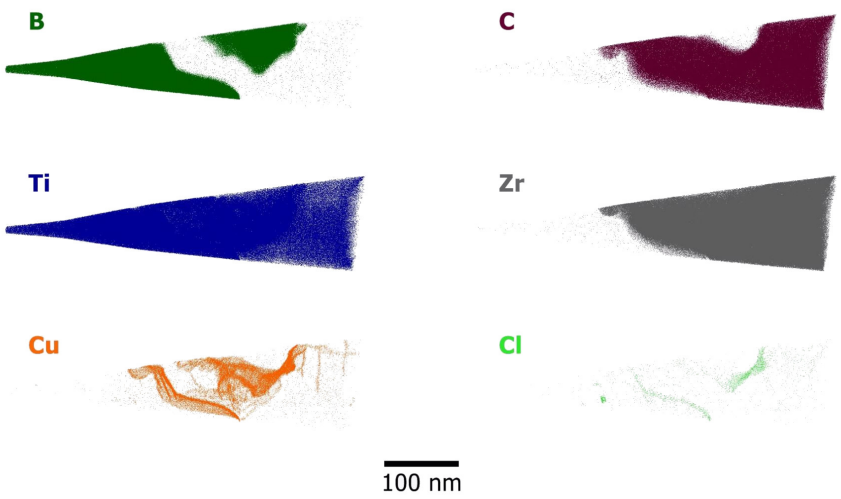

Figure 5.8.: 3D atom probe tomography of the ceramic matrix containing Cu

In comparison, UHTC grains of a sample infiltrated with pure Zr were investigated using 3D atom probing. The B source was also an amorphous B powder dispersed inside a polycarabosilane resin. The polycarbosilane sample introduced a Si addition into the composition. After impregnation of the TiB_2-coated fiber preforms, the samples were pyrolysed and formed a porous B/SiC matrix. The pure Zr melted above 1850 °C and formed the ZrB_2/ZrC matrix. As with the Cu for Zr_2Cu alloys, the Si accumulated at the grain boundaries of the ZrB_2, TiB_2, and ZrC phases, as shown in figure 5.9.

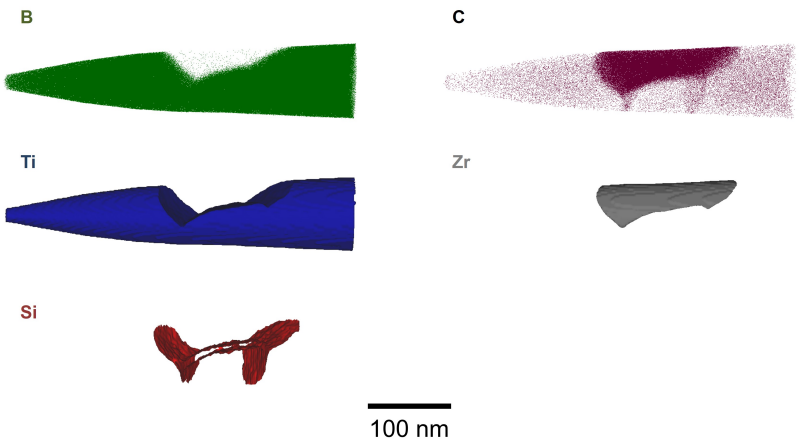

Figure 5.9.: 3D atom probe tomography of the ceramic matrix containing Si

The large bottom part of the needle shows a TiB_2 grain represented by the B and Ti detection. The separate top section is a ZrC grain, represented by the Zr and C detection, between which a Si layer is detected, shown in the bottom left picture of figure 5.9. The amorphous SiC inside the pyrolysed preform reacts with the Zr during RMI to form ZrC,

segregating Si at the grain boundaries. As with the Cu, a clear separation of Si atoms between the grains of a few nm is visible.

5.2. Mechanical Characterization

The mechanical characterization is split into two groups, TiB_2 fiber-coated fabrics and uncoated fabrics, both of which are Granoc XN-80 carbon fibers. Investigations of fiber-coated fabrics are limited to three-point bending tests, while uncoated samples are tested in three-point bending, compression, fracture toughness, and tensile strength. The description of each test according to the available standards can be found in chapter 3. The three Zr melts, pure, Cu, and Ag additions, were investigated using the coated fibers in combination with two resins. Uncoated fibers were only investigated using a Zr_2Cu alloy and Zr_9B in combination with a phenolic resin in order to avoid Si adopting the process parameters.

5.2.1. Fiber Coated Samples

TiB_2 coating was applied using a CVI process described in section 4.2.3. The investigations evaluated the influence of three different melt alloys and two resin types.

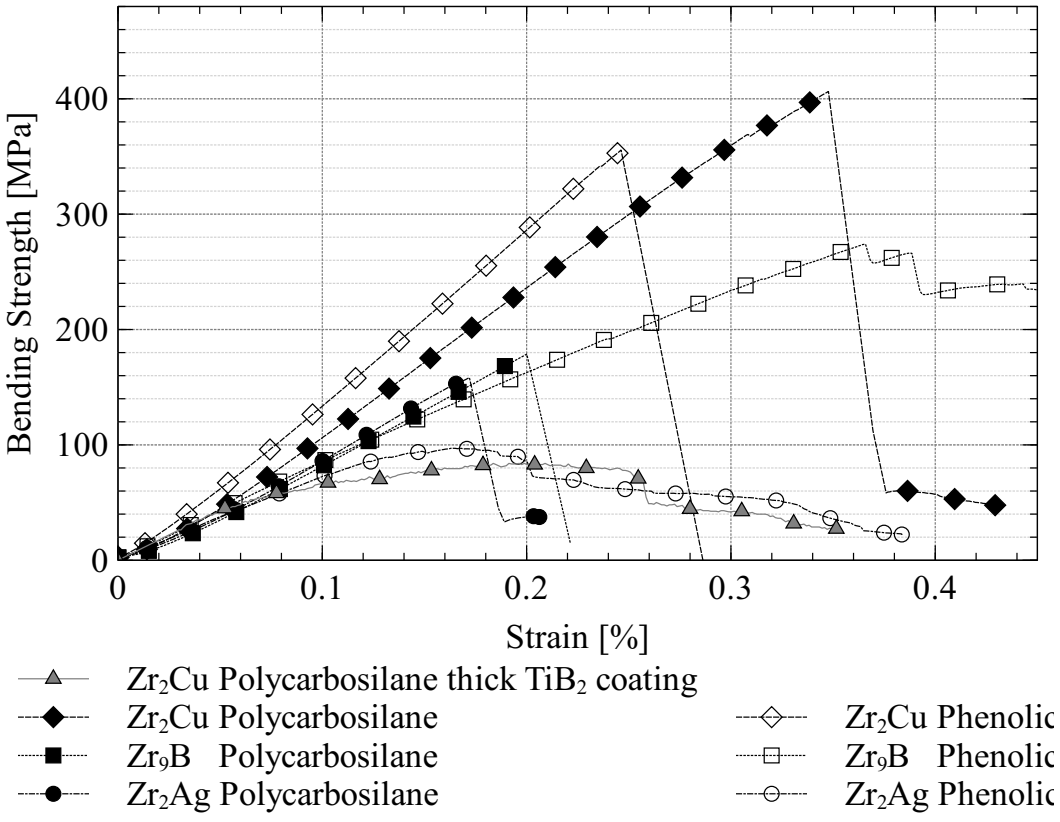

Figure 5.10.: Summary of bending tests from fiber coated UHTCMC samples

Figure 5.10 shows 3PB tests of different TiB_2 fiber coated samples. The solid lines with markers show the behavior of a thick 4 μm fiber coating. The elongation is higher compared to samples with a 2 μm fiber coating, plotted as solid lines without markers. Bending strength is influenced by the thick fiber coating due to an insufficient infiltration of the fiber bundles, leaving residual porosity within the samples. The thin fiber coated samples were used to compare the influence on mechanical properties using different melts in combination with two different preform manufacturing routs, polycarbosilane and phenolic. The large spread of ultimate bending strength shows the large influence of different Zr-alloys used. The following section will discuss these factors in detail.

Influence of Various Melt Alloys

Table 5.3 shows the results of three-point bending tests performed for each melt and preform. A total of five samples for each set was tested with an exception of three samples for the Zr_9B sets. Zr_2Cu-1%atB reaches the highest bending strength and ultimate strain, with the polycarbosilane-based preform being slightly higher than the phenolic-based preform. All specimens initialized a crack on the bottom side under tensile loading. Every combination shows fiber pull-out and crack deflection. However, these mechanisms are not as distinct as for the thick TiB_2 fiber coating.

Table 5.2.: Mechanical properties, ultimate stress σ_B, Modulus E and ultimate strain ϵ_B of tested melt and preform combinations; polycarbosilane (PCS) and phenolic (PH)

	σ_B [MPa]		E [GPa]		ϵ_B [%]	
	PCS	PH	PCS	PH	PCS	PH
Zr_2Cu-1at%B	393 ± 27	363 ± 10	147 ± 2	183 ± 10	0.39 ± 0.09	0.21 ± 0.01
Zr_2Ag-1at%B	134 ± 21	78 ± 19	210 ± 86	128 ± 10	0.07 ± 0.02	0.15 ± 0.09
Zr_9B	190 ± 32	181 ± 81	144 ± 13	162 ± 25	0.16 ± 0.06	0.14 ± 0.09

Zr_2Cu-1at%B melts reach 393 MPa three-point bending strength compared to 190 MPa of Zr_9B at room temperature. Cu phases are low within the Zr_2Cu-1at%B samples and can be reduced further; however, high temperature strength might be less influenced when using the Zr_9B melt.

5.2.2. Uncoated Fiber Samples

Uncoated fiber samples were manufactured using a B_2O_3 treatment, described in detail in chapter 4. As mentioned in this chapter, distribution of B_2O_3 within the sample is vital in order to keep fiber degradation due to the carbothermal reduction to a minimum. As Zr_2Cu-1at%B alloys show the highest strength using a fiber coating and Zr_9B alloys renounce any low melting phases, these two melts were used to investigate the mechanical performance of UHTCMCs without fiber coating.

Zr_2Cu-1at%B samples show a homogeneous micro structure and have minimal fiber degradation, visible in figure 5.12. However, there are areas within the micro structure without

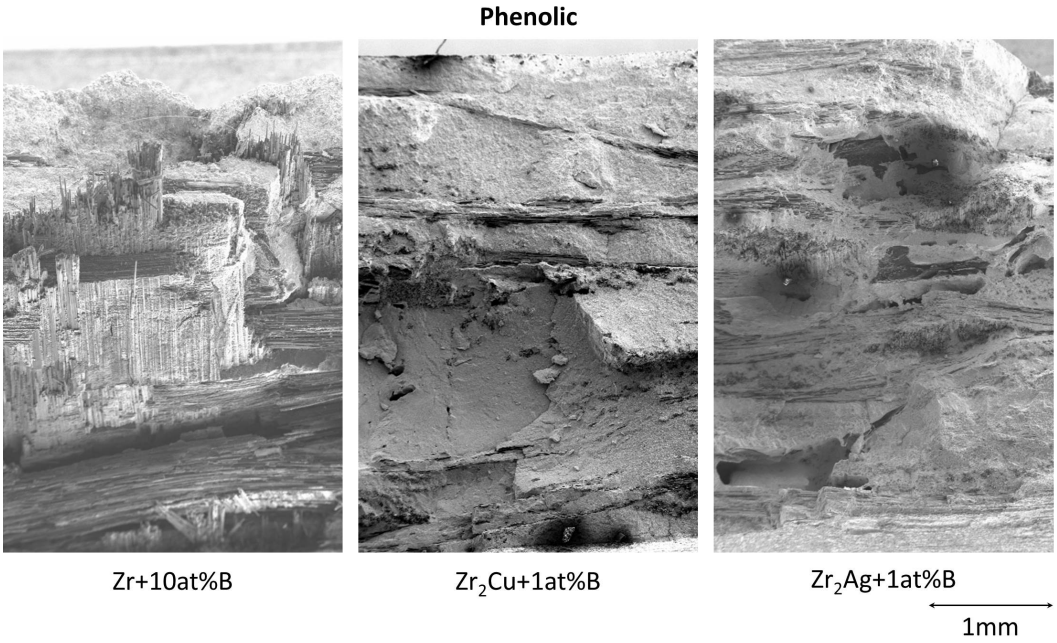

Figure 5.11.: Fracture surface after three-point bending of the phenolic preform for each of the three melts

any UHTC phases or fibers. Image a) in figure 5.12 shows one of these areas marked in red. These regions form during the impregnation of the carbon fiber sheets. Hence, uni-directional fabrics are used for manufacturing UHTCMCs. These sheets contained a polyamide thread which kept the single rovings in place. This thread leaved a void of resin and powder while decomposing during pyrolysis. Depending on the infiltration height of the sample and the size of the void, these voids were either filled with residual melt or left as pores inside the UHTCMC. In order to avoid these defects, samples would have to be re-infiltrated with a low viscosity slurry after pyrolysis. A different option would be to impregnate woven fabrics without any threads, but impregnation of powders between the fiber bundles is more effective when using uni-directional fabrics.

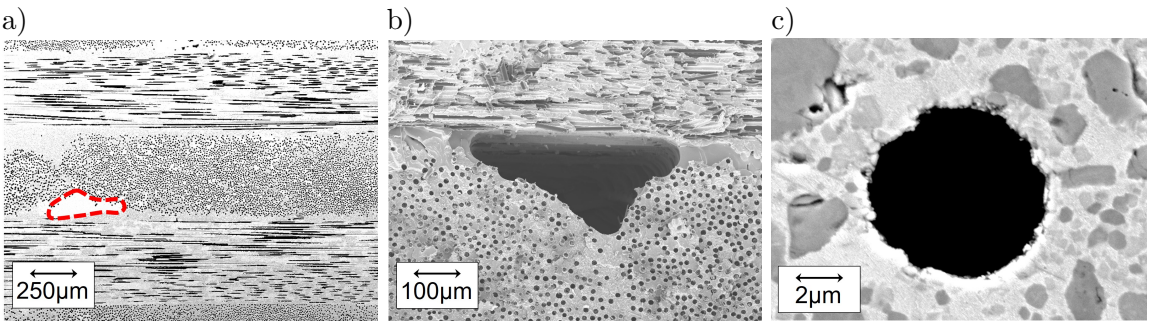

Figure 5.12.: Micro structure of UHTCMC infiltrated with Zr_2Cu-1at%B and without fiber coating

These voids influenced the mechanical performance, especially when appearing on the tension side of a bending sample. Graph 5.13 shows the influence of a sample with voids, reaching around 320 MPa in strength, and of a sample without voids, reaching around 650 MPa in strength. All of the low-yield strength samples failed upon initializing first failures during loading. Samples without any voids on the tension side of the sample achieved bending strengths of above 600 MPa. Figure 5.14 shows the crack formation after the 3PB test. Image a) shows the loading according to SEM images. One sample shown in image b) indicates a crack deflection behavior due to the fiber reinforcement. Further magnification of the sample shown in image c) also shows fibers bridging across the crack propagation.

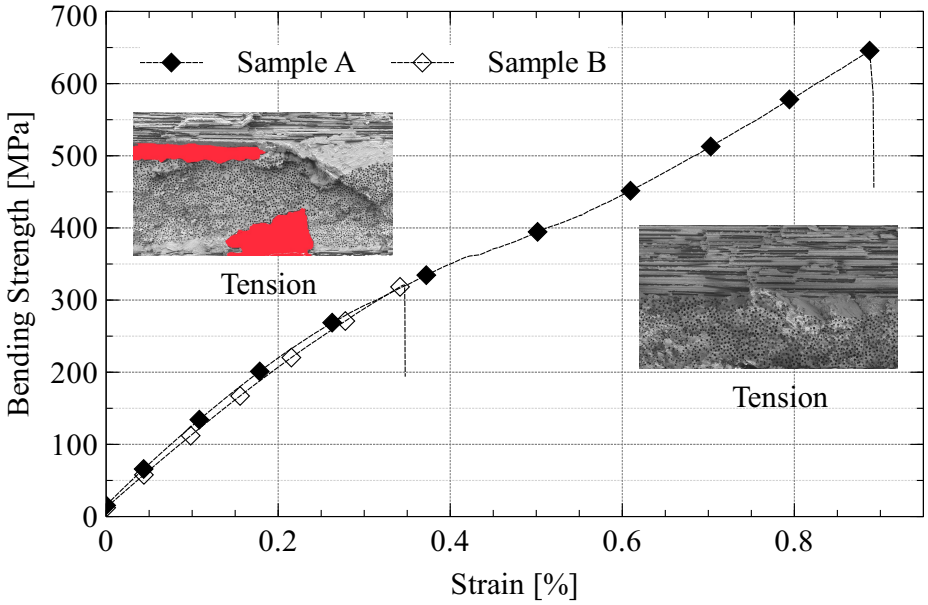

Figure 5.13.: Influence of larger pores in UHTCMC samples without fiber coating, on 3 point bending strength

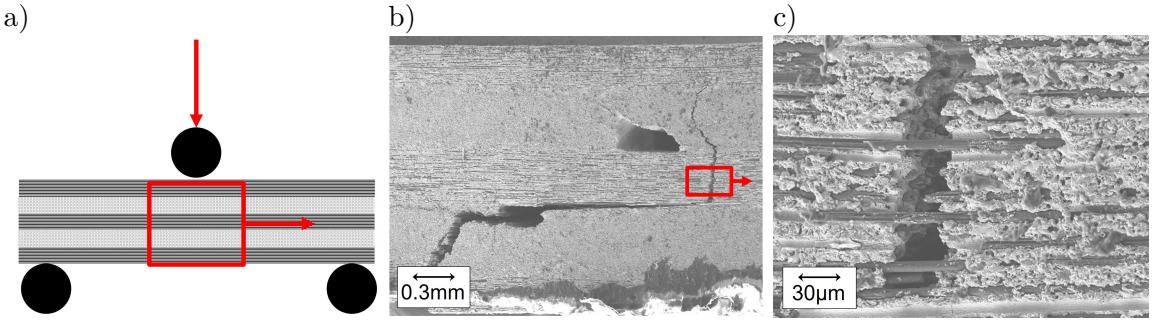

Figure 5.14.: Fracture surface of UHTCMC infiltrated with Zr_2Cu-1at%B and without fiber coating, after 3PB test

The sample infiltrated with Zr_9B melt tended to have fewer voids arising from threads of the fabrics. However, these samples, just as the fiber-coated samples, have areas of not infiltrated fiber bundles. Figure 5.15 shows a Zr_9B infiltrated sample in image a) and a Zr_2Cu-

1at%B infiltrated sample in image b). Image a) displays an area not being infiltrated above the red line spreading along a fiber bundle. In addition to the influence from the residual melt on the mechanical performance of the sample, these non-infiltrated areas limited the ultimate strength of Zr_9B samples. Due to the lack of matrix support within these regions, Young's modulus, determined using 3PB, is not as representative as with fully infiltrated samples, while the modulus determined during tensile tests is less affected. Figure 5.16 compares stress-strain curves of one representative sample of each melt. Due to insufficient fiber bundle infiltration, also represented by the high porosity of these samples in table 5.3, the Zr_9B samples exhibit a lower ultimate tensile strength. As known from literature [56, 118], the strength of monolithic ZrB_2 is influenced by grain size. Larger grains generate lower mechanical strength. Hence, large ZrB_2 grains caused by Zr_9B infiltration influence the mechanical strength of the matrix. The Young's modulus of Zr_9B samples was over 60% higher than that of Zr_2Cu-1at%B samples. As described in section 5.1, a lower modulus of the Cu-containing samples is caused by the Cu phases between the UHTC grains and properties of the residual melt.

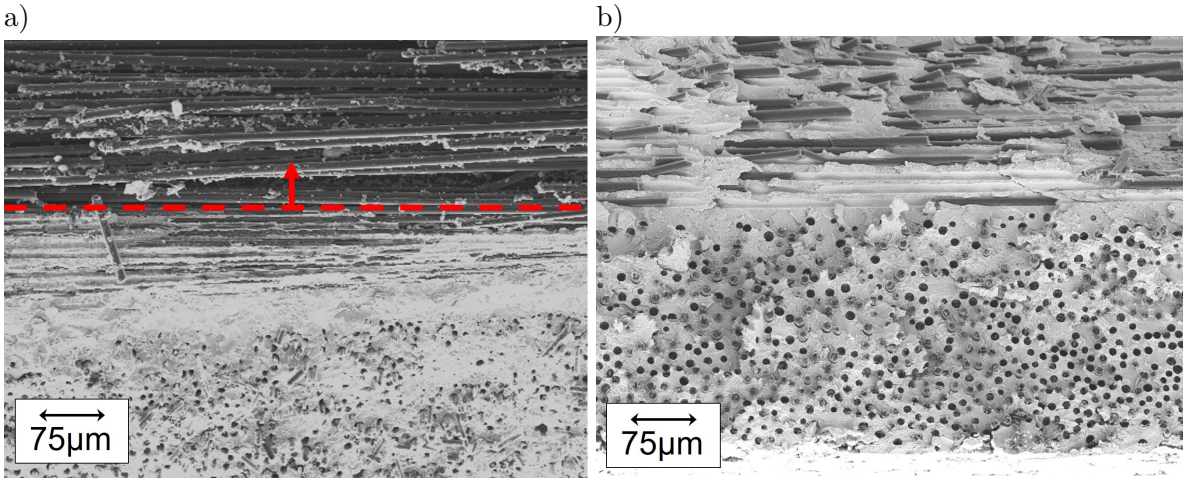

Figure 5.15.: Comparison of UHTCMC micro structure of samples infiltrated with a) Zr_9B and b) Zr_2Cu-1at%B

As with tensile tests, compression strength and the modulus of the Zr_9B samples were influenced by an incomplete infiltration of fiber bundles. Figure 5.17 shows compression tests performed at 500 °C, loaded perpendicular to the fiber plain. While the Zr_2Cu-1at%B sample remained in one piece after testing, the Zr_9B samples shattered into several pieces.

Figure 5.18 shows the fracture toughness of Zr_2Cu-1at%B samples tested according to SENB. The K_{1C} value of the tested samples was calculated to $11 MPa\sqrt{m}$ and exceeded the values of monolithic UHTCs, as described in chapter 2. While observing the samples during testing, there was a small non-critical crack propagation before dropping to lower load levels. As seen from the diagram, crack propagation stabilized for a short period at this level before further declining.

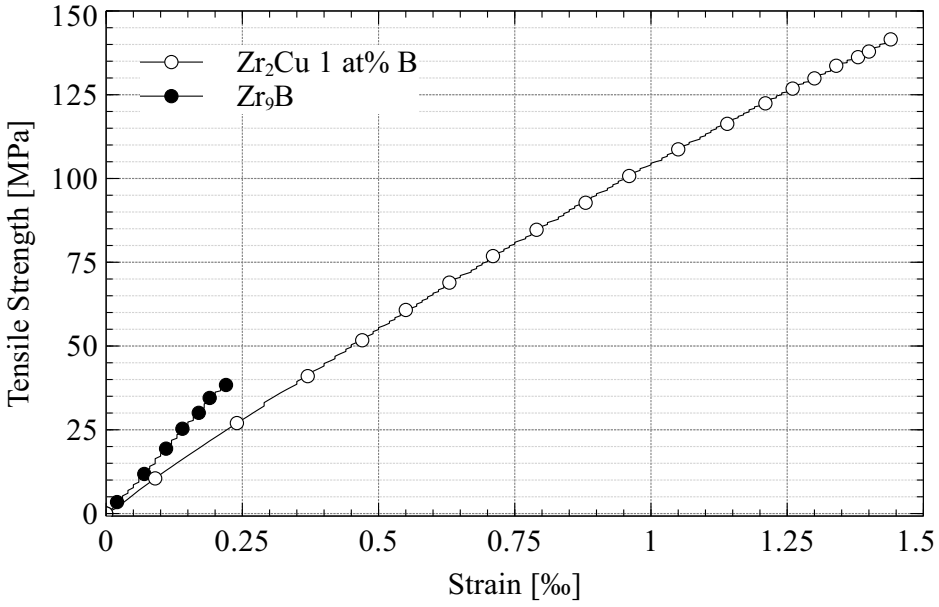

Figure 5.16.: Influence of melt alloy on UHTCMC tensile strength and Young's modulus

The crack opening after fracture toughness tests is displayed in figure 5.19. The surface of the sample is colored white to track crack propagation by image analysis. None of the samples shattered in half during testing. Image a) shows crack formation after testing, spreading almost over the entire height of the sample. Image b) and c) show the magnification of the crack opening from the top. As 3PB samples, these samples show fiber pull-out and crack bridging effects.

Figure 5.20 compares 3PB tests of samples with and without TiB_2 fiber coating. While the initial modulus of the two samples was similar, the samples without fiber coating became less stiff when exceeding 100 MPa. This effect is either caused by the Ti inside the UHTC matrix or due to the voids present in the non-coated samples.

Table 5.3 summarizes the mechanical values of uncoated UHTCMC samples. A total of eight to ten specimens for each bending set was tested, the total of compression and tension was between three and five for each set and a total of seven fracture toughness specimens were tested. As described earlier, the deviation of strength and elongation of bending samples was considerably higher due to the influence of voids present inside the sample. The bending strength of Zr_2Cu-1at%B exceeded the values of tensile strength by far due to the utilization of the fiber strength and the porous matrix within these UHTCMCs. Calculating the fiber utilization factor from tensile tests, with ultimate strength from XN-80 fiber of 3430 MPa and 15 % fiber volume content in 0°, gives a utilization of 27 %.

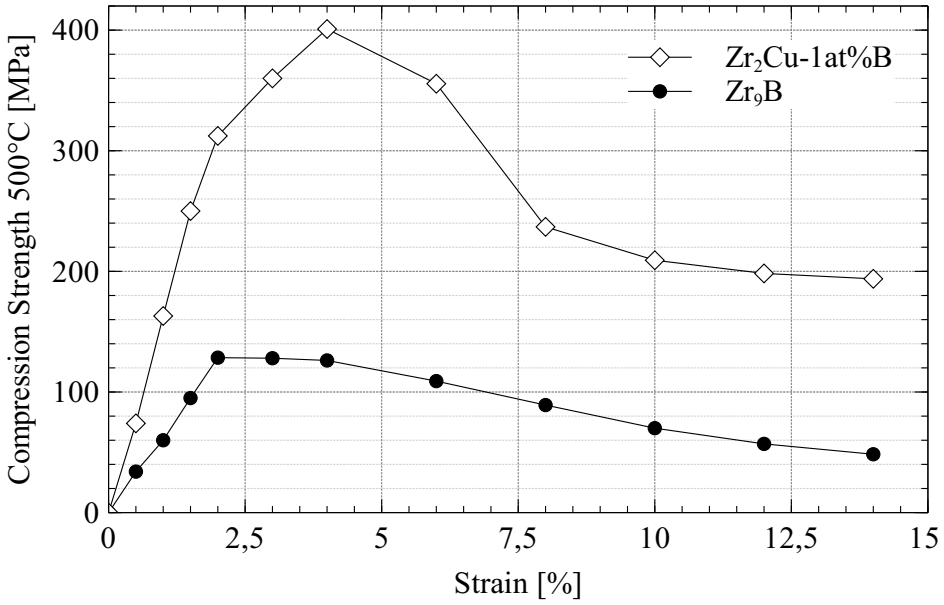

Figure 5.17.: Influence of melt alloy on UHTCMC compression strength

5.3. Oxidation

As pure Zr and Hf diborides form a porous pillar-like structure of Zr or Hf oxide, Kaufman et al. [123] investigated SiC additions in 1970 in order to close the voids between the pillar structure with SiO_2 glass. Levine et al. [128] showed a four-layer oxidation zone upon oxidation at 1627 °C. These layers consisted of a SiO_2 glassy layer on the top, followed by ZrO_2 with SiO_2 filled pores, ZrB_2 depleted of SiC, and the base composition of ZrB_2 and SiC on the bottom. The residual melt of RMI-manufactured UHTCs acts similarly to SiC additions. However, during investigations of the RMI UHTC at 1800 °C, no glassy phases were found. Figure 5.21 shows the oxidation layer of a monolithic ZrB_2/ZrC fabricated by RMI using a Zr_2Cu alloy. The samples were oxidized using a furnace and stagnant air at 1800 °C for a duration of 8 h. Similarly to ZrB_2 with a SiC addition, neglecting the glassy phase, the sample formed three layers:

- Zirconia in a columnar skeleton structure,
- ZrB_2 region depleted in Zr-alloy, and
- ZrB_2/ZrC and residual melt, the base material.

The Si addition inside the residual melt can be used to form SiO_2 phases. However, these phases are not stable at temperatures above 1800 °C at ambient pressures.

Each investigated melt, Zr_2Cu, Zr_2Ag, and Zr_9B, influenced the oxidation behavior and the oxides formed. However, the porosity or degree of infiltration is an important factor which must be taken into account. If the sample has voids, as described for the Zr_9B-infiltrated TiB_2 fiber coated sample in section 5.1, the C fibers are subject to active oxidation and the ZrO_2 layer must grow fast enough to close the void.

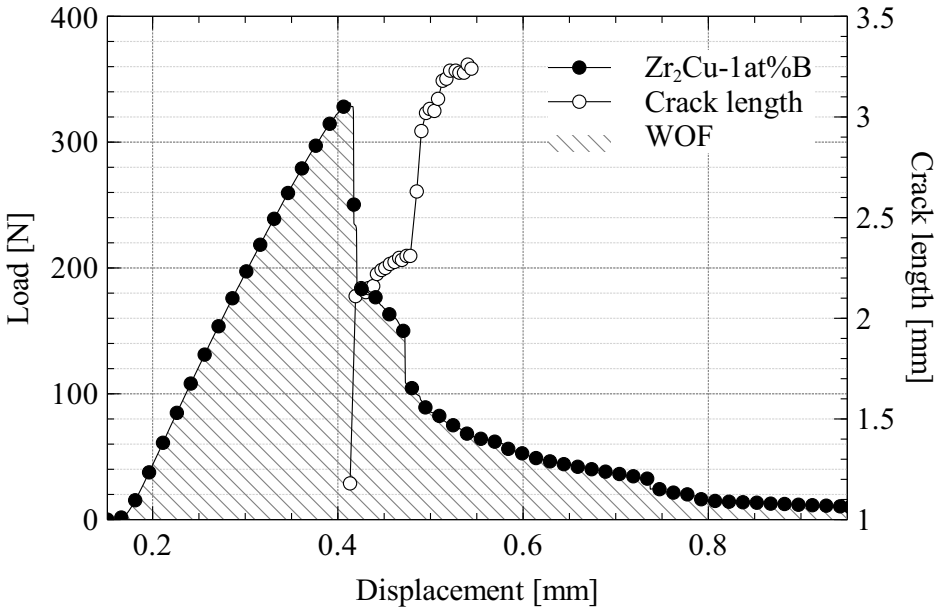

Figure 5.18.: Fracture toughness of UHTCMC without fiber coating and Zr_2Cu-1at%B infiltration

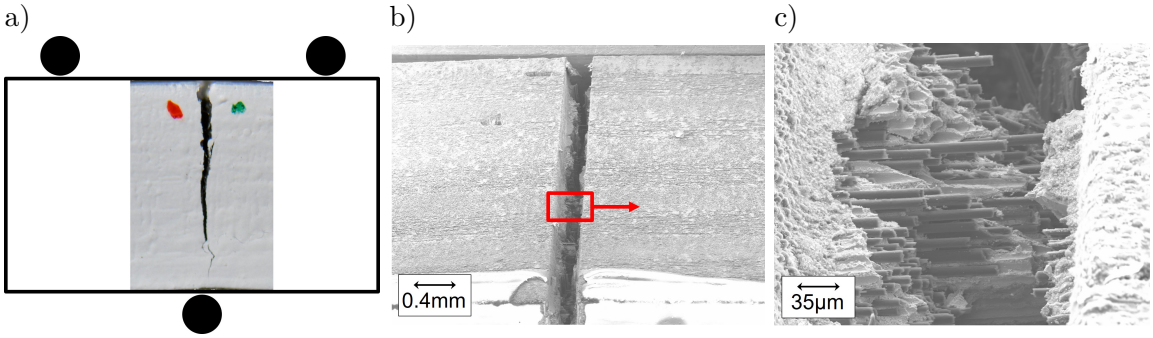

Figure 5.19.: Fracture surface of UHTCMC infiltrated with Zr_2Cu-1at%B and without fiber coating, after fracture toughness test

In order to examine these UHTCMCs at 2200 °C, they were tested using an induction heating facility. The facility has a ZrO_2-insulating enclosure, heated via inductive coupling into a graphite plate. This graphite plate heats the test chamber via radiation and oxygen is fed into the chamber using a valve inlet at one side of the chamber when reaching peak temperature. The air flow is active during the 5 min holding time at peak temperature at a flow rate of $5l/min$. Both samples, figure 5.22 and 5.23, have a TiB_2 fiber coating and were infiltrated using a Zr_2Cu-1at%B alloy. Figure 5.22 uses polycarbosilane as a precursor, and hence, includes Si phases inside the micro structure. As shown in the left top image in figure 5.22, the matrix starts to blister underneath the oxide layer. As described by Parthasarathy et al. [237], this is due to the formation of SiO at the ZrB_2/ZrO_2 interface. Compared to samples containing SiC, the formation of SiO in these samples is caused by the oxidation of

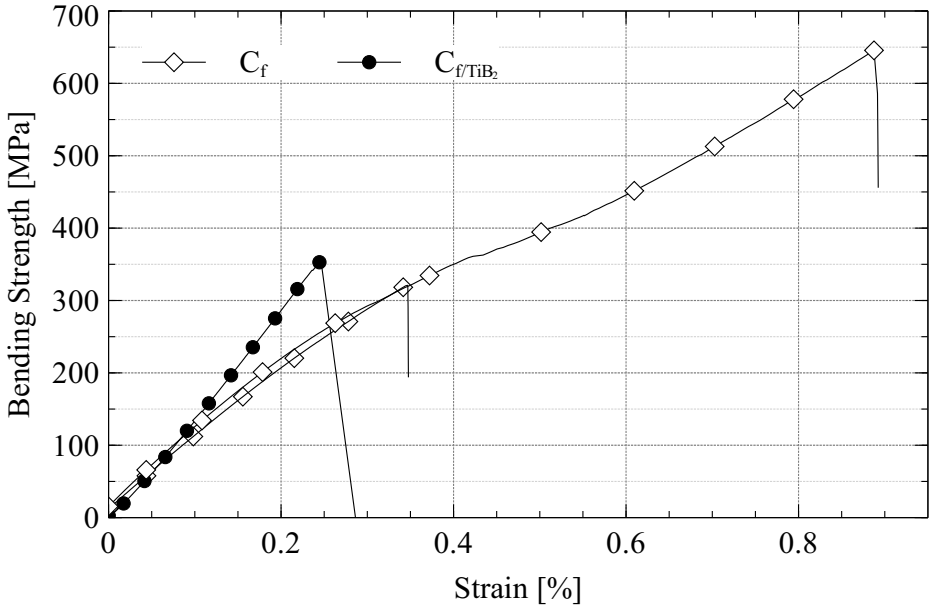

Figure 5.20.: Influence of fiber coating on 3PB strength

Zr_2Si. Parthasarathy et al. described the formation of SiO to be caused by the oxidation of SiC to produce CO and SiO_2, according to the following equations:

$$2SiC + 3O_2 \longrightarrow 2CO + 2SiO_2, \tag{5.1}$$

$$2CO + O_2 \longrightarrow 2CO_2, \tag{5.2}$$

$$SiC + 2CO_2 \longrightarrow SiO + 3CO. \tag{5.3}$$

Due to the absence of SiC in the tested sample, the formation of CO was caused by the oxidation of ZrC and the formation of SiO_2 due to the oxidation of Zr_2Si:

$$2ZrC + 3O_2 \longrightarrow 2CO + 2ZrO_2, \tag{5.4}$$

$$Zr_2Si + 3O_2 \longrightarrow 2ZrO_2 + SiO_2. \tag{5.5}$$

The sample in figure 5.23 does not contain any Si phases, using a phenolic precursor when manufacturing the samples. As seen in the top left image, these samples do not form any blisters during oxidation. Due to the lack of Si, no SiO formed underneath the ZrO_2 layer. In addition, this means the formation of CO and CO_2 does not cause any blistering because there is no glassy layer between the ZrO_2 structure. The EDX element mapping in figure 5.22 and 5.23 only shows Si present in the oxide layer of the polycarbosilane sample. For both samples, the major phase of the oxide layer is ZrO_2.

Table 5.4 shows the mass loss of the different melts, also tested mechanically in section 5.2, manufactured with a TiB_2 fiber coating. As described, they are oxidized at 2200 °C with an ambient air inlet as an oxygen source. The mass change of the samples is a combination

Table 5.3.: Mechanical and physical properties of UHTCMCs without fiber coating

Alloy	FVC*	ρ	e'	Tensile test			Bending test		Comp. test**	K_{1C}
	[%]	$\left[\frac{g}{cm^3}\right]$	[%]	σ_T [MPa]	ϵ_T [‰]	E [GPa]	σ_B [MPa]	ϵ_B [%]	σ_{comp} [MPa]	$\left[MPa*\sqrt{m}\right]$
Zr_2Cu 1at%B	30	5.5 ±0.2	< 2	140 ±14	1.48 ±0.16	110 ±3	446 ±133	0.50 ±0.20	397 ±36	10.6 ±1.5
Zr_9B	27	5.2 ±0.3	8 ±0.3	39 ±5	0.23 ±0.03	181 ±18	139 ±42	-	138 ±10	-

* Determined without the loss of fibers reacting during RMI
** at 500°C

of mass loss due to gaseous phases forming and mass gain due to oxide formation. Samples containing Zr_2Si phases generated an overall mass loss due to the formation of gaseous SiO and SiO_2. Samples infiltrated with Zr_9B with an infiltration temperature of 1900 °C had a low number of Zr_2Si phases, and therefore, did not exhibit any mass loss. The alloy converting the most oxides is Zr_9B due to the stability of the residual melt and large ZrB_2 grains. In terms of oxidation resistance at temperatures exceeding 2000 °C, a preform route without any Si phases should be favored.

Table 5.4.: Mass change of UHTCMCs during oxidation at 2200 °C for 5min

	Zr_2Cu-1at%B		Zr_2Ag-1at%B		Zr_9B	
	PCS	PH	PCS	PH	PCS	PH
Mass change [%]	-16%	1%	-12%	-9%	3%	3%

5.4. Discussion of Characterization

Due to the adaption of resins, powders, and melts, the composition of the UHTCMC matrix can be varied on a broad spectra. Melting temperature or infiltration temperature affects the grain size of diboride grains forming from B powder, yet passive grains forming from passive diboride powders maintain their grain size or slightly increase. This method would even allow for a large spectra of grain sizes inside the UHTC matrix. In addition, the ratios of carbides and diborides can be altered using phenolic or polycarbosilane-based preforms. As investigated by Opeka et al. [12], the oxidation layer thickness at 1300 °C can be reduced by combining ZrB_2 and ZrC. When using the phenolic-based route, the ZrB_2/ZrC ratios can be changed by altering the amount of B_2O_3. Further additions to the matrix composition, such as Y, can be included by using different powder combinations or by changing the alloy composition, as shown in section 4.1.3, with Zr_2Ag - 5 at% Y 1 at% B. Cu and Si additions

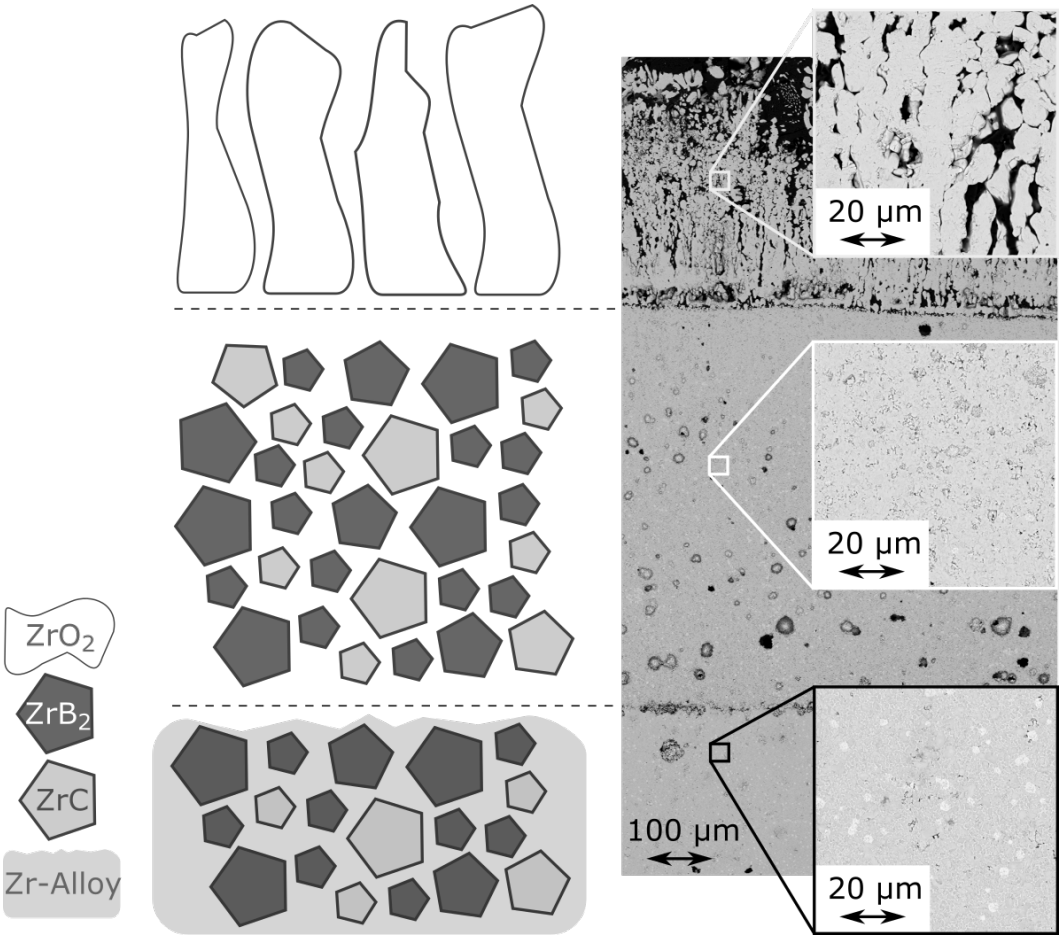

Figure 5.21.: Oxidation behavior of the RMI UHTC; 1800 °C in stagnant air for 8h

resulting from the melt alloy or polycarbosilane separate at the grain boundaries and can be used to adapt the UHTCMC's behavior. Si additions can enhance oxidation resistance at lower temperatures, while Cu additions allow for brazing or welding, and therefore, provide different options for structural interfaces.

When using the phenolic-based manufacturing route, the infiltration temperatures can be decreased low enough to use SiC fibers without fiber coating as reinforcement. However, due to the poly-crystalline structure of these fibers, they would be in need of a mechanical fiber matrix interface to achieve a damage-tolerant behavior. Pitch-based C fibers have the advantage of their intrinsic interface as described in this chapter. This interface allows for a damage-tolerant behavior without the need for any additional fiber coating provided that the fibers survive RMI. Furthermore, the structure of the pitch-based C fibers, enabling this intrinsic interface, makes the fibers less sensitive to any reactions when forming the matrix. Any reaction decreases the fibers cross section, but does not pose a critical failure when some of the external layers react, see figure 5.2.

The UHTCMCs manufactured via RMI, investigated mechanically in this chapter, have a fiber volume content of around 30 %. This low value is due to limitations of the slurry im-

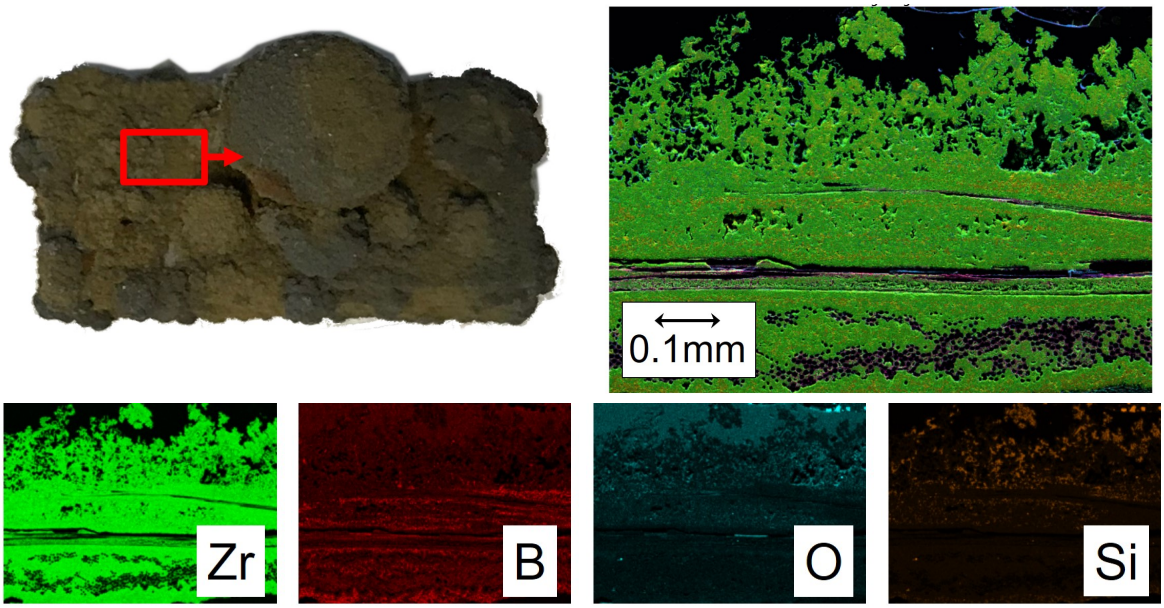

Figure 5.22.: Oxidation of polycarbosilane-based UHTCMC; 2200°C for 5min

pregnation and the porosity necessary to provide enough volume for the volume expansion of the occurring reactions. The low strength of the pyrolysed preform caused by a porosity higher than 40 % cannot sustain the thickness of the samples during pyrolysis and infiltration. This caused the FVC to drop below 30 % within the UHTCMC. In order to further improve the mechanical performance of these composites, FVC must be increased. For example, this could be achieved by applying mechanical pressure during the infiltration process. Using passive powders such as ZrB_2 reduces the volume expansion, but also increases residual melt. The most effective way of adapting volume expansion and pore distribution would be a non-particle-based B source. Like the FVC, UHTC content of the matrix can also be increased. Increasing the UHTC content decreases the amount of residual melt inside the UHTCMC and improves high temperature capabilities of the composite. A higher UHTC grain density would increase the interface areas, and hence, increase temperature stability of the matrix. Compared to monolithic UHTCs with a fracture toughness of 3-6 $MPa\sqrt{m}$ [22, 116, 128], the investigated fiber reinforcement increased fracture toughness, even exceeding a K_{1C} value of 10 $MPa\sqrt{m}$. The most important factors necessary to achieve this toughness are the intrinsic fiber interface of pitch-based C fibers and the residual melt between the UHTC grains. Other pitch-based UHTCMCs manufactured by Zoli et al. [32] also exceeded K_{1C} values of 10 $MPa\sqrt{m}$. The matrices of these composites were processed using sintering techniques and were tested using the chevron-notched beam method. This fracture toughness showed the potential to increase fracture toughness of a ZrB_2-based UHTC via a pitch-based C fiber reinforcement.

The UHTCMC matrix fabricated by RMI was able to withstand 2200 °C for a short duration, forming a ZrO_2 layer. The C reinforcement fibers, however, were subject to active

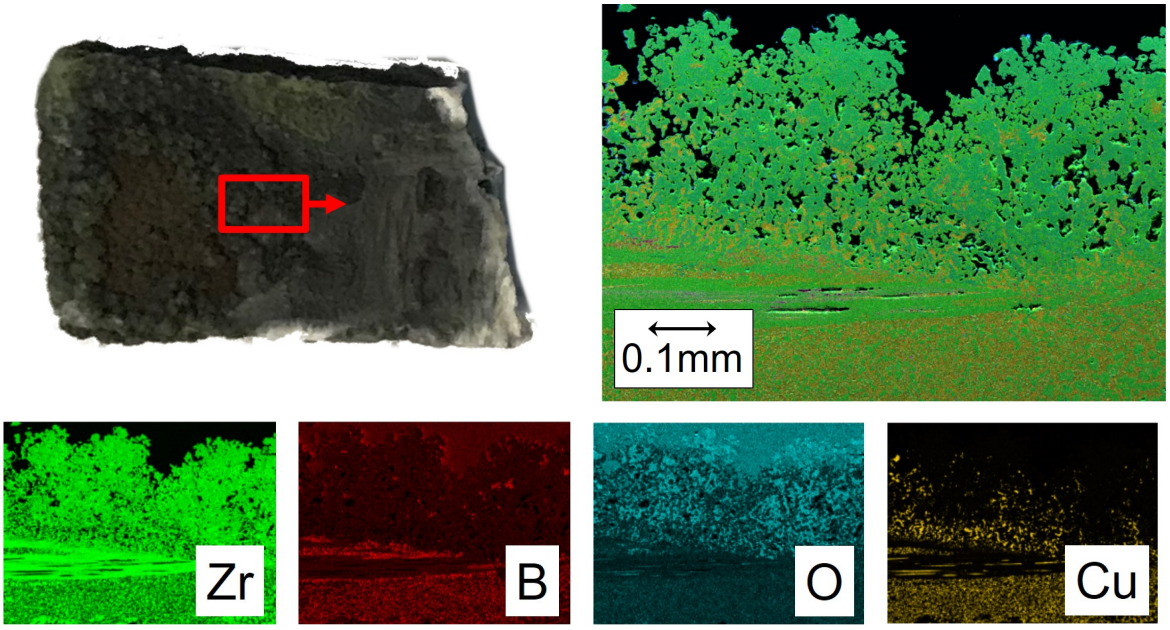

Figure 5.23.: Oxidation of phenolic-based UHTCMC; 2200°C for 5min

oxidation and began to dissolve quickly, especially when the sample surface perpendicular to the fiber plain was unprotected and the sample size was small. Compared to the mechanical performance of the UHTCMC samples, the residual melt helps during oxidation to generate a less porous ZrO_2 layer. Due to the formation of gaseous SiO at the ZrB_2/ZrO_2 interface, Si phases should be avoided in order to keep the oxidation layer from blistering. In terms of oxidation resistance, Zr_9B has the highest potential if the infiltration process and pore structure are adapted to ensure a full infiltration of all fiber bundles.

Passive UHTC powders grow dentrits during infiltration and hence inter connect the RMI matrix, most likely contributing to the damage tolerant behavior of the RMI-UHTCMC. As this increases mechanical properties at room temperature, the goal of UHTCMC are mechanical properties at ultra high temperatures and therefor any residual phases apart from UHTC's should be kept at a minimum. Especially during operation, not reacted phases have to potential to increase wall temperature due to the exothermic reactions. Residual melt, without reacting any B or C to react with, could act as an metal ablator and dissipate heat. This is difficult to achieve when using C fibers as an reinforcement and hence has to be investigated in detail during further oxidation tests.

6. Summary

Advanced technologies, such as hypersonic flight vehicles and fusion reactors, are in need of new materials capable of operating in extreme temperatures. The material class of UHTCs is a viable option to achieve the performance needed for such applications. Current developments of these materials support short duration cases, but are not able to increase ultra high temperature fracture toughness and oxidation.
The adopted RMI process developed as a goal of this research enables the manufacturing of fiber reinforced UHTCMC structures for each of these applications. The major advantage of RMI is the flexibility of preform design, and hence, part geometry and size.
The most critical property of monolithic UHTCs, as with many monolithic ceramics, is their brittle fracture behavior, and therefore, low damage tolerance. This research focuses on the mechanisms known from CMCs and the use of fiber reinforcements to create a pseudo-plastic behavior of a UHTC matrix. With a variety of investigations conducted, ZrB_2 was chosen as the matrix composition to determine the increase in fracture toughness by fiber reinforcements.
Sustaining the fiber reinforcement while the molten Zr fully infiltrates the parts is the key element during manufacturing with regard to process development. As with any RMI process, capillary forces were used to infiltrate a molten alloy into a porous preform. In this study, liquid Zr reacted with B to form the solid ZrB_2 matrix. In order to manufacture large parts, it is vital to sustain the infiltration process without sacrificing performance of the composite. Therefore, effects such as volume expansion, exothermic energy, and wetting behavior as described in chapter 4 must be adopted to produce a UHTC composite. Both C-based and Si-based polymers were examined for preform manufacturing and influence the properties of a UHTCMC. While Si-containing preforms achieve higher mechanical strength at room temperature, Si limits the UHT oxidation resistance. C-based preforms show a slightly lower mechanical performance, 8% bending strength, with a promising oxidation resistance. However, they require an additional B_2O_3 treatment during manufacturing. Both options require a slurry impregnation of the fiber sheets to include B into the preform. Keeping a sufficient porosity and pore distribution while increasing ZrB_2 content requires the right ratio of B powder and precursor. A specific porosity for each preform composition, described in chapter 4, is necessary for the liquid metal to infiltrate far enough into the samples.
Due to the formation of Zr_2Si, Si-based preforms have a lower infiltration temperature limit of 1500 °C in order to keep the volume expansion minimal during infiltration. This limit requires the C fibers to be protected by a fiber coating from Zr_2Cu and Zr_2Ag alloys. With-

out a fiber coating, fiber degradation is too severe and mechanical strength decreases. TiB_2 and ZrB_2 were tested to achieve a sufficient protection for these Zr alloys and exceeded their melting point by far. The CVI process used to coat fibers influences the mechanical strength of the C fibers. SiC fibers do not pose as an alternative to C fibers due to the reaction with the melt and the lack of a mechanical interface. Pitch-based carbon fibers show an important advantage regarding the mechanical fiber/matrix interface, as there is no need for an additional mechanical fiber/matrix interface due to their layered structure and the intrinsic interface generated by these layers. In addition, no fiber coating is required at all when using a C-based preform in combination with a B_2O_3 treatment. The B_2O_3 reacts with the C inside the preform to form a B_4C structure. The absence of Si and the low contact angles on B_4C allow for a reduction of the temperature required for infiltration. B_2O_3 treatment, however, is also potentially subject to fiber degradation, and hence, must be controlled. The local quantity of B_2O_3 must be enclosed inside the polymer or C matrix to ensure no reaction with the carbon fibers. In addition, B_2O_3 can be used to control the volume ratio of ZrB_2 and ZrC inside the matrix.
Using Zr_9B as an alloy allows both preform routs to be used without any fiber coating. The matrix formed during these high infiltration temperatures contains large grain structures. These large grains form at a higher grain growth rate due to the elevated temperatures. In combination with a higher viscosity upon melting, a full infiltration within the fiber bundles is prevented. The large grains can block smaller pore channels, choking the infiltration. The insufficient infiltration limits the mechanical performance at room temperature. However, the alloy itself poses a higher potential to perform at ultra high temperatures.
Based on the operation temperature, different alloy and preform combinations can be used to adopt oxidation resistance and mechanical strength. Without the formation of SiO at the oxidation layer, Si-based preforms can achieve a better oxidation protection at lower temperatures. A graded structure with Cu additions at the cold wall side makes integration of the UHTCMC TPS much easier due to the possibility of brazing and welding.
The key elements of RMI manufacturing UHTCMCs are

- pitch-based carbon fibers due to their intrinsic mechanical interface,
- managing exothermic energy,
- adopting the porosity and pore size distribution,
- adopting the viscosity of the melt, and
- adopting the contact angle of melt and preform.

In addition to the modulus of pitch-based carbon fibers, which increases crack propagation energy itself, their internal graphite layers make them very versatile to increase damage tolerance in ceramic matrices. Each degraded layer during manufacturing decreases the effective fiber diameter, and hence, the ultimate load capability of this fiber, but it does not cause a critical failure of the fiber. There are two ways to limit the peak temperature arising in combination with exothermic energy from the reaction of Zr and B. The first is to decrease temperature when the infiltration is initiated, described as the infiltration temperature. This

involves the adoption of alloy and preform composition in order to prevent effects such as volume expansion. The other method is to limit the amount of energy released from the reaction by replacing active elements like B with passive elements such as ZrB_2. This decreases the total energy release, but also decreases the ultimate temperature reached during infiltration due to the heat capacity of the passive powders.
Without any fiber coating, handling the C fibers is much more flexible, and the RMI-UHTCMC process allows for the fabrication of large TPS tiles and axisymmetric parts. The adoption of parameters for slurry infiltration of fiber sheets can also be used for the impregnation of single rovings during winding. Due to the physical limit of capillary forces, the wall thickness is limited to approximately 50 mm. Width and height of UHTCMC parts is, however, limited by the available furnace dimension.
The oxidation resistance of UHTCMCs is achieved by the composite's matrix. The C fibers themselves pose a weakness regarding their reaction with oxygen. As research continues to further enhance UHTC compositions for oxidation resistance which can be potentially used for the matrix, it's essential to not overlook the design of UHTCMC components regarding oxidation resistance. Wherever applicable, fiber orientation should be perpendicular to surfaces in contact with oxygen, as oxidation progresses much faster along the fiber orientation. The manufactured UHTCMC, either using Zr_9B or Zr_2Cu alloys, develops a ZrO_2 oxidation layer. The use of C fibers does not prevent a homogeneous formation of this protective layer. As described for monolithic UHTCs, the pillar-like structure and oxygen diffusion limit the performance of this ZrO_2 layer. The residual melts within the UHTCMC behave similarly to the liquid SiO_2 glassy phase of monolithic ZrB_2-SiC. At operating temperature, the residual melt becomes liquid and fills the pore structure of the ZrO_2 layer. The most critical side effect is the reaction of liquid residual melt with C fibers, increasing fiber degradation and releasing exothermic energy during operation. UHTCMCs manufactured from Granoc XN-80 0°/90° fabrics without any fiber coating reach around 450 MPa in bending strength at a FVC of 30%. The fracture toughness almost doubles to 10.6 $MPa/m^{1/2}$ when compared to monolithic ZrB_2 UHTCs [23, 25, 59, 62, 90, 116]. Increasing FCV further decreases the density of the composites and increases strength and fracture toughness. The mechanical properties of the manufactured UHTCMC exceed the values necessary to be applied for parts like leading edges, chombustors or control surfaces in hypersonic flight. The developed process can be used to manufacture parts for characterizing the material thoroughly and increase technology readiness level to go into flight testing.

The European project C3HARME investigates different manufacturing techniques in order to fabricate UHTCMC TPS and Nozzle parts. Different research institutes focus on their experience regarding manufacturing of UHTC or CMC materials. In addition to the RMI process by DLR, the University of Birmingham investigates a CVI based approach and Institute of Science and Technology for Ceramics (ISTEC) investigates a sintering approach. Each of these processes have the impregnation of fabric preforms with powder slurries in common.

According to Binner et al. [238] continuous fiber composites have the potential to improve fracture toughness to meet the structural requirements for flight applications. PIP and slurry infiltration are the preferred preform manufacturing routs for these type of composites. Sintering methods, HP and SPS, increase densities and decrease manufacturing times. As with any manufacturing route, the key aspect is to keep the integrity of the fiber reinforcement. High pressure and temperature can be reduced by means of sintering aids, keeping close attention not to reduce the benefits by brittle phase forming on grain or fiber-matrix boundaries. RMI generates residual metal phases inside the composite structure, in addition to metal corrosion of fibers. CVI of all processes uses the lowest temperatures, keeping a high level of fiber integrity. According to Binner et al. [238] the combination of different processes yields the opportunity to further tailor the necessary micro structure and hence properties. Non-brittle character of UHTCMC will only be achieved for well-processed materials and fibers are not damaged during fabrication. For RMI and HP residual stresses are induced between matrix and fibers due to their mismatch of CTE. Binner et al. also note the importance of testing at temperatures present during application for these type of composites and the limited data available so far.

7. Outlook

Future research should concentrate on improving the performance of the current UHTCMCs to the special demands for each application scenario and examine methods of joining or connecting these type of materials to CMCs or metals. This will enable for example a UHTCMC leading edge to be integrated into a full vehicle design. In terms of UHT properties, Zr_9B has the highest potential to achieve higher strength and oxidation resistance above 2000 °C. For cylindrical parts in particular, single roving impregnation such as winding poses an effective option to manufacture nozzles or combustion chambers. In addition, the oxidation performance can be adapted by modifying the matrix composition. This can be achieved either by adding passive powders into the slurry or by using different alloys for infiltration. Y and Ta offer interesting options to stabilize the oxidation layer. Contact angles for a Y-containing alloy were already investigated in this study. Furthermore, the composition of ZrB_2/ZrC or HfB_2/HfC within the matrix can be varied in order to influence mechanical strength and oxidation resistance. As described by Zolli et al. [32], higher modulus pitch-based C fibers show a greater mechanical strength within a ZrB_2 matrix. The high modulus of these fibers decreases the elastic mismatch, and therefore, requires a lower interface fracture energy to prevent fiber failure.

The Cu phases found in the micro structure of the Zr_2Cu infiltrated UHTCMC can be used to tailor the thermal and electric conductivity. This would allow for the investigation of either electric propulsion or heat pipe design TPS.

The methods and rules achieved in this study can also be adapted to manufacture HfB_2-based composites. Monolithic HfB_2 materials provide an even higher oxidation resistance. It must be evaluated for each application whether increased oxidation resistance is required and if the high cost of Hf alloys is justified.

The developed processes in this research established a broad spectra of adapting the UHTCMC properties to various requirements. Examinations can be extended in terms of part manufacturing, which comprises infiltration depth, in-situ bonding, matrix micro structure, and fiber matrix interface optimization. Depending on the application demands, which material properties need further improvement must be evaluated.

Improving the material properties of UHTCMCs will further increase the performance or flight duration of hypersonic vehicles. While the current material enables short duration flight, future UHTCMCs might enables sustained long duration hypersonic flight.

List of Figures

1.1. Applications in need of ultra high temperature properties; ITER Fusion reactor (top) [4], X-51 hypersonic waverider (middle) [5] and re-entry experiment SHEFEX III (bottom) [6] . . . 2
1.2. Schematic of high heat loads for scramjet components . . . 6
1.3. Schematic of heat flux of a blunt and sharp leading edge [14] . . . 6
1.4. Transition from active to passive oxidation of SiC according to Ogasawara et al. [45] in a high enthalpy flow and a low enthalpy flow of Singhal [46] and Balat [47–49] . . . 7

2.1. Material-specific strength as a function of application temperature in an inert atmosphere [102] . . . 13
2.2. Stress-strain curve of monolithic and composite ceramics [104] . . . 14
2.3. Crack front debond diagram indicating the range of relative interface fracture energy in which debonding occurs in preference to fiber failure [107] . . . 15
2.4. Schematic indicating debonding and sliding behaviors that accompany matrix crack propagation in a WIC [107] . . . 16
2.5. Residual tensile strength of Tyranno Fibers after heat-treatment in Argon for 1h [109] . . . 17
2.6. Different types of interfaces in ceramic matrix composites [110]: a) weak fiber/-coating interface, b) interface with a layered crystal structure, c) multi-layer interface and d) porous interface . . . 18
2.7. Temperature-dependent thermal stress resistance parameter for steady-state heat flow [113] . . . 20
2.8. Influence of SiC grain size on strength of ZrB_2-SiC composites [118] . . . 21
2.9. SEM and EDX line of ZrB_2-SiC after oxidation in air at 1627°C for 10 cycles, each 10mins [128] . . . 22
2.10. Schematic of convection cells forming on oxidation of ZrB_2-SiC at 1500-1600 °C, showing the surface covered with cells that have ZrO_2 cores (white) located in larger SiO_2 cells (grey) with B_2O_3 rich patterns (black) surrounding the cores [144] . . . 24

3.1. Contact angle schematic of a sessile drop . . . 29
3.2. Drop shape image of Cu on SiSiC substrate . . . 30
3.3. Schematic of the influence of insulation layer during EPD . . . 31

3.4. Crack opening classes; Mode I under tensile stress, mode II under shear stress perpendicular to the crack opening and mode III under shear stress parallel to the crack opening [159] 35

4.1. Matrix porosity as a function of density before reaction 40
4.2. Temperature influence on volume expansion during infiltration 41
4.3. XRD of a polycarbosilane sample at 1300 °C and 1500 °C 41
4.4. Cu-rich phases forming at the propagating infiltration zone 42
4.5. EDX analysis of TiB_2 substrate after wetting with Zr_2Cu 45
4.6. EDX analysis of TiB_2 substrate after wetting with Zr_2Ag 46
4.7. EDX analysis of TiB_2 substrate after wetting with Zr_2Cu-1 at% B 47
4.8. EDX analysis of TiB_2 substrate after wetting with Zr_2Cu-1 at% C 48
4.9. Contact angle of various Zr-melts on TiB_2 substrate 49
4.10. EDX analysis of TaC substrate after wetting with Zr_2Cu 50
4.11. EDX analysis of TaC substrate after wetting with Zr_2Ag 51
4.12. Contact angle of ZrB_2 substrate and different melts 52
4.13. Contact angle of various Zr-melts on SiC substrate 53
4.14. Contact angle of carbon substrate and various melts 54
4.15. Contact angle of B_4C substrate and various melts 55
4.16. Contact angle of B and B_4C substrate and various melts 56
4.17. Contact angles of various substrates 57
4.18. Schematic of heat flux during RMI 57
4.19. HT-DTA measurement of Zr_2Cu and B powder with and without ZrB_2 addition 58
4.20. Main classes of Si-polymer as precursors for ceramics [192] 59
4.21. Schematic of boron powder formation 60
4.22. Schematic of B powder expansion, with and without controlled distance . . . 61
4.23. Degree of oxidation for various B_4C particle sizes [197] 62
4.24. XRD of boron powder and H_2O_2 treated boron powder 63
4.25. Mass gain of H_2O_2 treated B powder 64
4.26. DSC measurement of epoxy resin 65
4.27. Micro-structure of phenolic a) and polycarbosilane b) resin between fibers after pyrolysis 66
4.28. Comparison of the pore size distribution of polycarbosilane and phenolic resin 67
4.29. Matrix micro-structure before a) and after B_2O_3 infiltration b) 68
4.30. Pore size distribution of pyrolysed polycarbosilane, phenolic resin, and phenolic resin after B_2O_3 infiltration 69
4.31. TG and contact angle analysis of B_2O_3 in an Ar atmosphere 70
4.32. XRD of pyrolysed phenolic samples with and without B_2O_3 infiltration 70
4.33. Pore size distribution of pyrolysed phenolic resin and phenolic resin after B_2O_3 treatments 71

4.34. Schematic of foulard mechanism 73
4.35. Influence of boron suspension on foulard deposition 74
4.36. Pore size distribution of pure B slurry and B/ZrB_2 mixture 77
4.37. Layered structure of a pan-based carbon fiber (HTA), pitch-based (YSH-50), and SiC fiber (SA3) 78
4.38. Mechanical behavior of PAN and pitch-based carbon fibers at elevated temperatures and tensile loading 79
4.39. Decrease in relative RT young's modulus E(T)/E_0 over temperature; E_0 = E (24 °C) 80
4.40. Degradation of a SiC fiber after RMI 81
4.41. TiB_2 fiber coating after a) 2h and b) 4h CVD coating time 81
4.42. Weibull distribution of single filament strength 83
4.43. Influence of fiber volume content on energy release rate fraction over the first Dundurs parameter [214] 84
4.44. Parametric studies of critical matrix cracking stress for multiple matrix cracking cases [216] 85
4.45. Viscosity as a function of temperature at three different shear rates for various melts 88
4.46. Schematic of RMI process 89
4.47. TG analysis of polycarbosilane in Ar atmosphere 90
4.48. TG analysis of phenolic resin in Ar atmosphere 91
4.49. Influence of pyrolysis temperature on mass loss and porosity 92
4.50. Influence of pyrolysis temperature on pore size distribution 93
4.51. Influence of B_2O_3 infiltration on mass loss and porosity 94
4.52. Mass change during pyrolysis and porosity of pure B slurry and B/ZrB_2 mixture 95
4.53. Schematics of lifting mechanism used for RMI 96
4.54. Calculated infiltration height for baseline values 98
4.55. Simulated infiltration height after a) 10,000 sec. and b) 100,000 sec. 98
4.56. Simulated infiltration height with contact angle of a) 1° and b) 70° 99
4.57. Simulated infiltration height with a surface tension of a) 0.12 and b) 12 $\frac{N}{m}$ . . 99
4.58. Simulated infiltration height with melt viscosity of a) 0.02 and b) 2 $Pa \cdot s$ . . 100
4.59. Simulated infiltration height with a choke diameter of a) 1.5 and b) 150 μm . 100
4.60. Cu segregation on annealing UHTCMC sample; a) heated middle section of the sample, b) Cu droplet, and c) small Cu drops forming at lower temperatures off-center on sample 102
4.61. Schematic infiltration process of Zr_2Cu entering a capillary within a B preform 104
4.62. Degradation of carbon fiber a) with plain carbon fibers, b) with adapted RMI process, and c) with TiB_2 fiber coating 106

5.1. Degradation of carbon fiber a) with plain SiC fibers, b) with plain carbon fibers, c) with TiB_2 fiber coating, and d) with adapted RMI process 108
5.2. Intrinsic fiber interface of pitch-based C_f within a UHTC matrix 109
5.3. UHTCMC matrix of polycarbosilane slurry with 40 wt.% and 60 wt.% B after Zr_2Cu infiltration 110
5.4. UHTCMC matrix of phenolic slurry with 30 wt.% and 40 wt.% B after Zr_2Cu infiltration 111
5.5. UHTCMC matrix of phenolic slurry with 40 wt.% B and 40 wt.% B including B_2O_3 treatment after Zr_2Cu infiltration 111
5.6. Matrix variations within the micro structure when using varioius melts and preforms 113
5.7. SEM image during preparation of 3D atom probe sample 114
5.8. 3D atom probe tomography of the ceramic matrix containing Cu 115
5.9. 3D atom probe tomography of the ceramic matrix containing Si 115
5.10. Summary of bending tests from fiber coated UHTCMC samples 116
5.11. Fracture surface after three-point bending of the phenolic preform for each of the three melts 118
5.12. Micro structure of UHTCMC infiltrated with Zr_2Cu-1at%B and without fiber coating 118
5.13. Influence of larger pores in UHTCMC samples without fiber coating, on 3 point bending strength 119
5.14. Fracture surface of UHTCMC infiltrated with Zr_2Cu-1at%B and without fiber coating, after 3PB test 119
5.15. Comparison of UHTCMC micro structure of samples infiltrated with a) Zr_9B and b) Zr_2Cu-1at%B 120
5.16. Influence of melt alloy on UHTCMC tensile strength and Young's modulus . 121
5.17. Influence of melt alloy on UHTCMC compression strength 122
5.18. Fracture toughness of UHTCMC without fiber coating and Zr_2Cu-1at%B infiltration 123
5.19. Fracture surface of UHTCMC infiltrated with Zr_2Cu-1at%B and without fiber coating, after fracture toughness test 123
5.20. Influence of fiber coating on 3PB strength 124
5.21. Oxidation behavior of the RMI UHTC; 1800 °C in stagnant air for 8h 126
5.22. Oxidation of polycarbosilane-based UHTCMC; 2200°C for 5min 127
5.23. Oxidation of phenolic-based UHTCMC; 2200°C for 5min 128

A.1. Analysis of gray scale SEM images for phase analysis; a) showing the gray scale image of a ZrB_2/ZrC matrix and b) the selected gray section of ZrB_2 marked in red 161

List of Tables

2.1. Fiber structures and properties [108] 17

4.1. Stability of boron suspensions 72
4.2. Influence of foulard parameters on boron content 73
4.3. Process combination of foulard and EPD on boron content 75
4.4. Stability of B/ZrB_2 suspensions 76
4.5. Process combination of foulard and EPD on boron content 79
4.6. Influence of fabrics on deposited boron content 80
4.7. Influence of fabrics on deposited boron content by multiple cycles 80
4.8. Mechanical properties, ultimate stress σ_0, and Modulus E of single filament tests 82
4.9. Baseline physical values for calculation of infiltration height 97

5.1. Volume ratio of ZrB_2 and ZrC within the UHTC matrix 112
5.2. Mechanical properties, ultimate stress σ_B, Modulus E and ultimate strain ϵ_B of tested melt and preform combinations; polycarbosilane (PCS) and phenolic (PH) 117
5.3. Mechanical and physical properties of UHTCMCs without fiber coating . . . 125
5.4. Mass change of UHTCMCs during oxidation at 2200 °C for 5min 125

Bibliography

[1] S. J. Zinkle and N. M. Ghoniem, "Operating temperature windows for fusion reactor structural materials," *Fusion Engineering and Design*, vol. 51-52, pp. 55–71, 2000.

[2] K. Ehrlich, "Materials research towards a fusion reactor," *Fusion Engineering and Design*, vol. 56-57, pp. 71–82, 2001.

[3] M. M. Nasseri, "The behavior of HfB2 at neutron irradiation: a simulation study," *Radiation Effects and Defects in Solids*, vol. 171, no. 3-4, pp. 252–258, mar 2016.

[4] Credit ITER Organization (2019, August 13), "ITER." [Online]. Available: https://www.iter.org/doc/all/content/com/gallery/media/7-technical/in-cryostatoverview130116.jpg

[5] VIRIN: 090717-F-0289B-222.JPG, "X-51A Waverider."

[6] C. Dittert, M. Selzer, and H. Böhrk, "Flowfield and pressure decay analysis of porous cones," *AIAA Journal*, vol. 55, no. 3, pp. 874–882, 2017.

[7] T. Reimer, M. Kuhn, A. Gülhan, B. Esser, M. Sippel, and A. van Foreest, "Transpiration cooling tests of porous CMC in hypersonic flow," in *17th AIAA International Space Planes and Hypersonic Systems and Technologies Conference*. San Francisco, California: AIAA, 2011, pp. 1–13.

[8] T. A. Jackson, D. R. Eklund, and A. J. Fink, "High speed propulsion: Performance advantage of advanced materials," *Journal of Materials Science*, vol. 39, no. 19, pp. 5905–5913, 2004.

[9] L. Kaufman and E. V. Clougherty, "Investigation of Boride Compounds for Very High Temperature Applications," ManLabs Inc., Wright-Patterson Air Force Base, Ohio, Tech. Rep., 1965.

[10] E. V. Clougherty and L. Kaufman, "Thermodynamic Study of Synthesis of New Compound Phases Under High Pressure," ManLabs Inc., Cambridge, MA, Tech. Rep., 1968.

[11] E. V. Clougherty, K. E. Wilkes, and R. P. Tye, "Research and development of refractory oxidation-resistant diborides. part 2, volume 5: Thermal, physical, electrical and optical properties," ManLabs Inc., Cambridge, MA, Tech. Rep., 1969.

[12] M. M. Opeka, I. G. Talmy, E. J. Wuchina, J. A. Zaykoski, and S. J. Causey, "Mechanical, Thermal, and Oxidation Properties of Refractory Hafnium and zirconium Compounds," *Journal of the European Ceramic Society*, vol. 19, no. 13–14, pp. 2405–2414, 1999.

[13] E. L. Courtright, H. C. Graham, A. P. Katz, and R. J. Kerans, "Ultra High Temperature Assessment Study - Ceramic Matrix Composites," Pacific Northwest Labotory, Richland, Washington, Tech. Rep., 1992.

[14] M. J. Gasch, D. T. Ellerby, and S. M. Johnson, "Ultra High Temperature Ceramic Composites," in *Handbook of Ceramic Composites*, N. P. Bansal, Ed. Springer US, 2005, pp. 197–224.

[15] H. Moissan, "Investigation of the properties of amorphous boron," *The London, Edinburgh, and Dublin Philosophical Magazine and Journal of Science*, vol. 35, no. 212, p. 80, 1893.

[16] M. H. Moissan, "On a new electrical furnace," *The London, Edinburgh, and Dublin Philosophical Magazine and Journal of Science*, vol. 35, no. 214, pp. 313–314, 1893.

[17] H. Moissan, *La fluor et ses composés*. G. Steinheil, 1900.

[18] S. Auchmuty Tucker and H. R. Moody, "II.—The production of hitherto unknown metallic borides," *Journal of the Chemical Society, Transactions*, vol. 81, pp. 14–17, 1902.

[19] W. Meissner and H. Franz, "Messungen mit Hilfe von flüssigem Helium. IX. Supraleitfähigkeit von Carbiden and Nitriden," *Zeitschrift für Physik*, vol. 65, no. 1-2, pp. 30–54, 1930.

[20] P. M. McKenna, "Tantalum Carbide its Relation to other Hard Refractory Compounds," *Industrial & Engineering Chemistry*, vol. 28, no. 7, pp. 767–772, 1936.

[21] R. Kiessling, "A method for preparing boron of high purity," *Acta Chemica Scandinavica*, vol. 2, pp. 707–712, 1948.

[22] A. L. Chamberlain, W. G. Fahrenholtz, G. E. Hilmas, and D. T. Ellerby, "High-Strength Zirconium Diboride-Based Ceramics," *Journal of the American Ceramic Society*, vol. 87, no. 6, pp. 1170–1172, jun 2004.

[23] F. Monteverde, S. Guicciardi, and A. Bellosi, "Advances in microstructure and mechanical properties of zirconium diboride based ceramics," *Materials Science and Engineering: A*, vol. 346, no. 1–2, pp. 310–319, apr 2003.

[24] J. K. Kurihara, T. Tomimatsu, Y. F. Liu, S. Q. Guo, and Y. Kagawa, "Mode I fracture toughness of SiC particle-dispersed ZrB2 matrix composite measured using DCDC specimen," *Ceramics International*, vol. 36, no. 1, pp. 381–384, 2010.

[25] F. Monteverde and L. Scatteia, "Resistance to Thermal Shock and to Oxidation of Metal Diborides–SiC Ceramics for Aerospace Application," *Journal of the American Ceramic Society*, vol. 90, no. 4, pp. 1130–1138, apr 2007.

[26] I. G. Talmy, J. A. Zaykoski, and M. M. Opeka, "High-Temperature Chemistry and Oxidation of ZrB2 Ceramics Containing SiC, Si3N4, Ta5Si3, and TaSi2," *Journal of the American Ceramic Society*, vol. 91, no. 7, pp. 2250–2257, jul 2008.

[27] J. L. Watts, "Stress Measurement and Development of Zirconium Diboride - Silicon Carbide Ceramics," Ph.D. dissertation, Missouri University of Science and Technology, 2011.

[28] G. Samsonov and I. M. Vinitskii, *Handbook of Refractory Compounds.* New York: Springer, 1980.

[29] J. W. Zimmermann, G. E. Hilmas, W. G. Fahrenholtz, R. B. Dinwiddie, W. D. Porter, and H. Wang, "Thermophysical Properties of ZrB2 and ZrB2–SiC Ceramics," *Journal of the American Ceramic Society*, vol. 91, no. 5, pp. 1405–1411, may 2008.

[30] H. Kinoshita, S. Otani, S. Kamiyama, H. Amano, I. Akasaki, J. Suda, and H. Matsunami, "Zirconium Diboride (0001) as an Electrically Conductive Lattice-Matched Substrate for Gallium Nitride," *Japanese Journal of Applied Physics*, vol. 40, no. 12A, p. L1280, 2001.

[31] M. Rahman, C. C. Wang, W. Chen, S. A. Akbar, and C. Mroz, "Electrical Resistivity of Titanium Diboride and Zirconium Diboride," *Journal of the American Ceramic Society*, vol. 78, no. 5, pp. 1380–1382, may 1995.

[32] L. Zoli and D. Sciti, "Efficacy of a ZrB2–SiC matrix in protecting C fibres from oxidation in novel UHTCMC materials," *Materials & Design*, vol. 113, pp. 207–213, 2017.

[33] A. Paul, D. D. Jayaseelan, and W. Lee, "UHTC composites for hypersonic applications," *The American Ceramic Society Bulletin*, vol. 91, no. 1, pp. 22–28, 2011.

[34] A. Paul, V. Rubio, J. Binner, B. Vaidhyanathan, A. Heaton, and P. Brown, "Evaluation of the high temperature performance of HfB2 UHTC particulate filled Cf/C composites," *International Journal of Applied Ceramic Technology*, vol. 14, no. 3, pp. 344–353, 2017.

[35] M. Kütemeyer, D. Shandler, D. Koch, and M. Friess, "Reactive melt infiltration of boron containing fiber reinforced preforms forming a zrb2 matrix," *Processing and Properties of Advanced Ceramics and Composites VII: Ceramic Transactions, Volume 252*, pp. 169–180, 2015.

[36] M. Kütemeyer, L. Schomer, T. Helmreich, S. Rosiwal, and D. Koch, "Fabrication of ultra high temperature ceramic matrix composites using a reactive melt infiltration process," *Journal of the European Ceramic Society*, vol. 36, no. 15, pp. 3647–3655, nov 2016.

[37] D. Glass, *Physical Challenges and Limitations Confronting the Use of UHTCs on Hypersonic Vehicles*, pp. 2011–2304. [Online]. Available: https://arc.aiaa.org/doi/abs/10.2514/6.2011-2304

[38] R. Loehman, E. L. Corral, H. P. Dumm, P. Kotula, and R. Tandon, "Ultra High Temperature Ceramics for Hypersonic Vehicle Applications," Sandia National Laboratories, Tech. Rep., 2006.

[39] M. M. Opeka, I. G. Talmy, and J. A. Zaykoski, "Oxidation-based materials selection for 2000°C + hypersonic aerosurfaces : Theoretical considerations and historical experience," *Journal of Materials Science*, vol. 39, pp. 5887–5904, 2004.

[40] L. Scatteia, R. Borrelli, G. Marino, A. Bellosi, and F. Monteverde, "Characterization and process of new metal diboride compound for TPS applications," in *AIAA/CIRA 13th International Space Planes and Hypersonic Systems and Technology Conference*, Capua, Italy, 2005.

[41] C. Dittert and M. Kütemeyer, "OCTRA-Optimized Ceramic for Hypersonic Application with Transpiration Cooling," *Advances in High Temperature Ceramic Matrix Composites and Materials for Sustainable Development*, vol. 263, p. 389, 2017.

[42] D. E. Glass, D. Capriotti, T. Reimer, M. Kütemeyer, and M. Smart, "Testing of DLR C/C-SiC and C/C for HIFiRE 8 Scramjet Combustor," *19th AIAA International Space Planes and Hypersonic Systems and Technologies Conference*, jun 2014.

[43] V. Wartemann, A. Wagner, and T. Eggers, "Passive Hypersonic Boundary Layer Control: The Potential of an Ultrasonically Absorptive Ceramic for HEXAFLY-INT," in *8th AIAA Flow Control Conference*, 2016.

[44] J. Steelant, T. Langener, F. Di Matteo, K. Hannemann, J. Riehmer, M. Kuhn, C. Dittert, F. Scheuerpflug, W. Jung, M. Marini, G. Pezzella, M. Cicala, and L. Serre, "Conceptual Design of the High-speed propelled experimental Flight Test Vehicle HEXAFLY," in *20th AIAA International Space Planes and Hypersonic Systems and Technologies Conference*, Glasgow, Scotland, 2015.

[45] T. Ogasawara, T. Ishikawa, and T. Matsuzaki, "Thermal Response and Oxidation of Tyranno™-Fiber-Reinforced Si-Ti-C-O Matrix Composites for a Thermal Protection System in High-Enthalpy Dissociated Air," *Journal of the American Ceramic Society*, vol. 86, no. 5, pp. 830–837, 2003.

[46] S. C. Singhal, "Thermodynamic analysis of the high-temperature stability of silicon nitride and silicon carbide," *Ceramurgia International*, vol. 2, no. 3, pp. 123–130, 1976.

[47] M. Balat, G. Flamant, G. Male, and G. Pichelin, "Active to passive transition in the oxidation of silicon carbide at high temperature and low pressure in molecular and atomic oxygen," *Journal of Materials Science*, vol. 27, no. 3, pp. 697–703, 1992.

[48] M. Balat, "Determination of the active-to-passive transition in the oxidation of silicon carbide in standard and microwave-excited air," *Journal of the European Ceramic Society*, vol. 16, no. 1, pp. 55–62, 1996.

[49] M. Balat-Pichelin, L. Charpentier, F. Panerai, O. Chazot, B. Helber, and K. Nickel, "Passive/active oxidation transition for CMC structural materials designed for the IXV vehicle re-entry phase," *Journal of the European Ceramic Society*, vol. 35, no. 2, pp. 487–502, 2015.

[50] L. Brewer, D. L. Sawyer, D. H. Templeton, and C. H. Dauben, "A study of the refractory borides," *Journal of the American Ceramic Society*, vol. 34, no. 6, pp. 173–179, 1951.

[51] P. Schwarzkopf, R. Kieffer, and F. Benesousky, *Refractory hard metals: Borides, carbides, nitrides and silicides.* New York: Macmillan, 1953.

[52] R. Kiessling, "The binary system zirconium-boron," *Acta Chem. Scand*, vol. 3, no. 1, pp. 90–91, 1949.

[53] G. A. Meerson and G. V. Samsonov, "Preparation of the borides of high melting metals by the vacuum thermal process," *Zh. Prikl. Khim*, vol. 27, p. 1115, 1954.

[54] G. V. Samsonov and K. I. Portnoy, *Alloys based on high-melting compounds.* Wright-Patterson AFB, Ohio: Foreign Technology Division, Translation Services Branch, 1962, vol. 62, no. 430.

[55] S. Henderson, W. G. Fahrenholtz, G. E. Hilmas, and J. Marschall, *High-Velocity Impact Resistance of ZrB2-SiC.* John Wiley & Sons, Ltd, 2006, ch. 1, pp. 3–9. [Online]. Available: https://ceramics.onlinelibrary.wiley.com/doi/abs/10.1002/9780470291313.ch1

[56] A. Rezaie, W. G. Fahrenholtz, and G. E. Hilmas, "Effect of hot pressing time and temperature on the microstructure and mechanical properties of ZrB2–SiC," *Journal of Materials Science*, vol. 42, no. 8, pp. 2735–2744, 2007.

[57] H. Zhang, Y. Yan, Z. Huang, X. Liu, and D. Jiang, "Properties of ZrB2–SiC Ceramics by Pressureless Sintering," *Journal of the American Ceramic Society*, vol. 92, no. 7, pp. 1599–1602, jul 2009.

[58] A. L. Chamberlain, W. G. Fahrenholtz, and G. E. Hilmas, "Low-Temperature Densification of Zirconium Diboride Ceramics by Reactive Hot Pressing," *Journal of the American Ceramic Society*, vol. 89, no. 12, pp. 3638–3645, dec 2006.

[59] F. Monteverde and A. Bellosi, "Effect of the addition of silicon nitride on sintering behaviour and microstructure of zirconium diboride," *Scripta Materialia*, vol. 46, no. 3, pp. 223–228, feb 2002.

[60] S. Baik and P. F. Becher, "Effect of Oxygen Contamination on Densification of TiB2," *Journal of the American Ceramic Society*, vol. 70, no. 8, pp. 527–530, aug 1987.

[61] E. V. Clougherty, L. Kaufman, and D. Kalish, "Refractory Diboride Materials," nov 1973.

[62] F. Monteverde and A. Bellosi, "Development and characterization of metal-diboride-based composites toughened with ultra-fine SiC particulates," *Solid state sciences*, vol. 7, no. 5, pp. 622–630, 2005.

[63] H. Wang, C.-A. Wang, X. Yao, and D. Fang, "Processing and mechanical properties of zirconium diboride-based ceramics prepared by spark plasma sintering," *Journal of the American Ceramic Society*, vol. 90, no. 7, pp. 1992–1997, 2007. [Online]. Available: https://ceramics.onlinelibrary.wiley.com/doi/abs/10.1111/j.1551-2916.2007.01665.x

[64] G. Zhang, Z. Deng, N. Kondo, J. Yang, and T. Ohji, "Reactive hot pressing of ZrB2–SiC composites," *Journal of the American Ceramic Society*, vol. 83, no. 9, pp. 2330–2332, 2000.

[65] W.-W. Wu, G.-J. Zhang, Y.-M. Kan, P.-L. Wang, K. Vanmeensel, J. Vleugels, and O. van der Biest, "Synthesis and microstructural features of ZrB2–SiC-based composites by reactive spark plasma sintering and reactive hot pressing," *Scripta Materialia*, vol. 57, no. 4, pp. 317–320, 2007.

[66] W. G. Fahrenholtz, "Reactive Processing in Ceramic-Based Systems," *International journal of applied ceramic technology*, vol. 3, no. 1, pp. 1–12, 2006.

[67] A. L. Chamberlain, W. G. Fahrenholtz, and G. E. Hilmas, "Reactive hot pressing of zirconium diboride," *Journal of the European Ceramic Society*, vol. 29, no. 16, pp. 3401–3408, 2009.

[68] F. Monteverde, "Progress in the fabrication of ultra-high-temperature ceramics: "in situ" synthesis, microstructure and properties of a reactive hot-pressed HfB2–SiC composite," *Composites Science and Technology*, vol. 65, no. 11-12, pp. 1869–1879, 2005.

[69] K. Lu, "Sintering of nanoceramics," *International Materials Reviews*, vol. 53, no. 1, pp. 21–38, jan 2008.

[70] K. Su and L. G. Sneddon, “A polymer precursor route to metal borides,” *Chemistry of Materials*, vol. 5, no. 11, pp. 1659–1668, nov 1993.

[71] H. O. Pierson and A. W. Mullendore, “Thick boride coatings by chemical vapor deposition,” *Thin Solid Films*, vol. 95, no. 2, pp. 99–104, sep 1982.

[72] A. L. Wayda, L. F. Schneemeyer, and R. L. Opila, “Low-temperature deposition of zirconium and hafnium boride films by thermal decomposition of the metal borohydrides (M[BH4]4),” *Applied Physics Letters*, vol. 53, no. 5, 1988.

[73] J. A. Jensen, J. E. Gozum, D. M. Pollina, and G. S. Girolami, “Titanium, zirconium, and hafnium tetrahydroborates as "tailored" CVD precursors for metal diboride thin films,” *Journal of the American Chemical Society*, vol. 110, no. 5, pp. 1643–1644, 1988.

[74] T. Takahashi and H. Itoh, “Ultrasonic chemical vapor deposition of TiB2 thick films,” *Journal of Crystal Growth*, vol. 49, no. 3, pp. 445–450, jul 1980.

[75] T. Shikama, Y. Sakai, M. Fukutomi, and M. Okada, “Deposition of TiB2 films by a co-sputtering method,” *Thin Solid Films*, vol. 156, no. 2, pp. 287–294, jan 1988.

[76] V. Rubio, J. Binner, S. Cousinet, G. Le Page, T. Ackerman, A. Hussain, P. Brown, and I. Dautremont, “Materials characterisation and mechanical properties of Cf-UHTC powder composites,” *Journal of the European Ceramic Society*, vol. 39, no. 4, pp. 813–824, 2019.

[77] V. Rubio, P. Ramanujam, and J. Binner, “Ultra-high temperature ceramic composite,” *Advances in Applied Ceramics*, vol. 117, no. sup1, pp. S56–S61, 2018.

[78] F. F. Lange, “Colloidal processing of powder for reliable ceramics,” *Current Opinion in Solid State and Materials Science*, vol. 3, no. 5, pp. 496–500, oct 1998.

[79] W. M. Sigmund, N. S. Bell, and L. Bergström, “Novel Powder-Processing Methods for Advanced Ceramics,” *Journal of the American Ceramic Society*, vol. 83, no. 7, pp. 1557–1574, jul 2000.

[80] C. Tallon, D. Chavara, A. Gillen, D. Riley, L. Edwards, S. Moricca, and G. V. Franks, “Colloidal Processing of Zirconium Diboride Ultra-High Temperature Ceramics,” *Journal of the American Ceramic Society*, vol. 96, no. 8, pp. 2374–2381, aug 2013.

[81] T. Huang, G. E. Hilmas, W. G. Fahrenholtz, and M. C. Leu, “Dispersion of Zirconium Diboride in an Aqueous, High-Solids Paste,” *International Journal of Applied Ceramic Technology*, vol. 4, no. 5, pp. 470–479, oct 2007.

[82] S.-H. Lee, Y. Sakka, and Y. Kagawa, “Dispersion Behavior of ZrB2 Powder in Aqueous Solution,” *Journal of the American Ceramic Society*, vol. 90, no. 11, pp. 3455–3459, nov 2007.

[83] V. Medri, P. Pinasco, A. Sanson, E. Roncari, S. Guicciardi, and A. Bellosi, "ZrB2-Based Laminates Produced by Tape Casting," *International Journal of Applied Ceramic Technology*, vol. 9, no. 2, pp. 349–357, mar 2012.

[84] S. L. Natividad, V. R. Marotto, L. S. Walker, D. Pham, W. Pinc, and E. L. Corral, "Tape Casting Thin, Continuous, Homogenous, and Flexible Tapes of ZrB2," *Journal of the American Ceramic Society*, vol. 94, no. 9, pp. 2749–2753, sep 2011.

[85] Z. Lü, D. Jiang, J. Zhang, and Q. Lin, "Aqueous Tape Casting of Zirconium Diboride," *Journal of the American Ceramic Society*, vol. 92, no. 10, pp. 2212–2217, oct 2009.

[86] C. J. Leslie, E. E. Boakye, K. A. Keller, and M. K. Cinibulk, "Development and Characterization of Continuous SiC Fiber-Reinforced HfB2-Based UHTC Matrix Composites Using Polymer Impregnation and Slurry Infiltration Techniques," *International Journal of Applied Ceramic Technology*, vol. 12, no. 1, pp. 235–244, 2015.

[87] Q. Li, S. Dong, Z. Wang, and G. Shi, "Fabrication and properties of 3-D Cf/ZrB2–ZrC–SiC composites via polymer infiltration and pyrolysis," *Ceramics International*, vol. 39, no. 5, pp. 5937–5941, jul 2013.

[88] Y. Wang, W. Liu, L. Cheng, and L. Zhang, "Preparation and properties of 2d c/zrb2-sic ultra high temperature ceramic composites," *Materials Science and Engineering: A*, vol. 524, no. 1, pp. 129–133, 2009, special Topic Section: Probing strains and Dislocation Gradients with diffraction. [Online]. Available: http://www.sciencedirect.com/science/article/pii/S0921509309007527

[89] L. Li, Y. Wang, L. Cheng, and L. Zhang, "Preparation and properties of 2D C/SiC–ZrB2–TaC composites," *Ceramics International*, vol. 37, no. 3, pp. 891–896, apr 2011.

[90] S. Zhang, S. Wang, Wei Li, Yulin Zhu, and Zhaohui Chen, "Preparation of ZrB2 based composites by reactive melt infiltration at relative low temperature," *Materials Letters*, vol. 65, no. 19–20, pp. 2910–2912, 2011.

[91] M. B. Dickerson, R. L. Snyder, and K. H. Sandhage, "Dense, Near Net-Shaped, Carbide/Refractory Metal Composites at Modest Temperatures by the Displacive Compensation of Porosity (DCP) Method," *Journal of the American Ceramic Society*, vol. 85, no. 3, pp. 730–732, 2002.

[92] W. Krenkel, "Development of a cost efficient process for the manufacture of CMC components," Dissertation, University of Stuttgart, 2000.

[93] F. H. Gern, "Capillarity and Infiltration Dynamics of Liquid Siliconized Carbon/Carbon Components," Dissertation, University of Stuttgart, 1995.

[94] E. Klatt, "Development of High Temperature Resistant Ceramic Matrix Composites Based on SiC- and Novel SiBNC-Fibres," Dissertation, University of Stuttgart, 2014.

[95] J. Happel and H. Brenner, *Low Reynolds Number Hydrodynamics.* Dordrecht, Netherlands: Martinus Nijhoff, 1983.

[96] H. Schade, E. Kunz, F. Kameier, and C. O. Paschereit, *Stroemungslehre*, walter de ed., Berlin, 2013.

[97] V. Levich, *Physicochemical Hydrodynamics.* Englewood Cliffs, N.J.: Prentice Hall, 1962.

[98] M. Muolo, E. Ferrera, R. Novakovic, and A. Passerone, "Wettability of zirconium diboride ceramics by Ag, Cu and their alloys with Zr," *Scripta Materialia*, vol. 48, no. 2, pp. 191–196, jan 2003.

[99] R. Voytovych, A. Koltsov, F. Hodaj, and N. Eustathopoulos, "Reactive vs non-reactive wetting of ZrB2 by azeotropic Au–Ni," *Acta Materialia*, vol. 55, no. 18, pp. 6316–6321, oct 2007.

[100] A. Passerone, M. L. Muolo, R. Novakovic, and D. Passerone, "Liquid metal/ceramic interactions in the (Cu, Ag, Au)/ZrB2 systems," *Journal of the European Ceramic Society*, vol. 27, no. 10, pp. 3277–3285, jan 2007.

[101] D. A. Mortimer and M. Nicholas, "The wetting of carbon by copper and copper alloys," *Journal of Materials Science*, vol. 5, no. 2, pp. 149–155, 1970.

[102] W. Schäfer and W. D. Vogel, *Faserverstärkte Keramiken hergestellt durch Polymerinfiltration.* John Wiley & Sons, Ltd, 2002, pp. 76–94. [Online]. Available: https://onlinelibrary.wiley.com/doi/abs/10.1002/3527607315.ch4

[103] A. A. Griffith, "The phenomena of rupture and flow in solids," *Philosophical transactions of the royal society of london. Series A, containing papers of a mathematical or physical character*, vol. 221, no. 1921, pp. 163–198, 1921.

[104] R. L. Lehman, S. K. El-Rahaiby, and J. B. Wachtman Jr, "Handbook on Continuous Fiber-Reinforced Ceramic Matrix Composites," Ceramics Information Analysis Center, West Lafayette, Indiana, Tech. Rep., 1995.

[105] D. Koch, "Microstructural Modeling and Thermomechanical Properties," *Ceramic Matrix Composites: Fiber Reinforced Ceramics and their Applications*, pp. 231–259, 2008.

[106] M.-Y. He and J. W. Hutchinson, "Kinking of a crack out of an interface," *Journal of Applied Mechanics*, vol. 56, no. 2, pp. 270–278, 1989.

[107] A. G. Evans, M. Y. He, and J. W. Hutchinson, “Interface debonding and fiber cracking in brittle matrix composites,” *Journal of the American Ceramic Society*, vol. 72, no. 12, pp. 2300–2303, 1989.

[108] H. Blumberg, “Die Zukunft der neuen Hochleistungsfasern,” *Chemiefasern/Textilindustrie*, vol. 34, no. 86, p. 808 ff, 1984.

[109] “UBE Industries LTD. (Yamaguchi, Japan): Tyranno Fiber (2017, June 14).” [Online]. Available: http://www.upilex.jp/catalog/pdf/tyranno_fiber_e.pdf

[110] R. R. Naslain, “The design of the fibre-matrix interfacial zone in ceramic matrix composites,” *Composites Part A: Applied Science and Manufacturing*, vol. 29, no. 9, pp. 1145–1155, 1998.

[111] B. Mainzer, R. Jemmali, P. Watermeyer, K. Kelm, M. Frieß, and D. Koch, “Development of damage-tolerant ceramic matrix composites (SiC/ SiC) using Si-BN/SiC/pyC fiber coatings and LSI processing,” *Journal of Ceramic Science and Technology*, vol. 8, no. 1, pp. 113–120, 2017.

[112] E. V. Clougherty, E. T. Peters, and D. Kalish, “Diboride Materials, Candidates for Aerospace Applications,” *Sci. Advan. Mater. Process Eng. Proc.*, vol. 15, pp. 297–308, 1969.

[113] “Strength, Fracture Mode, and Thermal Stress Resistance of HfB2 and ZrB2,” *Journal of the American Ceramic Society*, vol. 52, no. 1, pp. 30–36, jan 1969.

[114] L. Kaufman, E. V. Clougherty, and J. B. Berkowitz-Mattuck, “Oxidation Characteristics of Hafnium and Zirconium Diboride,” *Trans. Met. Soc. AIME*, vol. 239, no. 458-66, 1967.

[115] J. S. Haggerty and D. W. Lee, “Plastic Deformation of ZrB2 Single Crystals,” *Journal of the American Ceramic Society*, vol. 54, no. 11, pp. 572–576, nov 1971.

[116] F. Monteverde, A. Bellosi, and S. Guicciardi, “Processing and properties of zirconium diboride-based composites,” *Journal of the European Ceramic Society*, vol. 22, no. 3, pp. 279–288, mar 2002.

[117] W.-M. Guo and G.-J. Zhang, “Oxidation resistance and strength retention of ZrB2–SiC ceramics,” *Journal of the European Ceramic Society*, vol. 30, no. 11, pp. 2387–2395, 2010.

[118] S. Zhu, W. G. Fahrenholtz, and G. E. Hilmas, “Influence of silicon carbide particle size on the microstructure and mechanical properties of zirconium diboride–silicon carbide ceramics,” *Journal of the European Ceramic Society*, vol. 27, no. 4, pp. 2077–2083, 2007.

[119] W. B. Johnson, T. D. Claar, and G. H. Schiroky, "Preparation and processing of platelet-reinforced ceramics by the directed reaction of zirconium with boron carbide," in *13th Annual Conference on Composites and Advanced Ceramic Materials, Part 1 of 2: Ceramic Engineering and Science Proceedings, Volume 10*, no. 7-8. John Wiley & Sons, 2009, p. 588.

[120] C. A. Hoffman, "Preliminary Investigation of Zirconium Boride Ceramals for Gas-Turbine Blade Applications," Lewis Flight Propulsion Lab., NACA, Tech. Rep., 1953.

[121] J. B. Berkowitz-Mattuck, "High-Temperature Oxidation III. Zirconium and Hafnium Diborides," *Journal of the Electrochemical Society*, vol. 113, no. 9, pp. 908–914, 1966.

[122] L. Kaufman and H. Nesor, "Stability Characterization of Refractory Materials under High Velocity Atmospheric Flight Conditions, Part I, Vol. I, Summary," Tech. Rep., 1970.

[123] L. Kaufman, *Boride Composites: A New Generation of Nose Cap and Leading Edge Materials for Reuseable Lifting Re-entry Systems.* American Institute of Aeronautics and Astronautics, 1970.

[124] W. C. Tripp and H. C. Graham, "Thermogravi metric Study of the Oxidation of ZrB2 in the Temperature Range of 800° to 1500° C," *Journal of the Electrochemical Society*, vol. 118, no. 7, pp. 1195–1199, 1971.

[125] W. C. Tripp, H. H. Davis, and H. C. Graham, "Effect of an SiC Addition on the Oxidation of ZrB2," *American Ceramic Society*, vol. 52, no. 8, pp. 612–616, 1973.

[126] M. Gasch, D. Ellerby, E. Irby, S. Beckman, M. Gusman, and S. Johnson, "Processing, properties and arc jet oxidation of hafnium diboride/silicon carbide ultra high temperature ceramics," *Journal of Materials Science*, vol. 39, pp. 5925–5937, 2004.

[127] P. Kolodziej, J. V. Bowles, and C. Roberts, "Optimizing hypersonic sharp body concepts from a thermal protection system perspective," in *8th AIAA International Space Planes and Hypersonic Systems and Technologies Conference*, Norfolk,VA,U.S.A., 1998, pp. 98–1610.

[128] S. R. Levine, E. J. Opila, M. C. Halbig, J. D. Kiser, M. Singh, and J. A. Salem, "Evaluation of ultra-high temperature ceramics foraeropropulsion use," *Journal of the European Ceramic Society*, vol. 22, no. 14-15, pp. 2757–2767, 2002.

[129] Q. N. Nguyen, E. J. Opila, and R. C. Robinson, "Oxidation of ultrahigh temperature ceramics in water vapor," *Journal of the Electrochemical Society*, vol. 151, no. 10, pp. B558–B562, 2004.

[130] E. Opila, S. Levine, and J. Lorincz, "Oxidation of ZrB2- and HfB2-based ultra-high temperature ceramics: Effect of Ta additions," *Journal of Materials Science*, vol. 39, pp. 5969–5977, 2004.

[131] W. G. Fahrenholtz, "Thermodynamic Analysis of ZrB2–SiC Oxidation: Formation of a SiC-Depleted Region," *Journal of the American Ceramic Society*, vol. 90, no. 1, pp. 143–148, 2007.

[132] I. G. Talmy, J. A. Zaykoski, M. M. Opeka, and A. H. Smith, "Properties of ceramics in the system ZrB2–Ta5Si3," *Journal of materials research*, vol. 21, no. 10, pp. 2593–2599, 2006.

[133] I. G. Talmy, J. A. Zaykoski, and M. A. Opeka, "Properties of ceramics in the ZrB2/ZrC/SiC system prepared by reactive processing," in *22nd Annual Conference on Composites, Advanced Ceramics, Materials, and Structures-A: Ceramic Engineering and Science Proceedings*, vol. 218. John Wiley & Sons, 2009, p. 105.

[134] F. Monteverde and A. Bellosi, "Oxidation of ZrB2-based ceramics in dry air," *Journal of the Electrochemical Society*, vol. 150, no. 11, pp. B552–B559, 2003.

[135] J. Han, P. Hu, X. Zhang, S. Meng, and W. Han, "Oxidation-resistant ZrB2–SiC composites at 2200˜°C," *Composites Science and Technology*, vol. 68, no. 3-4, pp. 799–806, 2008.

[136] F. Monteverde and A. Bellosi, "The resistance to oxidation of an HfB 2–SiC composite," *Journal of the European Ceramic Society*, vol. 25, no. 7, pp. 1025–1031, 2005.

[137] W. G. Fahrenholtz, "The ZrB2 volatility diagram," *Journal of the American Ceramic Society*, vol. 88, no. 12, pp. 3509–3512, 2005.

[138] A. K. Kuriakose and J. L. Margrave, "The Oxidation Kinetics of Zirconium Diboride and Zirconium Carbide at High Temperatures," *Journal of The Electrochemical Society*, vol. 111, no. 7, pp. 827–831, 1964.

[139] F. Monteverde, "The thermal stability in air of hot-pressed diboride matrix composites for uses at ultra-high temperatures," *Corrosion science*, vol. 47, no. 8, pp. 2020–2033, 2005.

[140] P. C. Setze, *A Review of the Physical and Thermodynamic Properties of Boric Oxide*. National Advisory Committee for Aeronautics, 1957.

[141] A. Rezaie, W. G. Fahrenholtz, and G. E. Hilmas, "Oxidation of zirconium diboride–silicon carbide at 1500°C at a low partial pressure of oxygen," *Journal of the American Ceramic Society*, vol. 89, no. 10, pp. 3240–3245, 2006.

[142] F. Monteverde, "Beneficial effects of an ultra-fine alpha-SiC incorporation on the sinterability and mechanical properties of ZrB2," *Applied Physics A: Materials Science & Processing*, vol. 82, pp. 329–337, 2006.

[143] R. Telle, "Boride and carbide ceramics," *Materials science and technology*, 1994.

[144] S. N. Karlsdottir, "Oxidation behavior of zirconium diboride-silicon carbide composites at high temperatures," Ph.D. dissertation, University of Michigan, Michigan, 2007.

[145] B. Esser and A. Gülhan, "Flow Field Characterisation of DLR's Arc Heated Facilities L2K and L3K," in *Aerothermodynamics for space vehicles*, vol. 426, 1999, p. 545.

[146] DIN EN 993-1:2019-03, *Methods of test for dense shaped refractory products - Part 1: Determination of bulk density, apparent porosity and true porosity; German version*, Berlin: Beuth.

[147] DIN EN 1389:2004-03, *Advanced technical ceramics - Ceramic composites - Physical properties - Determination of density and apparent porosity; German version*, Berlin: Beuth.

[148] DIN ISO 15901-1:2019-03, *Evaluation of pore size distribution and porosity of solid materials by mercury porosimetry and gas adsorption - Part 1: Mercury porosimetry*, Berlin: Beuth.

[149] E. W. Washburn, "The dynamics of capillary flow," *Physical Review*, vol. 17, no. 3, pp. 273–283, 1921.

[150] T. Young, "Iii. an essay on the cohesion of fluids," *Philosophical Transactions of the Royal Society of London*, vol. 95, pp. 65–87, 1805. [Online]. Available: https://royalsocietypublishing.org/doi/abs/10.1098/rstl.1805.0005

[151] L. Besra and M. Liu, "A review on fundamentals and applications of electrophoretic deposition (EPD)," vol. 52, no. 1, pp. 1–61, 2007. [Online]. Available: http://www.sciencedirect.com/science/article/pii/S0079642506000387

[152] A. Goldschmidt and H.-J. Streitberger, *BASF-Handbuch Lackiertechnik*. Hannover: Vincentz Network GmbH & Co KG, 2002.

[153] S. Vogel, "Prozessentwicklung zur elektrophoretischen Abscheidung keramischer Schichten und Mikrostrukturen," Dissertation, University of Freiburg (Breisgau), 2010.

[154] J. Zeiner, "Untersuchungen zur herstellung von mikrostrukturen aus nanoskaligen pulvern mittels elektrophoretischer abscheidung," Dissertation, Saarland University, 2007. [Online]. Available: http://dx.doi.org/10.22028/D291-22409

[155] DIN 51006:2005-07, *Thermische Analyse (TA) - Thermogravimetrie (TG) - Grundlagen*, Berlin: Beuth.

[156] R. F. Egerton, "The Scanning Electron Microscope," in *Physical Principles of Electron Microscopy*. Springer, Cham., 2016, vol. 56, pp. 121–147. [Online]. Available: https://doi.org/10.1007/978-3-319-39877-8_5

[157] H. Stanjek and W. Häusler, "Basics of X-ray diffraction," *Hyperfine Interactions*, vol. 154, no. 1-4, pp. 107–119, 2004.

[158] DIN EN 658-3:2002-11, *Advanced technical ceramics - Mechanical properties of ceramic composites at room temperature - Part 3: Determination of flexural strength*, Berlin: Beuth.

[159] J. Riesch, "Entwicklung und Charakterisierung eines wolframfaserverstärkten Wolfram-Verbundwerkstoffs," Dissertation, Technical University of Munich, 2013.

[160] J. Rösler, H. Harders, and M. Bäker, *Mechanisches Verhalten der Werkstoffe*. Wiesbaden: Springer Vieweg, 2012.

[161] H. Salmang, *Physikalische und chemische Grundlagen der Keramik*, 3rd ed., H. Höppli, Ed. Springer-Verlag, Berlin, 2007.

[162] D. Gross and T. Seelig, *Bruchmechanik*. Berlin Heidelberg: Springer, 1996, vol. 2.

[163] M. Kütemeyer, D. Shandler, D. Koch, and M. Friess, "Reactive Melt Infiltration of Boron Containing Fiber Reinforced Preforms Forming a ZrB2 Matrix a ZrB2 Matrix," *Processing and Properties of Advanced Ceramics and Composites VII: Ceramic Transactions*, vol. 252, p. 169, 2015.

[164] Y. Yuan and T. R. Lee, "Contact angle and wetting properties," *Springer Series in Surface Sciences*, vol. 51, no. 1, pp. 3–34, 2013.

[165] J. G. Li and H. Hausner, "Reactive wetting in the liquid-silicon/solid-carbon system," *Journal of the American Ceramic Society*, vol. 79, no. 4, pp. 873–880, 1996.

[166] R. Kennedy and A. Karantzalis, "The incorporation of ceramic particles in molten aluminium and the relationship to contact angle data," *Materials Science and Engineering: A*, vol. 264, no. 1-2, pp. 122–129, 1999.

[167] F. Valenza, M. L. Muolo, A. Passerone, G. Cacciamani, and C. Artini, "Control of interfacial reactivity between ZrB2and Ni-based brazing alloys," *Journal of Materials Engineering and Performance*, vol. 21, no. 5, pp. 660–666, 2012.

[168] X. B. Zhou and J. T. M. De Hosson, "Reactive wetting of liquid metals on ceramic substrates," *Acta Materialia*, vol. 44, no. 2, pp. 421–426, 1996.

[169] J. V. Naidich, "The wettability of solids by liquid metals," in *Progress in surface and membrane science*. Elsevier, 1981, vol. 14, pp. 353–484.

[170] O. Dezellus, S. Jacques, F. Hodaj, and N. Eustathopoulos, "Wetting and infiltration of carbon by liquid silicon," in *Journal of Materials Science*, vol. 40, no. 9-10, 2005, pp. 2307–2311.

[171] M. L. Muolo, E. Ferrera, and A. Passerone, "Wetting and spreading of liquid metals on ZrB2-based ceramics," in *Journal of Materials Science*, vol. 40, no. 9-10, 2005, pp. 2295–2300.

[172] M. Aizenshtein, N. Froumin, and N. Frage, "The nature of TiB2 wetting by Cu and Au," *Journal of materials engineering and performance*, vol. 21, no. 5, pp. 655–659, 2012.

[173] S. K. Rhee, "Wetting of TaC by Liquid Cu and Liquid Ag," *Journal of the American Ceramic Society*, vol. 55, no. 3, pp. 157–159, 1972.

[174] F. Monteverde and A. Bellosi, "Beneficial effects of AlN as sintering aid on microstructure and mechanical properties of hot-pressed ZrB2," *Advanced Engineering Materials*, vol. 5, no. 7, pp. 508–512, 2003.

[175] ——, "Development and characterization of metal-diboride-based composites toughened with ultra-fine SiC particulates," *Solid State Sciences*, vol. 7, no. 5, pp. 622–630, 2005.

[176] R. Klein, M. Desmaison-Brut, P. Ginet, A. Bellosi, and J. Desmaison, "Wettability of silicon nitride ceramic composites by silver, copper and silver copper titanium alloys," *Journal of the European Ceramic Society*, vol. 25, no. 10 SPEC. ISS., pp. 1757–1763, 2005.

[177] S. Hernesniemi, "Wetting and Reactivity between Nitride Ceramics and Molten Copper and Silver Alloys," Dissertation, Tampere University of Technology, 2012. [Online]. Available: https://trepo.tuni.fi//handle/10024/114030

[178] G. A. Yasinskaya, "The wetting of refractory carbides, borides, and nitrides by molten metals," *Soviet Powder Metallurgy and Metal Ceramics*, vol. 5, no. 7, pp. 557–559, jul 1966.

[179] R. Voitovitch, A. Mortensen, F. Hodaj, and N. Eustathopoulos, "Diffusion-limited reactive wetting: Study of spreading kinetics of Cu-Cr alloys on carbon substrates," *Acta Materialia*, vol. 47, no. 4, pp. 1117–1128, 1999.

[180] J. Drelich, J. D. Miller, and R. J. Good, "The effect of drop (bubble) size on advancing and receding contact angles for heterogeneous and rough solid surfaces as observed with sessile-drop and captive-bubble techniques," *Journal of Colloid and Interface Science*, vol. 179, no. 1, pp. 37–50, 1996.

[181] P. J. Uggowitzer, G. C. Gullo, and A. Wahlen, "Metallkundliche aspekte bei der semi-solid formgebung von leichtmetallen," ETH Zürich, Zürich, Tech. Rep., 2000.

[182] E. E. Underwood, "Quantitative Stereology Chap. 5 Addison-Wesley," *Reading, Mass*, 1970.

[183] A. D'Angio', J. Zou, J. Binner, H. B. Ma, G. E. Hilmas, and W. G. Fahrenholtz, "Mechanical properties and grain orientation evolution of zirconium diboride-zirconium carbide ceramics," *Journal of the European Ceramic Society*, vol. 38, no. 2, pp. 391–402, 2017.

[184] S. Hermanek, "Boron chemistry: introduction," *Chemical Reviews*, vol. 92, no. 2, p. 175, 1992.

[185] A. Holleman and E. Wiberg, *Lehrbuch der Anorganischen Chemie*. Berlin: Walter de Gruyter GmbH & Co KG, 1995, vol. 53.

[186] E. Muetterties, *Boron hydride chemistry*. Amsterdam: Elsevier, 2012.

[187] J. T. Mague, "Gmelin Handbook of Inorganic Chemistry. 8th Edition Rh," *Organometallics*, vol. 3, no. 6, p. 948, 1984.

[188] D. Das and K. Kumar, "Chemical vapor deposition of boron on a beryllium surface," *Thin Solid Films*, vol. 83, no. 1, pp. 53–60, sep 1981.

[189] J. Berjonneau, G. Chollon, and F. Langlais, "Deposition Process of Amorphous Boron Carbide from CH4/ BCl3/ H2 Precursor," *Journal of the Electrochemical Society*, vol. 153, no. 12, pp. C795–C800, 2006.

[190] L. Vandenbulcke and G. Vuillard, "Structure of Deposits-Process Relationships in the Chemical Vapor Deposition of Boron," *Journal of The Electrochemical Society*, vol. 124, no. 12, pp. 1937–1942, 1977.

[191] ——, "Chemical vapor deposition of amorphous boron on massive substrates," *Journal of The Electrochemical Society*, vol. 123, no. 2, pp. 278–285, 1976.

[192] P. Colombo, G. Mera, R. Riedel, and G. D. Sorarù, "Polymer-Derived Ceramics: 40 Years of Research and Innovation in Advanced Ceramics," *Journal of the American Ceramic Society*, vol. 93, no. 7, pp. 1805–1837, 2010.

[193] R. Hyam, K. Subhedar, and S. Pawar, "Effect of particle size distribution and zeta potential on the electrophoretic deposition of boron films," *Colloids and Surfaces A: Physicochemical and Engineering Aspects*, vol. 315, no. 1-3, pp. 61–65, 2008.

[194] R. S. Hyam, K. M. Subhedar, and S. H. Pawar, "Suspension stability studies for the electrophoretic deposition of boron films," *Colloids and Surfaces A: Physicochemical and Engineering Aspects*, vol. 297, no. 1-3, pp. 172–178, 2007.

[195] H. F. Rizzo, "Oxidation of Boron at Temperatures between 400 and 1300° C in Air," in *Boron Synthesis, Structure, and Properties*. Springer, 1960, pp. 175–189.

[196] A. Jain and S. Anthonysamy, "Oxidation of boron carbide powder," *Journal of Thermal Analysis and Calorimetry*, vol. 122, no. 2, pp. 645–652, 2015.

[197] Y. Q. Li and T. Qiu, "Oxidation behaviour of boron carbide powder," *Materials Science and Engineering: A*, vol. 444, no. 1-2, pp. 184–191, 2007.

[198] W. Zhang, S. Sun, J. Xu, and Z. Chen, "Kinetic Study of Boron Oxide Prepared by Dehydration of Boric Acid." *Asian Journal of Chemistry*, vol. 27, no. 3, 2015.

[199] S. Balcı, N. A. Sezgi, and E. Eren, "Boron oxide production kinetics using boric acid as raw material," *Industrial & Engineering Chemistry Research*, vol. 51, no. 34, pp. 11 091–11 096, 2012.

[200] S. Wiebel, "Untersuchung zur thermischen Langzeitstabilität von Epoxidharzen der elektrischen Isoliertechnik in Abhängigkeit von oxidativen Umgebungseinflüssen," Dissertation, Technische Universität Darmstadt, 2012.

[201] G. Ziegler, I. Richter, and D. Suttor, "Fiber-reinforced composites with polymer-derived matrix: processing, matrix formation and properties," *Composites Part A: Applied Science and Manufacturing*, vol. 30, no. 4, pp. 411–417, 1999.

[202] A. Alizadeh, E. Taheri-Nassaj, and N. Ehsani, "Synthesis of boron carbide powder by a carbothermic reduction method," *Journal of the European Ceramic Society*, vol. 24, no. 10, pp. 3227–3234, 2004.

[203] C. H. Jung, M. J. Lee, and C. J. Kim, "Preparation of carbon-free B4C powder from B2O3 oxide by carbothermal reduction process," *Materials Letters*, vol. 58, no. 5, pp. 609–614, 2004.

[204] P. Singh, B. Singh, M. Kumar, and A. Kumar, "One step reduction of Boric Acid to boron carbide nanoparticles," *Ceramics International*, vol. 40, no. 9 PART B, 2014.

[205] A. Napolitano, P. B. Macedo, and E. G. Hawkins, "Viscosity and Density of Boron Trioxide," *Journal of the American Ceramic Society*, vol. 48, no. 12, pp. 613–616, 1965.

[206] P. Li, A. C. Ghose, and G. Su, "Viscosity Determination of Boron Oxide and Binary Borates," *Journal of the American Ceramic Society*, vol. 45, no. 2, pp. 83–88, 1962.

[207] M. Aslan, R. Nass, R. Nonninger, and H. Schmidt, "Sinterkörper aus Siliciumcarbid oder Borcarbid und Verfahren zu deren Herstellung," German Patent DE4233626A1 April 07, 1994.

[208] S. Goldberg and C. Su, "New advances in boron soil chemistry," in *XU F. et al. (eds) Advances in Plant and Animal Boron Nutrition.* Springer, Dordrecht, 2007, pp. 313–330. [Online]. Available: https://doi.org/10.1007/978-1-4020-5382-5_31

[209] T. Reimer, I. Petkov, D. Koch, M. Frieß, and C. Dellin, *Fabrication and Characterization of C/C-SiC Material Made with Pitch-Based Carbon Fibers.* John Wiley & Sons, Ltd, 2015, ch. 28, pp. 277–293. [Online]. Available: https://ceramics.onlinelibrary.wiley.com/doi/abs/10.1002/9781119183860.ch28

[210] C. Sauder, J. Lamon, and R. Pailler, "The tensile behavior of carbon fibers at high temperatures up to 2400 °C," *Carbon*, vol. 42, no. 4, pp. 715–725, jan 2004.

[211] T. A. Parthasarathy, R.A. Rapp, M. Opeka, and R.J. Kerans, "A model for the oxidation of ZrB2, HfB2 and TiB2," *Acta Materialia*, vol. 55, no. 17, pp. 5999–6010, 2007.

[212] F. Vautard, J. Dentzer, M. Nardin, J. Schultz, and B. Defoort, "Influence of surface defects on the tensile strength of carbon fibers," *Applied Surface Science*, vol. 322, pp. 185–193, dec 2014.

[213] H. Ming-Yuan and J. W. Hutchinson, "Crack deflection at an interface between dissimilar elastic materials," *International Journal of Solids and Structures*, vol. 25, no. 9, pp. 1053–1067, 1989.

[214] B. Ahn, W. Curtin, T. Parthasarathy, and R. Dutton, "Criteria for crack deflection/penetration criteria for fiber-reinforced ceramic matrix composites," *Composites Science and Technology*, vol. 58, no. 11, pp. 1775–1784, 1998.

[215] W. A. Curtin, "Theory of Mechanical Properties of Ceramic-Matrix Composites," *Journal of the American Ceramic Society*, vol. 74, no. 11, pp. 2837–2845, nov 1991.

[216] A. Chulya, J. P. Gyekenyesi, and R. T. Bhatt, "Mechanical behavior of fiber reinforced SiC/RBSN ceramic matrix composites: Theory and experiment," in *ASME 1991 International Gas Turbine and Aeroengine Congress and Exposition.* American Society of Mechanical Engineers, 1991.

[217] H. Hu, J. Wang, Y. Zhang, Q. Wang, and X. He, "Preparation and Characterization of C/SiC-ZrB2 Composites via Precursor Infiltration and Pyrolysis Process," in *Ceramic Materials and Components for Energy and Environmental Applications.* John Wiley & Sons, Inc., 2010, pp. 467–472.

[218] S. Pompidou and J. Lamon, "Analysis of crack deviation in ceramic matrix composites and multilayers based on the Cook and Gordon mechanism," *Composites science and technology*, vol. 67, no. 10, pp. 2052–2060, 2007.

[219] S. Zhang, S. Wang, Y. Zhu, and Z. Chen, "Fabrication of ZrB2–ZrC-based composites by reactive melt infiltration at relative low temperature," *Scripta Materialia*, vol. 65, no. 2, pp. 139–142, jul 2011.

[220] D. Loidl, H. Peterlik, O. Paris, M. Müller, M. Burghammer, and C. Riekel, "Poisson ratio of carbon fibers at the microscopic and the nanoscopic scale," in *International Conference on Carbon*. Citeseer, 2004.

[221] S. Kaur, "Single-Source-Precursor Synthesis of SiC-Based Ceramic Nanocomposites for Energy-Related Applications," Dissertation, Technische Universität Darmstadt, Darmstadt, 2016.

[222] A. Gardziella, L. A. Pilato, and A. Knop, *Phenolic resins: chemistry, applications, standardization, safety and ecology*. Springer Science & Business Media, 2013.

[223] J. Hetper and M. Sobera, "Thermal degradation of novolac resins by pyrolysis-gas chromatography with a movable reaction zone," *Journal of Chromatography A*, vol. 833, no. 2, pp. 277–281, feb 1999.

[224] C. A. Lytle, W. Bertsch, and M. McKinley, "Determination of novolac resin thermal decomposition products by pyrolysis-gas chromatography-mass spectrometry," *Journal of Analytical and Applied Pyrolysis*, vol. 45, no. 2, pp. 121–131, 1998.

[225] M. Sobera and J. Hetper, "Pyrolysis-gas chromatography-mass spectrometry of cured phenolic resins," *Journal of Chromatography A*, vol. 993, no. 1-2, pp. 131–135, 2003.

[226] K. J. Millman and M. Aivazis, "Python for Scientists and Engineers," *Computing in Science Engineering*, vol. 13, no. 2, pp. 9–12, 2011.

[227] P. Virtanen, R. Gommers, T. E. Oliphant, M. Haberland, T. Reddy, D. Cournapeau, E. Burovski, P. Peterson, W. Weckesser, J. Bright, S. J. van der Walt, M. Brett, J. Wilson, K. J. Millman, N. Mayorov, A. R. J. Nelson, E. Jones, R. Kern, E. Larson, C. J. Carey, İ. Polat, Y. Feng, E. W. Moore, J. VanderPlas, D. Laxalde, J. Perktold, R. Cimrman, I. Henriksen, E. A. Quintero, C. R. Harris, A. M. Archibald, A. H. Ribeiro, F. Pedregosa, P. van Mulbregt, and SciPy 1.0 Contributors, "SciPy 1.0: Fundamental Algorithms for Scientific Computing in Python," *Nature Methods*, vol. 17, pp. 261–272, 2020.

[228] J. D. Hunter, "Matplotlib: A 2D Graphics Environment," *Computing in Science Engineering*, vol. 9, no. 3, pp. 90–95, 2007.

[229] H. Lipowsky and E. Arpaci, *Properties of the Copper Materials*. John Wiley & Sons, Ltd, 2006, ch. 6, pp. 55–77. [Online]. Available: https://onlinelibrary.wiley.com/doi/abs/10.1002/9783527611652.ch6

[230] R. Kieffer, G. Jangg, and P. Ettmayer, *Sondermetalle: Metallurgie/Herstellung/Anwendung*. Wien: Springer-Verlag, 2013.

[231] F. Benesovsky, *Metalle für die Raumfahrt: Vorträge, gehalten auf dem 5. Plansee Seminar "De Re Metallica," 22. bis 26. Juni 1964, Reutte/Tirol*, ser. Plansee Seminar "De Re Metallica" / Plansee Seminar De Re Metallica Reutte: Plansee Seminar "De Re Metallica". Reutte, Tirol: Metallwerk Plansee, 1965.

[232] M. Caccia, M. Tabandeh-Khorshid, G. Itskos, A. R. Strayer, A. S. Caldwell, S. Pidaparti, S. Singnisai, A. D. Rohskopf, A. M. Schroeder, and D. Jarrahbashi, "Ceramic–metal composites for heat exchangers in concentrated solar power plants," *Nature*, vol. 562, no. 7727, p. 406, 2018.

[233] P. Galizia, S. Failla, L. Zoli, and D. Sciti, "Tough salami-inspired cf/zrb2 uhtcmcs produced by electrophoretic deposition," *Journal of the European Ceramic Society*, vol. 38, no. 2, pp. 403 – 409, 2018. [Online]. Available: http://www.sciencedirect.com/science/article/pii/S0955221917306635

[234] S. Failla, P. Galizia, L. Zoli, A. Vinci, and D. Sciti, "Toughening effect of non-periodic fiber distribution on crack propagation energy of UHTC composites," *Journal of Alloys and Compounds*, vol. 777, pp. 612–618, 2019.

[235] M. Kütemeyer, T. Helmreich, S. Rosiwal, and D. Koch, "Influence of zirconium-based alloys on manufacturing and mechanical properties of ultra high temperature ceramic matrix composites," *Advances in Applied Ceramics*, vol. 117, no. sup1, pp. s62–s69, 2018. [Online]. Available: https://doi.org/10.1080/17436753.2018.1509810

[236] D. D. Hall and I. Mudawar, "Optimization of quench history of aluminum parts for superior mechanical properties," *International journal of heat and mass transfer*, vol. 39, no. 1, pp. 81–95, 1996.

[237] T. A. Parthasarathy, R. A. Rapp, M. Opeka, and M. K. Cinibulk, "Modeling Oxidation Kinetics of SiC-Containing Refractory Diborides," *Journal of the American Ceramic Society*, vol. 95, no. 1, pp. 338–349, 2012.

[238] J. Binner, M. Porter, B. Baker, J. Zou, V. Venkatachalam, V. R. Diaz, A. D'Angio, P. Ramanujam, T. Zhang, and T. S. R. C. Murthy, "Selection, processing, properties and applications of ultra-high temperature ceramic matrix composites, uhtcmcs – a review," *International Materials Reviews*, vol. 65, no. 7, pp. 389–444, 2020. [Online]. Available: https://doi.org/10.1080/09506608.2019.1652006

A. Appendix

In this chapter, important equations and theoretical contexts are listed, which have been applied in the scope of this thesis. Furthermore, the implementation of important evaluation methods is dealt with.

A.1. Calculation of Phase, Mass and Volume Fractions

As information for the composition of multiple phase systems (e.g. via EDX), different units are used depending on the application. Selected equations for the conversion of the different units are listed below:

- Conversion of phase to mass fraction:

$$w_i = \frac{m_i}{m_T} = \frac{M_i \cdot n_i}{\sum_{i=1}^{n} m_i} = \frac{M_i \cdot \chi_i}{\sum_{i=1}^{n} (M_i \cdot \chi_i)} \tag{A.1}$$

- Conversion of phase to volume fraction:

$$\varphi_i = \frac{V_i}{V_T} = \frac{\frac{m_i}{\rho_i}}{\sum_{i=1}^{n} (\frac{m_i}{\rho_i})} = \frac{\frac{M_i \cdot n_i}{\rho_i}}{\sum_{i=1}^{n} (\frac{M_i \cdot n_i}{\rho_i})} = \frac{\frac{M_i \cdot n_i}{\rho_i \cdot n_T}}{\sum_{i=1}^{n} (\frac{M_i \cdot n_i}{\rho_i \cdot n_T})} = \frac{V_{mol,i} \cdot \chi_i}{\sum_{i=1}^{n} (V_{mol,i} \cdot \chi_i)} \tag{A.2}$$

- Conversion of mass to volume fraction:

$$\varphi_i = \frac{V_i}{V_T} = \frac{\frac{m_i}{\rho_i}}{\sum_{i=1}^{n} (\frac{m_i}{\rho_i})} = \frac{\frac{m_i}{\rho_i \cdot m_T}}{\sum_{i=1}^{n} (\frac{m_i}{\rho_i \cdot m_T})} = \frac{\frac{w_i}{\rho_i}}{\sum_{i=1}^{n} (\frac{w_i}{\rho_i})} \tag{A.3}$$

with:

χ_i	phase fraction of element i $[-]$
w_i	mass fraction of element i $[-]$
φ_i	volume fraction of elment i $[-]$
m_i	mass of element i $[g]$
m_T	total mass of all phases $[g]$
n_i	phase amount of element i $[mol]$
n_T	total phase amount of all phases $[mol]$
V_i	volume of element i $[cm^3]$
$V_{mol,i}$	molar volume of element i $[cm^3/mol]$
V_T	total volume of all phases $[cm^3]$
M_i	molar mass of element i $[g/mol]$
ρ_i	density of element i $[g/cm^3]$

The percentage share can be determined from the each fraction. Conversion of the equations listed, also enables unit conversion in the opposite direction.

A.2. Image Phase Analysis

ImageJ is a software which can evaluated images according to gray scales. In this thesis it is used to determine the matrix composition or volume fractions. The selected are has to be representative for the investigated sample or multiple images have to be evaluated. Furthermore, it is assumed for the determination of the composition that the area components (2D information) analyzed by the image section can be transferred to the third dimension in order to be able to make statements about volume components (3D information). The procedure for the determination of the matrix composition by means of ImageJ is shown here in detail using the example of a ZrB_2/ZrC matrix, manufactured by RMI: The requirement for good image evaluation is a high-contrast image in which the different phases are represented with as many different grey levels as possible. With the ZrB_2/ZrC matrix, the AsB detector is particularly suitable when taking SEM images, showing density differences with high contrast. In the example shown, image A.1 a), ZrB_2 is shown as dark gray. ImageJ can analyze different gray scale ranges and determine the area fractions of the selected range. The selected gray scale range is marked in red, see image A.1 b). Depending on the contrast and difference of the gray levels of the raw image, minor errors may occur in the phases to be separated. For example, very dark grey ZrB_2 areas can be mistakenly counted as ZrC areas. This must be taken into account when determining the grey scale ranges. The area fractions of the ZrB_2 can then be used to determine to the volume fraction of the respective phase with a 3-dimensional approach.

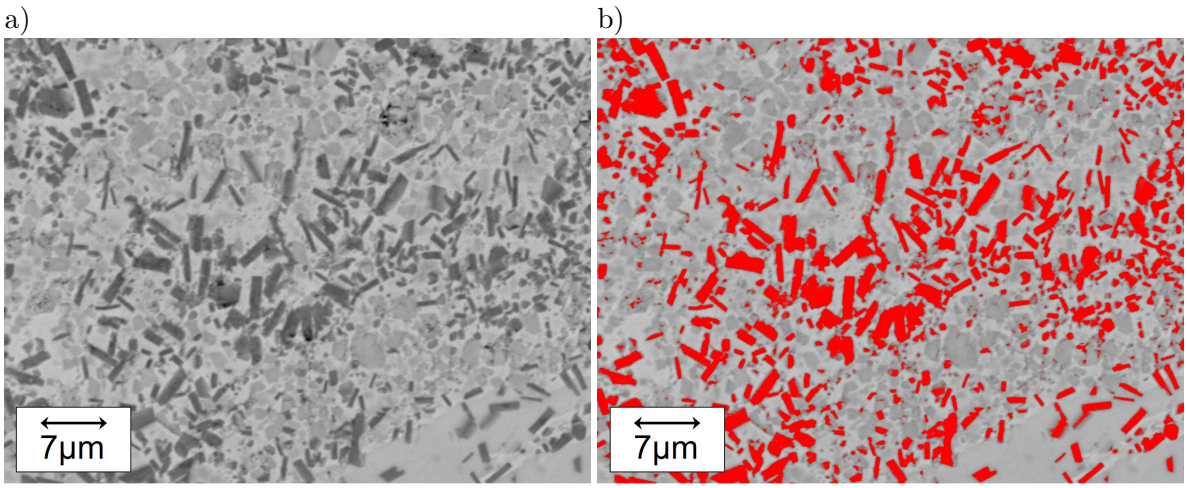

Figure A.1.: Analysis of gray scale SEM images for phase analysis; a) showing the gray scale image of a ZrB_2/ZrC matrix and b) the selected gray section of ZrB_2 marked in red

B. List of Publications

Glass, David E., et al. "Testing of DLR C/C-SiC and C/C for HIFiRE 8 scramjet combustor." 19th AIAA International Space Planes and Hypersonic Systems and Technologies Conference. 2014.

Kütemeyer, Marius, et al. "Reactive Melt Infiltration of Boron Containing Fiber Reinforced Preforms Forming a ZrB2 Matrix." Processing and Properties of Advanced Ceramics and Composites VII: Ceramic Transactions, Volume 252 (2015): 169-180.

Glass, David E., et al. "Testing of refractory composites for scramjet combustors." Journal of Propulsion and Power 32.6 (2016): 1550-1556.

Kütemeyer, Marius, et al. "Fabrication of ultra high temperature ceramic matrix composites using a reactive melt infiltration process." Journal of the European Ceramic Society 36.15 (2016): 3647-3655.

Dittert, C., and Kütemeyer, M. "Octra-Optimized Ceramic for Hypersonic Application with Transpiration Cooling." Advances in High Temperature Ceramic Matrix Composites and Materials for Sustainable Development 263 (2017): 389

Dittert, Christian, et al. "Process Optimization of Ceramic Matrix Composites for Ultrasonically Absorptive TPS Material." 2018 Joint Thermophysics and Heat Transfer Conference. 2018.

Kütemeyer, Marius, et al. "Influence of zirconium-based alloys on manufacturing and mechanical properties of ultra high temperature ceramic matrix composites." Advances in Applied Ceramics 117.sup1 (2018): s62-s69.

Vinci, Antonio, et al. "Reactive melt infiltration of carbon fibre reinforced ZrB2/B composites with Zr2Cu." Composites Part A: Applied Science and Manufacturing 137 (2020): 105973.